The electron quantum radar : interferometric detection of time-dependent electromagnetic fields at the sub-nanosecond time scale and using single electron excitations

Hubert Souquet-Basiège

THÈSE
en vue de l'obtention du grade de Docteur, délivré par

l'ÉCOLE NORMALE SUPERIEURE DE LYON

École Doctorale N°52
Physique & Astrophysique de Lyon

Discipline : Physique

Soutenue publiquement le 29/09/2023, par :

Hubert Souquet-Basiège

Le radar à électrons

Détection interférométrique de champ électromagnétiques dépendant du temps aux échelles sub-nanoseconde au moyen d'excitations à un électron

---

Devant le jury composé de :

ANTHORE, Anne	PR	Université Paris Cité	Rapporteure
FERRARO, Dario	PR	Università di Genova	Rapporteur
BIENFAIT, Audrey	CR CNRS	ENS de Lyon	Examinatrice
HUARD, Benjamin	PR	ENS de Lyon	Examinateur
BAUERLE, Christopher	DR CNRS	Institut Néel	Examinateur
PARMENTIER, François	CR CEA	CEA Saclay	Examinateur
DEGIOVANNI, Pascal	DR CNRS	ENS de Lyon	Directeur de thèse

Contents

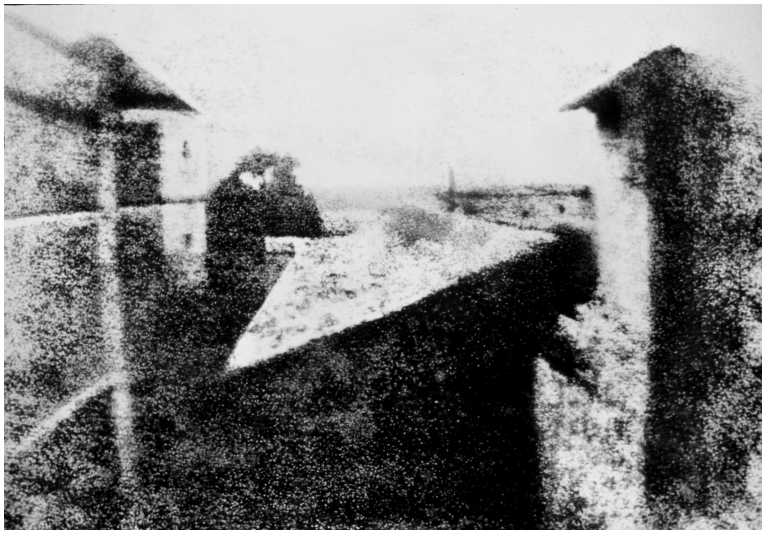

Figure 1: The heliographic image “Point de vue du gras” by Nicéphore Niépce is known as the oldest photography taken in Human history (1827).

Introduction

0.1 Context and motivation

0.1.1 Probing matter with light

The image presented in Fig. 1 is the first known recording of light using human technology. It was captured in 1827 by the French inventor Nicéphore Niépce from a window of his abode in Saint-Loup-de-Varennes, a small village in France. This was a formidable achievement for the era: Niépce invented a photosensitive plate that could harness light and process to cut-off its photosensitivity, thereby permitting observation without degradation. Of the entire electromagnetic spectrum, the visible spectrum was the most natural part for humans to invent image recording systems given our innate ability to perceive it with our eyes. But other windows of the electromagnetic spectrum were explored a few decades after Niépce's breakthrough with Roentgen's first X-ray image and also with the development of radio technology towards the end of the 19-th century.

In 1888, the German physicist H. Hertz conducted the first demonstration of radio wave transmission and measurement in the atmosphere with the apparatus displayed on Fig. 2. By applying a voltage pulse to an antenna, thereby radiating a 454 MHz wave, he detected the same signal using a secondary antenna. This groundbreaking experiment pioneered the development of wireless communication thanks to the excellent propagation properties of radio frequencies and microwaves in the atmosphere. From a basic science perspective, his experiment confirmed the electromagnetic nature of radio waves and comforted Maxwell's work on the unification of electric and magnetic phenomena in his classical theory of electromagnetism. Notably, he observed that radio waves are reflected by metal surfaces, a characteristic of crucial importance as we shall see now.

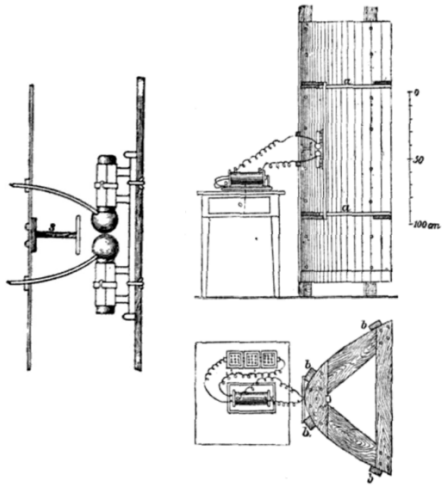

Figure 2: Schematics of the first radio transmitter and antenna used by H. Hertz in 1888 to demonstrate that radio waves, as much as light, behave as an electromagnetic field.

In 1897, Alexander Popov, a physicist affiliated with the Imperial Russian Navy, inadvertently discovered that radio waves could be used for detection during a radio communication test between two ships based in the Baltic sea: a third ship interrupted the signal as it sailed between them, providing the first evidence of using radio waves for detection. A few years later, in 1903, Hülsmeyer, inspired by the reflective properties of radio waves on metallic surfaces, devised the Telemobiloskop which is an active radio detection system. This technology was able to point out the presence of a ship within a 3 km range in a given direction but was not able to characterize the distance of the ship. Although it was originally motivated by proximal ships detection and helping navigation in low visibility conditions, its relatively short range and the problem of multiple echoes prevented this technology to become widely used and it fell into oblivion. During the 1920s and 1930s, a multiplicity of progresses in antenna design, radio emitters and electronics enabled people to emit very short and intense focused radio pulses and to measure their time of flight when reflected off a metallic surface. This gave rise to a descendent of Hülsmeyer's invention: the Radio Detection And Ranging system (RADAR) which unraveled its full strategic potential during the battle of Britain in the early months of World War II. Since these

groundbreaking developments, radiofrequency and microwave detection has evolved tremendously in accuracy, range, and power. Among all the developments, the continuous wave radars used frequency modulated signals fed into an interferometric design to obtain information both on the range and velocity of the target objects by comparing the reflected wave with the original one kept as a reference.

The multiple avatars of the RADAR as well as its optical version called LIDAR (Light Detection and Ranging) are examples of electromagnetic interferometers used to probe matter. Other examples include interferometric microscopy which aims at approaching the ultimate limits of optical resolution [105, 121]. However, with the advent of quantum theory, it became clear that matter and light are in a sense dual to each other: quantum light is described in terms of particles with the introduction of the photon and the quantum behavior of matter is associated with probability amplitudes which behave as waves. The Kapitza Dirac effect which consists of the diffraction of matter by a standing wave of light [112, 89] was the first historical example of this dual point of view.

Following this line of thought, one can then ask how to probe light or more generally electromagnetic radiation using matter. As we will see, this will bring us naturally to the idea of the electron radar which is the topic of this PhD.

0.1.2 Probing light with matter

Atomic interferometers directly descend from this idea which consists in exploiting particle/wave duality unraveled even before the full formalization of quantum theory. They were experimentally demonstrated thirty years ago [39, 115] and since then have been developed and applied as sensors for several quantities, including measuring rotation with the Ramsey–Bordé interferometer [25] (see Ref. [50] for a review). Applications of atomic interferometers concern basic science (high precision measurements of the fine structure constant and of $\hbar/M$ where M is the mass of interfering particles, tests of relativity) but also measurement of the local gravitational field. Concerning this latter application, high precision gravimeters able to reach the 10^{-10} sensitivity on the measurement of the local gravitational field have been commercialized by the MuQuans company[1] based in Bordeaux. Remarkably, matter interferometers have also been used to obtain information on quantum

[1] Web site: `https://www.muquans.com`

electromagnetic fields, thereby implementing the dual of what a radar does, *i.e.* probing electromagnetic fields using quantum matter wave interferences.

A prominent example is the Rydberg atom interferometer used as a sensor for quantum electromagnetic fields, demonstrated in the seminal experiments conducted by S. Haroche and his team. In a series of remarkable experiments [28, 131, 88, 94, 27, 54, 150] (see [100] for a review as well as S. Haroche's Nobel lecture for an historical perspective), they have used two level systems (built from Rydberg atoms) in a Ramsey interferometer to capture information about the number operator for a trapped electromagnetic microwave mode (see Fig. 3). The phase information retrieved from the Ramsey interferometer is related to the cavity field through the ac-Stark shift, therefore the phase information is related to the photon number in the cavity [100]. In a nutshell, modulo experimental imperfections, this Ramsey interferometer performs a QND measurement [26] of the photon number. It should also be noted that Rydberg atoms based quantum electrometers [63] have reached record sensitivities but for static fields.

0.1.3 Sensing electromagnetic fields on a short time scale

All these experiments demonstrate the performances and usefulness of matter interferometers in probing quantum and classical electromagnetic fields. Nevertheless, accessing the dynamical properties of a field over very short time scales is still extremely challenging. However, the rapid development of quantum technologies based on solid state system (superconducting circuits, semi-conducting platforms for quantum spin manipulation, etc) call for a practical technology able to probe quantum electromagnetic fields on a sub-nano second time scale which are the typical dynamical time scales for the quantum dynamics of such solid state quantum mesoscopic devices.

Fast electrical modulation of optical systems enables measuring the electric field up to a THz-bandwidth [37]. However, such optical systems are not suitable for quantum mesoscopic devices due to the difficulty of combining optics and microwave electronics within the same cryostat and the large size of the sensing area (25 µm). On-chip systems based on nano-mechanical resonators [47, 43], rf-capacitive gate based sensing [1], NV-centers in diamond [57] as well as quantum dots have been demonstrated, often as charge sensors able to detect a single electron charge at a few tens of nm. But their bandwidth is still limited to 1

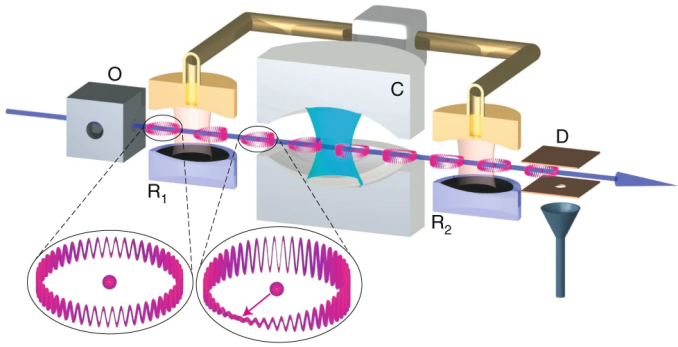

Figure 3: (Extracted from [99]) Ramsey interferometric scheme for photon number in a cavity. Initially being prepared in the appropriate circular Rydberg state $|g\rangle$. These are states where the last electron of is sent far from the ionic core, in a very high principal quantum number n and $l = m = n - 1$ quantum state. These circular Rydberg atoms are then sent in a superposition of two circular Rydberg states $|e\rangle$ and $|g\rangle$ whose main quantum number n differ by 1 by a classical resonant microwave pulse (R1). The resulting superposition, which then has a large dipolar momentum, interacts with a quantum electromagnetic mode in a cavity (C), with a dispersive phase shift depending on their state and proportional to the photon number in the cavity, before they are again rotated by a classical microwave pulse in (R2). A photo-ionization detector performs a measurement of the state of the two level atom in the $(|e\rangle, |g\rangle)$ basis.

to 10 MHz at best. Moreover, they are not designed to detect quantum features of the electromagnetic field such as non-classical fluctuations.

Reaching sub-nanosecond time scales or, equivalently tens to hundreds of GHz bandwidth is a formidable challenge since we are speaking about a measurement bandwidth comparable to the frequencies associated with the microwave spectrum. It is as if we would probe optical radiation on the femto-second time scale, a notoriously difficult challenge if one remembers what it took to develop and master ultra-short coherent classical pulses light sources [180, 97]. Ideally, such a system should be somehow tunable in terms of time resolution and frequency range within the GHz to THz window. And finally, it should be sensitive enough to probe quantum radiation consisting of one to a few photons due to the very low powers at which mesoscopic quantum devices are operated. The central challenge is to identify a technology that could fullfill these requirements. This thesis explores the potential of Electron Quantum Optics (EQO) to achieve this goal.

0.2 Single electrons for probing electromagnetic fields

Over the last 15 years, electron Quantum Optics emerged from the development of on-demand single electron sources [70, 59, 11] and has changed our approach of quantum coherent in micro and nano-electronics. It has allowed access to the wave functions of individual excitations carried in quantum electrical currents propagating through ballistic quantum conductors such as quantum Hall edge channels [23]. After a decade of developments, it has reached a maturity with the demonstration of electronic interferometry at the single and two particle levels. This culminated in the implementation of tomography protocols [110, 17, 72] in a variety of systems. When coupled to signal processing algorithms [163], they have given access to the individual wave functions of electrons and hole propagating in a quantum Hall edge channel, together with their emission probabilities and coherences [17]. Moreover, fifteen years of progresses in electronic decoherence modelization [181, 126, 127, 52, 125, 189, 65, 176, 35, 106, 157], characterization via various electronic interferometry experiments [161, 134, 183, 159] and also in electronic decoherence control [2, 104, 61] have potentially paved the way to highly controlled single electron interferometry experiments. This unprecedented ability to generate, characterize and possibly manipulate electronic quantum states in

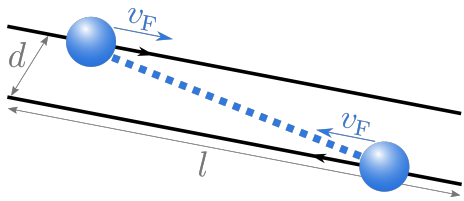

Figure 4: Single electrons collider. It's a setup made of two channel separated by a distance d and capacitively coupled over a length l. Two counter-propagating electrons propagating at velocity v_F interact through Coulomb interaction.

a quantum conductor suggests that EQO has reached a level of maturity sufficient for exploring its diverse applications. A potential sensing application that has gathered part of the EQO community in a collaborative research project called SEQUOIA (Single-electron quantum optics for quantum-enhanced measurements)[2] funded by the European Metrology Program for Innovation and Research is the development of interferometric quantum sensing of quantum electromagnetic fields. This is the idea of the electron radar which we will now introduce and explain.

0.2.1 Phase shifts in electron/electron collision

Electrons, given their charge, are susceptible to their surrounding electromagnetic environment. Such an environment can thus alter the electron's quantum state. A single electron state is defined by its corresponding wave packet. Therefore, an electromagnetic field exhibiting rapid time-dependence is anticipated to imprint a phase modulation on the wave packet.

We can estimate this phase shift when electron and radiation evolve in a mesoscopic physics design as depicted in Fig. 4. This figure illustrates two one-dimensional channels separated by a distance d and capacitively coupled over a distance l. The probing electron propagates in one channel while the radiation is contained in the other. This setup aids in determining if a single electron can efficiently probe the field radiated by another electron counter-propagating in the second channel. This configuration allows for a dominant Coulomb interaction over the all length l.

Assuming both electrons to be in an initial state of free propagation

[2]Web site: `https://www.ptb.de/empir2018/sequoia/project/`

at a characteristic velocity v_F, dependent on the circuit material, their states will be modified by a phase factor $\mathrm{e}^{\mathrm{i}\delta\phi_{\mathrm{cou}}}$. The electric phase shift $\delta\phi_{\mathrm{cou}}$ is computed as

$$\delta\phi_{\mathrm{cou}} = \frac{e}{\hbar}\int V(\mathbf{x}(t),t)\,\mathrm{d}t \tag{1}$$

where $V(\mathbf{x},t)$ denotes the potential experienced by the electron along the trajectory $t \mapsto \mathbf{x}(t)$. Because the electronic velocity v_F is much smaller than c and the size of the system is much smaller than the wavelength of the radiation emitted at frequencies v_F/l, propagation effects for the EM field can be ignored and a quasi-stationary approximation of electromagnetism can be applied (see below for numerical estimates). In the present case, the phase shift is mostly electric and $V(\mathbf{x},t)$ is obtained from Coulomb's law. After calculation, the phase shift is obtained as

$$\delta\phi_{\mathrm{cou}} = \alpha_{\mathrm{eff}}\,\mathrm{arcsinh}\,(l/d) \tag{2a}$$

$$\alpha_{\mathrm{eff}} = \frac{e^2}{4\pi\varepsilon_0\varepsilon_{\mathrm{r}}\hbar v_F} = \frac{\alpha_{\mathrm{qed}}}{\varepsilon_{\mathrm{r}}}\,\frac{c}{v_F}\,. \tag{2b}$$

Considering the circuit at the junction of AlGaAs/AsGa semiconductors, widely used in condensed matter experiments, with a relative permittivity $\varepsilon_{\mathrm{r}} = 12.9$ and a typical Fermi velocity $v_F = 10^5\,\mathrm{ms}^{-1}$, we derive $\alpha_{\mathrm{eff}} \sim 1.7$. Assuming now a typical $d = 100\,\mathrm{nm}$ and an interaction time of merely one hundredth of a nanosecond[3] corresponding to $l = 1\,\mu\mathrm{m}$, we get approximately $\delta\phi_{\mathrm{cou}}/2\pi \simeq 0.81$. This significant phase shift suggests that a single electron could potentially probe extremely low-intensity radiation corresponding to the excitation of a single electron current in the radiation channel.

Single electrons also offer the advantage that they can be generated in very short electronic wave packets down to the tens of ps. It gives an efficient way to sample the effect of an electromagnetic field over a sub-nanosecond time scale, positioning single electrons as strong candidates for quantum sensing. The remaining challenge is to find an apparatus that extracts the quantum phase shift from the single electron wave packet.

[3]This corresponds to an electromagnetic wavelength of 3 mm, considerably larger than the micro-metric dimensions of the system.

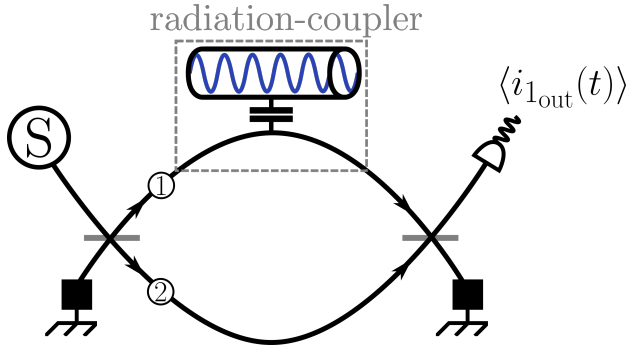

Figure 5: Draft of the electronic quantum radar, an electronic circuit with a Mach Zhender interfermoter geometry. A single electron source is placed at the entrance. It can emit a single electron which then propagates accross the interferometer. The upper arm is capacitively coupled to a radiation. The measurement of the average current is conducted at the output of the interferometer.

0.2.2 The electron radar proposal

We suggest to build an interferometric measurement system in the spirit of Haroche's previously discussed experiment, not using Rydberg atoms but a single electron. We propose for this task a Mach-Zehnder interferometer (MZI) geometry as pictured Fig. 5 which is nothing but a space domain version of a Ramsey interferometer. In this setup, the probe is a single electron emitted at the entrance, the targeted radiation is coupled to one branch called the target branch, and the average outgoing electrical current is measured. Right after its emission, the single electron gets delocalized in both branches by the electronic beam splitter. Propagating through both of them, each amplitude of the electron accumulates a different quantum phase which is related to the local electromagnetic environment. Recombination of the amplitudes via a second beam splitter and subsequent measurement of the outgoing current yields the quantum phase difference, providing valuable information about the probed radiation.

However, it should be noted that despite the similarities with Haroche's quantum measurement, there are crucial differences. The Ramsey interferometer used in Haroche's experiment provides a quantum nondemolition (QND) measurement of the photon number, whereas the electron radar does not. The coupling between electrons and the electro-

magnetic field within an electrical circuit occurs via a time-dependent voltage, which can be traced back to a quadrature of the field. As pointed out in early QND theory literature [26], a quadrature evolves over time, thus, a QND measurement of a time-dependent quadrature presents a different challenge than measuring a time-independent photon number. This is not what the electron radar does. Instead, as we shall see in this thesis, this system parallels radar technology which leverages classical electromagnetic wave amplitude to determine the velocity and location of distant objects, justifying the name of "electron quantum radar".

In this PhD thesis, we construct a theoretical model for the "electron radar", an interferometric measurement system that harnesses a single electron's sensitivity to the electromagnetic field and its extended coherence time to probe low-amplitude radiation in either classical or quantum states. We establish the pivotal equation linking the measured electron signal to the properties of the probe and the field. Alongside this, we present theoretical tools to ascertain the radar's time and frequency resolution. We substantiate the value of this system through examples that demonstrate the potential to probe non-trivial quantum states of the electromagnetic field.

0.3 Plan and outline of the main results

Structure of the manuscript After a first review chapter on electron quantum optics (Chapter 1), this manuscript is mostly focused on the various key elements of the electron radar. This includes the radiation coupler that couples the electromagnetic radiation we want to probe to the electronic interferometer (Chapter 2). This also includes single electron wave packets which, as we shall see, determine the resolution power of the electron radar (see Chapter 3). This chapter will introduce the electronic ambiguity function, a new representation of the excess single electron coherence which is the quantum version of an existing concept in classical radar theory. Finally, the fully quantum theory of the single electron radar incorporating a quantum radiation coupler as well as single electron source and interaction effects will be presented in Chapter 4. Predictions on the ability of the electron radar to probe quantum radiations will also be presented and discussed in this chapter.

This progression has been retained to provide the reader with a progressive path towards this last chapter, introducing the concepts used in

the electron radar theory one at a time. All the notational and technical details are presented in a series of appendix so that the reader can get a self contained exposition of the results presented in this manuscrit with an emphasis on the concepts and underlying physics but without being forced to go though all technical steps.

Let us now review in more details the contents of each chapter:

Electron quantum optics Chapter 1 aims at reviewing the necessary background in electron quantum optics needed for the rest of this manuscript. It lays the foundations for the quantum single electron radar theory which is the main result presented in this manuscript.

We start by a brief presentation of the the state of the art in electron quantum optics, including a rapid introduction to the physics of quantum Hall edge channels and quantum points contacts. These elements are the building blocks of all electronic interferometers demonstrated so far in electron quantum optics with the AlGaAs/AsGa platform [23]. Conventional single electron sources used to generate single electron excitation will then be reviewed[4]. We will then present the theoretical foundations of electron quantum optics, introducing the electronic first-order coherence function which is the electronic analogue of Glauber's quantum coherence introduced in quantum optics. Its basic properties and representations will be discussed as well as their relations to measurable quantities. The last section of this chapter will be devoted to bosonization, a theoretical tool that plays a crucial role in treating Coulomb interactions, inherent in the full single electron radar model presented in Chapter 4.

Radiation couplers Chapter 2 is devoted to the study of radiation couplers. In our approach, a radiation coupler is viewed as an elastic scatterer between the photons propagating in the radiation channel and bosonic excitations, more specifically chiral charge/current density waves at the edges of the 2DEG which are called edge-magnetoplasmons (EMPs), propagating within the electron radar. Section 2.2 reviews the basics of this approach and also the important connexion between the EMP scattering matrix and the finite frequency admittance of the radiation coupler viewed as a multi-terminal circuit element.

[4]We will focus on the ones demonstrated in Refs. [70, 58] but see Ref. [11] for an exhaustive review.

Various radiation coupler models directly relevant for the electron radar will then be considered. Our exposition proceeds by increasing complexity, starting with models coupling a classical time dependent voltage drive to a quantum Hall edge channels in Sec. 2.3. Then, motivated by probing quantum radiation, Sec. 2.4 discusses a model coupling the interferometer to a real dynamical radiation channel. It involves two capacitively coupled counter-propagating edge channels.

The electronic ambiguity function Chapter 3 aims at introducing the important concept of *electronic ambiguity function* which describes the resolution capabilities of a single electron excitation in the electron radar. Since this concept is indeed imported from classical radar theory, this chapter starts by reviewing classical radar theory in Sec. 3.1. Motivated by pedagogy, we present a unidimensional toy model of a classical radar which enables us to explicitly understand how a radar can measure the distance to a target but also its velocity[5] as is well known by all car drivers. In the process, the classical radar equation will be derived together with the concept of ambiguity function in signal processing.

This initial exploration sets the stage for our journey towards the electron quantum radar theory: in Sec. 3.2, a simplified model of the electron radar will be presented. It assumes that the effect of the external radiation on electrons propagating within it can be described using the framework of time dependent single particle scattering. This is a very strong hypothesis which assumes two things: (1) that the back-action of the radiation on the radar can be described in purely classical terms, (2) that there are no effects of Coulomb interactions within the interferometer. This apparently naive approach will nevertheless lead to the electron radar equation and enable us to introduce the electronic ambiguity function, the quantum counterpart of the one appearing in classical radar theory.

The rest of the chapter will be devoted to presenting the properties of the electronic ambiguity function (Sec. 3.3) and discuss how it acts as a filter on the signal we wish to reconstruct which is a time frequency representation of a time dependent single particle scattering matrix.

The chapter wraps up with Sec. 3.4 where we discuss the experimental limitations in the time and frequency scales accessible when using state of the art single electron sources. We then explore how techniques commonly used in classical radar engineering can be transposed into the

[5]Based on the Doppler effect.

electron quantum optics context to improve both the resolution as well as the range of time and frequency scales accessible to an electron radar.

The quantum single electron radar theory Finally, chapter 4 presents the full quantum electron radar theory. It advances beyond the limitations of the previous chapter by enabling us to take into account the effects of Coulomb interactions under a linear screening hypothesis[6]. Since it incorporates the full description of the radiation coupler, involving dynamical degrees of freedom of the radiation channel, this theory enables us to discuss to what extent the electron radar can provide specific signatures of quantum radiation.

For the sake of pedagogy, in Sec. 4.1, we presents the underlying physics behind the electron radar by extending the famous discussion of Elitzur-Vaidman's interferometric bomb detection [62]. From this perspective, the electron radar is not an "interaction-free measurement" but a fully quantum measurement in which "not too strong" interactions enable us to capture more information on the system than just its presence or absence. In particular, we show that this discussion incorporates all the basic elements of quantum measurement theory. It underlines the role of the measurement's backaction on the probed system. The key point is that decoherence and backaction effects must not be too strong otherwise the interferometric signal is killed. But they must not be too weak because they are used to collect information on the system.

Then, a derivation of the quantum single electron radar equation is presented in Sec. 4.2. The remarkable result is that this equation is exactly of the same form than the one derived within a single particle framework even if many body effects are present. It involves an effective single particle scattering amplitude that can be computed from the EMP scattering description of the radiation coupler and involves the quantum state of the probed radiation. This is the central theoretical result of this thesis.

To understand how these results can be used in experiments, we consider in Sec. 4.3 the limiting regimes where the probe single electron wave packet is either resolved in time or in energy. While the energy-resolved case is straightforward to discuss, short duration wave packets require a more careful discussion since they cannot be fully localized due to the presence of the Fermi sea. A full quantitative analysis of the electron radar signal for Levitons of given duration is presented that in-

[6]Commonly used in many previous works on electronic decoherence [34]

corporates the potentially detrimental effects of electronic decoherence. This analysis provides the explicit description of the experimental signal that could be measured in an experiment.

In Sec. 4.4, this formalism is used to obtain explicit predictions for the electron radar signatures of quantum radiation. In particular, we propose a method for squeezing detection, illustrating that it should be within experimental reach on the example of a squeezed vacuum around a given frequency with realistic parameters. In the same way, we discuss the possibility of the electron radar to detect a single EMP within a given mode. Here also, the results we obtain suggest that single EMP detection should also be experimentally achievable in forthcoming experiments.

We finally conclude this thesis and discuss the theoretical and experimental perspective opened by this work.

Chapter 1

Electron Quantum Optics

The initial chapter of this work aims to review the progress of electronic transport over the past decades, evolving from a purely condensed matter perspective to a paradigm inspired by quantum optics. This change has been accelerated by experimental advancements that have lead to the controlled preparation and manipulation of novel states of electronic fluid, down to single-electron excitations in structures analogous to optical fibers for electrons. Subsequently, new theoretical concepts have been elaborated to interpret the experiments based on these advances. These concepts take inspiration from quantum optics, such as coherence functions introduced by Roy Glauber in the 1960s [86, 87].

In this chapter, our primary focus will be on the experimental tools that have led to the transition from coherent electronic transport to electron quantum optics. These tools are reminiscent of the standard components found on an optical table: optical fibers, which will be supplied by the chiral edge channels in the integer quantum Hall effect; beamsplitters adjustable through metallic top gates; and sources for single to few electrons, two categories of which will be introduced in Section 1.1.

The latter part of this chapter will concentrate on presenting the theoretical framework developed to comprehend and conceptualize these novel experiments. Two central concepts will be introduced here and utilized throughout the manuscript. Firstly, we will present electronic coherence functions, discussing their primary properties, various representations, and the physical quantities they give access to. Secondly, we will explore bosonization, which establishes the correspondence between electron and photon quantum optics.

1.1 Experimental tools

1.1.1 Flying electrons

Electronic coherent transport

In the field of optics, photons propagate either freely in vacuum or through conventional media, maintaining their quantum coherence over kilometers due to their weak interaction with matter. This property makes photons highly suitable for communication as they preserve the initial signal over vast distances. However, their weak interaction poses a challenge for computing, as it necessitates sophisticated technologies to operate logical gates on photons [178]. Conversely, electrons, with their inherent mass and charge, are highly sensitive to their environment, making it challenging to maintain their coherent propagation over distances long enough to perform controlled quantum operations which are at the heart of "electronic flying qubits" proposals [107, 14, 13, 194, 15] This issue is especially pronounced for electrons in metals, as realistic crystals contain impurities and phonons that interact with electrons and also because of electron/electron screened Coulomb interactions [6, 67].

To demonstrate controlled quantum operations on electrons, we need circuits with a size L small enough to preserve coherence but large enough for manipulation. The inelastic length l_{in} represents the typical distance over which electronic phase coherence is preserved, *i.e.*, the length scale over which electron waves can interfere. Coherent electrical transport occurs when $L < l_{\mathrm{in}}$. In condensed matter, electron-phonon interactions and electron-electron interactions as well as effective screened Coulomb electron/electron interactions. Among inelastic processes, electron-phonon interactions are responsible for Joule heating of electric wires when electrical currents flows within them. In most materials at room temperature, l_{in} is of the order of ten nanometers or below, which is several orders of magnitude too small for constructing quantum circuits based on coherent electronic transport. Reducing the temperature to a few milli-Kelvin minimizes electron-phonon interactions of thermal origin and thereby increase l_{in}. Note that lowering the temperature also enables manipulation and measurement of quantum electronic signals with lower frequencies comparable to thermal energy, *i.e.* GHz frequencies.

In metallic systems, at temperatures where phonons are not anymore an issue, the effect of dynamical quantum (magnetic) impurities is important and lead to a lot of studies in the 2000s. Nevertheless,

in ultra-clean samples, electron/electron interactions induce electronic relaxation and decoherence for electronic excitations above the Fermi sea but do not jeopardize the Fermi liquid paradigm in 3D systems (see [172] for a review and [67] for a more general introduction).

An approach to further increasing l_{in} is by confining the conductor to a two-dimensional electron gas (2DEG) and considering the new conductors that can be made using this type of systems. One way to achieve this is through heterostructures formed at the interface between two semiconductors, such as gallium arsenide (GaAs) and aluminum gallium arsenide (AlGaAs). At these junctions, a triangular potential well is created, leading to quantization of transverse quasi-momenta. In the optimal regime, only electronic bands associated with the lowest quantized transverse quasi-momenta are relevant, forming a 2DEG at the interface [5].

These structures offer two significant advantages: first, electrons in the 2DEG usually originate from donor atoms located approximately 100 nm away from the 2DEG. The potential associated with these ionized impurities is thus smoothed out by this distance, reducing electron interaction with charged impurities and leading to high mobility in the material [5]. Second, the semiconductors are fabricated using molecular beam epitaxy, a technique that grows thin films of single-crystal materials with atomic-scale precision [44]. Consequently, the crystal at the interface is virtually defect-free. These two facts lead to a mean free path l_{el} between elastic collisions that electrons undergo with impurities in the crystal [6] that can reach hundred of nanometers.

When $L < l_{\text{in}} \ll l_{\text{el}}$, the specific regime of coherent electronic transport is referred to as the ballistic regime. This regime is of interest in our case, as it serves as the electrical analog of freely propagating photons. When $l_e \ll l_{\text{in}}$ electronic transport is still coherent but multiple elastic scatterings of electrons on static impurities occur leading to phenomena such as weak quantum localization [12] (see [137] for an extensive review). This regime of quantum transport is called diffusive. It is the one occuring in ordinary metallic conductors such as the ones reviewed in [172] and not the one considered in this thesis.

As we shall see in the present chapter, these systems also present the advantage of being extremely controllable. More precisely, it is possible to confine the electron in quasi-1D structures that play the role of optical fiber for electrons. Then, we will see that it is also possible to control, to some extent, the screening of Coulomb interactions by the use of metallic

top gate. Overall, the corpus of techniques in electronic lithography and nano-fabrication was so well developped in the early 21st century that it is not very surprising that AlGaAs/AsGa turned out to be the birth platform for electron quantum optics.

Finally, it is worth noting that the graphene [147] is an alternative platform for 1D and 2D coherent ballistic electronic transport, which has demonstrated remarkable electronic properties [40] and the potential for novel quantum devices [80]. We don't evoke it in the rest of this manuscript, but it can potentially be an adequate platform for the experimental realization of the quantum sensor modelled in chapter 4

Electronic analogous of optical fiber

Progresses in lithography techniques have enabled the shaping of electron gas to obtain quantum electrical circuits. By etching samples or depositing metallic gates with sub micrometer precision, it allows to design a wide range of circuits. However, the unrestricted propagation of electrons in any direction of the plane and the resulting elastic scattering effects can pose a practical challenge to the application of such systems for electron quantum optics as their size increases.

Fortunately, this obstacle can be overcome by the application of a strong perpendicular magnetic field to a cryogenically cooled 2DEG. This enables entry into a new regime of electronic transport called the integer quantum Hall effect (QHE), which was discovered by von Klitzing in 1980 [118] and later awarded the Nobel Prize. As we will review now, the integer quantum Hall effect provides the original system of choice for electron quantum optics.

2DEG under strong perpendicular magnetic field In the quantum Hall regime, the propagation of electrons is confined to the edges of the 2DEG, creating one-dimensional metallic states known as quantum Hall edge channels. Their number is quantized and determined by the magnitude of the magnetic field. Their propagation is chiral, following a single direction dictated by the field which prevents any backscattering within one of these channels. The quantum Hall edge channels thus exhibit properties similar to those of optical fibers making them highly interesting for electron quantum optics.

To understand the integer quantum Hall effect at the intuitive level, we consider an infinite 2DEG subjected to a perpendicular magnetic field $\mathbf{B} = B\hat{z}$. In such a system, the motion of electrons becomes quantized

into discrete energy levels, known as Landau levels, which are described by the following expression:

mettre une citation

$$E_n = \hbar\omega_c \left(n + \frac{1}{2}\right), \tag{1.1}$$

where $\hbar$ is the reduced Planck constant, n is an integer representing the Landau level index and ω_c is the cyclotron pulsation, *i.e.* the pulsation associated with the classical circular motion of electrons in a magnetic field. This energy spectrum is plotted on the left panel of Fig. 1.1. These levels are highly degenerate and are equivalent to equally spaced harmonic oscillator levels, with an energy separation of $\hbar\omega_c$ between them. The cyclotron pulsation ω_c is related to the magnetic field strength B and the effective mass of the electron m^*:

$$\omega_c = \frac{eB}{m^*}\,. \tag{1.2}$$

As the magnetic field increases, the Landau levels thus become more widely separated. The spin degeneracy of electrons is also lifted in the presence of a magnetic field, leading to a Zeeman energy separation of $\hbar\omega_Z$ between the two spin populations.

This simple Landau level energy spectrum is of great help to understand the conduction properties of the sample. When the chemical potential μ set by our voltage is inside one Landau level, the system is a conductor and both the longitudinal and transverse resistivities have finite values. However, if the chemical potential is between two Landau levels, there are no states allowing electronic conduction that are available and the system becomes an insulator with infinite resistivity. It should be noted that disorder in the 2DEG can be advantageous since it leads to the presence of localized states that trap extra electrons when the chemical potential is between two Landau levels, thereby stabilizing the insulating behavior of the sample. However, disorder should not be too strong, as it changes the degeneracy of Landau levels and can result in the loss of energy localization of levels. A more comprehensive review of this topic can be found in the lectures given by D. Tong at Cambridge University[1].

In a real experiment, such as the one conducted by von Klitzing and illustrated schematically in the left panel of Fig. 1.1, the two-dimensional

[1]See: `https://www.damtp.cam.ac.uk/user/tong/qhe.html`.

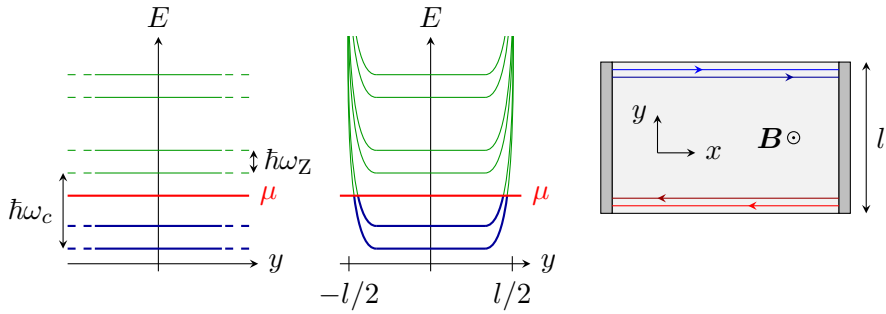

Figure 1.1: Figure extracted from [34] *Left*: Energy spectrum of an infinite 2DEG under a perpendicular magnetic field. The energy gap between two Landau levels is denoted by $\hbar\omega_c$, while $\hbar\omega_Z$ represents the energy associated with the Zeeman splitting. Given that the chemical potential lies between two levels, this sample exhibits insulating properties. *Middle*: Here, the energy spectrum of a finite size 2DEG confined to a region of size l along the y axis is displayed. The confinement potential results in bent levels at the edges. Consequently, the chemical potential intersects two levels at these edges, thereby creating two conduction channels. *Right*: This schematic represents chiral edge channels of a sample under a perpendicular magnetic field denoted as $\boldsymbol{B} = B\,\mathbf{e}_z$. This perpendicular magnetic field imposes a chirality to the edge states, leading to one-way transport channels around the sample's boundary.

electron gas (2DEG) is not infinite and has edges. This means that the energy spectrum of the system must be modified to take into account the confinement potential at the edges. It bends the energy levels as shown in the middle panel of Fig. 1.1 and allows for transverse conductivity. When the chemical potential is at the same energy as one of the original Landau levels, not much changes, but when it lies between them, the chemical potential crosses every filled Landau level near the edges of the system, creating one-dimensional metallic states that are electronic conduction channels. This is known as the quantum Hall regime. The number of conduction channels depends on the strength of the transverse magnetic field and is given by the number of Landau levels that cross the chemical potential. As the magnetic field gets stronger, this number decreases.

Moreover, since the electronic velocity is linked to the gradient of the potential, electrons within a given channel propagate in the oppo-

site direction to those of the opposite edge, leading to chiral electronic propagation as represented on the right panel of Fig. 1.1. This chirality implies that no backscattering is possible along one edge of the sample, and when the two edges are sufficiently far apart, any backscattering event from one channel to another is prohibited.

The unique properties of the quantum Hall edge channels, including chirality, 1D-confinement, and low temperature operation, make them highly suitable for realizing coherent ballistic transport over distances of several micrometers, with minimal electronic decoherence. As we shall see, development started in the late 80s have also enabled us to build an ideal electronic beam splitter, a basic component of electron quantum optics which plays a crucial role in the first on-demand single electron source that we will review now.

ajouter des refs

1.1.2 Manipulating electronic edge states

Over the past few decades, researchers in quantum optics have developed an extensive range of experimental tools to manipulate the propagation of photons. These tools can modulate the amplitude, phase, or frequency of light using passive elements such as waveplates and polarizers, or active elements such as acousto-optic modulators (AOMs) and electro-optic modulators (EOMs). Photons can be delocalized among two paths or recombined into the same beam using beam splitters. Additionally, amplifiers can be used to boost signals, and single-mode optical fibers can select spatial modes of quantum light states. The development of these tools has been pivotal in realizing groundbreaking experiments. For example, AOMs played a crucial role as optical switches in the experiment by Alain Aspect and his collaborators testing Bell's inequalities [7].

Manipulating electronic states however is much more challenging, as any interaction can potentially induce significant electronic decoherence. Two techniques have been predominantly employed thus far. The first approach involves physically etching the edges of circuits. This defines the confining potential for the electrons thereby defining the circuit. Unfortunately, this method is not very versatile because of the fixed nature of the edge shape. Etching quality may also be an issue. This is why a second method has been developed which relies on top gates. As we will see this is the key method for building some of the basic

components of electron quantum optics.

Top gate

The drawbacks of physical etching can be circumvented by placing a gate on top of the heterojunction, above the edge channels to shape. When a voltage is applied on it, an electric field is created between the gate and the 2DEG. This electric field modifies the local electrostatic potential of the 2DEG, leading to the confinement or repulsion of the charge carriers depending on the sign of the applied voltage. It can be used to control the spatial distribution and properties of these edge channels.

Quantum point contact

Going one step further, one can put two gates on top of a circuit as pictured Fig. 1.2. In this configuration, applying a negative voltage on both gates generates a saddle-shaped confining potential for electrons which is called quantum point contact (QPC). It was first used, by Wees et al. and independently by Wharam et al., to demonstrate the quantized conductance in one dimensional conductors. When electrons pass through the constriction, their motion becomes quantized due to the confinement, and the conductance takes discrete values, which are integer multiples of the fundamental unit of conductance $2e^2/h$.

citation

By creating a QPC in a 2DEG under the quantum Hall regime, it can be used to bring the two counter-propagating edge channels close together, enabling electron tunneling between them. The tunneling amplitude (and hence the splitting ratio) can be tuned by adjusting the gate voltages, allowing precise control over the electron beam splitting process.

To gain a comprehensive understanding of the QPC as a beam splitter, let us describe what happens when the QPC is gradually closed in the presence of a 2DEG under the quantum Hall regime. A schematic diagram of the process is presented Fig. 1.2. Initially, the QPC is open, allowing for unimpeded electron transport through the constriction. Closing the QPC leads to a narrowing of the constriction in the 2DEG, enabling the tunnelling in the edge channels with the higher energy levels (those located further away from the physical boundary). As the constriction narrows, these channels are sequentially pinched off. Eventually, when the QPC is sufficiently narrow, all edge channels are

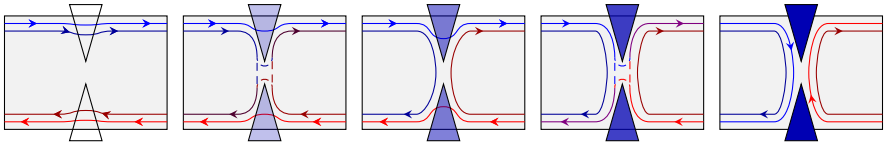

Figure 1.2: Schematic illustration of a QPC's action on edge channels in the context of quantum Hall systems. *From left to right*: Starting with a small negative bias applied to the QPC. At this stage, all edge channels are transmitted through the QPC. As we decrease the bias, the repulsive potential at the QPC increases, causing the edge channels' trajectories to bend. Initially, the channel closest to the edge continues to be fully transmitted, while the other one can be either transmitted or reflected to the opposite edge. As we continue to decrease the potential, both channels can either be transmitted or reflected. This situation introduces a mix of transmission and reflection in the edge channel behavior. Eventually, as we further decrease the potential, all channels get reflected, and no transmission through the QPC is observed. This situation corresponds to a closed QPC, where all incoming edge channels are reflected back, and the conduction through the QPC vanishes.

pinched off, and the conductance through the constriction is effectively zero. At this point, the QPC is considered to be in a closed state, with no electron transport between the two larger electron reservoirs.

The QPC as an electron beam splitter can be incorporated into a variety of electron interferometer setups, such as Fabry-Perot, Mach-Zehnder, or Aharonov-Bohm interferometers. These devices use the beam splitter to create two spatially separated electron paths that later recombine, resulting in interference patterns that reveal information about the electron coherence, phase, and interactions with the environment. It is thus a key feature to build quantum sensors based on a interferometric setup such as the electron quantum radar.

Ohmic contacts

The last building block of electron quantum optics is the Ohmic contact which are used to contact the 2DEG burried 100 nm below the surface of the sample, at the junction between AsGa and AlGaAs. Technically, an Ohmic contact is a low resistance junction, non rectifying, between a metal to semi-conductor and vice-versa. This implies that no large Schottky barrier appears at the interface between the metal and the

semi-conductor. Ohmic contacts in AsGa are usually made using an Au Ge alloy which forms an eutectic at 361 °C and, with the adjunction of Nickel, has been shown to lead to very small contact resistivities (see [8] for a review).

The physics of metal/semiconductors interfaces, and among them of Ohmic contacts has been studied since decades and is quite complicated, at the crossroads of physics, material science and chemistry [173, 182, 187]. Because the fabrication process is quite "brutal" (a metallic alloy melts its way into the very clean crystalline structure manufactured by molecular beam epitaxy), a microscopic modeling of this (disordered) interface is extremely difficult. Nevertheless, it is possible to summarize some of the higher level characteristics of such a contact.

This is based on the idea that, close to an Ohmic contact, a 2DEG is under strong influence of the contact: first of all, because of the very small barried between the 3D metal and the 2DEG, electrons tunnel between the two and consequently, the Ohmic contact plays the role of an electronic reservoir in the sense of Markus Büttiker: it absorbs any incoming current. Moreover, the small distance between the two leads to a very strong electrostatic coupling between the two. Consequently, the Ohmic contact emits an equlibrium electronic fluid characterized by its chemical potential corresponding to its electrical potential[2] and its temperature. This is enough to describe an Ohmic contact connected to a dc or even ac generator. In this case, the Ohmic contact is an absorber for the incoming currents and an emitter whose properties are determined by its electronic temperature and the possibly time dependent voltage applied to it. This explains the importance of the Ohmic contact: when connected to the a lead with an amplification chain and a voltmeter, it can be used to collect currents and then perform average current or current noise measurements. It can also be connected to a generator and act as a DC or AC source depending on the generator.

Following the same physical high level picture, Slobodeniuk and collaborators have elaborated a model for a small floating[3] Ohmic contact [177]. In this model, a floating Ohmic contact is a conductor which has the following properties when connected to quantum Hall edge channels:

- It has a charge and an electrical potiential
- The charge and the currents entering and exiting the contact obey

[2] In the case where a time dependent potential is applied to it, this is more subtle.
[3] Not directly connected to a generator.

the usual charge conservation equation

- The voltage of the contact is determined by the electrostatic coupling to other conductors
- The current in each outgoing channel is determined by Hall's relation from the Ohmic contact's potential.

As recalled in the introduction of this thesis, this component has been used in many important experiments by the C2N group. In this case, the floating contact can be viewed as a "galvanic node" that allows electrical transport even in the DC regime, but in which electronic coherence is lost (contrary to a very single quantum Hall edge channel). However, this does not mean that a small Ohmic contact cannot be used in quantum coherence nano-electronics as has been demonstrated recently [60].

1.1.3 Single electron sources

In this rapid review, we will discuss two commonly used single electron sources: one is able to emit single electron excitations a few tens of µeV above the Fermi sea (see Sec. 1.1.3) whereas the other one emits them close to the Fermi surface but is much simpler to build and is much more stable (see Sec. 1.1.3). Or course this are not the only sources demonstrated and we refer the reader to [11] for an exhaustive review.

The mesoscopic capacitor

On-demand single-photon sources are essential components of optical tables, widely used to investigate fundamental quantum physics such as the particle-wave duality with double-slit experiments REF or the bosonic statistics of photons through Hong-Ou-Mandel (HOM) experiments [103]. These sources are now integrated to various quantum technologies, including quantum computing, quantum cryptography, and quantum communication.

In the same way, the birth of electron quantum optics can be traced back to the demonstrations of the first on-demand coherent single electron sources. The first one has been demonstrated in the Pierre Aigrain laboratory at the École Normale Supérieure (ENS) in Paris by G. Fève and collaborators during his PhD supervised by D. C. Glattli. This experimental work [70, 68] followed previous theoretical work by M. Büttiker and his (many) collaborators both for small and large drives

[33, 154, 18, 146]. Characterization of this source was done by measuring and analyzing both its finite frequency average current [130] and its finite frequency current noise [129, 148] a quantity whose measurement requires significant experimental developments [149].

Since then, this source has been extensively used in fundamental quantum electron optics experiments such as the electronic analogous of Hanbury Brown–Twiss [24] and Hong–Ou–Mandel [20] experiments. It has also been used for studying electronic decoherence in quantum Hall edge channels [74, 134]. Extensive reviews of this series of experiments can be found in the PhDs thesis of E. Bocquillon [21], V. Freulon [73] and A. Marguerite [132] as well as in recent reviews [23, 133].

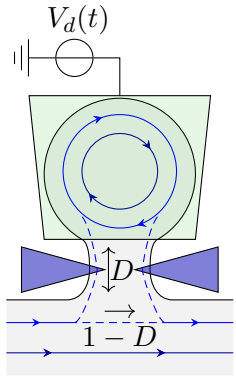

Figure 1.3: Extracted from [34]. Schematic view of the mesoscopic capacitor. A small cavity formed in the 2DEG is defined by a QPC. This arrangement results in a Fabry-Pérot type quantization of energy levels within the cavity, akin to the behavior of light in an optical Fabry-Pérot interferometer. The energy levels can be manipulated by applying a voltage to a metallic top gate covering the dot. This voltage can shift the energy levels, allowing for the control of electron transport through the dot.

This source, schematically depicted on Fig. 1.3 is commonly called the mesoscopic capacitor as it built from of two armatures. The first one is a metallic top gate while the second one is a quantum dot in the integer quantum Hall regime placed beneath it. The dot is delimited partly by etching and partly by a QPC isolating it from the rest of the 2DEG when totally closed. Due to its small size, the level spacing Δ for electrons trapped in this circular quantum Hall edge channel has a typical value of about 10^{-4}eV when the dot size is approximately

1 µm. to the confinement of electrons within the quantum dot. The transmission coefficient T of the QPC can be adjusted by varying the gate voltage V_g applied to it so that T takes values from 0 to 1. This coefficient determines the typical time τ_e for an electron to leak from the dot to the rest of the circuit [68]:

$$\tau_e = \frac{h}{\Delta}\left(\frac{1}{T} - \frac{1}{2}\right) . \tag{1.3}$$

Opening the dot then reduces the escape time of the electron and, by time/energy uncertainty, broadens the resonance associated with the corresponding level within the electronic cavity. The QPC transmission T thus appears as an experimentally controlled parameter for shaping the duration of the electronic wave packet.

The source is driven by appliying a periodic square drive voltage V_d to the top gate, with a period τ_d typically between 0.1 and 10 ns. Under the effect of this drive, the energy levels of the quantum dot shift non adiabatically, rising an occupied level well above the Fermi level which causes the emission of a coherent single electron from the dot into the outgoing quantum Hall edge channel during the first half of the source's duty cycle. This emission is then followed by a non-adiabatic drive of this now empty level below the Fermi level, thereby leading to the emission of a hole during the second half part of the duty cycle. A schematic diagram of this duty cycle is presented in Fig. 1.4.

Initially, the voltage V_d is chosen so that the Fermi level is equidistant from the first unoccupied level of the quantum dot and the last occupied one. By applying a voltage $V_d(t) = -\Delta/e$ during the first half of the period, the energy of the last occupied level of the quantum dot is shifted upward, just above the Fermi sea of the circuit. To guarantee that only one level is promoted above the Fermi level, it is essential to ensure that the energy level spacing Δ is greater than the width of each level $\hbar/\tau_e$. It is also crucial that $\tau_d > \tau_e$ for the source to operate in the single electron regime, ensuring that only a single is emitted. These two requirements can be expressed by:

$$\frac{\hbar}{\Delta} < \tau_e < \tau_d \, , \tag{1.4}$$

which clearly illustrates that a compromise has to be found between these two requirements to operate the source in the single electron regime. During the second half of the period, the energy levels return to their initial positions, the now-empty discrete level fills up again, allowing a hole to be emitted.

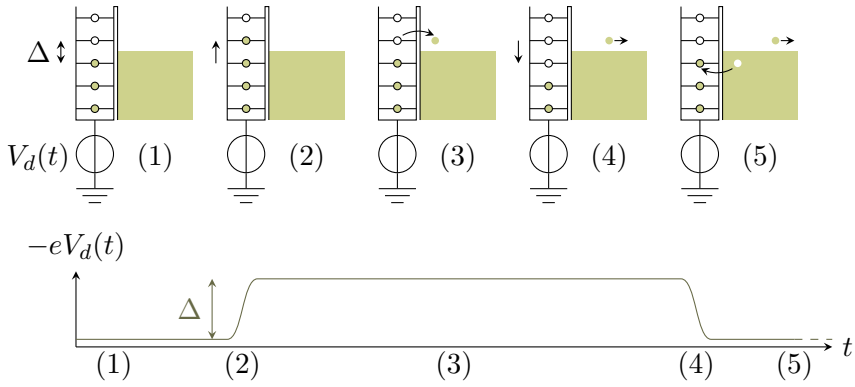

Figure 1.4: Extracted from [34]. Schematic representation of the ideal duty cycle of the electron source. It is achieved by applying a square voltage of suitably tuned amplitude to the top gate. (1) Initially, all energy levels below the Fermi level are filled with electrons. (2) A sudden increase in voltage leads to a rapid shift in the energy levels. As a result, one of the energy levels is propelled above the Fermi level. (3) Within a characteristic leaking time denoted by τ_e, the electron that has been promoted to the higher energy level tunnels out of the cavity and propagates into the sample. (4) Subsequently, the voltage is abruptly reduced, causing an empty energy level to shift below the Fermi level. (5) An electron tunnels into the dot to occupy this empty level, leading to the emission of a hole into the sample. This returns the system to the initial state. By continuously repeating this cycle, a source is created that emits an electron and a hole per period, separated from each other by half a period.

One last requirement for the mesoscopic capacitor to operate in optimal conditions, is that the voltage drive's rising time must be significantly smaller than τ_e. It prevents hybridization between the quantized states of the quantum dot and the continuum of single particle states in the circuit. Otherwise the electron may tunnel out of the quantum dot as soon as it crosses the Fermi level of the circuit, resulting in an excitation with poor energy resolution.

Of course, one has to keep in mind that the description above is an idealized one. So far, for $T < 1$, the mesoscopic capacitor has been modelized within a single particle time dependent scattering approach. Several results have been obtained analytically [141, 138], but it is also

possible to implement numerical simulations as in [92, 64]. Assessing the quality of the mesoscopic capacitor as a single electron source can be done by using the recently developped algorithm for extracting the single electron and home excitations from a time periodic single electron coherence [163]. This method has been used in the case of a square and sinusoidal drives applied to the top gate of the mesoscopic capacitor and confirm that the optimal regime is obtained by an appropriate tuning of the amplitude of the drive and of the transmission probability of the QPC. A higher transmission opens the way to emitting more than one excitation per half period wheres, a lower transmission of the QPC tends to generate a quantum superposition of no emission and a single electron/hole pair emission.

At the optimal operating points, the shape of the electron and hole wavepackets depend on the shape of the drive as well as on the various parameters used. In the case of the square drive, the wave packets is of Lorentzian lineshape in the frequency domain, as expected for the problem of a resonant level decaying in a continuum. This is the so-called Landau quasi particle because it corresponds to an energy resolved, up to its natural line width, single electron excitation.

The Leviton source

The other single electron source commonly used in electron quantum optics is the Leviton source [59]. This source is based on a proposal by Lee, Levitov and Lesovic inspired by the observation that an appropriate voltage drive applied to an electron reservoir could lead to a reshuffling of the electronic levels preserving the Fermi sea and thus generating only purely electronic excitations on top of the Fermi sea [124].

Their prediction was that a Lorentzian voltage drive applied to a single edge channel of amplitude such that the resulging Lorentzian current pulses carries an integer multiple (say n) of the electron charge $-e$ generates a Slater determinant built from n mutually orthogonal wave packets above the Fermi level. For $n = 1$, only one electronic excitation is generated, called the Leviton.

Generation of these excitations is performed by applying the appropriate time dependent voltage drive to an large enough Ohmic contact which plays the role of an electron reservoir for the 2DEG in contact with it. The diagnostic for their emission consists in monitoring the low frequency current noise at the output of a quantum point contact where the source is connected at one input and the reference equilibrium at

the other. As will be reviewed in Sec. 1.2, this is a measurement of the partition noise of all the single particle excitations arriving to the QPC from the source. These include electronic but also hole excitations. In the case of the Lorentzian pulses, the theoretical prediction is that this noise is minimal when no spurious electron/hole pairs are emitted or, equivalently, when the current pulse is Lorentzian and carrying an integer multiple of $-e$. Ref. [58] contains an in-depth discussion of partition noise diagnostic of such a purely electronic state generation.

It should be noted that generating such voltage pulses with a short duraction is not so obvious. Denoting by τ_e the temporal width of the associated current pulse, the energy scale of the corresponding Leviton is $\simeq \hbar/\tau_e$. In order to have such an energy scale well above the thermal energy scale $k_B T_{\rm el}$ where $T_{\rm el}$ denotes the electron fluid temperature (typically 30 to 100 mK in the experiments), τ_e needs to be smaller than $\hbar/k_B T_{\rm el}$ which is in the 25 to 76 ps range in this temperature range. Advanced waveform generators with a basic time step of 40 ps and 10 bit encoding started to be used in the 2010s and opened the way to generating such excitations. Fourier synthesis with 4 harmonics has also been used [16] but this is limited by the microwave cable's bandwidth and still limits τ_e in the tens of ps. Alternative methods involving the use of a frequency comb have been recently investigated and reach $\tau_e \simeq 27$ ps. Photoconductive switches are now envisioned to reach the THz bandwidth which would translate into 1 to 10 ps current pulses.

1.2 First order coherence

1.2.1 Historical perspective

The aim of this section is to present the basic concept of electron quantum optics which are the electronic quantum coherences. This concept is indeed directly borrowed from quantum optics where it has been introduced by R. Glauber in the early 60s [87]. Glauber himselff published a paper in the 90s on the generalization of these functions to fermions having in mind its applications to cold fermionic atoms [36] but this work was totally overlooked in the electronic quantum transport community. The introduction of electronic coherences dates back to the PhD thesis of Charles Grenier [90] following his publications on the subject [52, 93, 92]. At the same time, the concept was also recognized by G. Haack in M. Büttiker's group [96, 95]. So far, these studies mainly focused on single electron coherence which, as we will recall, contains all the

information on single particle physics in the electronic fluid.

Two electron coherence was first sudied by M. Moskalets [140, 139] within the framework of time dependent scattering theory and then in full generality by E. Thibierge during his thesis [184] with a proposal to reconstruct it from a generalized Franson (two particle) interferometry [185]. Two-electron decoherence study has been initiated by C. Cabart in his PhD thesis but the topic is not closed as of now [34]. Two electron coherence will not be mentioned more in the present manuscript. So far only single electron coherence has been reconstructed under certain hypotheses [110] or measured without any assumptions [17, 72]. Two electron coherence requiring at least finite frequency noise measurements [185] or maybe noise of the noise measurements, this quantity is much harder to capture experimentally.

A deeper understanding of these objects came when realizing that they cold be viewed as the *quantum signals* carried by a beam of electrons [165] and that all ideal electronic interferometry experiments could indeed be viewed as on-chip analog quantum signal processing turning these quantum signals into measurable quantities. Benjamin Roussel's thesis provides a nice introduction to this point of view [162].

Here, we will present the basic elements on single electron coherence needed to understand the present manuscript. This material is based on all previously published material and also on the recent technical report of the SEQUOIA project mentioned in the introduction of this thesis [113].

1.2.2 Definition and physical content

Definition

The formal definition of single electron coherence mimics the one of photonic coherencesintroduced by Glauber:

$$\mathcal{G}_{\rho}^{(e)}(X, X') = \mathrm{Tr}\left(\psi(X)\,\rho\,\psi^{\dagger}(X')\right) \tag{1.5}$$

where $\psi(X)$ (resp. $\psi^{\dagger}(X')$) denote the destruction (resp. creation) operator for an electron at space-time position $X = (x, t)$ resp. $X' = (x', t')$ and ρ the reduced density operator for the electron fluid. Note that this definition is valid for electrons within a metal, a superconductor, or even within an electron beam within an electronic microscope.

In quantum coherent nano-electronics, $x = x'$ will denote the position of a detector or a specific position within the electrical circuit in

consideration and we will mostly focus on single electron coherence in the time domain:

$$\mathcal{G}^{(e)}_{\rho,x}(t,t') = \mathcal{G}^{(e)}_{\rho}((x,t);(x,t')) \tag{1.6}$$

and, whenever these is no ambiguity on the x position, this index may very well be omitted.

Physical content

To begin with, let us consider the case where the reference state is the vacuum state $|\emptyset\rangle$. We consider that an N-electron Slater determinant has been introduced in the system at time $t = 0$, based on N mutually orthogonal[4] normalized wave packets $\varphi_1, \cdots, \varphi_N$:

$$|\Psi_N\rangle = \prod_{k=1}^{N} \psi^\dagger[\varphi_k] \; |\emptyset\rangle \; . \tag{1.7}$$

Denoting by $\mathcal{G}^{(e)}_{|\Psi_N\rangle,t=0}(x|x')$ the equal time single electron coherence taken at $t = 0$, a straightforward computation leads to:

$$\mathcal{G}^{(e)}_{|\Psi_N\rangle,t=0}(x,x') = \sum_{k=0}^{N} \varphi_k(x)\, \varphi_k(x')^* \tag{1.8}$$

The single electron coherence therefore appears as the sum of the contributions of each of the individual electronic wavefunction involved in the state $|\Psi_N\rangle$. Each wavefunction φ_k contributes by $\varphi_k(x)\varphi_k(x')^*$, thereby showing that information on the phase of the wavefunction $\varphi_k(x)$ is present for $x \neq x'$. The local single electron coherence $\mathcal{G}^{(e)}_{\rho,x}(t,t')$ can be viewed as the single particle "quantum signal" accessible at position x.

The number of non zero correlators in electron quantum optics is much lower than in photonics. For example

$$\langle \psi(x,t) \rangle_\rho = 0 \tag{1.9}$$

which means that there is no classical value associated with a fermionic field. This follows from the so-called parity super-selection rule that was originally discovered in relativistic quantum field theory [191, 75] but is

[4]This condition is indeed quite generic: because of the fermionic statistics, any Slater determinant can be seen as built from mutually orthogonal wave packets.

indeed ultimately related to no-signaling [109]. The parity superselection rules states that quantum states involving a superposition of fermion numbers with different parities are physically forbidden.

In condensed matter physics, the many-body state of a metal does not allow any superposition of different numbers of electrons and therefore satisfies the parity superselection rule. By contrast, a superconductor does allow superposition involving numbers of electrons differing by 2: this leads to a non zero BCS order parameter

$$\langle \psi(x,t)\psi(x',t'')\rangle_{\rm BCS} \neq 0 \tag{1.10}$$

but in both cases, Eq. (1.9) is satified. In a signal processing language, an electronic or more generally a fermionic quantum beam does not carry any classical fermionic amplitude (contrary to a bosonic or photonic beam). The first non trivial quantum signals associated with a fermionc quantum beam are the fluctuations of the fermionic field. In the case of a metallic system, the first non zero correlator is the single electron coherence defined by Eq. (1.6). In a superconductor, one should also consider the BCS order parameter defined by (1.10). This points out an important fact about the electron radar: it is intrinsically a quantum radar since there is no classical field on which it is based.

It is interesting to use Eq. (1.8) to compute the single electron coherence within a Dirac sea corresponding to an infinite filling of single electron plane wave $\varphi_k(x) = e^{ikx}$ along a line from $k = -\infty$ to $k = k_F$. A similar computation leads to the following expression:

$$\mathcal{G}^{(e)}_{F,t=0}(x,x') = \frac{1}{2\pi}\frac{e^{ik_F(x-x')}}{x'-x+i0^+}\,. \tag{1.11}$$

à voir de plus prêt le com de Dario

The same quantity can also be computed for the equilibrium state of these fermions, at a chemical potential $k_F(\mu)$ dependent on the chemical potential μ and electronic temperature $T_{\rm el}$:

$$\mathcal{G}^{(e)}_{\mu,T_{\rm el},t=0}(x,x') = \frac{1}{2\pi l_{\rm th}(T_{\rm el})}\frac{e^{ik_F(\mu)(x-x')}}{\sinh\left(\frac{x'-x}{l_{\rm th}(T_{\rm el})}+i0^+\right)}\,. \tag{1.12}$$

which now reveals the thermal coherence length $l_{\rm th}(T_{\rm el}) = \hbar v_F/k_B T_{\rm el}$ of the electrons at non-zero temperature $T_{\rm el}$. The $1/T_{\rm el}$ dependence of this coherence length can be traced back to the linear dispersion relation

of the fermions close to the Fermi point. By contrast, when considering non-relativistic particles with dispersion relation $E(k) = \hbar^2 k^2/2m$ at vanishing chemical potential, the corresponding coherence length would exhibit the scaling of the De Broglie thermal length $l_{\rm dB}(T_{\rm el}) = h/\sqrt{2\pi m k_B T_{\rm el}}$.

Excess single electron coherence

voir com Dario

Let us now turn to the case of usual metallic conductors in which excitations are present within the electron fluid on top of this reference vacuum state $|F_\mu\rangle$. These corresponds to the excitations emitted by the electron sources present in the circuit when they are switched on at zero temperature. The appropriate notion that contains information on the single particle excitations is the excess single electron coherence $\Delta_\mu \mathcal{G}^{(e)}$ defined by

$$\mathcal{G}^{(e)}_{\rho,x} = \mathcal{G}^{(e)}_{|F_\mu\rangle,x} + \Delta_0 \mathcal{G}^{(e)}_{\rho,x}\,. \tag{1.13}$$

Note that this quantity depends on the reference chemical potential μ. In the rest of this manuscript, if not specified otherwise, we shall consider $\mu = 0$ and omit this index if not needed.

Within a 1D chiral system, relating $\mathcal{G}^{(e)}_{\rho,x+\Delta x}(t,t')$ to $\mathcal{G}^{(e)}_{\rho,x}(t,t')$ corresponds to computing the evolution of single-electron coherence during propagation along the chiral channel under consideration. This is a dynamical problem that will be discussed in a forthcoming section. However, it has a trivial expression in the case of ballistic propagation at velocity v_F:

$$\mathcal{G}^{(e)}_{\rho,x+\Delta x}(t,t') = \mathcal{G}^{(e)}_{\rho,x}(t - \Delta x/v_F, t' - \Delta x/v_F) \tag{1.14}$$

which corresponds to delaying $\mathcal{G}^{(e)}_{\rho,x}$ by the time of flight $\Delta x/v_F$.

Several important examples in the context of electron quantum optics can be discussed which involve single electron and single hole excitations on top of the Fermi sea.

- One single electron excitation on top of the Fermi sea with wavefunction φ_e: the many body state is $\psi^\dagger[\varphi_e]\,|F\rangle$ in which $\psi^\dagger[\varphi_e]$ creates a single electron excitation in the normalized single particle state $|\varphi_e\rangle$. Such a state would be generated by an ideal single

electron source operated one time only. The excess single electron coherence is then:

$$\Delta\mathcal{G}^{(e)}(t,t') = \varphi_e(-v_F t)\,\varphi_e(-v_F t')^* \tag{1.15}$$

- One single hole excitation on top of the Fermi sea with wavefunction φ_h: the many body state is $\psi[\varphi_h]\,|F\rangle$ in which $\psi[\varphi_h]$ destroys a single electron excitation in the normalized single particle state $|\varphi_h\rangle$. Such a state would be generated by an ideal single hole source operated one time only. The excess single electron coherence is then:

$$\Delta\mathcal{G}^{(e)}(t,t') = -\varphi_h(-v_F t)\,\varphi_h(-v_F t')^* \tag{1.16}$$

  where the minus sign comes from the removal of one electron with from the Fermi sea.

- A single electron hole pair, obtained by transfering a single electron from the hole single particle state φ_h to the electronic single particle state φ_e corresponds to the the many-body state $\psi^\dagger[\varphi_e]\psi[\varphi_h]\,|F\rangle$. This state would ideally be generated during one period by an ideal AC source emitting exactly one electronic and one hole excitation per period. It has an excess single electron coherence given by

$$\Delta\mathcal{G}^{(e)}(t,t') = \varphi_e(-v_F t)\,\varphi_e(-v_F t')^* - \varphi_h(-v_F t)\,\varphi_h(-v_F t')^* \tag{1.17}$$

  Finally it is possible to generate a quantum superposition involving a pristine Fermi sea and the state that we have just considered, thereby leading to

$$|\Psi\rangle = \Big(u + v\psi^\dagger[\varphi_e]\psi[\varphi_h]\Big)\,|F\rangle \tag{1.18}$$

  in which $|u|^2 + |v|^2 = 1$. Then, the corresponding excess single electron coherence is

$$\Delta\mathcal{G}^{(e)}(t,t') = |v|^2\left(\varphi_e(-v_F t)\,\varphi_e(-v_F t')^* - \varphi_h(-v_F t)\,\varphi_h(-v_F t')^*\right) \tag{1.19a}$$

$$+ uv^*\varphi_e(-v_F t)\,\varphi_h(-v_F t')^* + u^* v\varphi_h(-v_F t)\,\varphi_e(-v_F t')^* \tag{1.19b}$$

  The second line in the r.h.s, which involves products of φ_e and φ_h^* or its complex conjugate, arises from the coherent superposition

between the presence and the absence of the electron-hole pair. These terms correspond to electron-hole coherences and play an important role in the discussion of HOM interferometry experiments.

Of course, in experiments, electron sources are rarely ideal. Due to difficulties in tuning their parameters, finite temperature effects, as well as interactions in some setups, the idealized forms we have just discussed do not correspond to the general form of the excess single electron coherence. In the next subsection, the various forms and representation of single electron coherences are discussed.

1.2.3 Representations of single electron coherence

Electronic atoms of signals

For T-periodic sources, a general decomposition can be found which appears as a natural generalization of the expressions discussed in the previous subsection [163]. This decomposition leads to a representation of single-electron coherence in terms of what are called electronic and hole atoms of signals [164]. These atoms of signal are electronic and hole single particle states forming orthonormal bases of the space of electronic and hole single particle excitations and which are covariant with respect to translation by the period T. More specifically, these states fall into families indexed by a, $|\varphi_{a,l}\rangle$, with $l \in \mathbb{Z}$, where the l index corresponds to a period of duration T so that translating $|\varphi_{a,l}\rangle$ by T in the time domain leads to $|\varphi_{a,l+1}\rangle$. Then, the most general form of the excess single electron coherence is given by

$$\Delta\mathcal{G}^{(e)}(t,t') = \sum_{l,l'}\sum_{a} g_a^{(e)}(l-l')\,\varphi_{a,l}^{(e)}(t)\,\varphi_{a,l'}^{(e)}(t')^* \tag{1.20a}$$

$$- \sum_{l,l'}\sum_{b} g_b^{(h)}(l-l')\,\varphi_{b,l}^{(h)}(t)\,\varphi_{b,l'}^{(h)}(t')^* \tag{1.20b}$$

$$+ \sum_{l,l'}\sum_{a,b} \Big(g_{a,b}^{(eh)}(l,l')\,\varphi_{a,l}^{(e)}(t)\,\varphi_{b,l'}^{(h)}(t')^* + g_{b,a}^{(he)}(l,l')\,\varphi_{b,l}^{(h)}(t)\,\varphi_{a,l'}^{(e)}(t')^* \Big)\,, \tag{1.20c}$$

in which we have both electronic atoms of signals (the $\varphi_{a,l}^{(e)}$) and hole atoms of signal (the $\varphi_{b,l}^{(h)}$).

Band theory [195, 174]	Floquet-Bloch analysis [163]
Spatial period	Time period
Single particle Hamiltonian	Single electron coherence
Band energy $\varepsilon_a(k)$	Floquet-Bloch probabilty spectrum $g_a(\nu)$
Quasi-momentum k	Quasi-energy ν
Wannier function $w_{a,l}(x)$	Atom of signal $\varphi_{k,l}(t)$

Table 1.1: Analogy between solid state band theory and signal processing of the excess single-electron coherence described in [163]: the spatial period of the crystal is replaced by the time period $T = f^{-1}$ of the electron source. Instead of diagonalizing a single particle Hamiltonian and spatial translations, one diagonalizes the projections of the single particle excess coherence operator in the electron and hole subspaces and time translation, thereby obtaining Floquet-Bloch bands. Eigenvalues are probabilities instead of energies and depend on a quasi-energy $0 \leq \nu \leq 2\pi f$ instead of a quasi-momentum. The electronic atoms of signal play the same role as the Wannier functions in band theory and are therefore subject to the same ambiguities [135].

com Dario + tableau

In these expressions, the real number $g_a^{(e)}(0)$ and $g_b^{(h)}(0)$ respectively represent the emission probabilities per period for the electronic atom of signal $\varphi_{a,l}^{(e)}$ and hole atom of signal $\varphi_{b,l}^{(h)}$. Note the $-$ sign in front of the hole contribution which expresses the fact that a hole is always the absence of an electron.

There are no coherences between the different families ($a \neq a'$) of electronic atoms of signal as well as between the different families ($b \neq b'$) of hole atoms of signal but there may be electron-hole coherences: $g_{ab}^{(eh)}(l, l')$ may be non-zero. In the same way, electronic atoms of signals may be correlated from one period to the other: $g_{aa}^{(ee)}(l, l')$ maybe non-vanishing even for $l \neq l'$, thereby reflecting the possibility of an electronic coherence time larger than the time-period T. Therefore, the use of electronic atoms of signal provides a discrete representation of single electron coherence which makes it easier to distinguish what are the single electron excitations emitted by an electron source from how they are emitted. This is the exact analogous, in the quantum domain, of describing music in terms of musical notes and of the music score (see Fig. 1.5).

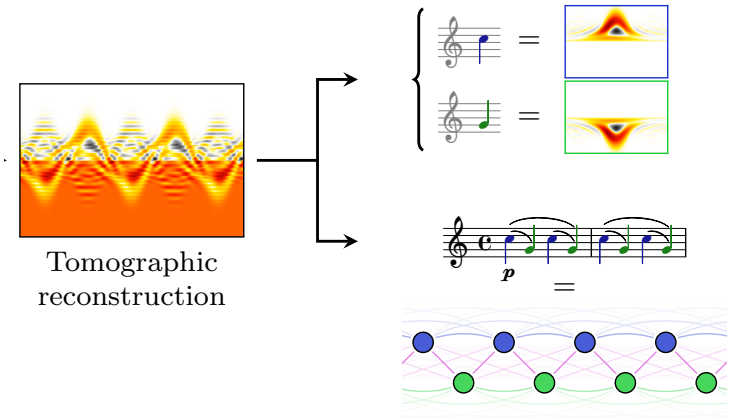

Figure 1.5: (Extracted from [113]) Schematic representation of the decomposition of the excess electronic coherence $\Delta W^{(e)}(t,\omega)$ in electron and hole atoms of signals (case of a low amplitude sinusoidal drive). The atoms of signal play the role of musical notes and the coherences appearing in Eq. (1.20) provide the analogous of the music score.

One should nevertheless keep in mind that the electronic atoms of signals are not unique, as expected by the analogy with the Wannier functions [190] in band theory (Table 1.1 summarizes the analogy between the two approaches). In band theory, Wannier functions are not unique because Bloch-functions, which are common eigenvectors of the electrons and of translation operators associated with the crystal's spatial periodicity, may be redefined at least generically by a phase. Consequently, Wannier functions have an intrinsic ambiguity, that is usually lifted by imposing an extra condition such as minimal spreading in space. In the present situation, it is the same: the atoms of signals may be chosen as having a minimal spreading in time. The reader is referred to Ref. [163] for the corresponding details.

Time-frequency representation: the Wigner function

The electronic Wigner distribution function[5]

$$W^{(e)}_{\rho,x}(t,\omega) = \int_{\mathbb{R}} v_F \mathcal{G}^{(e)}_{\rho,x}\left(t+\frac{\tau}{2}, t-\frac{\tau}{2}\right) e^{i\omega\tau} \mathrm{d}\tau \qquad (1.21)$$

[5]The v_F prefactor ensures that $W^{(e)}(t,\omega)$ is dimensionless.

introduced in Ref. [64] is real and gives access to both time-dependence and energy content at the single particle level. In particular, the average time dependent electric current, the electronic occupation numbers and even the average instantaneous excess energy current $\langle j_E(x,t)\rangle_\rho$ can be related to the excess Wigner distribution function which is defined in the same way from the excess single electron coherence $\Delta\mathcal{G}^{(e)}_{\rho,x}$:

$$\langle i(x,t)\rangle_\rho = -e\int_{\mathbb{R}} \Delta W^{(e)}_{\rho,x}(t,\omega)\mathrm{d}\omega \tag{1.22a}$$

$$\langle j_E(x,t)\rangle_\rho = \hbar\int_{\mathbb{R}} \omega\,\Delta W^{(e)}_{\rho,x}(t,\omega)\mathrm{d}\omega \tag{1.22b}$$

$$f_e(\omega) = \lim_{T\to+\infty}\left[\frac{1}{T}\int_{-T/2}^{T/2} W^{(e)}_{\rho,x}(t,\omega)\,\mathrm{d}t\right]. \tag{1.22c}$$

In systems with electron-hole symmetry, such as the dispersionless chiral fermion description of Quantum Hall edge channels, the electronic Wigner distribution can be related to the hole Wigner distribution function $W^{(h)}$ which is defined from the hole coherence by Eq. (1.21): $W^{(e)}_{\rho,x}(t,\omega) = 1 - W^{(h)}_{\rho,x}(t,-\omega)$.

It is important to distinguish the electronic Wigner function from the Wigner function used in quantum optics for description of coherences of a single electromagnetic mode at different orders. In photon quantum optics, Wigner representation is usually used for conjugate continuous variables (so called optical quadratures) governing a single harmonic oscillator corresponding to the relevant spatio-temporal mode of the quantum electromagnetic field. The quantum optical Wigner function of optical quadratures characterizes arbitrarily high order Glauber coherences of this electromagnetic mode and thus is fundamentally different from the Wigner representation of the conjugate variables x and p describing 1D spatial propagation.

Before discussing the notion of electronic atoms of signal, it is useful to discuss a few examples of the various representations of the single electron coherence associated with simple single electron excitations. Let us consider for example the case of the single electron excitation emitted by the emptying of a single resonant level with energy $\hbar\omega_e$ above the Fermi energy into a chiral edge channel. This leads to an electronic wavefunction with a truncated Wigner-Weisskopf spectral shape, that is a truncated Lorentzian wave-function in the frequency domain,

$$\widetilde{\varphi_e}(\omega) = \sqrt{\frac{v_F\gamma_e}{\mathcal{N}}}\,\frac{\Theta(\omega)}{\omega-\omega_e+i\gamma_e/2}\,, \tag{1.23}$$

in which γ_e denotes the excitations' natural width, $\Theta(\omega)$ the Heaviside function and $\mathcal{N}$ is a normalization factor. The resulting frequency and time domain representations as well as the electronic Wigner distribution function are depicted in Fig. 1.6.

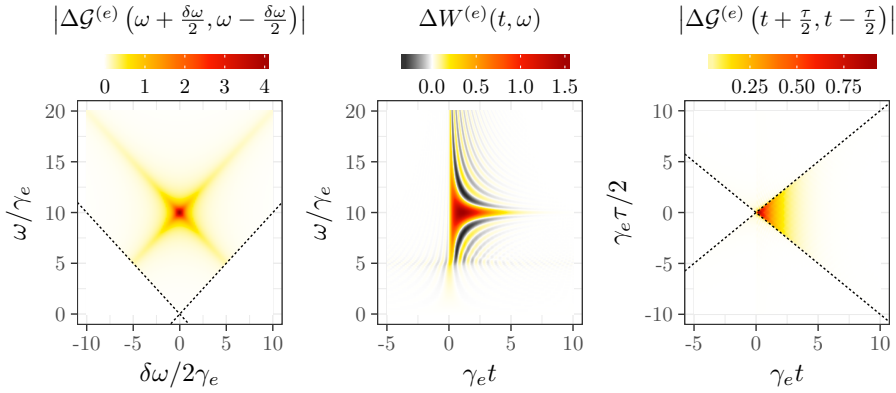

Figure 1.6: Representations of the coherence (Extracted from [162]). Here are depicted three representations of the single electron coherence of a typical wave packet emitted by the mesoscopic capacitor in the single-electron source regime. On the left, we have the modulus of the energy representation of the single-electron coherence $\varphi_e(t)\,\varphi_e(t')^*$ which is only non-vanishing in the electron quadrant as expected. On the right, we have the modulus of the time representation. We can see that the average current is an exponential decay. On the middle, we have plotted the electronic Wigner distribution function which is real and contains both positive and negative values. We can see both the energy dependence of the excitation (which populates only positive energies) and its time dependence (which is an exponential decay).

It is also interesting to consider the Levitons whose generation has been discussed in Sec. 1.1.3. Fig. 1.7 shows the electronic Wigner function of a Fermi sea to which a Lorentzian pulse has been applied, with the resulting current carrying an integer multiple of the elementary charge $-e$.

$$v_F\mathcal{G}^{(e)}(t,t') = \mathcal{G}_F^{(e)}(t-t')\,e^{\frac{ie}{\hbar}\int_{t'}^{t}V(\tau)\,\mathrm{d}\tau} \tag{1.24}$$

in which $\mathcal{G}^{(e)}_{\mu,T_{\mathrm{el}}}(t-t')$ is the single electron coherence of the reference Fermi equilibrium distribution with chemical potential μ and electronic

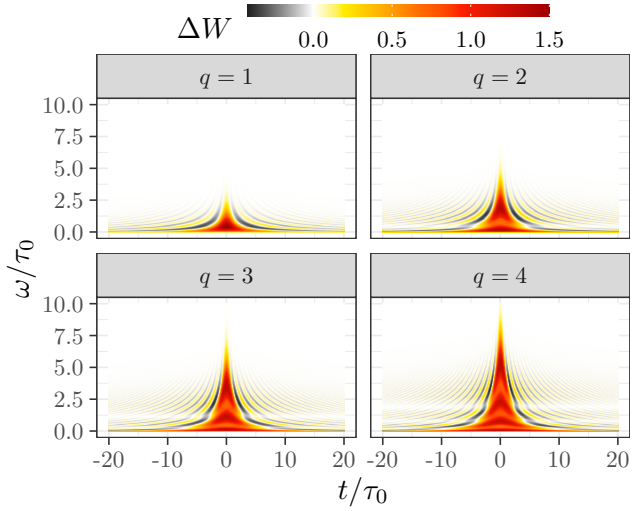

Figure 1.7: (Figure extracted from [113]) Excess Wigner function for the n-Leviton excitations up to $n = 4$. Note that $\Delta W^{(e)}(t = 0, \omega)$ exhibits n maxima which arise from the addition of the contributions of the n individual single particle states depicted on 1.8: each of them adds one more spot with negativities close to $t \simeq 0$ at higher values of ω.

temperature $T_{\rm el}$, and

$$V(t) = \frac{V_0}{1 + (t/\tau_0)^2} \tag{1.25}$$

with $V_0 = nh/(e\pi\tau_0)$ to ensure that the resulting current pulse $\langle i(t)\rangle = e^2 V(t)/h$ carries the charge $-ne$. As shown in [64], at zero temperature, this state is a Slater determinant of n mutually orthogonal normalized wave packets whose expression is

$$\langle \omega | \varphi_{k,\tau_0} \rangle = \sqrt{2\tau_0}\, \Theta(\omega)\, e^{-\omega\tau_0} L_{k-1}(2\omega\tau_0) \tag{1.26}$$

where $L_k(X)$ denotes the k-th Laguerre polynomial. Their Wigner function are depicted on Fig. 1.8 for $k = 1$ to $k = 4$.

adapter la figure avec le com de Dario

To conclude this rapid discussion of examples, we stress that the above graphs are depictions of ideal wavepackets which could, in principle, only be observed at zero temperature and with fine tuned parameters of the source. In reality, the source may emit more than a single electron excitation per duty cycle. We refer the reader to [17] where the

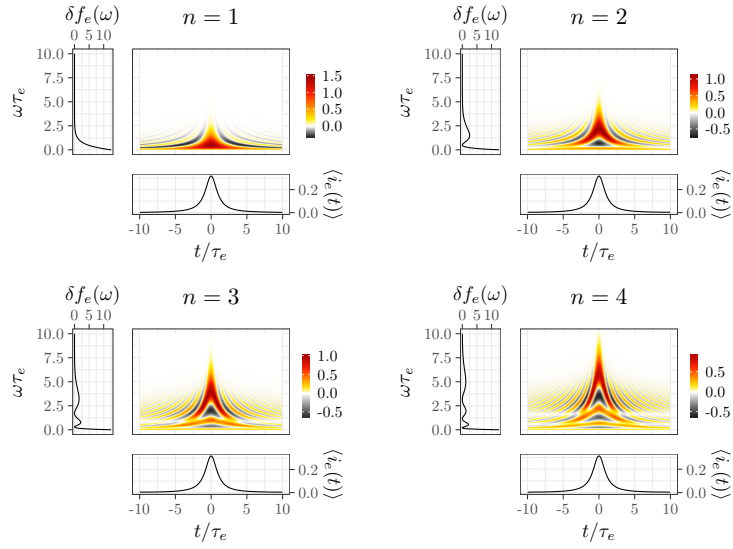

Figure 1.8: (Figure extracted from [162]) Wigner representation of the single-electron wavefunctions building the n-Leviton excitations up to $n = 4$.

single electron coherence emitted by an Ohmit contact driven by a train of Lorentzian pulses calibrated to emit a train of Levitons have been reconstructed by HOM tomography. The extration of single electron excitations from these tomographic data clearly showed that the single particle content does not involve only one electronic atom of signal per period (see Fig. 5 of [17] for example). These remarks bring us to the last part of this section devoted to single electron question: how is it measured in experiments ?

1.2.4 Single electron tomography

Experimentalists in mesoscopic physics have long been used to measuring quantities related to charge transport. These include the DC average current, but also finite frequency average currents [77, 78, 22], low frequency noise current with sensitivities down to 10^{-31} A^2/Hz [84, 83] and current noise at finite frequency [149] which has been used to characterize single electron emission by the mesoscopic capacitor. Numerous results have been obtained via current noise measurement such as confirmation of the quantum shot noise reduction [85] and of high frequency

quantum shot noise theory [193], the determination of the fractional charge of elementary excitations in the fractional quantum Hall effect [171], as well as of the spectrum of emitted photons by a DC biased junction at fractional charge [16] which confirmed non-equilibrium fluctuations relations established by I. Safi and collaborators [165, 170]. Non stationary current noise has even been measured, thereby leading to the demonstration of electromagnetic squeezing in tunnel junctions [79] and in integer quantum Hall systems [9]. Finally, it was instrumental in the first experimental evidence of fractional statistics in the fractional quantum Hall effect [10].

But the average current, as well as current noise, only represent a part of single or two electron coherence. For example,

$$\langle i(t)\rangle_{\rho,x} = -ev_F\,\Delta\mathcal{G}^{(e)}_{\rho,x}(t,t) \tag{1.27}$$

which shows that only the diagonal part of single electron coherence in the time domain can be accessed. For the current noise, the situation is similar since only the diagonal part of the intrinsic excess two electron coherence is involved in the current noise correlators [184]. Accessing the off-diagonal part of these quantum signals thus require more than direct measurement of average currents and of the noise.

There are basically two tomographic methods for reconstructing single electron coherence. The first one is based on the use of a time dependent filter which is a parametrically driven quantum conductor which is fed by the quantum electrical current whose excess single electron coherence we would like to determine. The outgoing average electrical current is then a linear function of this unknown quantum signal and we have a linear inversion problem with a kernel determined by the experimental parameters of the parametric drive of the filter. This process has been partly implemented to determine the occupation number in out of equilibrium quantum Hall edge channels but with a time-independent filter [3] and, much more recently with a time-dependent filter, it has lead to the tomography of the solitary electronic excitations emitted by a time dependent barrier [72].

The second method relies on quantum point contact, which is of course a very simple quantum conductor. Its scheme of principle is depitected on Fig. 1.9. Here, the parametric driving of the previous method is replaced by the injection of a controlled single electron coherence on one of the input channels, while the quantum signal to be characterized is sent on the other one. This is the principle of Hong-Ou-Mandel tomography introduced in [92] and demonstrated in its generic form in [17]. It

relies on two particle quantum interferences and the measured signal is the low frequency current noise at the outcome of the Hong-Ou-Mandel interferometer.

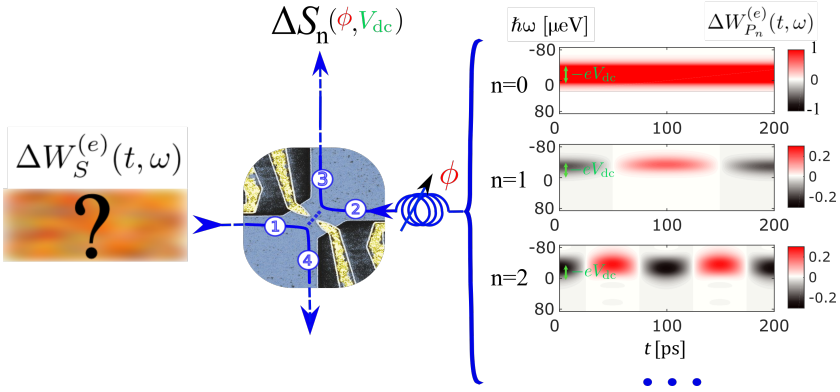

Figure 1.9: (Figure extracted from [113]) HOM tomography protocol: Two particle interferences between the unknown periodic electronic Wigner distribution $W_S^{(e)}$ in the incoming channel (1) and a modulated reference Fermi sea signal, called the probe signal, $W_{P_n}^{(e)}$ incoming in channel (2), generated by a voltage $V_{P_n}(t)$ applied to a contact, occurs at a QPC. The low frequency current noise is measured at the output (3) as function of relative phase and reference probe amplitude. The measurement is repeated with a set of known reference probes at harmonics of the base frequency of the unknown signal. For each harmonic, one then varies the DC bias of the probe to sweep the position in ω thereby leading to a reconstruction of the ω-dependence of the n-th harmonic of the unknown excess Wigner distribution $\Delta W_S^{(e)}(t,\omega)$ [17]. Wigner distributions of the probe signal correspond to weak harmonic modulation (see Eq. (1.32)).

When both sources S_1 and S_2 are switched on, this excess low frequency current noise, denoted by $\Delta S_{11}^{(S_1\&S_2)}$, is the sum of three contributions [64]:

$$\Delta S_{11}^{(S_1\&S_2)} = \Delta S_{11}^{(S_1)} + \Delta S_{11}^{(S_2)} + \Delta S_{11}^{(\mathrm{HOM})}, \tag{1.28}$$

where $\Delta S_{11}^{(S_1)}$ and $\Delta S_{11}^{(S_2)}$ are the excess current noises when only the

source S_j ($j = 1,\ 2$) is switched on. These terms are given by:

$$\Delta S_{11}^{(S_1)} = e^2 T^2 \int_{\mathbb{R}} \overline{\Delta W_{S_1}^{(e)}(t,\omega)}^{t} \left(1 - 2f_{\rm eq}(\omega)\right) \frac{\mathrm{d}\omega}{2\pi}. \tag{1.29a}$$

$$\Delta S_{11}^{(S_2)} = e^2 R^2 \int_{\mathbb{R}} \overline{\Delta W_{S_2}^{(e)}(t,\omega)}^{t} \left(1 - 2f_{\rm eq}(\omega)\right) \frac{\mathrm{d}\omega}{2\pi}. \tag{1.29b}$$

where R and T denote the reflection and transmission probabilities of the QPC and f_{eq} the equilibrium Fermi distribution of the incoming channels. These terms correspond to the excess noise in Hanbury Brown and Twiss (HBT) experiments performed on each of the sources [24]. Since $1 - 2f_{\rm eq}(\omega) = \tanh\left(\hbar\omega/2k_B T_{\rm el}\right)$ this expression counts the total number of excitations (electrons and hole) whose energy are above $k_B T_{\rm el}$ injected by the source S_j. When the other channel (called the probe) is at zero temperature, it is exactly the total number of excitations injected by S_j. The last term is called the HOM contribution since it requires both sources to be switched on. It is given by

$$\Delta S_{11}^{(\rm HOM)} = -2e^2 RT \int_{\mathbb{R}^2} \overline{\Delta W_{\rm 1in}^{(e)}(t,\omega) \Delta W_{\rm 2in}^{(e)}(t,\omega)}^{t} \frac{\mathrm{d}\omega}{2\pi}, \tag{1.30}$$

where $\overline{\cdots}^{t}$ denotes the average over time t. This contribution is the overlap of the excess single-electron coherences arriving at the QPC [64] and encodes the effect of two-particle interferences between the excitations emitted by these sources. Finally, the minus sign comes from the fermionic statistics of electrons. Viewing $\Delta W_{\rm 1in}^{(e)}$ as the unknown quantum signal $\Delta W_{S}^{(e)}$ and $\Delta W_{\rm 2in}^{(e)}$ as a well controlled probe signal, Eq. (1.30) is a linear filtering equation connecting the signal to be reconstructed to the measured quantity $\Delta S_{11}^{(\rm HOM)}$. This time, the filter is nothing but the probe signal $\Delta W_{\rm 2in}^{(e)}$. This explains why this tomography protocol, based on the measurement of the current noise, gives a clear meaning to Landauer's aphorism "The noise is the signal" [122].

The last point to explain is the choice of the probe signals. In the generic protocols originally proposed in [92], is was proposed to used as probe signal small AC drives at all the frequencies that could appear in the unknown excess coherence, supplemented by a DC bias. This comes from the evaluation of the single electron coherence induced by a small AC drive. Let us consider Eq. (1.24) and expand it in power of $V_{\rm a.c.}$ we obtain at first order in $V_{\rm AC}$:

$$\Delta\mathcal{G}^{(e)}(t,t') = \mathcal{G}^{(e)}_{0,T_{\rm el}}(t-t') \frac{e}{\hbar} \int_{t'} V_{\rm AC}(\tau)\, \mathrm{d}\tau\,. \tag{1.31}$$

Considering the case $V_{\rm AC}(t) = V_{\rm AC}\cos(2\pi nft + \phi)$ and evaluating the resulting Wigner function leads to the probe's electronic distribution function at first order in[6] $eV_{\rm AC}/hf$:

$$\Delta W^{(e)}_{{\rm P}_n}(t,\omega) = \frac{eV_{\rm AC}}{hf}\,\frac{1}{|n|}\,\chi_{\pi|n|f,T_{\rm el}}(\omega)\,\cos(2\pi nft - \phi) \tag{1.32}$$

where for $\omega' > 0$, we define

$$\chi_{\omega',T_{\rm el}}(\omega) = f_{T_{\rm el}}(\omega - \omega') - f_{T_{\rm el}}(\omega + \omega') \tag{1.33}$$

where $f_{\rm el}(\omega)$ denotes the Fermi distribution at vanishing chemical potential and electronic temperature $T_{\rm el}$. The above expression reduces to the characteristic function of the interval $[-\omega', \omega']$ for $T_{\rm el} = 0\,{\rm K}$. At non zero temperature, it is a thermal smearing of this pulsation interval over $k_B T_{\rm el}/\hbar$. Eq. (1.32) thus shows that the small AC drive at frequency nf just generates the temporal modulation of this drive within a smeared interval of ω of width $2\pi|n|f$ around the Fermi level. This is exactly what is depicted on the right part of Fig. 1.9. In the electronic Wigner representation, the probes P_n characterized by the frequency nf, its phase ϕ, its AC amplitude $V_{\rm AC}$ such that $eV_{\rm AC}/hf \lesssim 1$ and its dc bias $V_{\rm DC}$ enable us to perform a Fourier transfom on the $n-th$ harmonic with respect to the basic frequency f over the interval $|\omega - \omega_{\rm DC}| \leq \pi|n|f$ where $\omega_{dc} = -eV_{\rm DC}/\hbar$ denotes the dc bias of the probe.

1.3 Bosonization

In the final section of this chapter, we present a succinct exploration of bosonization—a potent analytical method tailored for addressing Coulomb interaction effects within electron quantum optics. This method elegantly maps electronic excitations onto quantized charge density waves, known as plasmons, which obey bosonic statistics.

To lay the foundation, we will first present a conceptual overview of bosonization devoid of mathematical formulations. Subsequently, we will elucidate the pivotal equations delineating the correspondence between electronic excitations and plasmons, their association with the electric current, and various essential properties invoked throughout this manuscript and its appendices.

[6]This dimensionless number corresponds to the number of photons of energy hf associated with the amplitude of the drive. We are indeed considering the limit dominated by single photon processes.

For a more in-depth comprehension, the interested reader is directed to the pertinent chapter of Clément Cabart's thesis [34], which delves deeper into the nuances and interpretations. Moreover, for an exhaustive grasp of bosonization, Giamarchi's seminal work[82] stands as a recommended reading; it not only introduces but also portrays the utility of bosonization in addressing theoretical quandaries in one-dimensional systems.

1.3.1 Conceptual overview

Fermi's theory, utilizing a perturbative approach, has demonstrated success in modeling the electron cloud within a solid characterized by weak Coulomb interactions in both two-dimensional (2D) and three-dimensional (3D) cases. However, this theory encounters substantial difficulties when applied to one-dimensional (1D) systems. Coulomb interactions in 1D systems prohibits a straightforward perturbative treatment of their effect. The dependence of dimensionality on the effects of electron-electron interactions may initially appear counter-intuitive, but can be elucidated through a simple thought experiment involving the conceptualization of electrons as rigid spheres.

In a 2D or 3D context, an electron seeking to pass another one has the option to navigate around the other electron, necessitating a relatively minimal energy expenditure since the region of high effective Coulomb potential can be avoided. Conversely, within a 1D system, the electron has no alternative but to probe the region of strong interaction with the other electron, intuitively justifying why interaction effects are drastic in 1D.

Consequently, the propagation of electronic excitation in a 1D metallic system does not rely on the perturbative image of an individual quasiparticle — a 'dressed' electron as proposed in Landau Fermi's theory [153] — but pushes to the front scene a collective excitation, akin to the behavior of a phonon. This specific collective excitation of the electron gas has been termed a plasmon. Given that our 1D channels are actually edge channels of the quantum Hall effect, we sometimes specifically denote these excitations as edge-magnetoplasmons.

One intriguing aspect of this conceptualization involves the bosonic statistical behavior of these edge-magnetoplasmon excitations, despite their origin from fermionic electrons. This property can be understood at a qualitative level without resorting to the full theoretical derivation.

In a metallic system, the ground state is not a particle void; in-

stead, it is a stationary Fermi sea with many electrons already present in the system. Therefore, an excitation can manifest as either a negatively charged 'electronic excitation' above the Fermi level or a positively charged 'hole excitation' which consists of extracting one electron below the Fermi level. Both these quasi-particles obey fermionic statistics and interact via Coulomb interactions. An electron-hole pair, viewed as a single entity, can also be perceived as a quasi-particles but with a bosonic statistic.

Edge-magnetoplasmons, in essence, constitute a coherent superposition of creating or not creating such electron-hole pairs, which accounts for their bosonic statistical behavior.

The discussion thus far suggests that it might be logical to solely utilize a bosonic framework for the analysis of 1D channels, given its congruence with experimental results. Yet, as educated readers may remember, quantum electronics in these channels have been explored without the requirement for bosonization.

Studies of these 1D systems typically prioritize single to few electron excitations over a short distance and in channels with strong Coulomb interaction effects limited to finite size regions. This is not always the case, a famous example being the Fractional Quantum Hall phases [186] in which exotic excitation of fractional charges and statistics have been predicted [123] and progressively unraveled experimentally by producing evidences for their fractional charge [171, 152] and then fractional statistics [10, 142] . Such "exotic phase" which should be called strongly correlated electronic fluids, are not considered in the present manuscript.

Under the weaker Coulomb interaction effects conditions that really define electron quantum optics, the Fermi sea remains a pertinent approximation for the electron fluid in a metallic conductor even in 1D. The fermionic framework of Landau Fermi's theory, however, may fall short in situations where Coulomb interactions still play a role. Two primary shortcomings arise. First, Fermi's theory can impose considerable computational burden when calculating electronic excitations in these interacting systems. Second, it may yield erroneous analytical results when treating Coulomb interactions effects perturbatively. In light of these issues, the bosonic formalism emerges as an effective alternative approach. This formalism will prove particularly useful when studying the radiation coupler in Chapter 2.

The theory in question is not without limitations. While a detailed mathematical derivation will not be developed here, it is crucial to note

that the form presented relies on the linearization of the energy spectrum around the Fermi energy. This implies a focus on energy levels close to the Fermi level. Furthermore, some of the techniques presented here are most efficient when the many-body states differs from the ground state by a few electron or hole excitations which is fortunately the case for most of the electron quantum optics experiments discussed in the present thesis. However, these limitations are not overly restrictive.

Next, we shall delve into the bosonization "recipe" which allows to express plasmons in terms of electronic operators and conversely.

1.3.2 Relations between electrons and bosons

As discussed, plasmons can be characterized as coherent superpositions of particle-hole pairs. At a given energy, there is no reason for treating pairs of single electron state differently depending on their energy. Consequently, the creation and annihilation operators for a plasmonic mode at frequency ω are defined as:

$$b(\omega) = \frac{1}{\sqrt{\omega}} \int_{-\infty}^{+\infty} c^\dagger(\omega' - \omega) c(\omega') \, \mathrm{d}\omega' \tag{1.34a}$$

$$b^\dagger(\omega) = \frac{1}{\sqrt{\omega}} \int_{-\infty}^{+\infty} c^\dagger(\omega' + \omega) c(\omega') \, \mathrm{d}\omega' \tag{1.34b}$$

in which $c^\dagger(\omega)$ and $c(\omega)$ denote the creation and annihilation operators for an electron at energy $\hbar\omega$, respectively. The $1/\sqrt{\omega}$ prefactor comes from the fact that, as shown by Clément Cabart In Section 1.4.1 of his thesis, these operators then obey the canonical commutation relations $\left[b(\omega), b^\dagger(\omega')\right] = \delta(\omega - \omega')$, thus proving that plasmons obey bosonic statistics.

Transitioning to the time domain, the operators that describe these plasmonic modes at time t are formulated in terms of the self-adjoint quantum field:

$$\phi(t) = \frac{\mathrm{i}}{\sqrt{4\pi}} \int_0^{+\infty} \left[\mathrm{e}^{\mathrm{i}\omega t} b^\dagger(\omega) - \mathrm{e}^{-\mathrm{i}\omega t} b(\omega) \right] \frac{\mathrm{d}\omega}{\sqrt{\omega}} \,. \tag{1.35}$$

Note that these bosonic modes are free: $b(\omega)$ and $b^\dagger(\omega)$ correspond to a mode of energy $\hbar\omega$. This is a remarkable statement: in the bosonic language, the electronic fluid's Hamiltonian for the Fermi gas is quadratic.

For the inverse representation, expressing a fermionic electron field in terms of plasmonic modes is done via the following relation:

$$\psi(t) = \frac{\mathcal{U}}{\sqrt{2\pi a}} \exp\left[\mathrm{i}\sqrt{4\pi}\phi(t)\right] \tag{1.36}$$

In this equation, the length a is a short-distance cutoff defining the limit beyond which bosonization loses validity and $\psi(t)$ is the electronic field operator at time t. The exponential component encompasses plasmonic information and ensures that creating an electron at time t provides the corresponding δ distribution in terms of charge density. However, it omits the fact that employing the $\psi(t)$ operator extracts a fermionic excitation from the many body system and thus changes its total fermion number. To accommodate this, the Klein ladder operator $\mathcal{U}$ must be included. It follows the anticommutation rules and commutes with all bosonic operators, its application is invariant with respect to the order of operations with the bosonic operators in Eq. (1.36). Also this operator works only for one kind of fermion. If we bosonize multiple species (fermions with varied spins or in different channels), we require as many Klein ladder operators as there are distinct fermionic species in the system and ensure that they obey the proper anti-commutation relations.

In a finite size system such as an electronic interferometer in the Coulomb dominated regime [98], these Klein operators could be associated with bosonic zero modes that have not been accounted for here since finite size effects associated for example with the charging energy in Coulomb dominated interferometer are neglected here.

1.3.3 Properties of the coherent displacement operator

The bosonic component of the fermionic operators in Eq. 1.36, represented by the exponential, can be understood as an infinite dimensional variant of the coherent displacement operators:

$$\mathcal{D}[\alpha] = \exp\left(\int_0^{+\infty} \left[\alpha(\omega)b^\dagger(\omega) - \alpha(\omega)b(\omega)\right] \mathrm{d}\omega\right) . \tag{1.37}$$

Applying this displacement operator on a vacuum of plasmons $|0\rangle$ generates an infinite dimensional multimode coherent state

$$\mathcal{D}[\alpha]\,|0\rangle = \bigotimes_{\omega>0} D(\alpha(\omega))\,|0_\omega\rangle = \bigotimes_{\omega>0} |\alpha(\omega)\rangle = |[\alpha]\rangle \ . \tag{1.38}$$

We will use this displacement operator in this manuscript, so let us exhibit their following essential characteristics:

$$\mathcal{D}[\alpha]\mathcal{D}[\beta] = \exp\left(\mathrm{i}\int_0^\infty \mathrm{Im}\left(\beta^*(\omega)\alpha(\omega)\right)\mathrm{d}\omega\right)\mathcal{D}[\alpha+\beta] \tag{1.39a}$$

$$\mathcal{D}[\alpha] = \exp\left(-\int_0^\infty \frac{|\alpha(\omega)|^2}{2}\mathrm{d}\omega\right) :\mathcal{D}[\alpha]: \tag{1.39b}$$

in which $:\mathcal{D}[\alpha]:$ denotes the normal ordered version of this displacement operator. By leveraging these properties, the scalar product between coherent states $\langle[\beta]||[\alpha]\rangle$ can be expressed as

$$\langle[\beta]||[\alpha]\rangle = \exp\left(\int_0^\infty \left[\mathrm{i}\,\mathrm{Im}\left(\beta^*(\omega)\alpha(\omega)\right) - \frac{|\alpha(\omega)-\beta(\omega)|^2}{2}\right]\mathrm{d}\omega\right) \tag{1.40}$$

and matrix elements can be computed via:

$$\langle[\alpha]|\, :\mathcal{D}[\gamma]:\, |[\beta]\rangle = \exp\left(\int_0^\infty \left[\gamma(\omega)\alpha^*(\omega) - \gamma^*(\omega)\beta(\omega)\right]\mathrm{d}\omega\right)\langle[\alpha]||[\beta]\rangle\,. \tag{1.41}$$

1.3.4 Relation between electrical current and plasmons

In condensed matter systems, a plasmonic coherent state can be generated by applying a standard AC voltage $V(t)$ to the electron fluid, for example via an Ohmic contact in the case of quantum Hall edge channels. To elucidate the relationship between $V(t)$ and the resultant coherent state, we consider the influence of $V(t)$ on an Ohmic contact interfacing with a Fermi sea. This interaction gives rise to a current whose average value is:

$$i(t) = \frac{e^2 V(t)}{h}\,. \tag{1.42}$$

Concurrently, by evaluating the Fourier transform $i(t)$ based on the equation given by Eq. 1.27, we establish that the finite-frequency components of the current are intrinsically associated with the plasmonic operators as follows ($\omega > 0$):

$$i(\omega) = -e\sqrt{\omega}\, b(\omega)\,. \tag{1.43}$$

From these two equations, it becomes evident that when a coherent state is formed by a voltage $V(t)$, all the current's finite-frequency components

align with those produced by the specified voltage. This is represented by

$$\forall \omega > 0, \quad -e\sqrt{\omega}\,\langle b(\omega)\rangle = \frac{e^2}{h}\widetilde{V}(\omega) \tag{1.44}$$

where $\widetilde{V}$ denotes the Fourier transform of $V(t)$. Hence, the coherent state under investigation can be described as

$$\mathcal{D}\left[-\frac{e\widetilde{V}(\omega)}{h\sqrt{\omega}}\right]|0\rangle \ . \tag{1.45}$$

Chapter 2

Radiation coupler

2.1 Introduction

The radiation coupler is a crucial element of the electron radar: it is the component that couples the MZI to the electromagnetic field to be probed. It involves a capacitive coupling between the edge channel of the upper branch of the MZI, also called the target branch, to the radiation channel. There are several types of radiation couplers. For example, the radiation channel can be an integer quantum Hall edge channel, a fractional one, or a classical transmission line.

In all cases, the radiation coupler will act as a filter between the radiation channel and the electron fluid, modulating in a frequency dependent way the coupling between the radiation to be probed and the electronic fluid. Depending on the type of radiation we wish to probe, some radiation couplers are better suited than others. This is why it is fundamental to have quantitative models for the various experimentally relevant radiation couplers.

These couplers can be viewed as linear scatterers, or equivalently beam splitters, for photons propagating within the radiation channel and EMPs propagating within the target branch. As long as all the conductors involved in the radiation coupler remain in the linear response regime, the radiation coupler can be described in terms of single particle scattering between photons and EMPs.

Moreover, the coefficients of this scattering matrix have a transparent physical interpretation in terms of finite frequency admittances. This connexion has been originally unravelled by I. Safi in the context of quantum wires [168, 169, 167] but has been since used in the context

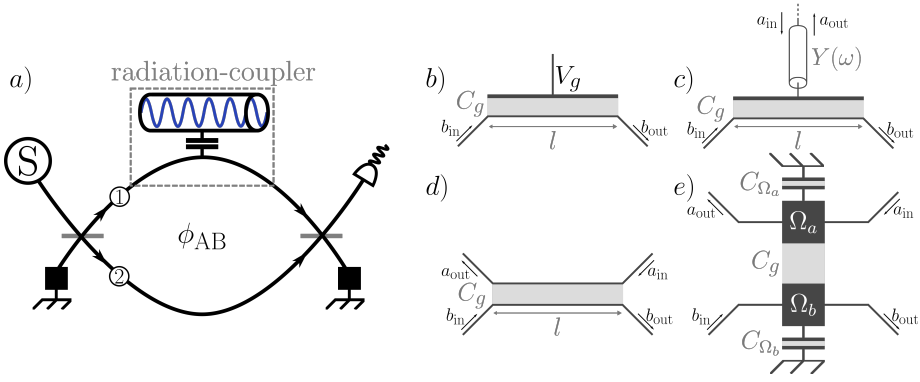

Figure 2.1: (a) Scheme of principle for sensing electromagnetic fields with single electron excitations: one of the branches of an electronic Mach-Zehnder interferometer (MZI) is capacitively coupled tothe external electromagnetic radiation. The region where this coupling is effective is called the radiation coupler.
Various types of radiation couplers are considered: (b) a top gate capacitively coupled to the quantum Hall edge channel of the target branch is driven by a classical time dependent voltage. (c) The top gate of (b) is connected to a transmission line. (d) The radiation channel is another quantum Hall edge channel capacitively coupled to the target branch of the MZI. (e) he rTadiation coupler consist of two small floating Ohmic contacts that are capacitively coupled.

of quantum Hall edge channels [53, 20]. It is a cornerstone for the discussion of electronic decoherence within quantum Hall edge channels [52, 65, 35] and it will be instrumental for the discussion of the electron radar in the presence of Coulomb interactions (see Chapter 4).

The radiation channel can also be another edge channel which can be viewed as a high impedance transmission line. In all these examples, the bosonization formalism will be instrumental in modeling the radiation coupler's properties. The main objective of this section is to determine the scattering matrix for electromagnetic excitations, photons or EMPs, propagating within the radiation channel and EMP modes within the MZI.

This chapter is organized as follows: in Sec. 2.2, the connexion between the EMP approach and the usual description of electronic circuit in terms of multi-terminal circuit elements will be reviewed. This representation will be particularly useful, as we will show that there is a direct link between the plasmonic scattering amplitude and the admittance matrix, which is an experimentally measurable quantity. We will then turn to the various models of interest depicted on Fig. 2.1.

In Sec. 2.3, the coupling of an electron to a classical electric potential will be considered via two coupler models: one that assumes that the electron directly feel the applied voltage drive and one, more realistic, where the time dependent voltage drive is applied to a top gate. However, by construction, these models can only describe the coupling to a classical voltage drive.

Motivated by the perspective of probing quantum radiation, we will study in Sec. 2.4, a coupler built from two counter-propagating edge channels in total mutual influence. In this case, an electron propagating along the target branch of the MZI probes the charge fluctuations, possibly of quantum origin, of the other channel.

2.2 From EMP scattering to electrical engineering and back

In this section, we will review the relation between the edge-magnetoplasmon (EMP) scattering for quantum Hall conductors and the more traditional point of view of electrical engineering which focuses on the current response of a multi-terminal device or circuit element to voltage drives applied to reservoirs. Our aim is not to present an exhaustive review of this topic but to give the reader the basic tools that will be useful for

understanding the underlying physics of the various radiation coupler models discussed in this chapter.

2.2.1 EMP scattering matrix

In its most general form, the radiation coupler is a system that capacitively couples together multiple radiation channels. We can picture it as a beam splitter between photons and EMP propagating in the channels to which it is connected. It is described by an EMP scattering matrix, also called plasmonic scattering matrix, with elements $\mathrm{S}_{\alpha\beta}(\omega)$:

$$b_\alpha^{\mathrm{out}}(\omega) = \sum_\beta \mathrm{S}_{\alpha\beta}(\omega)\, b_\beta^{\mathrm{in}}(\omega) \tag{2.1}$$

which connect the bosonic mode $b_\alpha^{\mathrm{out}}(\omega)$ leaving the coupler through channel α to the bosonic mode $b_\beta^{\mathrm{in}}(\omega)$ entering the coupler through channel β. A drawing of a radiation coupler connected to multiple charge reservoirs is shown Fig. 2.2. Each reservoir α, to which we apply an AC voltage $V_\alpha(\omega)$, is connected to the coupler by a lead with an input and an output channel which, for simplicity, is assumes to be an integer quantum Hall chiral edge channel. Other types of radiation channels such as fractional Hall edge channels or transmission lines can also be considered only if we introduce the appropriate prefactors in the relation between the EMP creation and destruction operators and the electrical current.

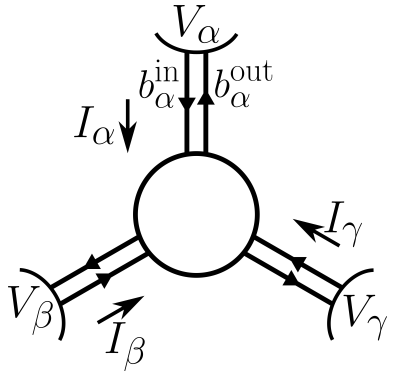

Figure 2.2: Drawing of a three-terminal circuit. Each reservoir β imposes a voltage V_β to the circuit which responds with an electric current I_α for each lead α.

In each of these channels, the EMP modes at frequency ω are described by the operators $b_\alpha^{\rm in}(\omega)$ and $b_\alpha^{\rm out}(\omega)$ which are

$$i_\alpha^{\rm in/out}(\omega) = -e\sqrt{\omega}\, b_\alpha^{\rm in/out}(\omega) \tag{2.2}$$

So, by inserting Eq.(2.1) in Eq. (2.2), the outgoing current in each channel is a function of all the incoming currents:

$$i_\alpha^{\rm out}(\omega) = \sum_\beta \mathrm{S}_{\alpha\beta}(\omega)\, i_\beta^{\rm in}(\omega)\,. \tag{2.3}$$

This allows us to derive the net total current at frequency ω injected into the coupler by the reservoir α:

$$I_\alpha(\omega) = i_\alpha^{\rm in}(\omega) - i_\alpha^{\rm out}(\omega) \tag{2.4}$$

$$= (1 - \mathrm{S}_{\alpha\alpha}(\omega))\; i_\alpha^{\rm in}(\omega) - \sum_{\beta\neq\alpha} \mathrm{S}_{\alpha\beta}(\omega)\, i_\beta^{\rm in}(\omega) \tag{2.5}$$

which is a function of the EMP scattering matrix of the incoming currents. All of these input currents are generated by the AC voltage $V_\alpha(\omega)$ imposed at each reservoir α which pump charges directly into the input channels at a frequency ω. The incoming currents are given by the Hall relation:

$$i_\alpha^{\rm in}(\omega) = \frac{V_\alpha(\omega)}{R_K} \tag{2.6}$$

with $R_K = h/e^2$ denoting the von Klitzing resistance. So we can write $I_\alpha(\omega)$ as a function of the AC voltages:

$$R_K\, I_\alpha(\omega) = (1 - \mathrm{S}_{\alpha\alpha}(\omega))\; V_\alpha(\omega) - \sum_{\beta\neq\alpha} \mathrm{S}_{\alpha\beta}(\omega)\, V_\beta(\omega) \tag{2.7}$$

In this equation, the radiation coupler is described as a system that responds with an AC electrical current $I_\alpha(\omega)$ linearly in terms of the AC voltage drives $V_\beta(\omega)$ applied to the reservoirs. This observation brings up an important point: we can describe a radiation coupler in terms of linear current/voltage characteristics, just as we usually do for a circuit in linear electrical engineering. The admittance matrix of a multi-terminal circuit is this response function. The above calculation shows that, for a radiation coupler, the coefficients of the admittance matrix can be related to those of the plasmonic scattering matrix (see Eq. (2.7)). Such a relation, which will be elaborated more precisely in the next section, is important because finite frequency admittances can indeed be measured experimentally in the 1 to 10 GHz range [77, 78, 22].

2.2.2 Discrete element description

In the linear regime, the AC electrical current response of a multi-terminal circuit exposed to AC voltages is described by the admittance matrix:

$$\mathrm{Y}_{\alpha\beta}(\omega) = \left.\frac{\partial I_\alpha(\omega)}{\partial V_\beta}\right|_{V=0} \tag{2.8}$$

which gives the average current entering the conductor from the lead α when a voltage driven at the same frequency $\omega/2\pi$ is applied to the reservoir β.

As stressed out by Büttiker [32], the finite frequency admittance matrix is constrained by two sum rules. First of all, it has to ensure charge conservation:

$$\sum_\alpha I_\alpha(\omega) = 0 \tag{2.9}$$

whatever time dependent voltages are applied to the reservoirs. Using Eq. (2.8), this leads to the charge conservation sum rule:

$$\sum_\alpha \mathrm{Y}_{\alpha\beta}(\omega) = 0\,. \tag{2.10}$$

The finite frequency admittance matrix also has to satisfy gauge invariance: the currents remain unchanged when the potential in each reservoir is shifted by the same time dependent potential. This leads to:

$$\sum_\beta \mathrm{Y}_{\alpha\beta}(\omega)\,(V_\beta(\omega) + (\delta V)(\omega)) = \sum_\beta \mathrm{Y}_{\alpha\beta}(\omega)\,V_\beta(\omega) \tag{2.11}$$

and we end up with the gauge invariance sum rule:

$$\sum_\beta \mathrm{Y}_{\alpha\beta}(\omega) = 0\,. \tag{2.12}$$

If we describe an EMP scatterer such as a radiation coupler as a multi-terminal circuit with an admittance matrix $\mathbf{Y}(\omega)$, then using Eq.(2.7) we find the relation:

$$R_K\mathbf{Y}(\omega) = \mathbb{1} - \mathbf{S}(\omega) \tag{2.13}$$

where $\mathbf{S}(\omega)$ the EMP scattering matrix.

Naively, if one builds a radiation coupler model, computes $\mathbf{S}(\omega)$ and then $\mathbf{Y}(\omega)$, one would expect that the admittance obey these conditions. However, depending on the specific model under consideration, the EMP

scattering matrix does not necessarily leads to a finite frequency admittance that satisfies Eqs. (2.10) and (2.12). A well known example is the computation of the 2×2 admittance matrix of a quantum wire between two gates in the Luttinger liquid theory [19]. In this case, the failure of the admittance matrix, obtained from the 2×2 EMP scattering matrix, to respect the charge conservation and gauge invariance sum rules, is the signature that the quantum wire is actually coupled to additional external gates.

To recover the conditions given by Eq. (2.10) and Eq. (2.12) we need to add a new ingredient to the model of this circuit. We can take in account these additional gates by adding a third lead capacitively coupled to the quantum wire which, in the computation, is assumed to be connected to the ground. Then, instead of having an electric dipole, we get a three-terminal device with an associated 3×3 admittance matrix. It contains the 2×2 admittance matrix given by Eq. (2.13) as a sub-matrix and satisfies the charge conservation and gauge invariance conditions. Note that the dynamics of the extra lead is not described in terms of 1D EMPs: the gates connected to the ground involve a large number of channels, unlike quantum Hall edge channels at low filling fractions.

We should emphasize that physically, this problem comes from the screening of Coulomb interactions by nearby gates. Thus, it is not surprising that this appears in Luttinger liquid models which assumed screened short range Coulomb interactions.

To directly ensure the charge conservation and the gauge invariance without extra gates, the capacitive couplings of the coupler have to be in total electrostatic influence. Consequently, these conditions translate into the following one for the EMP scattering matrix:

$$\sum_{\beta} \mathrm{S}_{\alpha\beta}(\omega) = \sum_{\alpha} \mathrm{S}_{\alpha\beta}(\omega) = 1 \,. \tag{2.14}$$

As long as the radiation coupler has no internal degrees of freedom through which energy can be dissipated, $\mathbf{Y}(\omega)$ and $\mathbf{S}(\omega)$ have to ensure energy conservation. It implies that $\mathbf{S}(\omega)$ have to be a unitary matrix. Moreover, the system being a purely passive one, it cannot generate more energy than what is sent into it and therefore $\Re(\mathbf{Y}(\omega))$ must be positive definite [29].

To illustrate these various constraints, let us now consider as an example a radiation coupler connected to two reservoirs as shown Fig. 2.3.

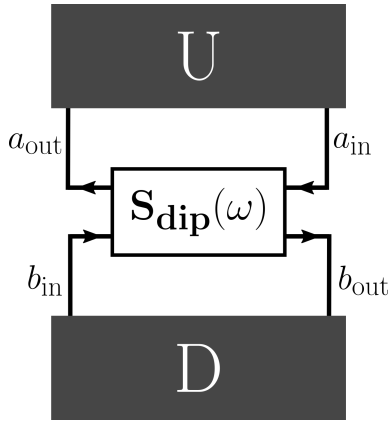

Figure 2.3: Drawing of a radiation coupler circuit with two integer quantum Hall edge channels. Each reservoir β imposes a time dependent voltage $V_\beta(t)$ to the corresponding edge channel. The EMP scattering matrix enables computing the outgoing current from the incoming ones and this determines the linear response of the electrical current I_α for each lead α.

The two branches inside the coupler are assumed to be in total electrostatic influence and the EMP scattering process is assumed to be energy conserving. The scattering is thus described by a 2 unitary matrix $\mathbf{S_{dip}}(\omega)$ which respects the conditions of gauge invariance and charge conservation summarized by Eq. (2.14). Thus the scattering matrix takes the form:

$$\mathbf{S_{dip}}(\omega) = \begin{pmatrix} t(\omega) & 1-t(\omega) \\ 1-t(\omega) & t(\omega) \end{pmatrix} \tag{2.15}$$

Energy conservation then forces

$$|t(\omega)|^2 + |1-t(\omega)|^2 = 1$$

which implies that

$$t(\omega) = \frac{1}{2}\left(1 + \mathrm{e}^{\mathrm{i}\vartheta(\omega)}\right) \tag{2.16}$$

where $\vartheta(\omega)$ is a real phase. The equivalent electrical circuit is a dipole with an admittance $\mathbf{Y_{dip}}(\omega)$ that can be computes using Eq. (2.13):

$$R_K \mathbf{Y_{dip}}(\omega) = R_K Y_{\rm dip}(\omega) \begin{pmatrix} 1 & -1 \\ -1 & 1 \end{pmatrix} = (1-t(\omega)) \begin{pmatrix} 1 & -1 \\ -1 & 1 \end{pmatrix} \tag{2.17}$$

Both matrices are entirely described by the single function $\omega \mapsto \theta(\omega)$ that encodes the full response of the radiation coupler. As we shall see, the model of two counter propagating integer quantum Hall edge channels in total mutual electrostatic influence considered in Sec. 2.4 will fall into this parametrization.

2.2.3 Summary and connexion to other works

The take home message of this review is that a system that stationary and elastically scatters one EMP of given energy into another EMP mode at the same energy can be described in terms of a finite frequency admittance that characterizes the linear current/voltage ac response.

The main consequence of this observation is that EMP scattering is indeed connected to experimentally accessible quantities since finite frequency admittances can be measured. Sometimes, the results of such measurement bring insight on the physics of the quantum Hall conductor as illustrated by Ref. [20].

This also tells us the limits of these results: any non elastic EMP scatterer in which there is a non zero amplitude for many-EMP production cannot be described in terms of linear current/voltage response functions. More response coefficients are needed such as, for example in the case of the mesoscopic capacitor operated in the single electron source regime [70].

So far, we have not discussed any predictive model for these quantities. Markus Büttiker and his collaborators have developed a long stream of works that aim at predicting the low frequency behavior of the finite frequency admittance of quantum conductors [32, 31, 154] as well as of quantum Hall conductors [46, 45] based on a mean field elaboration of his approach of quantum transport based on single electron scattering (see [18] for a complete review). In the following sections, we will consider radiation couplers that do not involve any quantum point contact but only capacitive couplings. For these systems, thanks to bosonization, it is possible to compute directly the EMP scattering matrix and therefore to obtain the results for finite frequency ac transport using the correspondence discussed in the above section. This is closer, in spirit, to the works of Büttiker and collaborators on the finite frequency admittance of quantum wires [19, 18] and also to the works of Ines Safi on quantum wires [168, 167] where the plasmon scattering approach was indeed pioneered.

2.3 The classically driven edge channel

The radiation couplers considered here are based on classically driven edge channels studied through two different models. In the first one, discussed in Sec. 2.3.1, a classical time and space dependent potential $U(x,t)$ is directly applied to the electrons propagating within the edge channel. In this model, electron/electron interactions are neglected but the applied potential imprints a time-dependent phase on each electron within the edge channel. However, in experiments, the external drive is not directly applied to the edge channel but to a top gate which is capacitively coupled to the edge channel. This leads us to the model discussed in Sec. 2.3.2. It involves a capacitive coupling between a finite length region of the edge channel and a top gate to which the time-dependent classical voltage is applied.

2.3.1 Direct coupling to the external voltage

We first consider electrons propagating within a chiral edge channel with Fermi velocity v_F and experiencing a time dependent potential $U(x,t)$ in the $|x| \leq l/2$ region. We first compute how the EMP modes are propagating across this radiation coupler.

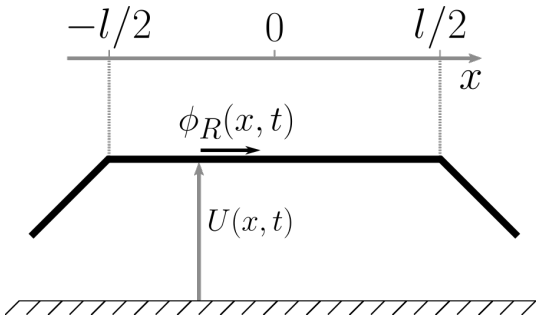

Figure 2.4: An edge channel in which the electrons in the region $|x| \leq l/2$ experience a classical time dependent electrical potential $U(x,t)$

EMP scattering

The starting point is the equation of motion for the chiral bosonic field $\phi_R(x,t)$ built from the edge-magnetoplmasmon modes of the chiral edge

channel:

$$(\partial_t + v_F \partial_x)\phi_R(x,t) = \frac{e\sqrt{\pi}}{h}\, U(x,t)\,. \tag{2.18}$$

This equation can be solved using the method of characteristics:

$$\begin{aligned}\phi_R(x + v_F\tau, t+\tau) &= \phi_R(x,t) \\ &\quad + \frac{e\sqrt{\pi}}{h}\int_0^\tau U(x + v_F\tau', t+\tau')\,\mathrm{d}\tau'\end{aligned} \tag{2.19}$$

which gives the outgoing field $\phi_{R,\mathrm{out}}(t) = \phi_R(l/2,t)$ in terms of the incoming field $\phi_{R,\mathrm{in}}(t) = \phi_R(-l/2,t)$ and of the time and space dependent potential $U(x,t)$:

$$\begin{aligned}\phi_{R,\mathrm{out}}(t) &= \phi_{R,\mathrm{in}}(t - l/v_F) \\ &\quad + \frac{e\sqrt{\pi}}{h}\int_0^{l/v_F} U(v_F\tau' - l/2, t + \tau' - l/v_F)\,\mathrm{d}\tau'\,.\end{aligned} \tag{2.20}$$

The incoming field thus propagates ballistically at velocity v_F and the space dependent potential adds a source term to the outgoing field.

Let us now assume $U(x,t)$ is uniform within the $|x| \leq l/2$ region and equal to the time-dependent potential $U(t)$ which is, for example, the externally applied time dependent voltage. We will compute how the $b(\omega)$ EMP annihilation operator is scattered. Specializing Eq. (2.20) for a spatially homogeneous time dependent potential $U(t)$ instead of $U(x,t)$, re-expressing it in the Fourier domain and using the $b(\omega)$ operators lead to:

$$b_{\mathrm{out}}(\omega) = t_0(\omega)\, b_{\mathrm{in}}(\omega) + \kappa_0(\omega)\, U(\omega) \tag{2.21}$$

in which, using the notation $X = \omega l/v_F$ and defining $f(X) = (\mathrm{e}^{\mathrm{i}X} - 1)/\mathrm{i}X$:

$$t_0(\omega) = \mathrm{e}^{\mathrm{i}X} \tag{2.22a}$$

$$\kappa_0(\omega) = \frac{\mathrm{i}\, e}{h}\sqrt{\frac{lX}{v_F}}\, f(X) \tag{2.22b}$$

Note that $\tau_l = l/v_F$ is the ballistic time of flight needed to cross the radiation coupler. In Eq. (2.22a), $t_0(\omega)$ is the amplitude for an incoming EMP mode at frequency ω to go through the coupler. It describes a non-dispersive phase shift $\omega l/v_F$ reflecting its ballistic propagation. The coefficient $\kappa_0(\omega)$ describes the linear response of $b_{\mathrm{out}}(\omega)$ to $U(\omega)$. Its explicit form depends on the assumptions of our model (here mainly

that $U(x,t)$ is uniform for $|x| \leq l/2$). Rewriting the scattering formula given Eq.(2.21) in terms of incoming and outgoing currents leads to:

$$i_{\rm out}(\omega) = {\rm e}^{{\rm i}\omega\tau_l} i_{\rm in}(\omega) - e\sqrt{\omega}\kappa_0(\omega)\, U(\omega) \tag{2.23}$$

Motivated by Sec. 2.2 we would like to rewrite the input output relation (2.23) which defines the EMP scattering in the present problem into an admittance matrix. To do so, we need to specify the reservoirs attached to the circuit, the voltages drives applied to them and finally to properly define the electrical currents flowing through the circuit.

Electrical dipole description

Folding the edge channels as depicted on Fig. 2.5-*a* enables us to view the radiation coupler as an electrical dipole with a current $I_d = i_{\rm in} - i_{\rm out}$ and a voltage $V_u = U$. Since in the present case, the upper part of the dipole is not modeled, we can assume that $I_d = -I_u$ as expected in full generality for an electrical dipole at finite frequency [32].

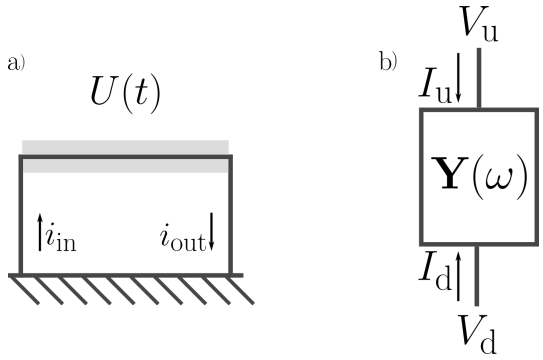

Figure 2.5: (a) Folding of the edge channel to obtain an electrical dipole. (b) Drawing of an electrical dipole with $\mathbf{Y}(\omega)$ its admittance matrix, $V_{\rm u}$, $V_{\rm d}$, $I_{\rm u}$ and $I_{\rm d}$ respectively denote the voltage and the average electrical current in the two connecting leads. In panel (a), $V_{\rm u} = U$, $V_{\rm d} = 0$ and $I_{\rm d} = -I_{\rm u} = i_{\rm in} - i_{\rm out}$.

Following the notations of Fig. 2.5-*b*, the finite frequency admittance matrix is defined by

$$\mathbf{Y_0}_{\alpha,\beta}(\omega) = \frac{\partial\langle i_\alpha(\omega)\rangle}{\partial V_\beta(\omega)} \tag{2.24}$$

where $(\alpha, \beta) \in \{u, d\}$. Gauge invariance then follows from the fact that

$$\mathrm{Y}_{ud}(\omega) = -e\sqrt{\omega}\kappa_0(\omega) = \frac{e^2}{h}\left(1 - t_0(\omega)\right) = -\mathrm{Y}_{uu}(\omega) \tag{2.25}$$

combined with $I_d = -I_u$ which ensures that charge conservation is satisfied. The admittance matrix is then determined by a single finite frequency admittance $Y_0(\omega)$ so that:

$$\mathbf{Y_0}(\omega) = Y_0(\omega)\begin{pmatrix} 1 & -1 \\ -1 & 1 \end{pmatrix} \tag{2.26}$$

with

$$Y_0(\omega) = \frac{e^2}{h}\left(1 - \mathrm{e}^{\mathrm{i}\omega l/v_F}\right) \tag{2.27}$$

These results are in agreement with Eq. (2.17). In the complex plane, $R_K Y_0(\omega)$ travels at uniform speed on a circle of radius 1 centered on 1. Evolution on a circle follows from the fact that $R_K Y_0(\omega) = 1 - t_0(\omega)$ where $|t_0(\omega)| = 1$ because of the absence of plasmon dissipation for $|x| \leq l/2$. The linear angular velocity reflects the dispersionless propagation of plasmons in the same region.

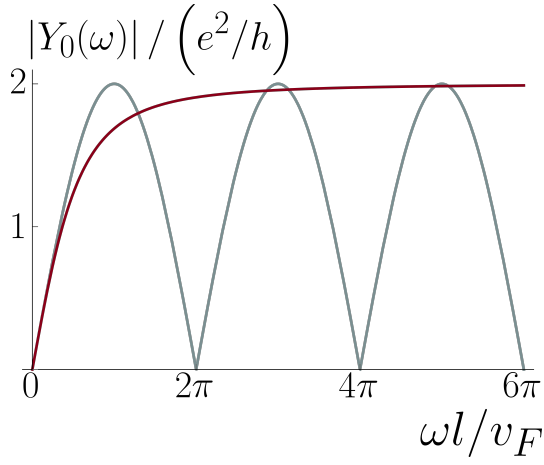

Figure 2.6: In gray is the modulus of the admittance of the classically driven edge channel. In red is the admittance of classical RC circuit with $C = \frac{e^2 l}{h v_F}$ and $R = \frac{h}{2e^2}$.

The low-frequency expansion of $Y_0(\omega)$ up to the second order in ω has the form of an RC circuit :

$$Y_0(\omega) = -\mathrm{i}C\omega + R(C\omega)^2 + O(\omega^3) \tag{2.28}$$

with

$$C = \frac{e^2 l}{h v_F} \tag{2.29a}$$

$$R = \frac{h}{2e^2} = \frac{R_K}{2} \tag{2.29b}$$

Note that $C_q = e^2 l / h v_F$ is the quantum capacitance arising from the finite density of state within the edge channel and $R_K/2$ is the quantized contact resistance associated with a single coherent chiral edge channel [30]. Fig. 2.6 depicts $R_K \, |Y_0(\omega)|$ alongside the modulus of the admittance of the RC circuit with parameters given by Eq. (2.29) whereas Fig. 2.7 depicts the phases of these admittances.

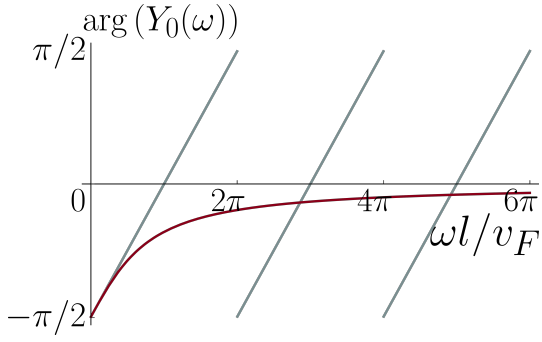

Figure 2.7: In gray is the argument of the admittance of the classically driven edge channel. In red is the argument of the admittance of classical RC circuit with $C = \frac{e^2 l}{h v_F}$ and $R = \frac{h}{2e^2}$.

Both admittances have the same shape at low frequency but deviate from each other as the frequency increases. Contrary to the impedance of the RC circuit which has a monotonic evolution, $Y_0(\omega)$ is periodic in frequency with a period of $2\pi v_f / l$, as expected here from the propagation of EMP at fixed velocities. The response of this linear coupler, characterized by $Y_0(\omega)$ vanishes for $\omega = 2\pi n v_F / l$ ($n \in \mathbb{N}$). As we shall see, such features are quite general when considering a direct capacitive coupling between two edge channels over a finite length. As a reminder, remember that describing the full behavior of $Y_0(\omega)$ in terms of usual discrete elements of electrical circuits such as capacitances and inductances requires going beyond the RC circuit and introducing more elements [29, 41].

As mentioned earlier, this model where the electrons are directly exposed to the external drive is an idealization since, in real experiments, the external voltage drive is usually applied using a top gate which is capacitively coupled to the edge channel. We will now discuss a discrete element model incorporating this physics explicitly.

2.3.2 The classically driven top gate

We now consider a coupler built from a top gate capacitively coupled to the $|x| \leq l/2$ region of a chiral edge channel. This top gate is classically driven by a time dependent voltage $V_g(t)$. The $|x| \leq l/2$ region forms a capacitor together with the top gate (see Fig. 2.8). In the spirit of the discrete element description *à la* Büttiker, these two conductors are assumed to be in total electrostatic influence, with a uniform time dependent potential. We denote by C_g the geometric capacitance of this radiation coupler. The propagating EMPs are still sensitive to an electric potential $U(t)$ which now depends on $V_g(t)$ but $U(t) \neq V_g(t)$ because of the potential drop at the capacitor.

The important point is that, by considering a capacitor, we are now introducing Coulomb interaction effects in the radiation coupler. The underlying physics can be understood by discussing what happens when charges are pumped into a conductor. Because of the time dependent drive applied to the reservoir, a time dependent charge involving electron and hole excitations is pumped from the reservoir into the conductor, where these excitations propagate. But the associated time dependent charge shifts the electrical potential in the conductor in a time dependent way, which in turn affects the propagation of electron and hole excitations. This is why, in contrast with dc transport, Coulomb interactions play an essential role in ac quantum transport. Büttiker understood this point and pointed out the importance of Coulomb interaction in AC transport in his works on finite frequency charge transport in mesoscopic conductors [32, 31]. To address this problem, he developed a self consistent mean-field approach to the AC quantum coherent transport [154], taking into account how the time dependent charge density within the conductor generates a time-dependent potential and thereby alters the scattering of electronic excitations by the conductor.

In the present discussion, Coulomb interaction effects are taken into account because the electrical potential $U(t)$ seen by the electrons propagating within the edge channel is not only determined by the external potential but also by the charge polarizing the capacitor via its geomet-

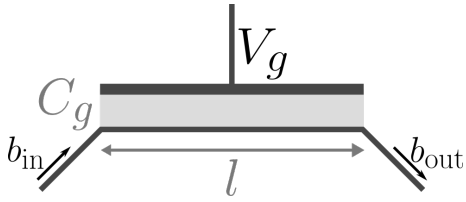

Figure 2.8: A top gate is capacitively coupled to the $|x| \leq l/2$ region of a chiral edge channel. It is driven by a time dependent gate voltage $V_g(t)$. Here C_g denotes the geometric capacitance between the two conductors.

ric capacitance C_g. We will now derive the input/output relation for the EMP modes in the presence of the AC drive $V_g(t)$ applied to the top gate.

EMP scattering

Similarly to Sec. 2.3.1, the bosonic field $\phi_R(t)$, built from the EMP modes of the chiral edge channel, propagates according to the following equation of motion in the $|x| \leq l/2$ region:

$$(\partial_t + v_F \partial_x)\phi_R(x,t) = \frac{e\sqrt{\pi}}{h}\, U(t) \tag{2.30}$$

where $U(t)$ is the electrical uniform time dependent potential felt by the electrons. It can be calculated from the potential drop across the capacitor to $V_g(t)$:

$$U(t) - V_g(t) = \frac{Q(t)}{C_g} \tag{2.31}$$

where $Q(t)$ denotes the excess charge in the $|x| \leq l/2$ of the chiral edge channel. Using

$$Q(t) = \frac{e}{\sqrt{\pi}}\left(\phi_{\rm in}(t) - \phi_{\rm out}(t)\right) \tag{2.32}$$

in addition to Eqs. (2.30) and (2.31), we can obtain a closed differential equation for $\phi_R(x,t)$ within the $|x| \leq l/2$ region. This method is identical to the one used to discuss the Coulomb interaction effects within a chiral edge channel in Ref. [35]. The final result can be expressed as connecting the outgoing plasmon modes $b_{\rm out}(\omega)$ (derived from the Fourier transform of $\phi_{\rm out}(t)$) to the incoming plasmon modes $b_{\rm in}(\omega)$ (associated with $\phi_{\rm in}(t)$) and to V_G:

$$b_{\rm out}(\omega) = t(\omega)\, b_{\rm in}(\omega) + \kappa(\omega)\, V_G(\omega) \tag{2.33}$$

in which, using $X = \omega l / v_F$:

$$t(\omega) = \mathrm{e}^{\mathrm{i}X} \frac{1 + \alpha\, f^*(X)}{1 + \alpha\, f(X)} = t_0(\omega) \frac{1 + \alpha\, f^*(X)}{1 + \alpha\, f(X)} \tag{2.34a}$$

$$\kappa(\omega) = \frac{\mathrm{i}\, f(X)}{1 + \alpha\, f(X)} \frac{e}{h} \sqrt{\frac{lX}{v_F}} = \frac{\kappa_0(\omega)}{1 + \alpha\, f(X)} \tag{2.34b}$$

where $f(X) = (\mathrm{e}^{\mathrm{i}X} - 1)/\mathrm{i}X$ as before. The dimensionless coupling constant

$$\alpha = \frac{e^2 l}{h v_F C_g} \tag{2.35}$$

is the ratio between the charging energy e^2/C_g for an electron and the kinetic energy scale $\hbar v_F / l$ associated with the $|x| \leq l/2$ region. It is also the ratio C_q/C_g of the quantum capacitance over the geometrical capacitance.

As such, α gives a measure of the importance of Coulomb interaction effects. For $\alpha \ll 1$, the potential drop at the capacitance vanishes and therefore the electrons directly see the gate voltage $V_g(t)$. We thus call it the voltage locked regime. On the other hand, in the the $\alpha \gtrsim 1$ regime, Coulomb interactions are so strong that they tend to block charge accumulation below the top gate: $Q(t) \simeq 0$. We thus call it the Coulomb blocked regime.

Exactly as in Sec. 2.3.1, $\kappa(\omega)$ and $t(\omega)$ are not independent. Eq. (2.34a) and Eq. (2.34b) imply that:

$$\kappa(\omega) = \frac{e}{h} \sqrt{\frac{l}{v_F}} \frac{t(\omega) - 1}{\sqrt{X}}\,. \tag{2.36}$$

This follows from the top gate and the edge channel being in total electrostatic influence. This relation would be violated if a third element, such as a side gate, were capacitively coupled to the other two. Focusing on $t(\omega)$, we see that its modulus is equal to one, as in the previous section. This is expected since there are no dynamical degrees of freedom in the top gate susceptible of dissipating energy. Consequently, $t(\omega)$ can be rewritten as:

$$t(\omega) = \mathrm{e}^{\mathrm{i}\theta(\omega)} = \mathrm{e}^{\mathrm{i}\omega l / v(\omega)} \tag{2.37}$$

with

$$v(\omega) = v_F \frac{X}{X + 2 \arctan\left(\frac{\alpha(\cos X - 1)}{X + \alpha \sin X}\right)} \tag{2.38}$$

the phase velocity of EMP beneath the top gate. Eqs. (2.37) and (2.38) show that Coulomb interaction manifest themselves as non linearities in the ω-dependence of $\theta(\omega)$. The coupler is now dispersive for the EMPs propagating in the target branch. However, in the absence of Coulomb interaction ($\alpha = 0$), $v(\omega) = v_F$, so we recover a non-dispersive medium and $t(\omega) = t_0(\omega)$. As expected, the model studied Sec. 2.3.1 is a simpler version of this one obtained when considering that Coulomb interactions play no role. We have plotted Fig. 2.9$-(b)$ $\theta(\omega)$ for different values of α. As expected, when $\alpha = 0$, $\theta(\omega)$ is linear with a slope l/v_F, but it deviates from this regime as we increase α.

We have also plotted $v(\omega)$ for several values of α on Fig. 2.9-a. Before discussing the ω dependence of the phase velocity $v(\omega)$, let us recall a point already discussed in Ref. [35]. Dispersion of the EMP, leads to distortion of classical current pulse but also to electronic decoherence beneath the gate. This was not the case in the model discussed in paragraph 2.3.1 where EMP propagate with an ω independent time of flight l/v_F. In the following section, we will focus more precisely on $v(\omega)$ and its implications for coupler.

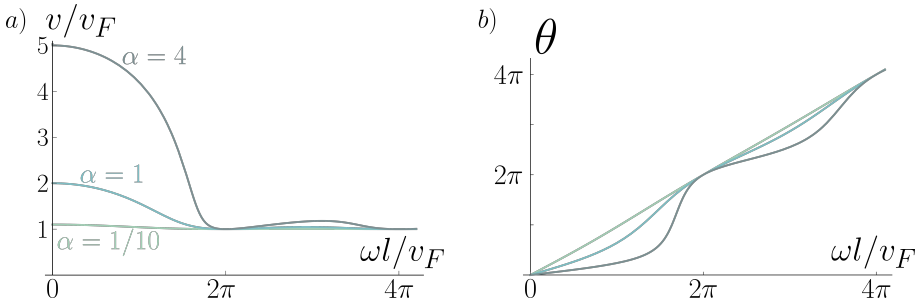

Figure 2.9: *a* Plot of $v(\omega)/v_F$ from Eq.(2.38) for $\alpha = 0.1, 1$ and 4. *b* Plot of the phase of the transmission coefficient $\theta(\omega)$ for $\alpha = 0.1$, 1 and 4.

Phase velocity Fig. 2.9-a depicts the variation of $v(\omega)/v_F$ as a function of $\omega l/v_F$, with α taking the values 0.1, 1, and 4. As previously noted in the context of $\theta(\omega)$, the presence of a non-zero α results in the dispersion of $v(\omega)$, which grows as α increases. Notably, as long as $\alpha \gtrsim 1$, $v(\omega)$ is large at low frequencies. Whereas at high frequencies the non-dispersive limit, with $v(\omega) \simeq v_F$, is recovered for any value of α. Between these two regimes, we observe that $v(\omega)$ exhibits damped

oscillations with a frequency period $2\pi v_F/l$ and $v(\omega) = v_F$ every time ω is an integer multiple of $2\pi v_F/l$.

Most of these observations can be attributed to the influence of Coulomb interactions. At low frequencies and when $\alpha \gtrsim 1$, the energy e^2/C_g associated with charges, is greater than the plasmon energy $\hbar\omega$, leading to significant deviations from the non-interacting case. We can also understand it from the electronic point of view: as mentioned earlier, when $\alpha \gtrsim 1$ the coupler is in the Coulomb blocked regime. In this one the transmission of electrons at the output of the coupler must occur rapidly to prevent charge accumulation below the top gate, which induces an increase of the velocity of plasmons to $v_0 > v_F$. Conversely, in the limit $\hbar\omega \gg e^2/C_g$, the Coulomb energy becomes negligible compared to the EMP energy. We thus expect their propagation to be almost unaffected by Coulomb interactions and we expect to recover dispersionless propagation with time of flight l/v_F. The transition from one regime to another as ω increases manifests itself in the damping of the oscillations.

However the oscillations can be attributed to the fact that the interactions between the edge channel and the top gate occur on a finite length l, thereby imposing boundary conditions that restrict the propagation of plasmons around these frequencies. In contrast, more relaxed boundary conditions would result in a different behavior of $v(\omega)$ in the vicinity of these frequencies.

The phase velocity $v(\omega)$ is the effective velocity associated with the phase accumulated during propagation within the radiation coupler for an EMP at pulsation ω. However, in the case of multimode plasmonic wave packets, a distinction needs to be made between the phase velocity and the group velocity. The group velocity represents the average velocity at which the energy of a wave packet propagates. In classical optics, there are scenarios where the phase velocity of a light wave exceeds c, the speed of light in vacuum, but the group velocity still follows to the laws of relativity and remains below c. In the following section, we will evaluate this group velocity and discuss its behavior in regard with the phase velocity.

Group velocity Let us consider an incoming plasmonic wave localized around ω_0 with a bandwidth γ. Its wave function is given by:

$$\phi_{\text{in}}(t) = \mathrm{e}^{-\mathrm{i}\omega_0 t} \int_{-\gamma/2}^{\gamma/2} \frac{\mathrm{d}(\delta\omega)}{2\pi} \mathrm{e}^{-\mathrm{i}\delta\omega\, t} \tilde{u}(\delta\omega) \tag{2.39}$$

with the low frequency envelope $\tilde{u}(\delta\omega)$ in the bandwidth $[-\gamma/2, \gamma/2]$. In this case the outgoing wave packet ϕ_{out} takes the form:

$$\phi_{\text{out}}(t) = \mathrm{e}^{-\mathrm{i}\omega_0 t} \int_{-\gamma/2}^{\gamma/2} \frac{\mathrm{d}(\delta\omega)}{2\pi} \mathrm{e}^{-\mathrm{i}\delta\omega t} \tilde{u}\left(\delta\omega\right) t\left(\omega_0 + \delta\omega\right) . \tag{2.40}$$

The computation of the outgoing wave $\phi_{\text{out}}(t)$ is a challenging task without any assumptions, as the phase $\theta(\omega)$ of the transmission amplitude is non-linear in ω. To make progress, we will focus on wave packets with parameters ω_0 and γ such that the transmission phase $\theta(\omega)$ is locally non-dispersive and thus the envelop of the wave packet doesn't get distorted. Specifically, we assume that $\theta(\omega)$ is quasi-linear in ω over the entire range $[\omega_0 - \gamma/2, \omega_0 + \gamma/2]$. The acceptable values of γ for which this approximation is valid depend on both ω_0 and α. Indeed, as shown in Fig. 2.9-*b*, the non linearities of $\theta(\omega)$ are concentrated near frequencies slightly smaller than $2\pi v_F/l$ and become more pronounced as α increases. If ω_0 is chosen within these highly nonlinear regions, the bandwidth γ is smaller than in less non linear regions. This forces us consider wave packets with a small bandwidth and therefore a large envelope in the time domain.

Assuming that ω_0, α and γ are such that $\theta(\omega_0 + \delta\omega) \simeq \theta(\omega_0) + \dot{\theta}(\omega_0)\delta\omega$, with $\delta\omega \in [-\gamma/2, \gamma/2]$, leads to:

$$t(\omega_0 + \delta\omega) \simeq \mathrm{e}^{\mathrm{i}\theta(\omega_0)} \mathrm{e}^{(\mathrm{i}\dot{\theta}(\omega_0)\delta\omega)} . \tag{2.41}$$

By injecting this expression into Eq.(2.40), we get:

$$\phi_{\text{out}}(t) \simeq \mathrm{e}^{-\mathrm{i}\omega_0 t + \mathrm{i}\theta(\omega_0)} \int_{-\gamma/2}^{\gamma/2} \frac{\mathrm{d}(\delta\omega)}{2\pi} \mathrm{e}^{-\mathrm{i}\delta\omega\left(t - \dot{\theta}(\omega_0)\right)} \tilde{u}\left(\delta\omega\right) \tag{2.42}$$

which can also be rewritten as:

$$\phi_{\text{out}}(t) \simeq \mathrm{e}^{-\mathrm{i}\omega_0 t + \mathrm{i}\theta(\omega_0)} \tilde{u}\left(t - \dot{\theta}(\omega_0)\right) . \tag{2.43}$$

The derivative $\dot{\theta}(\omega_0)$ thus appears as the time of flight of the wave packet across the radiation coupler. It leads to a group velocity $v_G(\omega)$:

$$v_G(\omega) = \frac{l}{\dot{\theta}(\omega)} = v_F \frac{\left(X + \alpha \sin X\right)^2 + \alpha^2 \left(\cos X - 1\right)^2}{X^2 + 2\alpha\left(1 - \cos X\right)} . \tag{2.44}$$

We can also write $v_G(\omega)$ in terms of $v(\omega)$. Indeed, we have :

$$\dot{\theta}(\omega) = \frac{l}{v_G(\omega)} = \frac{l}{v(\omega)} - \frac{l\omega}{v^2(\omega)} \frac{\mathrm{d}v(\omega)}{\mathrm{d}\omega} \tag{2.45}$$

which then leads to

$$\frac{v_G(\omega)}{v(\omega)} = \frac{1}{1 - \frac{\omega}{v(\omega)}\frac{\mathrm{d}v(\omega)}{\mathrm{d}\omega}}\,. \tag{2.46}$$

From this equation follows that $v_G(\omega) > v(\omega)$ whenever $v(\omega)$ is increasing ($\frac{\mathrm{d}v(\omega)}{\mathrm{d}\omega} > 0$). Otherwise, it will be smaller.

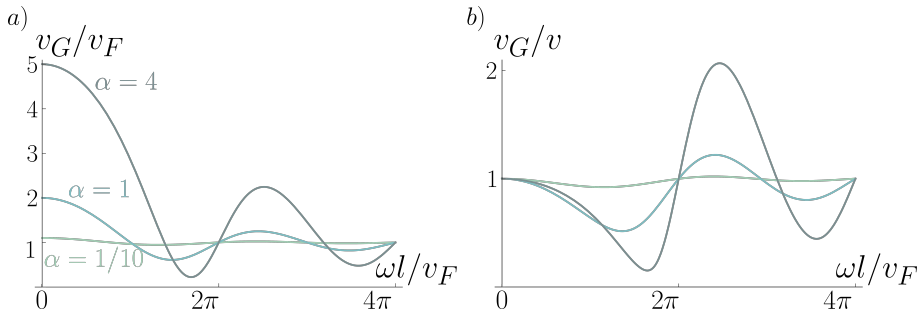

Figure 2.10: Plot of $v_G(\omega)/v_F$ as a function of $\omega l/v_F$ from Eq. (2.44) for $\alpha = 0.1$ 1 and 4.

We have plotted $v_G(\omega)$ (left panel) and $v_G(\omega)/v(\omega)$ (right panel) for $\alpha = 0.1$, 1 and 4 on Fig. 2.10. At low and high frequencies, as well as for $\alpha \ll 1$, both the group velocity $v_G(\omega)$ and phase velocity $v(\omega)$ exhibit similar behaviors. In addition $v_G(\omega)$ also have damped oscillations with a period l/v_F. However, as suggested by Eq.(2.46), there exist certain frequency ranges where $v_G(\omega)$ exceeds $v(\omega)$ and others where $v_G(\omega) < v_F < v(\omega)$ (see panel (b) on Fig. 2.10). The striking point is the low value of $v_G(\omega)$ for some values of ω. It is clearly the result of an interference effect between EMP modes whose transmission phase rapidly vary with ω as we increase α. Note that part of the effect reflects the assumption that Coulomb interactions are abruptly screened beyond the radiation coupler (for $|x| > l/2$). Therefore, ultimately, only measurements of transmission phases provide a reliable way to assess for these features in a real sample.

To conclude this discussion, let us stress that current pulses with very short duration will not propagate according to the phase nor to the group velocity considered here because they are broadband with respect to the acceptable bandwidth where $\theta(\omega)$ can be approximated by a linear function of ω. Such large bandwidth/short current pulses are especially sensitive to dispersion as they propagate through the coupler.

What the above discussion suggests is that time of flight measurement for very short current pulses which are routinely performed in laboratories [119, 111, 166] should probably be supplemented by frequency domain measurements as in Ref. [120] to get a sharper insight on EMP propagation.

Electrical dipole description

By folding the edge channels as we did in Sec. 2.3.1, we can model the coupler as an electric dipole with a matrix admittance $\mathbf{Y}(\omega)$. Because of total mutual influence between the channel and the top gate, the finite frequency admittance matrix takes the form:

$$\mathbf{Y}(\omega) = Y(\omega) \begin{pmatrix} 1 & -1 \\ -1 & 1 \end{pmatrix} \tag{2.47}$$

with

$$Y(\omega) = \frac{e^2}{h} \frac{1 - \mathrm{e}^{\mathrm{i}X}}{1 + \alpha f(X)} = \frac{Y_0(\omega)}{1 + \alpha f(X)} \,. \tag{2.48}$$

Since $t(\omega) = \mathrm{e}^{\mathrm{i}\theta(\omega)}$, $R_K Y(\omega) = 1 - t(\omega)$ spans a circle of radius 1 centred on 1 in the complex plane[1]. As in Sec. 2.3.1, the low frequency expansion of $R_K Y(\omega)$ is, at second order in ω the one of an RC circuit:

$$R_K Y(\omega) \simeq -\mathrm{i} \frac{\omega l / v_F}{1 + \alpha} + \frac{1}{2} \frac{(\omega l / v_F)^2}{(1 + \alpha)^2} + \cdots \tag{2.49}$$

which enables us to identify

$$R_K C_\mu = \frac{l}{(1 + \alpha) v_F} \quad \& \; R = \frac{R_K}{2} \,. \tag{2.50}$$

As expected, the contact resistance of a single coherent edge channel is recovered and C_μ appears as the series addition of the quantum capacitance of the edge channel with the geometric capacitance C_g since

$$C_\mu = \frac{C_q}{1 + \alpha} = \frac{C_q}{1 + C_q / C_g} = \frac{C_q C_g}{C_q + C_g} \,.$$

[1]The radius one reflects the relaxation resistance $R_q = R_K/2$ of the circuit predicted by Büttiker [33].

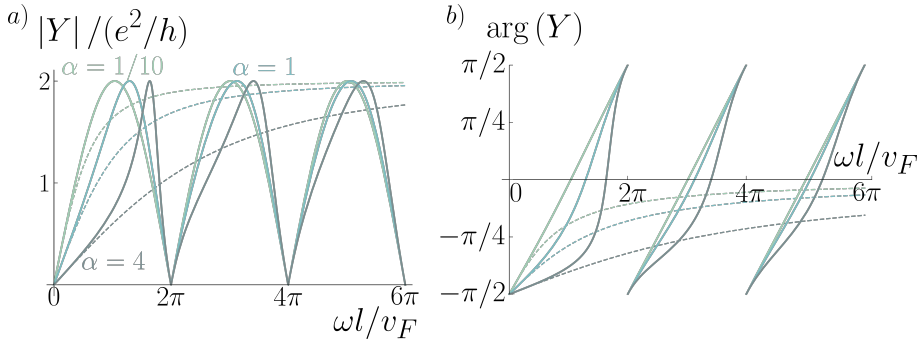

Figure 2.11: *a* Plot of the modulus $R_K\,|Y(\omega)|$ as a function of $\omega l/v_F$ for three different values of the coupling: $\alpha = 0.1, 1$ and 4. For each of these values of α, the modulus of the impedance of the classical RC circuit with $R = R_K/2$ and for the corresponding R_K and C_μ circuit is plotted in dashed lines with the same colors. *b* Plot of $\arg(Y)$ for the same examples as in the left panel (coloring identical to the left panel).

Fig. 2.11 shows the behaviour of $|R_K \mathrm{Y}(\omega)| = |1 - t(\omega)|$ (panel *a*) as well as of $\arg(Y(\omega))$ (panel *b*) as functions of $\omega l/v_F$ and for different values of the dimensionless coupling constant α.

As can be seen in the two panels, $Y(\omega)$ has an almost identical evolution to $Y_0(\omega)$ (Fig. 2.6 and Fig. 2.7) when $\alpha \ll 1$. This is expected since, in the voltage locked regime, the potential drop is zero at the capacitor and the electrons within the edge channel directly see the electric potential $V_g(\omega)$ applied to the top gate.

By contrast, when $\alpha \gtrsim 1$, $Y(\omega)$ keeps the same periodicity in $2\pi v_f/l$ but $Y(\omega) \simeq Y_0(\omega)$ is only recovered at high frequencies. At lower frequencies, the phase of $Y(\omega)$ deviates from the simple linear evolution and the peaks of $|\mathrm{Y}(\omega)|$ become sharper and less symmetric as α increases. We also note that the phase $\theta(\omega)$ plotted on Fig. 2.9-*b* displays the typical features of a phase resonance: it tends to vary more slowly at small ω (reflecting $Y(\omega) \simeq -\mathrm{i}C_\mu\omega$ at low frequency) and then rapidly turns by 2π for ω close to $2\pi v_F/l$. The same pattern then repeats itself but in a less pronounced way until the linear behavior observed at small α is recovered. We also observe that increasing the Coulomb interaction increases the sharpness of these resonances.

Such a behavior is not a surprise: for $\hbar\omega \ll e^2/C_g$, Coulomb interaction effects are expected to be dominant whereas, above this characteristic scale, this is not the case. It is thus expected to recover the low-α

behavior at large ω. The frequency scale that naturally appears in the problem is $R_K C_\mu$. In the voltage locked regime, $C_g \gg C_q$ and therefore $R_K C_\mu \simeq R_K C_q = l/v_F$. This sets the frequency scale v_F/l observed in this regime. But at large α, $C_g \ll C_q$ and thus $R_K C_\mu \simeq R_K C_g \ll l/v_F$. This sets the frequency scale $1/R_K C_\mu \simeq 1/R_K C_g$ for the transition between the low and large ω regimes.

To conclude this section, we have studied a radiation coupler model driven by a classical voltage drive $V_g(t)$. In this model, depending on the importance of Coulomb interaction effects, we are either in a voltage locked regime where the electrons propagating within the target branch directly experience the time dependent potential $V_g(t)$, or in a Coulomb blocked regime where charge accumulation beneath the top gate is avoided.

The first model discussed in Sec. 2.3 can be seen as the $\alpha \ll 1$ of the present model. Only in this limit can we forget about dispersion of EMP modes which, as explained in Ref. [35], means that electronic decoherence is quite weak. In this case, at small but non zero α, we may consider that the gate voltage $V_g(t)$ is filtered into an effective time dependent voltage $U_{\rm eff}(t)$ via

$$U_{\rm eff}(\omega) = \frac{V_G(\omega)}{1 + \alpha\, f\,(\omega l/v_F)}\,. \tag{2.51}$$

However, all the models considered in the present section assume that a classical drive is applied to the target branch of the electron radar. In the perspective of using this device to probe quantum electromagnetic radiation, we have to go beyond this limitation and consider a radiation coupler that couples the target branch to a channel where electromagnetic excitations can propagate. This is the object of the forthcoming section.

2.4 Two counter-propagating edge channels

In this section, we consider a radiation coupler involving two counter-propagating edge channels, capacitively coupled over a region of length l as illustrated Fig. 2.12. We describe Coulomb interaction by an effective long range interaction though a Büttiker discrete element like approach [154] which assumes that the electrons within a conductor feels a time dependent but uniform potential. Therefore, we will consider the two facing edge channels form a capacitor whose geometric capacitance will

be denoted by C_g. We also assume that these two chiral conductors are in total mutual influence in order to ensure maximal electrostatic coupling between them.

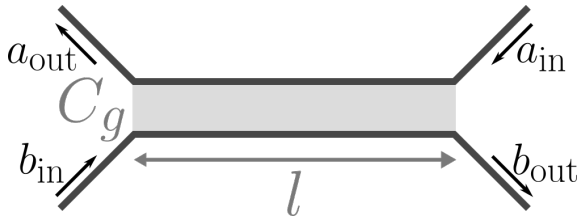

Figure 2.12: Two counter-propagating edge channels are capacitively coupled over a range l with a geometrical capacitance C_g. The incoming and outgoing EMP modes are described by the operators a_{in}, a_{out} in the upper branch and b_{in}, b_{out} in the lower branch.

This modeling is exactly the one used in Ref. [55] for a rectangular quantum Hall bar of length l at filling fraction $\nu = 1$. The EMP scattering matrix can thus be directly extracted from Ref. [56] and we will discuss its various limiting regimes.

2.4.1 The EMP scattering matrix

Denoting by b the EMP modes of the lower branch (target branch of the electron radar) and a the EMP modes of the upper branch (the radiation channel), the EMP scattering matrix $S(\omega)$ is given by the result of Sec. III of Ref. [56] specialized for $\nu = 1$:

$$\kappa_{ec}(\omega) = S_{ba}(\omega) = S_{ab}(\omega) = \frac{-\mathrm{i}Xf(X)}{2 + \alpha f(X)} \tag{2.52a}$$

$$t_{ec}(\omega) = S_{aa}(\omega) = S_{bb}(\omega) = 1 - \kappa_{ec}(\omega)\,. \tag{2.52b}$$

where α, X and $f(X)$ have been introduced in Sec. 2.3. This time $\kappa_{ec}(\omega)$ couples a plasmonic mode to another one unlike the previous sections where $\kappa_0(\omega)$ (see Sec. 2.3.1) and $\kappa(\omega)$ (see Sec. 2.3.2) describe the couplin of an EMP mode to the external classical voltage drive.

The regime of low α ($C_g \gg C_q$) is the regime where the potential drop at the capacitor, formed by the two channels facing each other, can be neglected: both channels see the same potential. Note that this is not a regime where the two edge channels are not interacting since the condition of equal voltage is indeed a strong constraint. In order to

decouple the two edge channels, one would indeed have to give up on the hypothesis of total mutual influence. Both edge channels would be coupled to external side gate whereas the geometric capacitance coupling them would vanish. But this is incompatible with a capacitance matrix for conductors in total electrostatic influence.

On the other hand, $\alpha \gg 1$ is the Coulomb blocked regime where Coulomb energy is so large that charging these length l regions is almost impossible.

We shall now discuss the limiting forms of the EMP scattering region in these two very different regimes. A key point in interpreting the results is the relation between the EMP scattering matrix and finite frequency impedances. Under the hypothesis of total screening, there is no leak of current to any external ground conductor. Thus the coupler has exactly the same shape as the example studied Sec. 2.2.1, so we are going to use the equations Eq. (2.15) and Eq. (2.17) that were derived there. Consequently, the finite frequency admittance of this conductor is

$$Y_{ec}(\omega) = \frac{e^2}{h}\, S_{ba}(\omega)\,. \tag{2.53}$$

At low enough frequency, this dipole can be viewed as an RC circuit with finite frequency admittance

$$Y_{ec}(\omega) = -\mathrm{i}C_\mu\omega + RC_\mu^2\omega + \mathcal{O}(\omega^3)\,. \tag{2.54}$$

Expanding $S_{ba}(\omega)$ up to second order in ω then leads to

$$C_\mu = \frac{C_q}{2+\alpha} = \frac{C_g C_q/2}{C_q/2 + C_g} \quad \& \; R = R_K\,. \tag{2.55}$$

We recover the expression of the quantum capacitance as the series addition of two single channel quantum capacitances (one for each edge channel) with the geometric capacitance C_g. The total resistance R_K is the sum of the two contact resistances $R_K/2$ for the two folded single edge channels.

As already discussed on Sec. 2.2.1 the EMP scattering amplitudes can be parametrized by:

$$t_{ec}(\omega) = \frac{1}{2}\left(1 + \mathrm{e}^{\mathrm{i}\vartheta(\omega)}\right) \tag{2.56a}$$

$$\kappa_{ec}(\omega) = \frac{1}{2}\left(1 - \mathrm{e}^{\mathrm{i}\vartheta(\omega)}\right) \tag{2.56b}$$

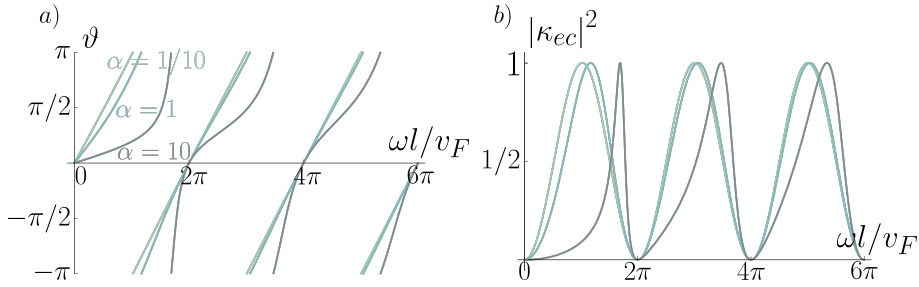

Figure 2.13: Left panel: Plot of the phase $\vartheta(\omega)$ as a function of $\omega l/2\pi v_F$ for two different values of the coupling: $\alpha = 1/5$ (blue full line) and $\alpha = 15$ (red full line). For each of these values of α, the angle for the $R_K C_\mu$ circuit is plotted in dashed lines with the same colors. Right panel: plots of $|S_{ba}(\omega)|^2$ for the same examples as in the top panel (coloring identical to the top panel).

where $\vartheta(\omega)$ is a real phase. Consequently, the parametric plot of $S_{ba}(\omega)$ and thus of $R_K Y_{ec}(\omega)$ in the complex plane is a circle of radius 1/2 centred on the point $z = 1/2$. Note that this is also the case for an RC circuit with resistance R_K and capacitance C_μ and $\vartheta(\omega) \simeq R_K C_\mu \omega$ at low frequency.

Fig. 2.13 displays $\vartheta(\omega)$ as a function of $\omega l/v_F$ for both a strong and a weak coupling case. The probability $|S_{ba}(\omega)|^2 = \sin^2(\vartheta(\omega)/2)$ for an EMP to be transmitted from the a edge channel into the b one is also plotted on the right panel. The latter quantity displays the filtering of the radiation coupler as a function of the frequency.

2.4.2 The voltage locked regime

The $\alpha \to 0$ limit of the EMP scattering matrix given by Eq. (2.52) is

$$\kappa_{ec} = \frac{1}{2}\left(1 - \mathrm{e}^{\mathrm{i}X}\right) \tag{2.57a}$$

$$t_{ec} = \frac{1}{2}\left(1 + \mathrm{e}^{\mathrm{i}X}\right) . \tag{2.57b}$$

which therefore implies that $\vartheta(\omega) = \omega l/v_F$. This is consistent with the full green line behaviour ($\alpha = 1/10$) displayed on the left panel of Fig. 2.13.

In this regime, the electrochemical capacitance is dominated by the quantum capacitance's contribution: $C_\mu \simeq C_q/2$ which means that the

corresponding time scale is $R_K C_\mu \simeq l/2v_F$. The fact that even at vanishing α, $\kappa_{ec}(\omega)$ is non-zero comes from the fact that this "weak coupling limit" is not a limit without interactions between the two counter-propagating edge channels: it only means that the potential drop at the capacitance vanishes and that both edge channels see the same voltage. In this regime, the transmission probability exhibits sinusoidal oscillations as a function of $\omega l/v_F$ just like a micro-wave directional coupler or two strongly coupled copropagating edge channels with local interactions would do (see Ref. [92]). This is why it is not very appropriate to quality the voltage locked regime ($\alpha \ll 1$) as a weak coupling regime.

As mentioned before, decoupling the two edge channels requires considering a model without the total screening hypothesis. However, note that, from the perspective of the electron radar, such a model would display a less efficient coupling between the two edge channels.

2.4.3 The Coulomb blocked regime

Increasing α introduces non-linearities in the phase $\vartheta(\omega)$ as shown on the left panel of Fig. 2.13. The phenomenology is then very similar to the one observed in the model discussed in Sec. 2.3.2: at high frequency, we recover a linear phase as a function of ω whereas, at low frequencies, we see phase resonances where $\vartheta(\omega)$ rapidly performs a 2π jump close to the resonance frequencies $2\pi n l/v_F$ ($n \in \mathbb{N}^*$).

The cross-over scale $1/R_K C_\mu$ is determined by the same considerations than in Sec. 2.3.2. In the Coulomb blocked regime, the electrochemical capacitance is dominated by the geometric capacitance $C_\mu \sim C_g$ since, in this regime, $C_g \ll C_q$. The $R_K C_\mu \sim R_K C_g$ time scale is then much shorter than the free electron time of flight $R_K C_q = l/v_F$. As a resultn $1/R_K C_\mu \gg v_F/l$.

Note that the right panel of Fig. 2.13. shows a strong distortion of the oscillations of the transmission probability $|S_{ba}(\omega)|^2$ for $\omega R_K C_\mu \lesssim 1$ which still reaches unity for ω slightly below $2\pi n v_F/l$ ($n \in \mathbb{N}^*$) but with narrow resonances. As n increases, these resonances become broader up to $\omega \simeq 1/R_K C_\mu$ above which they disappear.

Consequently, it appears that at high enough α and low frequency ($\omega R_K C_\mu \ll 1$), this radiation coupler is indeed selective in frequency. This is indeed an interesting feature for building a frequency selective detector, the narrowest resonance being the first one for $\omega/2\pi = l/v_F$. Of course, this does not mean that designing such a large α radiation coupler represents the best technical option for producing a narrow-band

radiation coupler. Introducing an LC-oscillator or and EMP cavity [38] may be an interesting alternative.

Away from these resonances, the EMP transmission amplitudes corresponds to a very short time of flight across the length l interaction region. This is the result of the zero charge constraint at infinite coupling: every charge density disturbance has to go out of the interaction region immediately and leads to no charge density change within the interaction region (hence the vanishing inter-channel EMP scattering amplitude).

Chapter 3

Ambiguity function

This chapter is an introduction to the electron radar theory. Because all these ideas are not familiar within the mesoscopic physics community, we have chosen to follow an inductive path that starts from classical radar theory, presented in Sec. 3.1 and introduces the basic concept of ambiguity function in signal processing which quantifies the ability of the radar to distinguish distances and velocities of a moving target. Because it is an important historical example and because it provides a pedagogical introduction to the problem of target reconstruction in radar theory, we will discuss this example in a toy model version quite extensively.

This concise review will enable us to move forward to the electronic radar theory which will the main topic in the present chapter (see Sec. 3.2). At this stage, for the sake of simplicity, our discussion will rely on a single particle scattering framework. The analogy and differences with classical radar theory will then appear clearly. This will enable us to introduce and study the core concept of single electron radar theory which is the electronic ambiguity function (see Sec. 3.3). This natural generalization of the well known concept in signal processing characterizes the resolution power of the electron radar in terms of effective time of flight and energy change of the electron within the time of flight. As we will see, the corresponding frequency scale is the inverse of the time scale of non stationary phenomenon that the electron radar is able to probe. We will see that the electronic ambiguity function is indeed the fourth, up to now unused, representation of the excess single electron coherence emitted by an electron quantum optics source.

Section 3.4 will then be devoted to characterizing the time/frequency

domain currently accessible to state of the art single electron source and also to discuss techniques directly adapted from classical radar theory to improve the resolution power of the electron radar and extend the time/frequency domain that could be accessed with state of the art single electron sources.

3.1 The ambiguity function in signal processing

The ambiguity function is a fundamental tool in radar and signal processing which quantifies the trade-off between the ability to measure the position and velocity of a target. This section aims at providing an overview of this concept, its history, its definition and its properties.

To begin with, we present a brief review of the history of radar theory and the emergence of the ambiguity fonction. Then, we will discuss the classical radar theory which provides the mathematical foundations for the ambiguity function. In particular, we will explain how it arises naturally in the equations that describe the measurement of the position and velocity of a target using interferometric measurements. We will provide a formal definition of the ambiguity function and demonstrate how it characterizes the resolution power of a radar system. Finally, we will rapidly mention some of the practical considerations and limitations of using the radar in real-world applications.

3.1.1 Historical overview and definition

The ambiguity function was first introduced by P. M. Woodward in 1953 [192] as a tool for analyzing radar signals in both the time and frequency domains. It has been a subject of intense research, leading to various extensions and generalizations, such as the Wigner-Ville distribution and Cohen class distributions [48]. The use of the ambiguity function has significantly improved the understanding of radar detection and resolution capabilities, making it an essential tool in modern radar system analysis and design. It has been employed in the design and analysis of advanced radar systems, such as synthetic aperture radar (SAR), inverse synthetic aperture radar (ISAR), and multiple-input multiple-output (MIMO) radar. These modern radar systems rely on the ambiguity function to optimize signal processing techniques, target detection, and imaging capabilities [158]. In communication systems, the ambiguity function has aided in the analysis and design of modulation

schemes like spread spectrum and orthogonal frequency-division multiplexing (OFDM) techniques, as well as the development of synchronization and channel estimation algorithms for robust, efficient systems [155].

3.1.2 Classical radar theory

The radar is nothing but an interferometric instrument capable of detecting a target (T) and quantifying its range ($c\,\tau_T$) and velocity (v_T) with respect to the observer. In real conditions, the captured signal is typically tainted with significant noise, originating from various sources such as atmospheric interference, equipment-induced noise and, in the context of military applications, potential jamming. However, for the purpose of this brief review, we will intentionally disregard these noise sources. Moreover, we will focus on the capabilities, concentrating instead on measurement and reconstruction capacities of the range $c\,\tau_T$ and velocity v_T of the target.

The radar, pictured in the left panel of Fig. 3.1, measures these two quantities along the direction determined by line of sight of the target from the observer's point of view. The fundamental principle behind radar operation involves comparing a reference signal to its reflection from the target, bearing similarities to a Mach-Zehnder interferometer represented in the right panel of Fig. 3.1.

Initially, a linear separator, functioning as a semi-reflecting beam splitter, divides the probe signal into two parts. The target, located on one of the two interferometer branches (called the target branch), scatters the probe signal. Subsequently, a second beam splitter combines the scattered signal with the reference signal that has freely propagated during a time τ_{ref} along the reference branch. By analyzing the interference contributions on the average light or radio intensity coming out of the interferometer in either the time or frequency domain, the round-trip propagation time of the probe between the observer and the target can be determined. Additionally, the frequency shift (Ω_T) experienced by the probe during its interaction with the target (T) gives information on the velocity of the target via its Doppler shift.

While radar technology offers numerous advantages, its measurement accuracy for position ($c\tau_T$) and velocity (v_T) cannot be made arbitrary small. The wave nature of the probe signal imposes limitations on measurement precision due to time-frequency uncertainty. To develop a more quantitative understanding of these idea, we will now discuss a

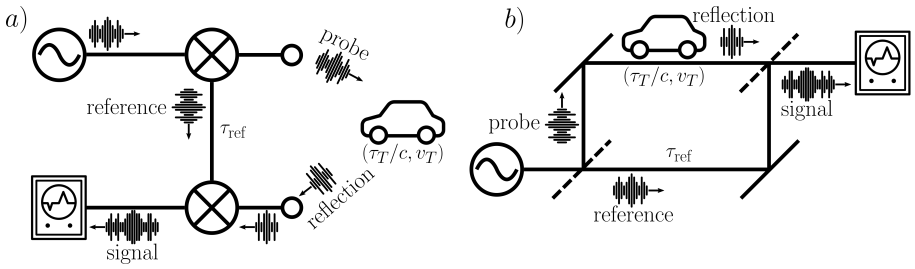

Figure 3.1: (a) A schematic diagram of a radar system probing the relative position $c\,\tau_T/2$ and velocity v_T of a car is presented. The input signal is divided into two parts: a probe that will be reflected by the car and a reference signal that is kept for a time τ_{ref} to be compared with the measured reflection. This process is analogous to a Mach-Zehnder interferometer (MZI) plotted in the right panel. (b) A schematic diagram of the MZI is shown. The wave source is at the input of the MZI and the average intensity is measured at the output. The car is placed in the upper branch of the system, while the reference signal propagates freely during a time τ_{ref} in the lower branch.

simplified 1D model for the classical radar based on modeling the target as a time dependent linear scatterer. Moreover, the discussion will be non-relativistic which is enough to explain the main features.

Being 1D and relying on a scalar signal, this model is an over-simplification compared to the realistic radar where wave polarization and 3D geometry should be considered. It nevertheless captures the essence of the physics of all radars used in aeronautics, of lidars as well as of natural or artificial sonars.

Time dependent scattering

Assuming that the target is accurately represented by a time-dependent scattering amplitude $R_T(t, t')$, it scatters an incoming scalar signal $x_{\text{in}}(t')$ arriving at time t' into an outgoing signal $x_{\text{out}}(t)$ equal to:

$$x_{\text{out}}(t) = \int_{t' \leq t} R_T(t, t')\, x_{\text{in}}(t') \mathrm{d}t' \tag{3.1}$$

where the condition $t' < t$ signifies that the target's response is causal[1].

[1] One could equivalently assume that $R(t, t') = 0$ for $t < t'$.

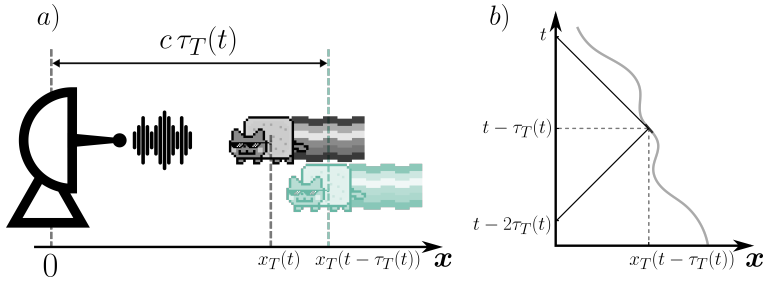

Figure 3.2: *Left panel* A radar positioned at $x = 0$ is probing a target moving along the x-axis with a time dependant position $x_T(t)$. The radar receives at time t a signal which has traveled from the target's initial position $x_T(t - \tau_T(t))$ back to the radar during a time $\tau_T(t)$. Upon signal reception, the target has since moved to the position $x_T(t)$. *Right panel* Space-time diagram featuring the probe signal's path (dark line) and the target's trajectory (grey curve) within the radar'sreference frame. The x-axis represents the spatial position and the y-axis denotes the temporal position. A signal measured at time t was reflected by the target at time $t - \tau_T(t)$ and has indeed been emitted at time $t - 2\tau_T(t)$.

To illustrate this, consider a scenario where the target is a solitary, perfectly reflective point moving along the x-axis, as depicted in the left panel of Fig. 3.2. The motion of this target is characterized by the function $x_T(t)$, where the radar is at the origin $x = 0$.

The right panel of the figure presents a spatio-temporal diagram of the situation, detailing the interplay of time and space coordinates. The radar initiates the process by emitting a right-moving signal probe, $\phi^p_R(t')$, at time t' and position $x = 0$. Subsequently, at time t, the radar receives a reflected, left-moving signal $\phi^r_L(t)$ at the same location. Our objective is to calculate the scattering matrix, essentially a relation between the reflected signal $\phi^r_L(t)$ and the emitted one $\phi^p_R(t')$.

To achieve this goal, we introduce $\tau_T(t)$, the time for the radiation to cross the distance between the radar and the target when the signal is measured at time t by the radar. It has thus been reflected by the target at time $t-\tau_T(t)$, at a distance $x_T(t-\tau_T(t))$ away from the radar. Given that the radiation propagates at the speed of light c, we obtain the implicit equation giving the time of flight $\tau_T(t)$:

$$c\,\tau_T(t) = x_T(t - \tau_T(t))\,. \tag{3.2}$$

Following a similar logic, the emission time of the signal received at

time t is determined to be $t' = t - 2\tau_T(t)$. The target, being a perfect reflector, ensures that the measured and emitted radiations are related for all time t by:

$$\phi_L^r(x = x_T(t), t) = \phi_R^p(x = x_T(t), t)\,. \tag{3.3}$$

Proving this relation requires going in the reference frame moving at the speed $\dot{x}_T(t) = -v_T(t)$ of the target[2]. Up to a space translation which is not relevant here, the formulae describing the Gallilean change of coordinates from the radar's frame (coordinates (x, t)) to this new frame (coordinates (x', t')) are

$$x' = x + vt \tag{3.4a}$$
$$t' = t \tag{3.4b}$$

and, the field being a scalar:

$$\phi'_\alpha(x', t') = \phi_\alpha(x, t) \tag{3.5}$$

for $\alpha = R$ or L. Perfect reflection in the moving reference frame is then expressed as

$$\phi'_{L,r}(x'_T(t'), t') = \phi'_{R,p}(x'_T(t'), t') \tag{3.6}$$

Consequently,

$$\phi_L^r(x_T(t), t) = \phi'_{L,r}(x'_T(t'), t') \tag{3.7a}$$
$$= \phi'_{R,p}(x'_T(t'), t') = \phi_R^p(x_T(t), t) \tag{3.7b}$$

which is Eq. (3.3). Including ballistic propagation of these left and right moving fields then leads to

$$\phi_L^r(t) = \phi_R^p(t' = t - 2\tau_T(t))\,. \tag{3.8}$$

The scattering amplitude $R_T(t, t')$ is then given by:

$$R_T(t, t') = \delta\left(t - t' - 2\tau_T(t)\right)\,. \tag{3.9}$$

The scattering amplitude is zero except when $t - t' = 2\tau_T(t)$, where $2\tau_T(t)$ represents the round-trip time of a photon to reach the target and return, measured at time t. So far, this is not surprising but understanding how the frequency shift emerges from this expression requires deriving and analyzing the radar equation.

[2]With this convention $v_T(t)$ is the velocity of the target towards the radar.

Radar equation

In the time domain By computing the interference contribution to the average light intensity measured at the detector at time t, we derive the following equation:

$$I(t, \tau_{\text{ref}}) = \int_{t'<t} R_T(t, t') x_{\text{in}}^*(t') x_{\text{in}}(t - \tau_{\text{ref}}) \mathrm{d}t' + \text{c.c.} \tag{3.10}$$

This equation, called the classical radar equation in the time domain shows that the quantity of interest $I(t, \tau_{\text{ref}})$ is mainly a convolution product of the scattering amplitude $R_T(t, t')$ with a kernel $x_{\text{in}}^*(t') x_{\text{in}}(t - \tau_{\text{ref}})$ whose shape is given by the waveform of the probe. This kernel is a quadratic functional of the amplitude of the incoming probe signal $x_{\text{in}}(t)$.

When probing the previously discussed target, characterized by the scattering matrix in Eq. (3.9), the form of $I(t, \tau_{\text{ref}})$ can be represented as follows:

$$I(t, \tau_{\text{ref}}) = x_{\text{in}}^* \left(t - 2\tau_T(t)\right) x_{\text{in}} \left(t - \tau_{\text{ref}}\right) + \text{c.c.} \tag{3.11}$$

From the derived equation, it is evident that the radar gauges the coherence of the probe within the time interval $t - 2\tau_T(t)$ and $t - \tau_{\text{ref}}$. But the exact information that can be retrieved from the target are not obvious. To further clarify this aspect, we assume that the probe signal has a Gaussian envelope and is described by the following equation:

$$x(t) = A_0 \, \mathrm{e}^{-\frac{(t-t_0)^2}{2\sigma_t^2}} \, \mathrm{e}^{-\mathrm{i}\omega_0 t} \tag{3.12}$$

with A_0 the maximal amplitude, t_0 the center of the Gaussian enveloppe, σ_t its temporal width and ω_0 the carrier frequency. The radar signal then becomes:

$$I(t, \tau_{\text{ref}}) = I_0 \cos\left(\omega_0 \left(\tau_{\text{ref}} - 2\tau_T(t)\right)\right) \mathrm{e}^{-\frac{\left(t-2\tau_T(t)-t_0\right)^2 + \left(t-\tau_{\text{ref}}-t_0\right)^2}{2\sigma_t^2}} \tag{3.13}$$

We also consider a target, depicted as a "flying cat"[3] on Fig.3.2, moving towards the radar at a constant velocity v_T. Its trajectory is parametrized by:

$$x_T(t) = x_0 - v_T t \,, \tag{3.14}$$

[3]Instead of a more realistic object such as a plane.

where x_0 represents its position at $t = 0$. By substituting this equation into Eq. (3.2), we can compute the associated time of flight $\tau_T(t)$:

$$\tau_T(t) = \frac{x_0 - v_T t}{c - v_T}\,, \tag{3.15}$$

allowing us to compute the measured signal:

$$\begin{aligned} I(t, \tau_{\text{ref}}) =& I_0 \cos\left[\omega_0 \left(\tau_{\text{ref}} + \frac{2v_T}{c - v_T}\, t - \frac{2x_0}{c - v_T} - t_0\right)\right] \\ & \times \exp\left[\frac{-\left(t - 2\frac{x_0 - v_T t}{c - v_T} - t_0\right)^2 - (t - \tau_{\text{ref}} - t_0)^2}{2\sigma_t^2}\right]. \end{aligned} \tag{3.16}$$

This equation gives us a better insight into the information the radar can provide about the target. This signal oscillates as a function of the measurement time tt with a Gaussian envelope. These oscillations are at the Doppler shift $\Delta\omega_0 = 2v_T\omega_0/c$: they result from the beating between the reference signal at ω_0 and the Doppler shifted reflected signal. Note that varying τ_{ref} changes the phase $\omega_0\tau_{\text{ref}}$ of the reference signal. By measuring the oscillations in t, the Doppler shift can be measured and the target's speed reconstructed. The resolution of this measurement is determined by the number of discernable oscillations in the radar signal, a quantity growing with the probe frequency ω_0 and the Gaussian width σ_t. The center of the Gaussian envelope is located at $\left(\tilde{t}, \tilde{\tau}_{\text{ref}}\right)$ in the (t, τ_{ref}) plane with:

$$\tilde{t} = \frac{2x_0 + t_0\,(c - v_T)}{c + v_T} \tag{3.17}$$

$$\tilde{\tau}_{\text{ref}} = 2\frac{x_0 + v_T t_0}{c + v_T} \tag{3.18}$$

Note that $\tilde{\tau}_{\text{ref}}$ is directly proportional to the target's distance $x_T(t_0)$. By estimating $\tilde{\tau}_{\text{ref}}$ which is the center of the Gaussian enveloppe of the radar signal in τ_{ref}, one can determine $x_T(t_0)$ with a relative error given by v_T/c when nothing is known on the speed of the target. The precision on the estimation of the centre of the Gaussian is better with a short probe signal or equivalently a small σ_t.

To illustrate this discussion , we have plotted on the top panel of Fig. 3.3 the Gaussian-shaped envelope of $I(t, \tau_{\text{ref}})/I_0$, assuming a single-point target moving towards the radar at a speed $v_T = 10^{-5}c$ from an

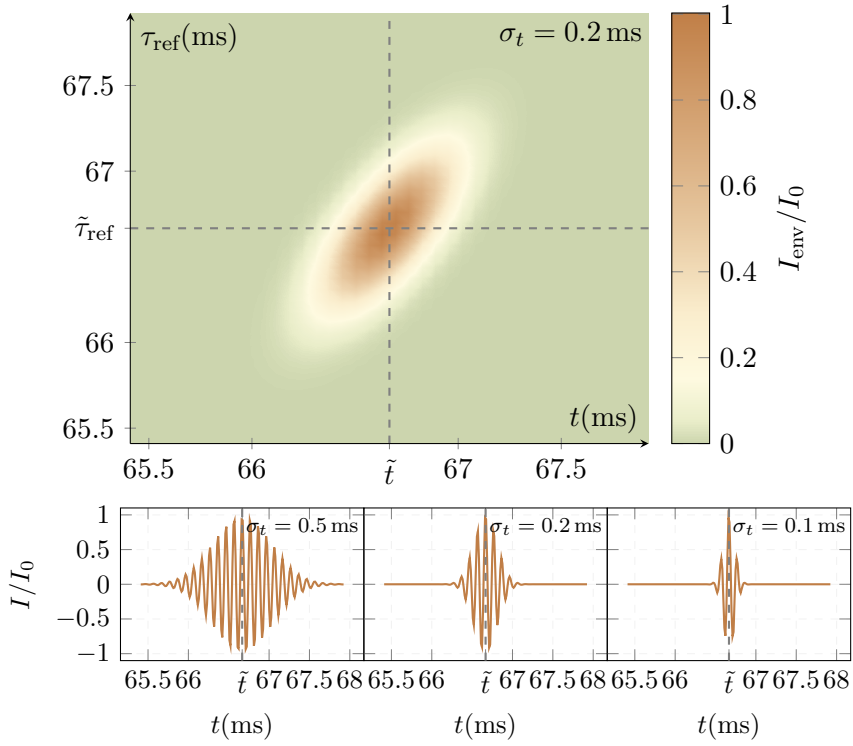

Figure 3.3: *Top panel* Plot of the envelop of the average light intensity I_{env} measured by the radar coming from the interference contributions. It is plotted according t and τ_{ref}. The signal emitted by the radar is a Gaussian radiation of frequency $\omega_0/2\pi = 500\,\text{MHz}$, with a timewidth $\sigma_t = 0.2\,\text{ms}$ and was emitted at time $t_0 = 0$. The target is a perfectly reflecting point, moving toward the radar with a speed $v_T = 3\,\text{km}\,\text{s}^{-1}$,and an initial position $x_0 = 10\,000\,\text{km}$. *Bottom panel* Plot of $I(t, \tilde{\tau}_{\text{ref}})/I_0$ for three various values of σ_t: 0.5 ms, 0.2 ms and 0.1 ms from left to right.

initial position $x_0 = 10\,000\,\text{km}$. The radar probes it with a Gaussian modulated signal with a duration $\sigma_t = 0.2\,\text{ms}$ and a carrier frequency $\omega_0/2\pi = 500\,\text{MHz}$ (UHF band used for very long range surveillance, typically like the long range radar stations used to monitor possible incoming ballistic missiles during the Cold War).

We consider $t_0 = 0$. Then, the expected Doppler shift is $\tilde{\omega}/2\pi = 2v_T\omega_0/2\pi(c - v_T) \simeq 10\,\text{kHz}$ and the expected round-trip time is $\tilde{\tau}_{\text{ref}} \simeq 66.66\,\text{ms}$. The Gaussian envelope is precisely centered at these expected

values. As σ_t increases, the anisotropic Gaussian envelope becomes larger.

The lower panel in the figure shows the normalized light intensity $I(t, \tilde{\tau}_{\text{ref}})/I_0$ for values of σ_t of 0.5 ms, 0.2 ms, and 0.1 ms. These curves, all centered at $\tilde{t}$, exhibit oscillations modulated by a Gaussian envelope, as predicted.

Increasing σ_t enhances the number of discernible oscillations in the envelope. In other words, the Fourier transform $\widetilde{I}(\Omega, \tilde{\tau}_{\text{ref}})/I_0$ becomes narrower around the Doppler shift $2v_T/(c-v_T)\omega_0$ with the augmentation of σ_t. This enables a more precise measurement of the velocity v_T, via the determination of the Doppler shift. But it simultaneously degrades the measurement resolution on $\tilde{\tau}_{\text{ref}}$ and thus on the target's distance. Consequently, there is an inherent trade-off between the resolution on the velocity and the resolution of the position of the target when using probes with a Gaussian shape.

Measuring $I(t, \tau_{\text{ref}})$ is optimal for assessing the target's distance, although velocity determination demands additional analysis on the measurements. We now pivot to a time-frequency representation to have a different view of the same problem. As we will see, this approach is advantageous for radar applications as it simplifies the identification of the propagation time and of the Doppler shift.

In the time-frequency domain By implementing a Fourier transformation on the aforementioned Eq. (3.10), while preserving the integral over $\tau = t - t'$ in the right-hand side of the equation, we obtain the radar equation in the time-frequency domain:

$$\tilde{I}(\omega, \tau_{\text{ref}}) = \int_{\mathbb{R}} \widetilde{R_T}(\omega - \Omega, \tau_{\text{ref}} - \tau) A_{\text{in}}(\Omega, \tau) \mathrm{e}^{\mathrm{i}\frac{(\Omega+\omega)\tau_{\text{ref}} - \omega\tau}{2}} \frac{\mathrm{d}\Omega \mathrm{d}\tau}{2\pi} \quad (3.19)$$

originally derived for the classical radar [192]. Here, $\widetilde{R_T}(\Omega, \tau)$ represents the scattering amplitude by the target in the time-frequency domain:

$$\widetilde{R_T}(\Omega, \tau) = \int_{\mathbb{R}} R_T\left(t + \frac{\tau}{2}, t - \frac{\tau}{2}\right) \mathrm{e}^{\mathrm{i}\Omega t} \mathrm{d}t. \quad (3.20)$$

This scattering matrix is obtained by applying the Fourier transform to $R_T(t, t')$, transforming it from the time domain to the time-frequency domain.

In our example of a target propagating toward the radar at a speed v_T, its scattering matrix in the time frequency domain is:

$$\widetilde{R_T}(\Omega,\tau) = \exp\left[\mathrm{i}\Omega\left(\frac{x_0}{v_T} - \frac{c\,\tau}{2v_T}\right)\right]. \tag{3.21}$$

This representation poses significant challenges when analyzing radiation behavior during propagation and subsequent reflection off the target. Interpreting the signal's characteristics in both time and frequency domains solely from Eq. (3.21) is nontrivial. Notwithstanding, it contains identical information as $R(t,t')$.

The ambiguity function, denoted as $A_{\mathrm{in}}(\tau,\Omega)$ in Eq. (3.19), is defined by:

$$A_{\mathrm{in}}(\tau,\Omega) = c\int_{\mathbb{R}} x_{\mathrm{in}}^*\left(t-\frac{\tau}{2}\right) x_{\mathrm{in}}\left(t+\frac{\tau}{2}\right)\,\mathrm{e}^{i\Omega t}\mathrm{d}\,t\,. \tag{3.22}$$

It is the Fourier Transform of the correlation function $x_{\mathrm{in}}^*\left(t-\frac{\tau}{2}\right) x_{\mathrm{in}}\left(t+\frac{\tau}{2}\right)$ appearing in the radar equation in the time domain Eq. (3.10). The Gaussian signal given by Eq. (3.12) has a Gaussian ambiguity function:

$$A_{\mathrm{Gauss}}(\Omega,\tau) = \mathrm{e}^{-\left(\frac{\tau}{2\sigma_t}\right)^2-\left(\frac{\Omega\sigma_t}{2}\right)^2}\mathrm{e}^{\mathrm{i}(\Omega t_0-\omega_0\tau)} \tag{3.23}$$

Its principal axes are the Ω and τ axis. Its modulus is plotted on Fig. 3.4. The ambiguity function is centred at $(\Omega,\tau)=(0,0)$ reaching a maximum value of one for properly normalized $x(t)$. It time extension is σ_t and its frequency extension is σ_t^{-1}. Because of the convolution form of the radar equation (3.19), the ambiguity function time/frequency extension directly give access to the radar resolution capabilities.

To illustrate this discussion and this new point of view, we have compute the radar signal given by Eq. (3.19) with the same example as before. Injecting Eq. (3.23) and Eq. (3.21) into Eq. (3.19) returns a Gaussian shaped $\tilde{I}(\omega,\tau_{\mathrm{ref}})$. Instead of writing its full (and rather cumbersome) expression, we have plotted $|\tilde{I}(\omega,\tau_{\mathrm{ref}})|$ on Fig. 3.5.

It is a 2D-Gaussian function centered at (τ,ω) given by the round-trip time $\tilde{\tau}_{\mathrm{ref}}$ and the Doppler shift $\delta\omega_0 \simeq 2v_T\omega_0/c$. The target's velocity and distance is then easy to read since we only need to retrieve these two coordinates. We have also plotted the lines for which $\left|\tilde{I}(\omega,\tau_{\mathrm{ref}})\right| = 0.3\left|\tilde{I}_0\right|$ assuming 3 different durations $\sigma_t = 0.1\,\mathrm{ms}$, $0.2\,\mathrm{ms}$ and $0.5\,\mathrm{ms}$. As expected, larger values lead to an elongated signal along the τ_{ref}-axis and compressed along the ω-axis.

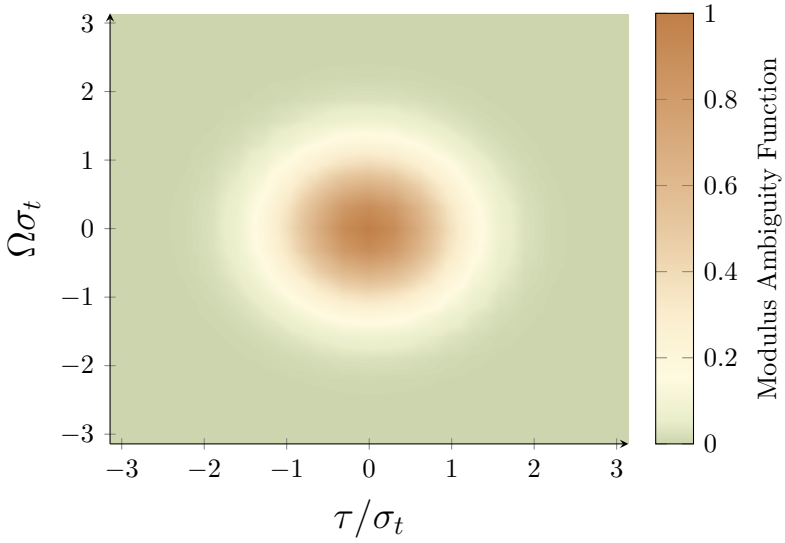

Figure 3.4: Modulus of the ambiguity function for a Gaussian signal centred at t_0 with a time extension σ_t. The axis are normalized in regards with σ_t.

3.1.3 Radar limitations

Besides the trade-off between range and Doppler resolution provided by the ambiguity function, several practical considerations and limitations exist when operating radar systems in real-world applications. These aspects have not been discussed in this section, but they are worth noting:

- *Signal bandwidth and duration*: Achieving good resolution in both frequency and time dimensions simultaneously necessitates the probing signal to have a broad spectrum and be elongated in time. One type of signal that fits these criteria is the white noise signal. However, its practical usage encounters technical limitations. The emission of true white noise is hard to achieve due to equipment bandwidth limitations. In the same way, measuring accurately white noise signal demands a receiving system which senses radiations in a wide bandwidth. Furthermore, the stochastic nature of white noise complicates signal processing and interpretation.

- *Clutter and interference*: Following successful data acquisition,

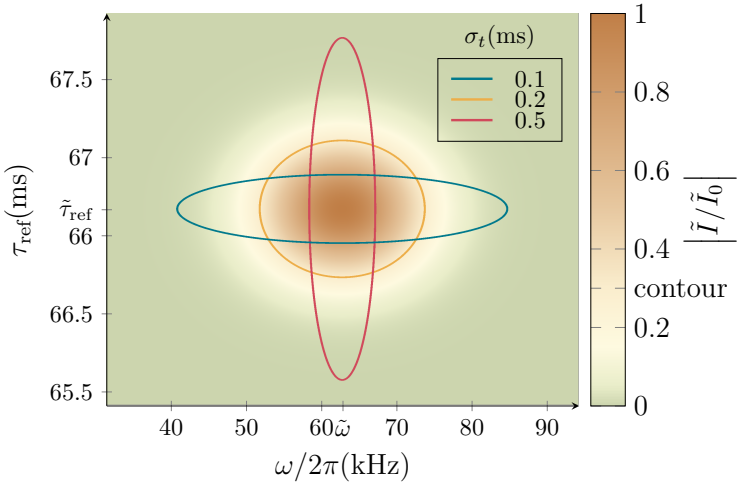

Figure 3.5: Plot of the average light intensity $|\tilde{I}(\omega, \tau_{\text{ref}})/\tilde{I}_0|$ normalized to its maximum value $\tilde{I}_0$ coming from the interference contributions measured by the radar in the time-frequency domain. The probe is a Gaussian radiation with a duration $\sigma_t = 0.2\,\text{ms}$. It is centred in $(\tilde{\omega}, \tilde{\tau}_{\text{ref}})$. The values used to plot the figure are the same than in Fig. 3.3. The blue, yellow and red curves indicate when $\left|\tilde{I}(\omega, \tau_{\text{ref}})\right| = 0.3\left|\tilde{I}_0\right|$ for signals with three different Gaussian timewidth σ_t, respectively 0.1 ms, 0.2 ms and 0.5 ms.

the primary signal processing task is to accurately reconstruct the scattering matrix from the data which is a convoluted signal with the ambiguity function. In real-world radar applications, this task is further complicated. The received signal is often polluted with noise, clutter, and interference from external sources. Such factors exacerbate the deconvolution problem and make it more challenging to accurately estimate the target's position and velocity.

- *Multipath propagation*: In a real-world three-dimensional space, radar measurements can be misinterpreted due to the presence of multiple propagation paths. These paths are caused by reflections and refractions off objects other than the intended targets. In such cases, knowing the specific reflection signature of the target can prove beneficial. This knowledge aids in distinguishing signals originating from direct path propagation from those derived from other sources.

- *Computational complexity*: The computation of the ambiguity function can be computationally intensive, especially for high-resolution radar systems or when processing large amounts of data. This may impose limitations on the real-time processing capabilities of the radar system.

In summary, the ambiguity function is a central concept in classical radar theory, offering a unified representation of both time delay and frequency shift resolution associated with the probing signal. Let us now discuss how an analogous concept appears for the electron radar.

3.2 The electron radar equation

In this section, we aim to derive an analogous result, called the electron radar equation. As we shall see, it will lead us to introduce the concept of single electron ambiguity function which plays the same role as the ambiguity function in the classical radar theory. However, we will see that the electron radar is intrinsically quantum since there is no classical signal associated with a single electron wave function.

For the sake of simplicity, we will model the electron radar as an ideal electronic interferometer where interaction effects are either neglected or effectively taken into account by using (time dependent) single particle scattering theory. This is a strong assumption but we will see in Chapter 4 how to overcome it. The advantage is that it allows us to discuss the electron radar equation and the associated concepts within the framework of "linear electron quantum optics".

3.2.1 The single particle scattering approach

We derive the radar equation under the hypothesis that electronic propagation inside the MZI is described in terms of time dependent single particle scattering. This means that we disregard electron-hole pair creation due to Coulomb interactions within the MZI. This hypothesis amounts to neglecting electronic decoherence within the MZI but we will see in Chapter 4 how to overcome this limitation. We aim to probe an unknown electromagnetic field localized at the vicinity of the target branch of the MZI as depicted Fig. 3.6. The effect of this external magnetical field will also be described, as we shall explain in this section, by an effective single particle scattering.

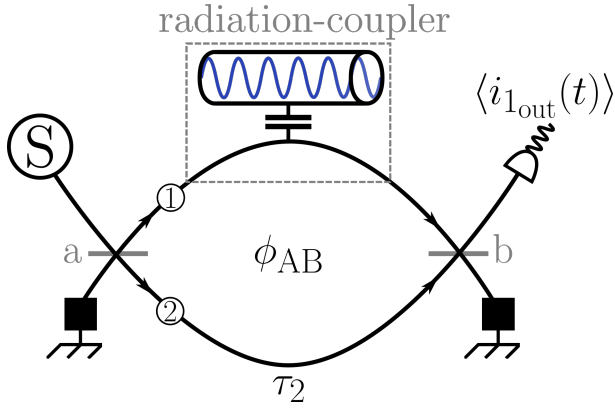

Figure 3.6: Schematic view of the electron quantum radar. The setup involves an electronic MZI formed by the conjunction of branches 1 and 2 with QPCs a and b. Branch 1 traverses the radiation coupler, while branch 2 allows free propagation during a time τ_2. The Aharonov-Bohm phase, denoted by ϕ_{AB}, is associated with the magnetic flux penetrating the MZI, which is generated by a perpendicular magnetic field. A single-electron source, labelled as S, is positioned on branch 1 immediately before QPC a. Additionally, a time-dependent average electrical current detector is placed on branch 1 just after QPC b. This configuration enables the electron quantum radar to probe an unknown electromagnetic field and measure its effects through the observed interference pattern in the MZI.

We also assume that a source generates a single electron in the wavepacket φ_e and injects it into the MZI. The electronic fluid state at the source's output is expressed as:

$$|\psi_S\rangle = \psi_S^\dagger[\varphi_e]\,|F\rangle\ . \tag{3.24}$$

For simplicity, we assume that the source is positioned right before the first QPC so that the injected single electron excitation is in the single particle state $|\varphi_e\rangle$.

We also assume that the two QPCs a and b are ideal electronic beam splitters with energy-independent scattering matrices:

$$M_\alpha^{\text{QPC}} = \begin{pmatrix} \sqrt{T_\alpha} & i\sqrt{R_\alpha} \\ i\sqrt{R_\alpha} & \sqrt{T_\alpha} \end{pmatrix}, \tag{3.25}$$

with T_α and R_α (α = a, b) denoting the electronic transmission and reflection probabilities satisfing $T_\alpha + R_\alpha = 1$.

The electron propagates ballistically for a time τ_2 within the reference branch, while it is scattered by the electromagnetic field under investigation in the target branch. We denote $R(t,t')$ as the amplitude for an electron to enter branch 1 at time t' and exit it at time $t \geq t'$. This amplitude encompasses the free propagation time before and after the radiation-coupler, as well as the action of the electromagnetic field on the electron within the radiation-coupler. The fact that propagation in the presence of an external electromagnetic field can be described within a single particle framework is an important hypothesis here. But exactly as for the effects of Coulomb interactions, going beyond it will be discussed in Chapter 4. At this stage, based on considerations of Chapter 2, if the radiation is classical and the associated time dependent potential directly applied to the electrons within the radiation coupler, this hypothesis is valid.

As the radar operates in the Aharonov-Bohm regime where charging effects can be neglected [98], both electronic amplitudes acquire a phase shift of opposite sign: $\pm\phi_{\mathrm{AB}}/2 = \pm\pi\Phi_B/\Phi_0$ ($\Phi_0 = h/e$ being the flux quantum). The second QPC recombines the two amplitudes and we measure the outgoing time-dependent average electrical current $\langle i_{1_{\mathrm{out}}}(t)\rangle$ leaving the first branch. The quantity of interest is the Aharonov-Bohm flux-dependent contribution to $\langle i_{1_{\mathrm{out}}}(t)\rangle$. In an MZI interferometer, the Aharonov-Bohm phase dependence of the outgoing average current simplifies to:

$$\langle i_{1_{\mathrm{out}}}(t)\rangle = -e\left(I_0(t) + \mathrm{e}^{\mathrm{i}\phi_{\mathrm{AB}}} I_+(t) + \mathrm{e}^{-\mathrm{i}\phi_{\mathrm{AB}}} I_+(t)^*\right). \tag{3.26}$$

since the Aharonov-Bohm can only be encircled once by a single electron. Finally, the Aharonov-Bohm flux, ϕ_{AB}, dependent contributions can be isolated from the background by applying a Fourier transform to $\langle i_{1_{\mathrm{out}}}(t)\rangle$ with respect to Φ_B/Φ_0. This allows us to specifically measure the quantity $I_+(t)$, which is of great interest since it contains the interference between the two paths traversed by the electron.

Denoting by $\mathcal{A}(S \xrightarrow{i} 1_{\mathrm{out}})$ the amplitude for an electron to be emitted by the source S, propagating along branch i between the two QPCs and be detected in 1_{out}, we have

$$I_+(t) = v_F \mathcal{A}(S \xrightarrow{1} 1_{\mathrm{out}})\, \mathcal{A}(S \xrightarrow{2} 1_{\mathrm{out}})^* \tag{3.27}$$

with

$$\mathcal{A}(S \xrightarrow{1} 1_{\text{out}}) = \sqrt{T_{\text{a}} T_{\text{b}}} \int_{\mathbb{R}} R(t,t') \varphi_e(t')\, \mathrm{d}t' \tag{3.28a}$$

$$\mathcal{A}(S \xrightarrow{2} 1_{\text{out}}) = -\sqrt{R_{\text{a}} R_{\text{b}}}\, \varphi_e(t-\tau_2)\,. \tag{3.28b}$$

Eq. (3.28a) describes propagation across a time dependent scatterer with scattering amplitude $R(t,t')$ representing the effect of external radiation. Eq. (3.28b) described ballistic propagation along the reference branch with a time of flight τ_2. Consequently, the outgoing current is proportional to the overlap between the amplitude of electron propagation in both branches.

To obtain a non-zero signal, it is essential that some coherence between the amplitudes in the two branches is preserved. This requirement ensures that the interference between the electron wavefunctions in the two branches can contribute to the detected signal, which is crucial for the operation of the quantum radar.

The quantity $X_+(t)$ defined by $I_+(t) = -\sqrt{R_{\text{a}} T_{\text{a}} R_{\text{b}} T_{\text{b}}}\, X_+(t)$ does not depends on the properties of the electronic beam splitters and completely determines the interference contribution to the average electrical current. It is equal to

$$X_+(t) = v_F \int_{\mathbb{R}} R(t,t') \varphi_e(t')\, \varphi_e(t-\tau_2)^* \mathrm{d}t'\,. \tag{3.29}$$

The expression mirrors the classical radar equation in the time domain (see Eq. (3.10)) of the previous section. This equation involves a time convolution between the function $R(t,t')$ which characterizes how the electron propagates within the target branch, and the correlation function $\varphi_e(t'), \varphi_e(t-\tau_2)^*$ which acts as a kernel describing the imaging characteristics of the radar.

In this analysis, we have assumed that the source S emits a single electron excitation in a pure state characterized by the wave function $\varphi_e(t)$. However, the electron radar equation can be generalized to cover any single electron source, including the ones emitting a single electron excitation in a statistical mixture of pure states. In such a situation, $\varphi_e(t'), \varphi_e(t)^*$ is replaced by the first-order excess single electron coherence $\Delta\mathcal{G}^{(e)}_{\text{S}}\left(t \middle| t'\right)$.

In the end, Eq. (3.29) can be written as:

$$X_+(t) = v_F \int_{\mathbb{R}} R(t,t')\, \Delta\mathcal{G}^{(e)}_{\text{S}}\left(t-\tau_2 \middle| t'\right)\, \mathrm{d}t'\,. \tag{3.30}$$

For the sake of generality, this general form will be used throughout the remainder of this section. This ensures that our treatment is sufficiently general to encompass a variety of electron sources, even imperfect ones.

On a side note, in the spirit of being closer to what can measured experimentally, we have also defined the quantity

$$I_+^{(\mathrm{dc})} = \int_{\mathbb{R}} I_+(t)\,\mathrm{d}t \tag{3.31}$$

which represents the interference contribution to the total charge detected on the output 1 of the MZI. Following the analogy, we can define:

$$X_+^{(\mathrm{dc})} = v_F \int_{\mathbb{R}^2} R(t,t')\varphi_e(t')\,\varphi_e(t-\tau_2)^*\mathrm{d}t\,\mathrm{d}t' \tag{3.32}$$

which expresses the experimental signal $X_+^{(\mathrm{dc})}$ as the linear filtering of the dynamical quantity of interest $R(t,t')$ by a filter which is the excess single electron coherence associated with the wave packet φ_e. It is the signal of interest in an experiment In particular, for a MZI with QPCs with 50 % transmission probability, the average dc current measured when the experiment is repeated at frequency f_d is given by:

$$\langle i_{1_\mathrm{out}}^{(\mathrm{dc})}\rangle = -\frac{e f_\mathrm{d}}{2}\left(1+\Re\left(\mathrm{e}^{\mathrm{i}\phi_{AB}} I_+^{(\mathrm{dc})}\right)\right). \tag{3.33}$$

We will now discuss the time frequency version of the radar equation.

3.2.2 The time frequency domain radar equation

A time frequency form of the single electron radar equation can be obtained by implementing a Fourier transformation on Eq. (3.30) while preserving the integral over $\tau = t - t'$ in the right-hand side of the equation. This leads to

$$\widetilde{X}_+(\omega) = \int_{\mathbb{R}^2} \widetilde{R}(\omega-\Omega,\tau_2-\tau)\,A_\mathrm{S}(\Omega,\tau)\,\mathrm{e}^{\mathrm{i}\frac{(\Omega+\omega)\tau_2-\omega\tau}{2}}\,\frac{\mathrm{d}\Omega\mathrm{d}\tau}{2\pi} \tag{3.34}$$

where we have introduced the time frequency scattering amplitude

$$\widetilde{R}(\Omega,\tau) = \int_{\mathbb{R}} R\left(t+\frac{\tau}{2},t-\frac{\tau}{2}\right)\,\mathrm{e}^{\mathrm{i}\Omega t}\,\mathrm{d}t\,. \tag{3.35}$$

This quantity is best interpreted within the framework of time-dependent single-particle scattering theory if we consider the incoming and outgoing electron modes at fixed energy, denoted by $c_\mathrm{in}(\omega)$ and $c_\mathrm{out}(\omega)$ respectively, which enter and exit the electronic channel of the radiation

coupler. Calculating the outgoing mode in terms of the incoming ones results in the following expression:

$$c_{\mathrm{out}}(\omega) = \int_{\mathbb{R}^2} \frac{\mathrm{d}\Omega\,\mathrm{d}\tau}{2\pi} \mathrm{e}^{i\omega\tau/2} \widetilde{R}(\Omega,\tau) c_{\mathrm{in}}(\omega-\Omega)\,\mathrm{e}^{\mathrm{i}(\omega-\Omega)\tau/2}\,. \tag{3.36}$$

Eq. (3.36) thus shows that $\widetilde{R}(\Omega,\tau)$ is the probability amplitude for an electron entering the target branch with an energy $\hbar(\omega-\Omega)$ to travel during a time of flight $\tau/2$, get a frequency shift of Ω and finally travels during $\tau/2$ at energy $\hbar\omega$. This dependence on Ω and τ contains the information on the energy transfers and effective time of flights experienced by the electrons within the target branch of the MZI under the influence of the radiation sent onto the radiation coupler.

The dimensionless quantity

$$A_{\mathrm{S}}(\Omega,\tau) = v_F \int_{\mathbb{R}} \Delta\mathcal{G}_{\mathrm{S}}^{(e)}\left(t+\frac{\tau}{2}\middle|t-\frac{\tau}{2}\right) \mathrm{e}^{i\Omega t}\,\mathrm{d}t \tag{3.37}$$

is called the *electronic ambiguity function* associated with the source S by analogy with classical signal processing [71] and with classical radar theory (see Sec. 3.1).

More specifically, the experimental signal of the electron radar is a convolution of the scattering amplitude $\widetilde{R}(\Omega,\tau)$ of the region to be probed by the ambiguity function of the source S. A point-like response $\widetilde{R}(\Omega,\tau) = \delta(\tau-\tau_0)\delta(\Omega-\Omega_0)$ corresponding to a ballistic propagation during τ_0 with a given frequency shift $\Omega_0/2\pi$ will be spread by the convolution kernel $A_{\mathrm{S}}(\Omega,\tau)$, thereby justifying its name in the electron quantum optics context. In optical terms, the electronic ambiguity function is the point spread function describing the resolving power of the imaging of $\widetilde{R}(\Omega,\tau)$ by the MZI. Although we've discussed the ambiguity function in the context of single-electron excitations, this concept is not confined to such signals. It can be extended to deal with signals involving multiple charges but the validity of the radar equation (3.34) is limited to the single particle scattering framework.

The form of the single electron radar equation given by Eq. (3.34) is very similar to the original radar equation derived Eq. (3.19). In the usual radar context discussed in Sec. 3.1, the time τ in $\widetilde{R}(\Omega,\tau)$ corresponds to the time to reach a target and come back whereas Ω denotes the Doppler shift during reflection by a moving target.

However, although both equations are derived from a Mach-Zehnder geometry, they should not be confused: contrary to electromagnetic

fields whose average value can be non-zero, fermionic fields have a vanishing quantum average [76, 109, 162]. Consequently, the electronic ambiguity function defined by Eq. (3.37) is not the ambiguity function of a classical signal: it is the fourth representation of the excess single electron coherence. It is thus related by the appropriate Fourier transforms to the time domain representation $\Delta\mathcal{G}_S^{(e)}(t|t')$, the frequency domain representation $\Delta\widetilde{\mathcal{G}}_S^{(e)}(\omega_+|\omega_-)$ and the excess electronic Wigner distribution $\Delta W_S^{(e)}(t,\omega)$ [64].

3.3 The electronic ambiguity function

In this section, we summarize the general properties of the electronic ambiguity function (see Sec. 3.3.1) and then discuss its role as a filter (see Sec. 3.3.2). The experimentally relevant examples of Landau and Leviton wave packets are then discussed in Sec. 3.3.3.

3.3.1 General properties

Exactly as for the electronic Wigner distribution function [64], the ambiguity function satisfies general properties that are always valid. Let us review them now:

Hermiticity and marginals

- *Conjugate symmetric* The hermiticity condition for the single electron coherence $\mathcal{G}_{\rm S}^{(e)}(t|t')$ which leads to the reality of the electronic Wigner distribution, translates into the conjugate symmetric of the ambiguity function with respect to τ and Ω :

$$A_{\rm S}(\Omega,\tau)^* = A_{\rm S}(-\Omega,-\tau) \tag{3.38}$$

- *Electrical current relation* At $\tau = 0$, the excess ambiguity function directly leads to the average finite frequency current

$$\langle i(\Omega)\rangle = -e\, A_{\rm S}(\Omega,\tau=0). \tag{3.39}$$

- *Ambiguity of stationnary and periodic signals* A stationary source such as a dc-bias or, more generally, a non equilibrium electron

distribution function $f_{\mathrm{e}}(\omega) = f_{\mathrm{eq}}(\omega) + \delta f_{\mathrm{e}}(\omega)$ generates a singular ambiguity function concentrated on the $\Omega = 0$ axis:

$$A_{f_{\mathrm{e}}}(\Omega, \tau) = \delta(\Omega) \int_{\mathbb{R}} \delta f_{\mathrm{e}}(\omega)\, \mathrm{e}^{-i\omega\tau}\, \mathrm{d}\omega \tag{3.40}$$

The spreading along the $\Omega = 0$ of the ambiguity function is therefore the coherence time of the excitations generated by the source. Note that for a T-periodic electron source, the ambiguity function is localized on the $\Omega = 2\pi n/T$ ($n \in \mathbb{Z}$) lines.

- *Peak value* The excess single electron coherence $\Delta\mathcal{G}_{\mathrm{S}}^{(e)}(t|t')$ carries information about all single particle excitations emitted by the source. However, the associated ambiguity function doesn't follow the same normalization constraint as an ambiguity function related to a $L^2(\mathbb{R})$ classical signal. Specifically, we have:

$$A_{\mathrm{S}}(\Omega = 0, \tau = 0) = \frac{-\langle Q \rangle}{e} \tag{3.41}$$

where $\langle Q \rangle$ denotes the average total charge injected by the source. The maximum value of the ambiguity function is found when $\tau = 0$ and $\Omega = 0$. Furthermore, if the signal consists of a single, purely electronic excitation, the normalization to unity is restored.

Time-energy uncertainty

The Wigner distribution function and the ambiguity function are both representations used to study the time-frequency characteristics of a signal. However, they exhibit different behaviors, particularly in terms of their spreading properties related to time-energy uncertainty.

The Wigner distribution function is known for its minimal spreading properties, which are intimately related to the Gabor-Heisenberg principle. It states that it is impossible to precisely determine both the energy and the time of a signal simultaneously. The product of the uncertainties in these two measurements is always bounded by a constant. In other words, if you try to confine the signal more in time, it spreads in frequency, and vice versa.

On the other hand, the ambiguity function does not always adhere to this principle. By its construction, the ambiguity function tends to be concentrated near the origin. This means that a signal with a broad frequency range and extended in time will have an ambiguity function

that is localized, both in terms of the absolute time delay $|\tau|$ and the absolute frequency shift $|\Omega|$.

For instance, let's consider the ambiguity function of ideal white noise, a theoretical signal that has infinite duration and infinite bandwidth. In the realm of signal processing, the ambiguity function of such a signal is proportional to $\delta(\Omega)\,\delta(\tau)$. This representation clearly violates the Gabor-Heisenberg principle, as both time and frequency are precisely defined.

Another example is the infinite chirp, a signal whose frequency increases or decreases over time. The ambiguity function of an infinite chirp is concentrated around a single line in the (Ω, τ) plane. This also exhibits localization properties contradicting the Gabor-Heisenberg principle.

In the context of electron quantum optics, these phenomena, namely the randomization effect seen in white noise and the chirping localization effect, are further discussed in Section 3.4. On a side note, these examples illustrate that, while the Wigner distribution and ambiguity functions are powerful tools for understanding the time-frequency characteristics of signals, they offer different perspectives and can exhibit unique behaviors depending on the nature of the signal under examination.

In the specific case of a source emitting precisely one single electron excitation, denoted as φ_e, there are certain properties that the associated ambiguity function, $A_{\varphi_\mathrm{e}}(\Omega, \tau)$, is known to satisfy. These properties, as outlined in the reference [71], are as follows:

$$|A_{\varphi_\mathrm{e}}(\Omega,\tau)| \leq |A_{\varphi_\mathrm{e}}(0,0)| \tag{3.42a}$$

$$|A_{\varphi_\mathrm{e}}(0,0)|^2 = \int_{\mathbb{R}^2} |A_{\varphi_\mathrm{e}}(\Omega,\tau)|^2 \,\frac{\mathrm{d}\Omega\,\mathrm{d}\tau}{2\pi}\,. \tag{3.42b}$$

None of these properties are linear with respect to the ambiguity function. As such, we cannot expect them to be satisfied for a general ambiguity function associated with a state that includes many-particle excitations on top of the Fermi sea. Similarly, these properties may not hold for an imperfect single electron source that samples a statistical ensemble of single electron wave-packets.

3.3.2 The ambiguity function as a filter

We have demonstrated that the single particle scattering matrix of a target is probed with a resolution given by the ambiguity function. Since

τ represents the time of flight of a single electron excitation across the upper branch of the MZI, $\widetilde{R}(\Omega,\tau)$ has non vanishing values for $\tau \in [\tau_{1,\min}, \tau_{1,\mathrm{dec}}]$. $\tau_{1,\min}$ defines the minimal time of flight for the electron to cross the upper branch between the two QPCs, and $\tau_{1,\mathrm{dec}}$ is the decoherence time within the upper branch of the MZI.

Its range in Ω is limited by the inverse of the characteristic time scale associated with the non-stationarity of the incoming radiation. This rectangle in the (Ω,τ) plane, whose precise extension will be discussed below, delimitates the domain of interest where we want to be able to probe the time dependent single particle scattering.

Howoever, because the ambiguity function depends on the single electron sources that we are able to use in experiments which are constrained by the experimental state of the art, it is important to to determine to what extent the experimentally adjustable parameters of realistic single electron sources enable us to explore the physically relevant time frequency range in the (Ω,τ) plane.

In practice, the decoherence time may be within the 100 ps range, which corresponds to a coherence length of approximately 10 µm. Furthermore, there is an interest in probing fast radiations down to time scales ranging from 1 to 10 ps, thereby corresponding to frequencies $\Omega/2\pi$ in the range of 100 GHz to 1 THz.

For an on-demand single electron source, there are a few parameters that can be manipulated to control the properties of the emitted electron wave packet. The emission time t_e is an apparent control parameter, and in some sources, such as the driven mesoscopic capacitor, an energy shift by $\hbar\omega_e$ can be applied to the emitted excitation. Additionally, the internal parameters of the source can provide some control over the envelope of the emitted wave packet.

The injection time and energy shifts (t_e,ω_e) of the single electron probe introduce only a phase factor in front of the ambiguity function. If $\mathrm{S}_{t_e,\omega_e}$ denotes the single electron source shifted by t_e in time and $\hbar\omega_e$ in energy, we can write:

$$A_{\mathrm{S}_{t_e,\omega_e}}(\Omega,\tau) = \mathrm{e}^{\mathrm{i}(\Omega\, t_e - \omega_e \tau)} A_{\mathrm{S}}(\Omega,\tau)\,. \tag{3.43}$$

By tuning t_e and ω_e, we can find the operating point where the phase shift $\mathrm{e}^{\mathrm{i}(\Omega t_e - \omega_e\tau)}$ of the ambiguity function cancels the linear component in (Ω,τ) of the phase factor appearing in the electron radar equation (3.34): $\mathrm{Arg}(\widetilde{R}(\Omega,\tau)) + \frac{\Omega\tau_2 - \omega\tau}{2}$. This linear phase cancellation can be used to optimize the performance of the quantum radar system be-

cause it suppresses the phase averaging in the (Ω, τ) integration in the radar equation (3.34).

These adjustments being done, the electron radar's resolution in the (Ω, τ) plane is given by the close to unity spots of $|A_{\mathrm{S}}(\omega - \Omega, \tau_2 - \tau)|$ when varying the control parameters ω and τ_2. A more quantitative analysis thus requires analyzing the ambiguity functions generated by the available single electron sources before discussing techniques to reshape them in order to extend the exploration range in the (Ω, τ) plane (which will be done in Sec. 3.4).

3.3.3 Examples

In this section, we discuss the ambiguity functions of the single particle excitations generated by the two most commonly used sources in electron quantum optics, *id est* the Landau quasiparticle and the Leviton.

The Landau quasi-particle

The Landau excitation [64] is a Lorentzian wave packet in energy, truncated to energies above the Fermi level:

$$\widetilde{\varphi}_e(\omega) = \frac{\mathcal{N}_e\, \Theta(\omega)}{\omega - \omega_e + \mathrm{i}\gamma_e/2} \tag{3.44}$$

where $\mathcal{N}_e$ ensures normalization, γ_e denotes the inverse of the wave packet's duration and $\hbar\omega_e$ is its emission energy. Landau excitations are emitted by the mesoscopic capacitor in the single electron source regime [70]. When they are in the energy resolved regime ($\gamma_e \ll \omega_e$), the truncation of the wave packet can be neglected. Within this regime, the associated ambiguity function can be approximated by:

$$A_{\mathrm{Lan}}(\Omega, \tau) = \frac{\gamma_e\, \mathrm{e}^{-\gamma_e|\tau|/2}}{\gamma_e - \mathrm{i}\Omega}\, \mathrm{e}^{\mathrm{i}\frac{\Omega|\tau|}{2}}\, \mathrm{e}^{-\mathrm{i}\tau\omega_e}\,. \tag{3.45}$$

Its modulus square has an exponential decay in τ over the time scale $\tau_e = 1/\gamma_e$ and a Lorentzian behavior in Ω over the scale γ_e (see Fig. 3.7).

Thus, the Landau excitation, allows to probe a radiation at a fixed frequency ω_e with a frequency resolution given by γ_e. Both of these parameters can be experimentally shifted over a limited interval which is why this excitation is of particular interest. Typical injection energies are of a few tens of µeV corresponding to $\omega_e/2\pi$ in the 10 to 20 GHz. The linewidth is of the order of the GHz corresponding to a duration of 1 ns [70, 130].

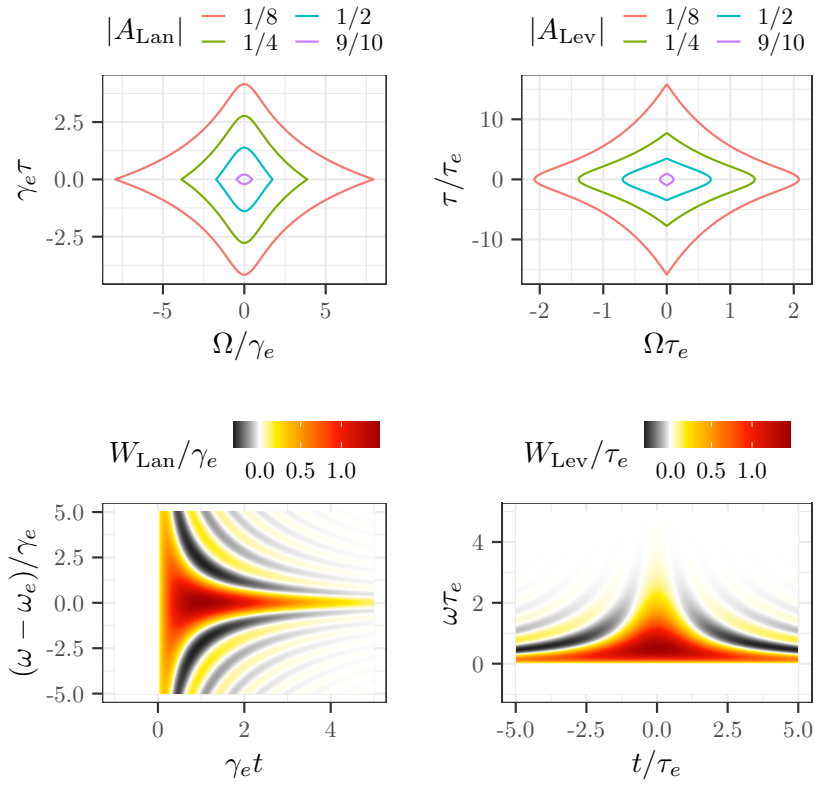

Figure 3.7: Contour plots for $|A(\Omega,\tau)| = 0.9$, 1/2, 1/4 and 1/8: (Top left) Landau excitation for large Ω_e/γ_e, plotted in terms of $(\Omega/\gamma_e, \gamma_e\tau)$; (Top right) Leviton excitation in the variables $(\Omega\tau_e, \tau/\tau_e)$. The difference between the direction of exponential and algebraic decay is quite visible. The corresponding electronic Wigner functions are also depicted on the row below in terms of dimensionless variables: $(\gamma_e t, (\omega-\omega_e)/\gamma_e)$ for the Landau excitation and $(t/\tau_e, \omega\tau_e)$ for the Leviton excitation.

The Leviton excitation

The Leviton [59] consists of a single electron excitation on top of the Fermi sea in a Lorentzian wave packet in position (or equivalently in time) with width τ_e. It is generated by applying a Lorentzian voltage pulse of total charge $-e$ on the Fermi sea [124].

In the context of practical implementations, the typical durations of

a Leviton are in the few tens of picoseconds range [166, 4]. However, advancements in terahertz technology suggest the possibility of generating significantly shorter Leviton pulses in the future [81]. It is worth noting that in order to prevent thermal fluctuations from significantly distorting the Leviton, its duration must be less than $\hbar/k_B T_{\rm el} \simeq 76\,\mathrm{ps}$ at an electronic temperature $T_{\rm el} \simeq 10\,\mathrm{mK}$.

The time-dependent wave function for a Leviton is given by:

$$\varphi_{\rm Lev}(t) = \sqrt{\frac{\tau_e}{\pi v_F}} \frac{1}{t - \mathrm{i}\tau_e} \tag{3.46}$$

and therefore its ambiguity function is given by:

$$A_{\rm Lev}(\Omega, \tau) = \frac{2\tau_e\, \mathrm{e}^{-\tau_e|\Omega|}}{2\tau_e + \mathrm{i}\tau}\, \mathrm{e}^{-\mathrm{i}|\Omega|\tau/2} \tag{3.47}$$

Apart from the phase factor $\mathrm{e}^{-\mathrm{i}\omega_{\rm e}\tau}$, Eqs. (3.45) and (3.47) are related by the duality $\Omega \leftrightarrow -\tau$, $\gamma_{\rm e} \leftrightarrow 2\tau_e$ which, in the limit $\omega_{\rm e} \gg \gamma_{\rm e}$ for the Landau quasi-particle, is expected (see Fig. 3.7).

Compared to the Landau excitation, the Leviton ambiguity function decays more rapidly in Ω for a value of the parameter τ_e. A practical consequence is that probing short time scales with Leviton excitations requires generating really short pulses as we shall see in the next section.

3.4 Shaping the ambiguity function

In this section, we consider the filtering effect associated with the electronic ambiguity function. We begin by discussing the practical limits associated with the Landau and Leviton wave packets taking into account realistic parameters.

Then, in Secs. 3.4.2 and 3.4.3, we discuss how two techniques used in the context of radars and sonars – chirping [116] and randomization [192] – can be adapted in the context of electron quantum optics and offer interesting perspectives for covering the physically relevant range in the (Ω, τ) plane.

3.4.1 Experimental limitations in the time frequency domain

As discussed in Sec. 3.3.2, optimizing the electron radar signal first involves adjusting the injection time t_e and, if possible, the energy $\hbar\omega_e$ in

order to avoid the linear phase averaging between the ambiguity function and the single particle scattering in the radar equation.

Then, one is left with ω which governs ne measurement frequency of the outgoing average electrical current and τ_2 the time delay along the reference branch. Bothe parameters can be adjusted in order to maximize the overlap of the single particle scattering amplitude $\widetilde{R}(\Omega, \tau)$ and the shifted ambiguity function $A_S(\omega - \Omega, \tau_2 - \tau)$ in modulus. In this section, we qualitatively explore this idea to get an image of the region accessible using the Levitov and Landau excitations.

Let us first review the current experimental limitations on the measurement frequency $\omega/2\pi$ and τ_2:

- Current laboratory equipment for measuring the finite frequency average current typically have a maximal bandwidth of 20 GHz.
- The range of accessible values for τ_2 varies between 10 ps to 40 ps, facilitated by a plunger gate proximate to the MZI's reference branch, which can manipulate its length by several hundred nanometers.

We have plotted this region as a rectangle on Fig. 3.8. Note that on this figure, the light red area represents the domain of interest limited by the electronic decoherence time $\tau_{1,\mathrm{dec}} = 100\,\mathrm{ps}$ and the minimal time of flight $\tau_{1,\mathrm{min}} = 10\,\mathrm{ps}$ along the target branch. In the Ω direction, we wish to probe phenomemon with characteristic frequencies up to $|\Omega|/2\pi \lesssim 100\,\mathrm{GHz}$, aligning with the probing of dynamical timescales in the tens of ps.

Figure 3.8 visually represents the overlapping of the physical region of interest with the regions where the Leviton and Landau ambiguity functions are concentrated when using realistic parameters. It shows ambiguity functions for four realistic Levitons in the (Ω, τ) plane, centered at $\omega/2\pi = 10\,\mathrm{GHz}$ and $\tau_2 = 20\,\mathrm{ps}$. The retained value range from 40 ps which is the current state of the art using an adwanced waveform generator [58] of Fourier harmonic synthesis such as in [16]. The lower values of 1 and 2.5 ps require new techniques that are currently under active development [4].

Considering these examples and varying ω and τ_2 within the limits discussed here shows that there is a part of the domain of physical interest that can be probed but that there are also regions which will not be accessible because none of the translated ambiguity functions considered here has significant values there.

Indeed short Leviton excitations ($\tau_e \lesssim 10\,\mathrm{ps}$) are able to reach $\Omega/2\pi$ in the tens of GHz but lack the ability to explore many different values of τ. Excitations with longer durations, such as the Leviton excitation of 40 ps, corresponding to typical parameters in experiments [134], can probe longer propagation times but lack the ability to explore physically relevant information for $\Omega/2\pi \gtrsim 20\,\mathrm{GHz}$ which encodes the short dynamical time scales of the incoming radiation.

In the end, the stripped area in Fig. 3.8 represents the region where it is close to impossible to get any information about the radiation without resorting to other wavepackets. This justifies the search for techniques to shape the ambiguity function in order to obtain information at specific values in Ω and τ.

3.4.2 Randomization

For single electron wave packets $\varphi_e(t) = \mathrm{e}^{-i\omega_e(t-t_e)}\chi_e(t-t_e)$ based on the envelope χ_e but emitted at random times t_e and energies ω_e, the ensemble averaged ambiguity function is related to the ambiguity function A_{χ_e} of the enveloppe through

$$A_{\mathrm{S}}(\Omega,\tau) = \mathbb{E}_{t_e,\omega_e}\left(\mathrm{e}^{\mathrm{i}(\Omega t_e - \omega_e\tau)}\right) A_{\chi_e}(\Omega,\tau)\,. \tag{3.48}$$

Consequently, averaging over the random t_e and ω_e localizes the ambiguity function in the (Ω,τ) plane. In the specific case where $t_e = \bar{t}_e + nT_e$ and $\omega_e = \overline{\omega}_e + m\Omega_e$ where n and m are independent random positive integer valued variables,

$$A_{\mathrm{S}}(\Omega,\tau) = \mathrm{e}^{\mathrm{i}(\Omega\bar{t}_e - \overline{\omega}_e\tau)}\,\widehat{p}_n(\Omega T_e)\,\widehat{p}_m(\Omega_e\tau)\,A_{\chi_e}(\Omega,\tau) \tag{3.49}$$

where $\widehat{p}_n$ and $\widehat{p}_m$ are the characteristic functions of the probability laws of the random integer valued variables n and m. Because we are dealing with integer valued variable, these functions are 2π-periodic which shows that the ambiguity function gets localized around the points of the square lattice defined by $\Omega T_e \in 2\pi\mathbb{Z}$ and $\Omega_e\tau \in 2\pi\mathbb{Z}$. For example, assuming that p_n and p_m are Poisson distributions with respective averages $\overline{n}$ and $\overline{m}$ leads to:

$$|A_{\mathrm{S}}(\Omega,\tau)| = \mathrm{e}^{-2\overline{n}\sin^2\left(\frac{\Omega T_e}{2}\right) - 2\overline{m}\sin^2\left(\frac{\Omega_e\tau}{2}\right)}\,|A_{\chi_e}(\Omega,\tau)|\,. \tag{3.50}$$

Randomized Leviton

As an illustrative example, Fig. 3.9 displays the modulus of the ambiguity function, denoted as $\left|A^{\overline{n}}_{\mathrm{Lev}}(\Omega,\tau)\right|$, for a Leviton emitted at a random

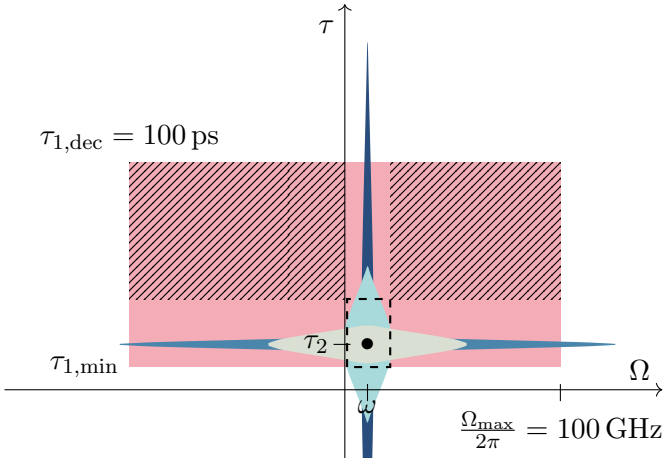

Figure 3.8: Probing $\widetilde{R}(\Omega, \tau)$ using Leviton ambiguity functions. The light red (or pink) rectangular region defines the region where $\widetilde{R}(\Omega, \tau)$ may be non-zero. The variable τ ranges from the shortest time of flight across branch 1, denoted as $\tau_{1,\mathrm{min}}$, to the decoherence time, $\tau_{1,\mathrm{dec}}$. Typical values for these parameters are $\tau_{1,\mathrm{min}} \simeq 10\,\mathrm{ps}$ and $\tau_{1,\mathrm{dec}} \simeq 100\,\mathrm{ps}$. The frequency limit $|\Omega|/2\pi$ is set to be less than 100 GHz, corresponding to probing phenomena on the tens of ps time scale. The ambiguity function $A_{\mathrm{Lev}}(\omega - \Omega, \tau_2 - \tau)$ is centred on the point (ω, τ_2) (indicated by a bullet), where $\omega/2\pi \simeq 10\,\mathrm{GHz}$ and $\tau_2 \simeq 20\,\mathrm{ps}$. The dotted rectangle demarcates the experimentally accessible zone for these parameters: between 1 and 20 GHz for $\omega/2\pi$ and 10 to 40 ps for τ_2. The plots of $|A_S(\omega - \Omega, \tau_2 - \tau)|$ are represented as colored regions bounded by $|A_S(\omega - \Omega, \tau_2 - \tau)| = 1/2$. The four plots correspond to Levitons with durations $\tau_e = 1\,\mathrm{ps}$ (blue), $\tau_e = 2.5\,\mathrm{ps}$ (light grey), $\tau_e = 10\,\mathrm{ps}$ (light blue), and $\tau_e = 40\,\mathrm{ps}$ (dark blue).

time $t_e = \bar{t}_e + nT_e$. Here, n follows a Poissonian distribution centered at $\overline{n}$. The plot showcases three distinct cases: $\overline{n} = 0$, $\overline{n} = 1$, and $\overline{n} = 5$. Note that the Leviton being created just above the Fermi surface, its emission energy cannot be shifted with respect to the Fermi energy. This is why, for Levitons, we only consider randomized emission times.

Since the ambiguity function becomes localized around ΩT_e integer multiples of 2π and because the Leviton's ambiguity functions typically spreads over $\Omega\tau_{\mathrm{Lev}} \lesssim 1$, the scale T_e of random emission times is chosen larger than the duration of the Leviton τ_{Lev} (three times in Fig. 3.9).

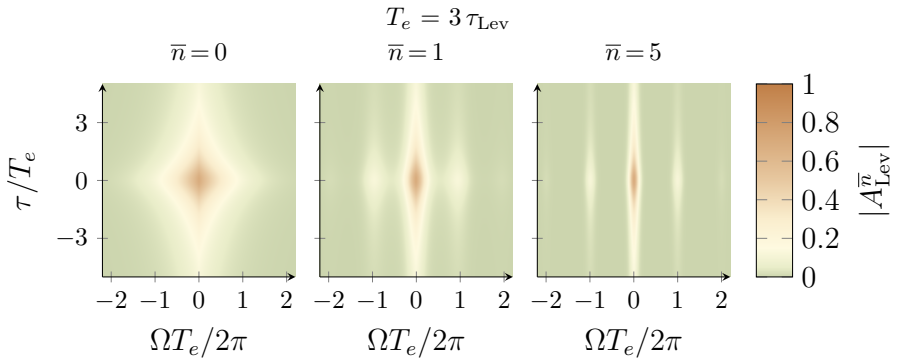

Figure 3.9: The modulus of the ambiguity function of a Leviton emitted at a random time, denoted by $\left|A^{\overline{n}}_{\mathrm{Lev}}(\Omega,\tau)\right|$, is examined in three distinct scenarios: $\overline{n}=0$, $\overline{n}=1$, and $\overline{n}=5$. In each case, the Leviton is randomly emitted at times $t_e = \bar{t}_e + nT_e$, where n follows a Poissonian distribution centered at $\overline{n}$. The horizontal axis represents the dimensionless frequency shift $\Omega T_e/2\pi$, while the vertical axis represents the dimensionless time τ/T_e. The plotted figures correspond to a period $T_e = 3\tau_{\mathrm{Lev}}$ In the scenario of $\overline{n}=0$, which corresponds to the trivial case of a single Leviton emitted at $\overline{t_e}$, the obtained results reproduces with those on Figure 3.7. For non-zero values of $\overline{n}$, $\left|A^{\overline{n}}_{\mathrm{Lev}}(\Omega,\tau)\right|$ becomes localized at Ω values integer multiples of $2\pi/T_e$. As $\overline{n}$ increases, the distribution of $\left|A^{\overline{n}}_{\mathrm{Lev}}(\Omega,\tau)\right|$ becomes sharper around these frequencies.

This guarantees that no more than one Leviton is emitted within each period.

As expected, $\left|A^{\overline{n}}_{\mathrm{Lev}}(\Omega,\tau)\right|$ becomes localized at frequencies Ω that are integer multiples of $2\pi/T_e$ while the temporal spread of the ambiguity function remains unaffected by the temporal randomization. As $\overline{n}$ increases, the distribution of $\left|A^{\overline{n}}_{\mathrm{Lev}}(\Omega,\tau)\right|$ becomes sharper around these frequencies since it reflects the total spreading of the emission time shifts nT_e.

In practice, Levitons in the 1 to 10 ps duration range are immune to thermal noise even while emitted close to the Fermi surface. Randomizing their emission times by integer steps of 100 ps leads to localization of the ambiguity function $A_{\mathrm{S}}(\Omega,\tau)$ around frequencies $\Omega/2\pi$ multiples of 10 GHz which can then be convenient for probing non stationary radiation with characteristic frequencies in the tens of GHz, up to 100 GHz, as expected for such short wave packets.

Randomized Landau particle

To illustrate the effects of randomization along both the time and frequency axis, we have also plotted Fig. 3.10 the modulus of the ambiguity function, denoted as $\left|A^{\overline{n},\overline{m}}_{\text{Lan}}(\Omega,\tau)\right|$, for a Landau particle emitted at a random time $t_e = \bar{t}_e + nT_e$ and a random frequency $\omega_e = \overline{\omega}_e + m\Omega_e$. Randomization of the emission energy is very easy to do for Landau excitation since the emission energy is controlled by the dc voltage applied to the top gate of the mesoscopic capacitor [70]. As in the randomized Leviton example, we have assumed that n and m follow independent Poissonian distributions respectively centred at $\overline{n}$ and $\overline{m}$. The plot showcases the nine configurations of $\overline{n}$ and $\overline{m}$ taking the values 0, 1 and 5.

Exactly as in the Leviton case, the period of random emission T_e is chosen to be three times greater than the temporal width of the Landau particle γ_e^{-1}. The frequency interval of random emission Ω_e is three time greater than the frequency width γ_e so that $2\pi/\Omega_e$ is smaller than the coherence time γ_e^{-1} of the Landau wavepacket. There is some room for such a randomization since one can vary the injection energy over a fraction of the level spacing Δ which is much larger than $\hbar\gamma_e$ without compromising single electron emission by the mesoscopic capacitor.

For Landau quasi-particles, which can be emitted far above the thermal noise energy scale and have durations in the ns range, shifting the emission energy by multiples of 20 µeV will localize the ambiguity function around times separated by multiples of 200 ps.

The results are quite similar to the one obtained for the randomized Levitons. For non zero values of $\overline{n}$ and $\overline{m}$, the ambiguity function get localized around points of coordinates $\left(k\frac{2\pi}{\tau_e}, k'\frac{2\pi}{\Omega_e}\right)$ with k and k' integers. As $\overline{n}$ and $\overline{m}$ increase, the localized peaks become narrower.

The main advantage of randomization is that, by localizing the ambiguity function around certain point, it might help reconstructing the single particle scattering amplitude with better resolution than without using this technique. Let us stress however that it does not extend the region of the (Ω,τ) plane where the ambiguity function has significant values. Therefore, in order to address the issue of unattainable regions discussed in Sec. 3.4.1, a new technique called "'chirping" has to be introduced.

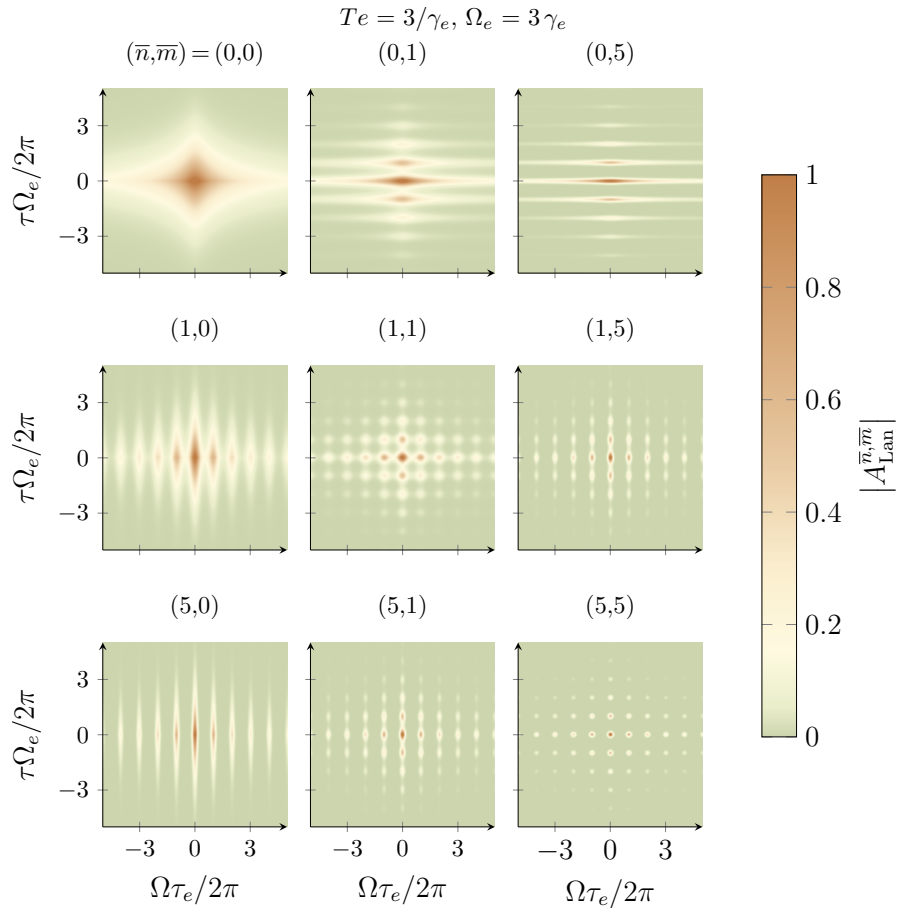

Figure 3.10: Modulus of the ambiguity function of a Landau particule emitted at random time and energy. In each case, the emission is at times $t_e = \bar{t}_e + nT_e$ and frequencies $\omega_e = \overline{\omega}_e + m\Omega_e$, where n and m follows Poissonian distributions centered at $\overline{n}$ and $\overline{m}$, both chosen among 0, 1 and 5. The Ω and τ are made dimensionless with respect to T_e and Ω_e. Here, $\Omega_e = 3\gamma_e$ and $T_e = 3/\gamma_e$.

3.4.3 Chirping

A chirp is defined as an electronic wave packet with a slowly varying envelop χ_e and a carrier whose frequency varies linearly with time:

$$\varphi_{\mathrm{e}}(t) = \chi_e(t)\,\mathrm{e}^{-\mathrm{i}(\omega_e + \kappa t/2)t}\,. \tag{3.51}$$

If we call $A_{\chi_e}(\Omega,\tau)$ the ambiguity function associated to the wave function $\phi_\chi = \chi(t)$, then the ambiguity function of the chirped electronic wave packet becomes:

$$A_{\varphi_e}(\Omega,\tau) = \mathrm{e}^{-\mathrm{i}\omega_e\tau} A_{\chi_e}(\Omega-\kappa\tau,\tau)\,. \tag{3.52}$$

Up to a phase factor $A_{\varphi_e}(\Omega,\tau)$ is the ambiguity function of the envelop χ_e with a Ω dependence shifted by $\kappa\tau$. An envelope χ_e with a narrow ambiguity function in Ω has a limited detection capacity in terms of the energy change $\hbar\Omega$. Nevertheless, because is spread in τ, one can still use it to probe the energy shift by chirping it. Using various values for κ then enables us to span the (Ω,τ) plane in a cone delimited by the maximal and minimal values of $|\kappa|$. The width τ_e of the original ambiguity function A_{χ_e} in τ enables us to access energy changes of the order of $\hbar\kappa\tau_e$. Applying a linear voltage ramp $V_\mathrm{r}(t) = \dot{V}_\mathrm{r}\,t$ leads to $\kappa = e\dot{V}_\mathrm{r}/\hbar$ and $\Omega_\mathrm{max} \sim e\dot{V}_\mathrm{r}\tau_e/\hbar$.

Although applying a linear voltage ramp to electrons generates a quadratically increasing electrostatic phase as in Eq. (3.51), such a phase applies to all the electronic wave function presents in the electronic channel under consideration and therefore may generate electron/hole pair excitations. This method may therefore be relevant for generating chirped excitation from solitary electrons [72] propagating within depleted regions.

For experiments performed in integer quantum Hall edge channels, a possible scheme avoiding the generation of electron/hole pairs maybe to tune the voltage drive applied to a mesoscopic capacitor in the single electron regime in order to directlty generate a chirped-like excitation.

In Ref. [114], Keeling, Shytov and Levitov have proposed a practical way to generate a chirped single electron excitation close to the Fermi surface by considering a resonant level crossing the Fermi sea at constant velocity $\omega_\mathrm{e}(t) = \kappa t$. They have showed that, at zero temperature, a single electron excitation is emitted with electronic wave function in the frequency domain given by[4]

$$\widetilde{\varphi}_\mathrm{KSL}(\omega) = \sqrt{\frac{2\pi\gamma}{v_F\kappa}}\,\Theta(\omega)\,\mathrm{e}^{-\gamma\omega/2\kappa}\mathrm{e}^{-\mathrm{i}\omega^2/2\kappa} \tag{3.53}$$

in which γ denotes the localized level linewidth which is assumed to be constant here. In its Wigner representation, the KSL excitation is

[4]We use our convention for $\tilde{\varphi}(\omega)$ so that the normalization condition (A.7) is satisfied.

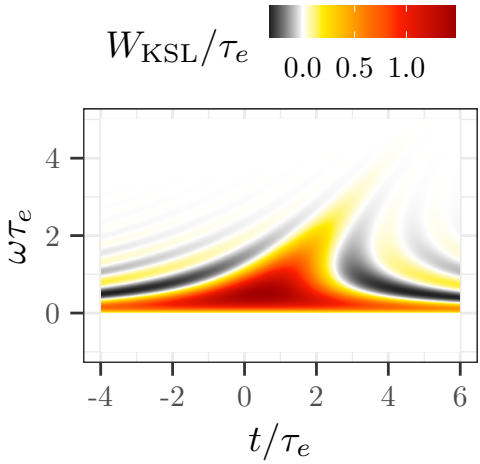

Figure 3.11: Wigner function of a KSL excitation plotted in terms of $(t/\tau_e, \omega\tau_e)$ where $\tau_e = \gamma/2\kappa$. For this example, $\kappa\tau_e^2 = 1$ or equivalently $\kappa = \gamma^2/4$. With $\gamma^{-1} = 40\,\mathrm{ps}$, this would correspond to a voltage ramp of $0.41\,\mathrm{mV\,ns^{-1}}$ and $\tau_e = 20\,\mathrm{ps}$.

a bended Leviton excitation with a time-shift proportional to ω (see Fig. 3.11). Its ambiguity function can be expressed in terms of the one of a Leviton of duration $\tau_e = \gamma/2\kappa$:

$$A_{\mathrm{KSL}}(\Omega, \tau) = A_{\mathrm{Lev},\tau_e}\left(\Omega, \tau - \frac{\Omega}{\kappa}\right). \tag{3.54}$$

Consequently, the range in Ω for this ambiguity function scales as $e\dot{V}_{\mathrm{r}}\tau_e/\hbar$ where as before, $\kappa = e\dot{V}_{\mathrm{r}}/\hbar$. Because most of its weight is located close to the Fermi sea, this excitation cannot be seen as a chirp in the sense of Eq. (3.52). Nevertheless, it also leads to a tilted ambiguity function in the (Ω, τ) plane. This excitation is the closest to a pure electronic chirp that can be generated close to the Fermi surface. In order to be above thermal fluctuations in realistic experimental conditions, τ_e should be kept below 40 ps which, for escape times around 100 ps requires a voltage ramp steeper than $1\,\mathrm{mV\,ns^{-1}}$.

Fig. 3.12 depicts a KSL excitation obtained by driving a resonant level with linewidth $\gamma = 2.5 \times 10^{10}\,\mathrm{s^{-1}}$ ($\gamma^{-1} = 40\,\mathrm{ps}$) with a voltage ramp from 2 to $8\,\mathrm{mV\,ns^{-1}}$. Exploring higher frequencies in Ω requires

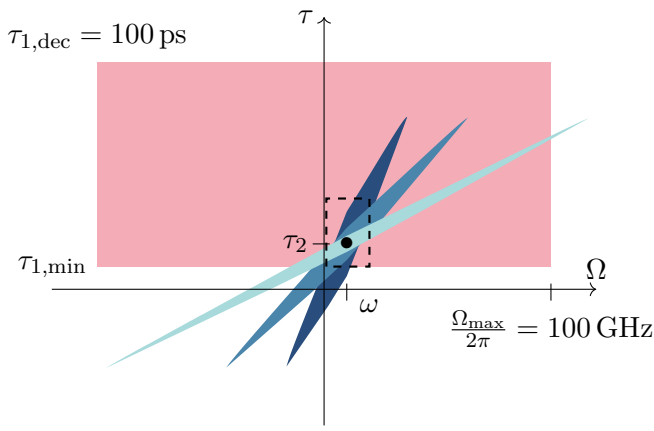

Figure 3.12: Probing the (Ω, τ) plane using KSL excitations at fixed level with width $\gamma^{-1} = 40\,\mathrm{ps}$ for different values of the voltage ramp: $2\,\mathrm{mV\,ns^{-1}}$ (light grey), $4\,\mathrm{mV\,ns^{-1}}$ (grey) and $8\,\mathrm{mV\,ns^{-1}}$ (dark grey). Exactly as in Fig. 3.8, each grey area represents the part of the plane where $|A_{\mathrm{S}}(\Omega, \tau)| \geq 1/2$ and the light red rectangle represents the domain of physical interest. We have assumed that $\omega/2\pi = 10\,\mathrm{GHz}$ and $\tau_2 = 10\,\mathrm{ps}$.

increasing the steepness of the voltage ramp. To keep the same slope in the dimensionless variables $\Omega\tau_e/2\pi$ and τ/τ_e, the level width γ must also be scaled up as $\sqrt{\kappa}$. Since, in experiments, γ^{-1} is of the order of a few tens of ps and the voltage ramp is limited to a few $\mathrm{mV\,ns^{-1}}$, the curves depicted on Fig. 3.12 are probably representative of what could reasonably be achieved with current technology.

Chirping from a Landau excitation which is emitted well above the Fermi sea would enable us to use longer wave packets, from 30 to 200 ps, and therefore would not require such a steep voltage ramp to reach the same range for $\Omega/2\pi$. Fig. 3.13 depicts a 40 ps Landau excitation as well as the result of its chirping using a voltage ramp or $0.5\,\mathrm{mV\,ns^{-1}}$ and $1\,\mathrm{mV\,ns^{-1}}$. Steeper voltage ranges, such as the ones considered for Fig. 3.12 applied to longer wave packets would easily lead to frequencies of several hundreds of GHz. However, as expected from electronic decoherence studies [189, 65, 134], chirped Landau excitations would require a stronger decoherence control between the source generating it and the first beam splitter of the MZI as well as during its propagation within the MZI along the reference branch and outside the radiation coupler.

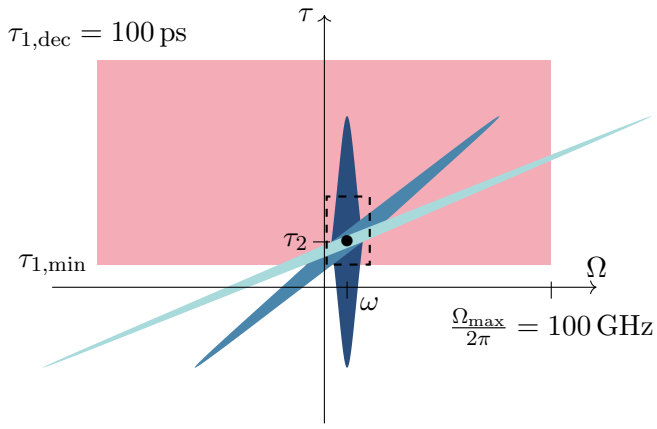

Figure 3.13: Probing the (Ω, τ) plane using a Landau excitation of duration $\tau_e = 40\,\mathrm{ps}$ (light grey) and then chirping it with a voltage ramp of $0.5\,\mathrm{mV\,ns^{-1}}$ (grey) and $1\,\mathrm{mV\,ns^{-1}}$ (dark grey). Exactly as on Fig. 3.8, each grey area represents the part of the plane where $|A_{\mathrm{S}}(\Omega, \tau)| \geq 1/2$ and the light red rectangle represents the domain of physical interest. As on Fig. 3.12, $\omega/2\pi = 10\,\mathrm{GHz}$ and $\tau_2 = 10\,\mathrm{ps}$.

Protection against electronic decoherence can be ensured by blocking energy relaxation into environmental channels [35], an idea which has been successfully implemented in experiments [2, 104, 61] at the price of a more complex sample.

Chapter 4

Electron Radar

Introduction

As explained in the introduction of this thesis, the MZI interferometer can sense the classical phase shift induced by an incident classical radiation. However, this image is not sufficient to discuss how the electronic MZI can probe a quantum radiation. A typical situation where it breaks down is when the incident radiation involves a single photon: absorbing it drastically alters the radiation. Proof that in some situation the backaction of the interferometer on the radiation cannot be neflected. This process may also generate an electron/hole pair in the electronic fluid of the MZI, thereby invalidating the naïve single particle image used to model the electron radar Sec. 3.2. Such a breakdown of single particle physics is a hallmark of Coulomb interaction effects. The issue of backaction and of Coulomb interactions are both addressed in this chapter by presenting a full quantum approach to the electronic MZI in the presence of external quantum radiation.

More precisely, we probe with the radar an incident quantum radiation and we show that, to avoid decoherence effects on the probe, a compromise must be found on the strength of the electron/radiation coupling. The discussion of back-action effects also explains why single electron interferometry is indeed appropriate for probing the quantum state of mesoscopic quantum radiation involving a low average number of photons. The key point is that a probe based on a single electron excitation has a weak enough back-action on the radiation to preserve the interference signal at the output of the MZI, allowing the extraction of some information from the franges.

In order to understand the underlying physics, a qualitative description of interferometric sensing of a quantum system is presented in Sec. 4.1. Then, in Sec. 4.2, the full single electron quantum radar theory is presented. In order to present an intuitive discussion of the main results, the limiting regimes where a time or an energy resolved wavepacket in used as a probe will be discussed in Sec. 4.3. Finally, explicit predictions for classical and quantum external radiations are presented in Sec. 4.4.

4.1 Interferometric sensing of a quantum system

To understand how a quantum interferometer can sense the state of a quantum system coupled to one of its branches, the road we take is based on a generalization of the Elitzur Vaidman bomb detector [62]. As we shall see, this discussion contrains the essential elements to understand the key points in the discussion of the electron radar.

In Elitzur and Vaidman's work, a quantum interferometer is used to detect the presence of a bomb without triggering its explosion. The bomb's trigger is activated as soon as a particle travels across branch 1 of the interferometer (see Fig. 4.1). This assumes that the bomb's trigger is a perfectly efficient particle detector. The idea is then to tune the optical paths of the MZI so that, in the absence of the bomb, the particle exits on one of its outgoing branch but not in the other. In the presence of the bomb, the particle exits with probability 1/4 in the branch where it would never exit in the absence of the bomb. This provides a sure diagnostic of its presence without interacting with its trigger, hence the commonly used term "interaction free measurement" to describe this process.

However, in the present context, we are interested into exploiting the interaction between the particle and the bomb's trigger to gain information about the quantum state of the latter. It calls for a more detailed model of interaction between the probe and the bomb trigger.

Initially in the $|\text{Idle}\rangle$ state, the bomb associated with its trigger has a richer dynamics. We denote by $\mathcal{A}_0$ the amplitude for the trigger to absorb the incoming particle, initially in the $|\Psi\rangle$, and detonate the bomb which then ends in the $|\text{Exploded}\rangle$ state. Assuming $|\mathcal{A}_0|^2 = 1$ is equivalent to consider the model of the dectector imagined by Elitzur and Vaidman. To take in account the non-destructive interactions we must

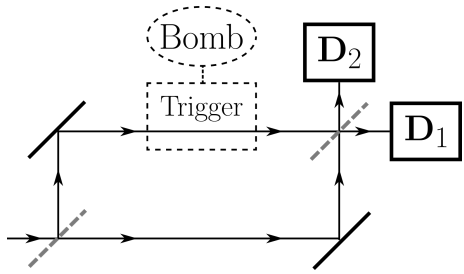

Figure 4.1: The Elitzur-Vaidman's interferometer: in the absence of the bomb, this single photon Mach-Zenhder interferometer is calibrated so that there is no click in $\mathbf{D}_2$. In the presence of the bomb, the trigger absorbs an incident photon with 100% efficiency and detonates the bomb. Interferences are destroyed and there is a probability 1/4 for the travelling particles to be detected by $\mathbf{D}_2$.

allow the possibility of fizzling described by a non vanishing amplitude $\mathcal{A}_1$. The bomb and its trigger end-up in the fizzled state $|\text{Fizzled}\rangle$, when the probing particle interacts with the trigger but the latter one fails to detect it. In this process, the particle is nevertheless affected and ends into the $|\Psi'\rangle$ state. The probabilities for these two alternatives sum to unity: $|\mathcal{A}_0|^2 + |\mathcal{A}_1|^2 = 1$. The full interaction between the particle and the bomb is then described by the quantum coherent process

$$\begin{aligned} |\Psi\rangle \otimes |\text{Idle}\rangle \longrightarrow \mathcal{A}_0\, |\emptyset\rangle \otimes |\text{Exploded}\rangle \\ + \mathcal{A}_1\, |\Psi'\rangle \otimes |\text{Fizzled}\rangle \end{aligned} \tag{4.1a}$$

in which $|\emptyset\rangle$ denotes the vacuum state (the particle has been absorbed). For balanced beam splitters, the conditional output probabilities are then given by the following expressions :

$$p(\text{No Particle}) = \frac{1}{2}(1 - |\mathcal{A}_1|^2) \tag{4.2a}$$

$$p(\mathbf{D}_1) = \frac{1}{4}(1 + |\mathcal{A}_1|^2) - \mathcal{P}_\text{q} \tag{4.2b}$$

$$p(\mathbf{D}_2) = \frac{1}{4}(1 + |\mathcal{A}_1|^2) + \mathcal{P}_\text{q} \tag{4.2c}$$

in which quantum interference effects are contained in the term

$$\mathcal{P}_\text{q} = \frac{1}{2}\Re\left(\mathcal{A}_1 \mathrm{e}^{\mathrm{i}\phi_\text{AB}}\, \langle\text{Idle}|\text{Fizzled}\rangle\, \langle\Psi|\Psi'\rangle\right) \tag{4.3}$$

which is sensitive to the (Aharonov-Bohm) phase difference $\phi_{\rm AB}$ associated with free propagation along the two branches of the MZI. $p(\mathbf{D}_i)$ indicates the conditional probabilty to detect the particle in the ith detector. Note that information on the quantum state of the bomb is contained in the product of the two overlaps $\langle\Psi|\Psi'\rangle$ and $\langle$Idle$|$Fizzled$\rangle$. When the bomb is viewed as a classical object whose physical state is unaltered by the interferometer, $|$Idle$\rangle$ and $|$Fizzled$\rangle$ just differ by a phase. We are then left with a simpler version of Eq. (4.3) which only depends on this relative phase, as well as of the scattering amplitude $\langle\Psi|\Psi'\rangle$ associated with propagation within the interferometer in the presence of this classical object.

From our perspective, the bomb plays the role of the incoming electromagnetic radiation and the particle is the quantum electrical current propagating within the MZI. The process in which the particle is absorbed and the bomb is detonated corresponds to a full electronic decoherence within the MZI. It occurs whenever Coulomb interactions lead to the generation of any extra electron/hole pair within the channel 1 of the MZI compared to ballistic propagation along channel 2. The resulting many-body state will then have a vanishing overlap with the ballistic propagation of a single electron excitation within branch 2 of the MZI. However, this is not the case of interest for the electron radar since, in this case, the interference contribution to the average electrical vanishes and, as in the Elitzur-Vaidman case, nothing can be learned on the quantum state of the incoming radiation.

By contrast, in the absence of generation of any extra electron/hole pair particles, the state of the electron propagating within branch 1 is altered by its coupling to the incoming radiation: this corresponds to the change $|\Psi\rangle \mapsto |\Psi'\rangle$ in the above discussion. For a classical radiation, this is the phase shift associated with the voltage experienced by the electrons (see Sec. 0.2.1).

Finally, the alteration of the bomb's state $|$Idle$\rangle \mapsto |$Fizzled$\rangle$ in the above discussion corresponds to the effect of the propagating electron on the incident radiation in the situation where no extra-electron/hole pairs are created. This is the back action of the interferometer, seen as a measurement device, on the radiation. The amplitude $\langle$Idle$|$Fizzled$\rangle$ measures the "quantum recoil" of the radiation upon propagation of a single electron and assuming that no extra electron/hole pair excitations are generated along branch 1. As we shall see in Sec. 4.2.2, this is precisely the part that will contain information on the quantum fluctuations

of the incoming radiation.

It is important to notice that when the back-action is too large, the overlap $\langle \text{Idle}|\text{Fizzled}\rangle$ may vanish and the interference signal is then lost. This point explains why quantum electrical currents carrying a single electronic excitations are relevant for probing mesoscopic quantum electromagnetic fields which involve a low average number of photons: besides decoherence which is generically less important for them, single electron currents lead to a smaller back-action than currents carrying more excitations.

In the end, this qualitative discussion suggests that, in order to be able to extract some information on the incoming radiation, a compromise is required: electronic decoherence as well as back-action on the quantum radiation has to be moderate to ensure an experimentally accessible experimental signal but strong enough to ensure sensitivity to the incoming quantum radiation.

4.2 The single electron radar equation

In this section, we derive the central result of this work which is the single electron radar equation expressing the interference contribution to the outgoing average current in terms of two distinct quantities. The first one is the excess single electron coherence of the injected wave packet which depends only on the electronic source S. The second one is the effective single particle scattering amplitude describing both the effects of electronic decoherence and of the incoming radiation. The latter quantity reflects the dynamics of the interferometer coupled to its electromagnetic environment.

Although this result is formally derived using bozonization of chiral quantum Hall edge channels detailed in Appendix B.2, a more intuitive derivation is presented in Sec. 4.2.2. Then, its connexion to a variant of Full Counting Statistics will be detailed in Sec. 4.2.3. But before this, let us briefly recall the framework used to model the radiation coupler which was presented in Chapter 2 of this thesis.

4.2.1 Radiation coupler modeling

We assume that the radiation coupler involves a capacitive coupling between a portion of the upper branch of the electronic MZI and the external radiation channel which is fed by the incoming electromagnetic radiation we want to study. Effect of Coulomb interactions within this

region will be described within the framework of edge-magnetoplasmon scattering. Originally introduced in the context of finite frequency quantum transport in 1D [168, 167, 169], it enables us to describe the scattering between the EMP modes propagating along the MZI upper edge channel and the bosonic modes within the external radiation channel [52].

For simplicity, we will consider that the whole upper branch of the MZI is included in the radiation coupler so that the EMP scattering matrix will account for the detailed geometry of the sample. We also assume that only the EMP modes associated with the $b(\omega)$ and $b^\dagger(\omega)$ destruction and creation operators and the external radiation modes associated with the $a(\omega)$ and $a^\dagger(\omega)$ operators appear in the scattering matrix $S(\omega)$:

$$\begin{pmatrix} a_{\rm out}(\omega) \\ b_{\rm out}(\omega) \end{pmatrix} = \begin{pmatrix} S_{aa}(\omega) & S_{ab}(\omega) \\ S_{ba}(\omega) & S_{bb}(\omega) \end{pmatrix} \begin{pmatrix} a_{\rm in}(\omega) \\ b_{\rm in}(\omega) \end{pmatrix} . \tag{4.4}$$

As discussed in detail in Chapter 2, depending on the design of the radiation coupler, the $(a, a^\dagger)$ modes may be photonic (case of Fig. 4.2-(b)) or edge-magnetoplasmonic (see Fig. 4.2-(a)). Note that these matrix elements are related to finite frequency admittances as explained in Refs. [168, 167, 53]. Consequently, these matrix elements could, in principle, be inferred from experimental measurements as in Ref. [22]. Quantitative predictions can also be made from theoretical models of the radiation coupler. Experimentally relevant examples include the case of two counter-propagating edge channels (see Fig. 4.2-(a)) as well as the case of a capacitive coupling to a transmission line (see Fig. 4.2-(b)).

4.2.2 The single electron radar equation

The discussion of Sec. 4.1 suggests that, in the presence of Coulomb interactions and of an incoming quantum radiation, the result takes the same form than Eq. (3.29) with an effective single electron scattering amplitude $R_{\rm eff}(t, t')$. This amplitude takes into account decoherence effects as well as the electron's back-action on the incoming quantum radiation. The formal derivation of this fact is given in Appendix B.2. However, to emphasize its physical meaning, we will acquire the form of the effective scattering amplitude $R_{\rm eff}(t, t')$ using semi-qualitative arguments in this section.

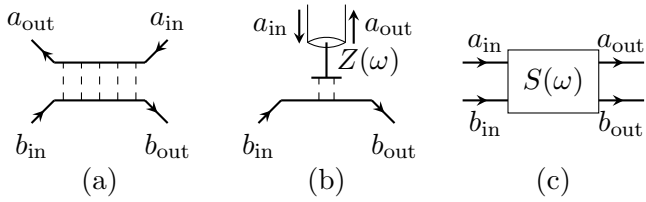

Figure 4.2: The edge-magnetoplasmon scattering approach describes many situations, such as for example (a) two counter-propagating edge channels capacitively coupled over a distance l, (see Fig. 4.4 for a realistic sample design), (b) a chiral edge channel capacitively coupled to a linear external circuit described by a frequency dependent impedance $Z(\omega)$. (c) Solving the equation of motions leads to a frequency dependent scattering matrix $S(\omega)$ between the channel's edge-magnetoplasmon modes and the bosonic modes of the other system.

Electronic Decoherence In the absence of incoming electromagnetic radiation, the amplitude $R_{\rm eff}(t,t')$ is the amplitude for a single electron to propagate elastically across the branch 1, taking into account the capacitive coupling to the radiation coupler's radiation channel. Any process leading to the generation of an extra electron/hole pair within the edge channel or of an excitation within the electromagnetic environment would lead to decoherence in the MZI. This elastic scattering amplitude has already appeared in studies of electronic decoherence in the MZI [42, 126, 144, 145]. In Ref. [160], electronic decoherence in MZI has been experimentally simulated by coupling an external voltage probe which consisted of an Ohmic contact connected to one branch via a QPC. This device probes which path is taken by the electrons propagating within the MZI, thereby showing a reduction of the interferometer's contrast when looking at the amplitude (square root of the probability) for the electron to be transmitted across the probed area.

Then without radiation, $R_{\rm eff}(t,t')$ should be the elastic scattering amplitude for an incoming single electron excitation injected at time t' in the presence of the Fermi sea to exit at time t without experiencing any inelastic scattering: $R_{\rm eff}(t,t') = \Theta(t-t')\,\mathcal{Z}_1(t-t')$ where

$$\mathcal{Z}_1(\tau) = \int_0^{+\infty} \widetilde{\mathcal{Z}}_1(\omega)\,\mathrm{e}^{-\mathrm{i}\omega\tau}\frac{\mathrm{d}\omega}{2\pi}\,. \tag{4.5}$$

is the Fourier transform of the elastic scattering amplitude $\widetilde{\mathcal{Z}}_1(\omega)$ for a single electron of energy $\hbar\omega > 0$ to cross branch 1 of the MZI without

being altered. Thus $\widetilde{\mathcal{Z}}_1(\omega)$ is called the elastic scattering amplitude associated with branch 1 of the MZI. This quantity, computed in Refs. [52, 93, 35], has recently been reconsidered in the light of new experimental studies of electronic relaxation [183, 159, 157]. As shown in Appendix B.2, an explicit expression in terms of the EMP transmission amplitude $t(\omega) = S_{bb}(\omega)$ can be obtained:

$$\mathcal{Z}_1(\tau) = \frac{1}{2\pi \mathrm{i}(\tau - \mathrm{i}0^+)} \exp\left[\int_0^{+\infty} (t(\omega) - 1)\mathrm{e}^{-\mathrm{i}\omega\tau} \frac{\mathrm{d}\omega}{\omega}\right] . \tag{4.6}$$

Going back to the discussion of Sec. 4.1, $\mathcal{Z}_1(\tau)$ corresponds to the product $\mathcal{A}_1 \langle\Psi|\Psi'\rangle \langle\mathrm{Idle}|\mathrm{Fizzled}\rangle$ when the radiation channel is fed with the vacuum state: $|\mathrm{Idle}\rangle = |0\rangle$.

Back-action factor We now have to discuss the back-action of an electron's detection in the presence of incoming radiation. For now on, we will consider the effect of the single electron current on the incoming quantum radiation. An electron leaving the radiation coupler at time t corresponds, in terms of EMP, to a localized current pulse coming out of the target branch of the MZI. Such a current pulse comes from an incoming pulse in the target branch of the MZI as well as a coherent pulse in the radiation channel whose amplitudes are determined via the EMP scattering matrix $S(\omega)$ of the radiation coupler and the amplitude of the outgoing EMP $b_{\mathrm{out}}(\omega)$. Indeed, denoting by $\Lambda_t(\omega) = -\mathrm{e}^{\mathrm{i}\omega t}/\sqrt{\omega}$ the amplitude of the mode $b_{\mathrm{out}}(\omega)$, the average amplitudes of the incoming modes associated a localized current pulse going out of the target branch of the MZI at time t are given by:

$$\langle b_{\mathrm{in}}(\omega)\rangle = S^*_{bb}(\omega)\, \Lambda_t(\omega) \tag{4.7a}$$

$$\langle a_{\mathrm{in}}(\omega)\rangle = S^*_{ba}(\omega)\, \Lambda_t(\omega)\,. \tag{4.7b}$$

Detecting an electron leaving the upper branch of the MZI at a given time t thus corresponds to detecting a an electron together with an electron/hole pair cloud described by $S^*_{bb}(\omega)\, \Lambda_t(\omega)$. It also translates the average $a_{\mathrm{in}}(\omega)$ by $S^*_{ba}(\omega)\, \Lambda_t(\omega)$. This translation is the "back-action" on the radiation mode $a(\omega)$ of a single electron detection at time t at the output of the target branch. To get the full back action, we have to take into account all the modes at pulsation $\omega \geq 0$. The operator describing the full back action process is thus the infinite dimensional displacement operator $D_{a_{\mathrm{in}}}[S^*_{ba}\Lambda_t]$ associated with the amplitude $\omega \mapsto (S^*_{ba}\Lambda_t)(\omega)$. The full back-action factor is then $\langle D_{a_{\mathrm{in}}}[S^*_{ba}\Lambda_t]\rangle_{\rho_{\mathrm{em}}}$: the average value

of $D_{a_{\rm in}}[S^*_{ba}\Lambda_t]$ in the reduced density operator $\rho_{\rm em}$ describing the state of the incoming quantum radiation. The amplitude $R_{\rm eff}(t,t')$ is thus proportional to $\langle D_{a_{\rm in}}[S^*_{ba}\Lambda_t]\rangle_{\rho_{\rm em}}$. However, we should not forget that the elastic scattering amplitude $\mathcal{Z}_1(\tau)$ already includes the back action factor $\langle D_{a_{\rm in}}[S^*_{ba}\Lambda_t]\rangle_{|0\rangle}$ on the vacuum state $|0\rangle$. This one need to be removed by dividing $R_{\rm eff}(t,t')$ with $\langle D_{a_{\rm in}}[S^*_{ba}\Lambda_t]\rangle_{|0\rangle}$, leading to ($\tau = t - t'$):

$$R_{\rm eff}(t,t') = \mathcal{Z}_1(\tau)\,\frac{\langle D_{a_{\rm in}}[S^*_{ba}\Lambda_t]\rangle_{\rho_{\rm em}}}{\langle D_{a_{\rm in}}\left[S^*_{ba}\Lambda_t\right]\rangle_{|0\rangle}}\,. \tag{4.8}$$

We define the ratio of $\langle D_{a_{\rm in}}[S^*_{ba}\Lambda_t]\rangle_{\rho_{\rm em}}$ to $\langle D_{a_{\rm in}}[S^*_{ba}\Lambda_t]\rangle_{|0\rangle}$ as the Franck-Condon factor $\mathcal{F}_{\rho_{\rm em}}(t)$. It is the excess back-action on the incoming radiation induced by a single electron excitation propagating across the upper branch of the MZI. It is equal to the average value of the bosonic normal ordered back-action displacement operator:

$$\mathcal{F}_{\rho_{\rm em}}(t) = \Big\langle :D_{a_{\rm in}}[S^*_{ba}\Lambda_t]: \Big\rangle_{\rho_{\rm em}}\,. \tag{4.9}$$

which justify the analogy with the Franck-Condon factor that appears in the spectroscopy of complex molecules [49] or in the Mössbauer effect [175, 188] where it is called the Lamb–Mössbauer factor.

Effective single particle scattering amplitude The quantum interference contribution to the average outgoing electrical current then has the form

$$X_+(t) = v_F\int_{-\infty}^{t} R_{\rm eff}(t,t')\,\varphi_e(t')\,\varphi_e(t-\tau_2)^*\,{\rm d}t' \tag{4.10}$$

in which the effective single particle scattering amplitude is given by

$$R_{\rm eff}(t,t') = \mathcal{Z}_1(t-t')\mathcal{F}_{\rho_{\rm em}}(t)\,. \tag{4.11}$$

Exactly as in the single particle approach, when repeated experiments are performed, statistical fluctuations in the imperfect emission of single electron excitations are accounted for by replacing $\varphi_e(t')\varphi_e(t-\tau_2)^*$ by the excess single electron coherence $\Delta\mathcal{G}^{(e)}_S(t'|t-\tau_2)$ emitted by S. Eq. (4.10) can then be interpreted as described on Fig. 4.3.

Expression (4.11) takes into account electronic decoherence and the effect of the incoming quantum radiation. Together with the expressions for $\mathcal{Z}_1(\tau)$ and for the Franck-Condon factor, Eqs. (4.10) and (4.11) form

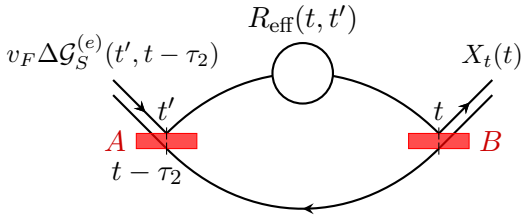

Figure 4.3: Physical interpretation of the linear radar equation (4.10) in the time domain showing the contribution of incoming single electron coherence in the frequency domain to the signal the temporal signal $X_+(t)$. The figure presents the product of two quantum amplitude: the one with an arrow oriented away from the source corresponds for a direct amplitude whereas the one, with the arrow arriving to the source corresponds to the complex conjugated amplitudes contributing to $X_+(t)$.

the central result of the single electron radar theory. The factorized form of the r.h.s. of Eq. (4.11) has an important consequence: the Franck-Condon factor appears as the ratio of the electron radar signal in the presence of external radiation to the one in the absence of it:

$$\frac{[X_+(t)]_{\rho_{\rm em}}}{[X_+(t)]_{|0\rangle}} = \mathcal{F}_{\rho_{\rm em}}(t)\,. \tag{4.12}$$

If we are able to measure the time resolved average current $\langle i_{1_{\rm out}}(t)\rangle$, this would give us a direct access to the Franck-Concon factor but, in experiments, the average current is measured at a given frequency and, when looking for the best sensitivity and precision, at zero frequency. We will thus have to analyze what information on $\mathcal{F}_{\rho_{\rm em}}(t)$ can be recovered from such measurements.

4.2.3 Connection to full counting statistics

Before discussing specific examples in the next section of this chapter, let us close the general discussion of the single electron radar equation by making an explicit connection between the work presented here and a paper by C. Flindt and his collaborators [51] who have proposed to use an electronic MZI to measure the so-called full counting statistics originally introduced in Ref. [124] (see also [143, 117] for more advanced discussions and examples).

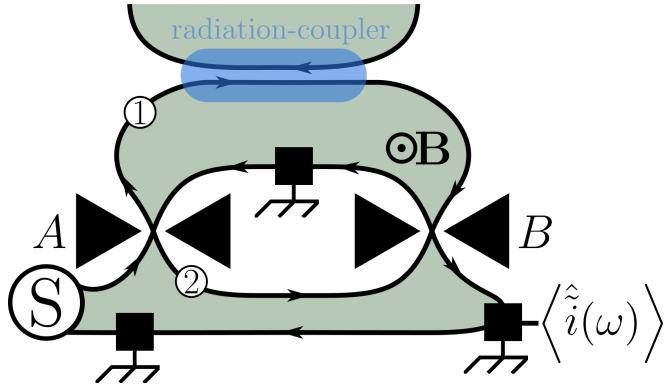

Figure 4.4: Sample design of the electron radar using chiral edge channels in the integer quantum Hall regime (2DEG in green). The blue region where two counter-propagating quantum Hall edge channels are facing each other at short ($\lesssim 100\,\mathrm{nm}$) distance forms a radiation coupler between the channel 1 of the MZI and the radiation channel in which the radiation to be analyzed is sent. The quantity of interest is the average outgoing current from the MZI and more precisely the first harmonic in the Aharonov-Bohm phase.

More precisely, in the context of experiments performed on AlGaAs/AsGa systems in the quantum Hall regime, the radiation channel may also be a chiral quantum Hall edge channel, as depicted on Fig. 4.4. In this case, the Franck-Condon factor $\mathcal{F}_{\rho_{\mathrm{em}}}(t)$ can be interpreted in terms of a form of full counting statistics for electronic transport in the radiation channel as was noticed in Ref. [51]. This work relied on a specific interaction model as well as on single particle scattering. We generalize this work here with a full many body derivation independent on the details of the Coulomb interaction model.

When the radiation channel is a single integer quantum Hall edge channel, the incoming electrical current arriving into the interaction region via this edge channel is, for $\omega > 0$:

$$i_{\mathrm{in}}(\omega) = -e\sqrt{\omega}\, a_{\mathrm{in}}(\omega) \tag{4.13}$$

Introducing the filtering function

$$\Gamma_{ba}(\tau) = \int_0^{+\infty} \frac{S_{ba}(\omega)}{-\mathrm{i}\omega}\, \mathrm{e}^{-i\omega\tau} \frac{\mathrm{d}\omega}{2\pi} + \mathrm{c.c.} \tag{4.14}$$

we define the normalized filtered charge operator

$$N(t) = \int_{\mathbb{R}} \Gamma_{ba}(t-\tau)\, \frac{i_{\rm in}(\tau)}{-e}\, {\rm d}\tau\,, \tag{4.15}$$

where $\tau \mapsto \Gamma_{ba}(t-\tau)$ can be viewed as a windowing function. $N(t)$ can be used to provide a compact expression of $\mathcal{F}_{\rho_{\rm em}}(t)$:

$$\mathcal{F}_{\rho_{\rm em}}(t) = \Big\langle :\, {\rm e}^{2\pi {\rm i} N(t)}\, : \Big\rangle_{\rho_{\rm em}}\,. \tag{4.16}$$

The $2\pi N(t)$ operator represents the quantum phase kicks felt by a localized electron propagating within the MZI. Note that the exponential of this quantum phase kick operator is normal ordered with respect to the bosonic modes $a_{\rm in}(\omega)$. It is possible to relate this normal ordering to the usual time ordering in full counting statistics. It would provide a precise connexion between $2\pi N(t)$ and the time ordered electrical current correlators.

Finally, let us comment on the interpretation of the windowing function $\Gamma_{ba}(t-\tau)$. Defining $\widetilde{\Gamma}_{ba}(\omega)$ as the Fourier transform of $\Gamma_{ba}(\tau)$, we end up with the relation $\widetilde{\Gamma}_{ba}(\omega) = {\rm i}S_{ba}(\omega)/\omega$ for $\omega > 0$. $\widetilde{\Gamma}_{ba}(\omega)$ is thus directly proportional to the non diagonal coefficient of the EMP scattering matrix $S_{ba}(\omega)$. Associating this relation with the one between the EMP scattering matrix and finite frequency admittances reviewed in Chapter 2 leads to

$$\Gamma_{ba}(\omega) = \frac{S_{ba}(\omega)}{-{\rm i}\omega} = \frac{R_K}{-{\rm i}\omega}\, \frac{\partial I_b^{(\rm out)}(\omega)}{\partial V_a^{(\rm in)}(\omega)} \tag{4.17}$$

in which $I_b^{(\rm out}(\omega)$ denotes the average total current going out from the radiation coupler in the upper channel of the MZI – the propagation channel for the b EMP modes – and $V_a^{(\rm in)}(\omega)$ denotes a classical voltage drive applied at the entrance of the radiation channel – the propagation channel for the a EMP modes –. This equation thus connects $\Gamma_{ba}(\omega)$ to the finite frequency admittance of the electrical dipole associated with the radiation coupler. Since the coupling is purely capacitive, one expects this finite frequency response to be capacitive. It of the form

$$\frac{\partial I_b^{(\rm out)}(\omega)}{\partial V_a^{(\rm in)}(\omega)} = -{\rm i}\omega\, C_{ba}^{(\rm eff)}(\omega) \tag{4.18}$$

in which the effective frequency-dependant capacitance $C_{ba}^{(\mathrm{eff})}(\omega)$ is non zero in the low frequency limit. Consequently $\Gamma_{ba}(\tau)$ appears as the effective response rate associated with this capacitance

$$\Gamma_{ba}(\tau) = \int_0^{+\infty} R_K C_{ba}^{(\mathrm{eff})}(\omega)\, \mathrm{e}^{-\mathrm{i}\omega\tau} \frac{\mathrm{d}\omega}{2\pi} + \mathrm{c.c.} \tag{4.19}$$

The matrix element $S_{ba}(\omega)$ of a radiation coupler made of two ungated counter-propagating edge channels of length l that are capacitively coupled to one another is computed in Sec. 2.4. In the limit $C_g \ll e^2 l/hv_F$, we get:

$$\Gamma_{ba}(\tau) \simeq \frac{1}{2}\, \mathbf{1}_{[0,l/v_F]}(\tau)\,, \tag{4.20}$$

where $\mathbf{1}_{[0,l/v_F]}(t)$ is 1 for $0 \leq t \leq l/v_F$ and zero otherwise. The case of non vanishing values of C_q/C_g can be treated numerically when needed.

4.3 Limiting regimes of the single radar equation

We now discuss the limiting regimes of a time or of a frequency resolved single electron excitation. The resulting limiting form of the electron radar equation will be relevant whenever the time (resp. frequency) extension of the probe is much smaller than the typical time (resp. frequency) length scales of the effective scattering matrix. As expected, time resolved wave packets are well suited to explore the time dependance of the scattering whereas energy resolved excitations gives access to the scattering amplitude in the frequency domain.

4.3.1 Energy resolved wave packets

Injecting energy resolved wavepackets suggests that we can indeed study energy transfers between the single electron and the radiation in the radiation coupler. To understand this more precisely, let us introduce the scattering amplitude represented in the frequency-frequency domain:

$$\widetilde{R}(\omega_+, \omega_-) = \int_{\mathbb{R}^2} R(t,t')\, \mathrm{e}^{\mathrm{i}(\omega_+ t - \omega_- t')} \mathrm{d}t\, \mathrm{d}t'\,. \tag{4.21}$$

It can be defined in the same way for the effective scattering amplitude $\widetilde{R}_{\mathrm{eff}}(\omega_+, \omega_-)$. It is is directly proportional to the amplitude probability

of an electron entering the radiation coupler at energy $\hbar\omega_-$ to leave it at energy $\hbar\omega_+$. Denoting by $\widetilde{X}_+(\omega)$ the Fourier transform of the signal $X_+(t)$ at frequency $\omega/2\pi$, the radar equation (4.10) then takes the form

$$\widetilde{X}_+(\omega) = \int_{\mathbb{R}^2} v_F \widetilde{\Delta\mathcal{G}}^{(e)}_{\rm S}(\omega_-, \omega_+ - \omega) \\ \mathrm{e}^{\mathrm{i}(\omega-\omega_+)\tau_2} \widetilde{R}_{\rm eff}(\omega_+, \omega_-) \, \frac{\mathrm{d}\omega_+ \, \mathrm{d}\omega_-}{(2\pi)^2} \tag{4.22}$$

in which $\Delta\widetilde{\mathcal{G}}^{(e)}(\omega_-|\omega_+)$ denotes the excess single electron coherence in the frequency domain:

$$\widetilde{\Delta\mathcal{G}}^{(e)}_\rho(\omega_+, \omega_-) = \int_{\mathbb{R}^2} \mathrm{e}^{\mathrm{i}(\omega_+ t_+ - \omega_- t_-)} \Delta\mathcal{G}^{(e)}_\rho(t_+, t-) \, \mathrm{d}t_+ \mathrm{d}t_- \, . \tag{4.23}$$

Expression (4.22) determines the interference contribution to the finite frequency average electrical current in the $1_{\rm out}$ branch of the MZI.

The physical interpretation of Eq. (4.22) is quite clear: for $\omega > 0$, the average finite frequency current $\langle i_{1_{\rm out}}(\omega)\rangle$ probes the outgoing electronic coherence between two frequencies ω_+ and $\omega_+ - \omega$. The last one is the frequency at which the electronic excitation is propagating along the branch 2 of the MZI. It propagates during a time of flight τ_2, hence picking a phase $\mathrm{e}^{\mathrm{i}(\omega_+ - \omega)\tau_2}$. Since it appears in the complex conjugated amplitude, this leads to the phase factor $\mathrm{e}^{\mathrm{i}(\omega-\omega_+)\tau_2}$ in Eq. (4.22). On the other hand, on the upper branch of the MZI, the electronic excitations enters the radiation coupler with energy $\hbar\omega_-$ and leaves it an energy $\hbar\omega_+$ with an amplitude $\widetilde{R}_{\rm eff}(\omega_+, \omega_-)$. Therefore, the contribution of the outgoing coherence between the frequencies ω_+ and $\omega_+ - \omega$ comes from an incoming coherence emitted by the source S between the frequencies ω_- and $\omega_+ - \omega$ as summarized on Fig. 4.5.

Eq. (4.22) can then be used to understand which information can be extracted from an energy resolved probe. To understand this more precisely, let us consider an resolved excitation with Gaussian lineshape, centered at energy $\hbar\omega_e$ and with linewidth $\gamma_e \ll |\omega_e|$. Its wave function in the energy domain, defined by Eq. (A.6) is:

$$\widetilde{\varphi}_e(\omega) = \mathcal{N}\Theta(\mathrm{sign}(\omega_e)\omega) \, \mathrm{e}^{-(\omega-\omega_e)^2/2\gamma_e^2} \tag{4.24}$$

where the normalization condition (A.7) gives[1] $\mathcal{N}^2\gamma_e/v_F\sqrt{4\pi} \simeq 1$. For $\omega_e > 0$ we are dealing with an electronic excitation, whereas for $\omega_e < 0$

[1]The truncation for positive or negative energies can be neglected provided $\gamma_e \ll |\omega_e|$.

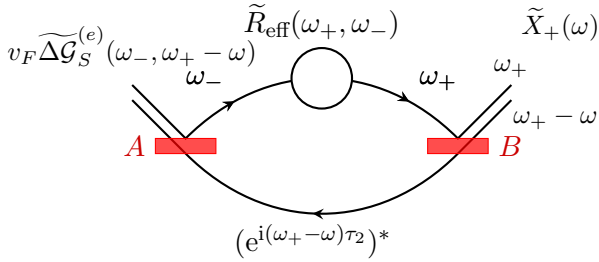

Figure 4.5: Physical interpretation of the linear radar equation (4.22) in the frequency domain showing the contribution of incoming single electron coherence in the frequency domain to $\widetilde{X}_+(\omega)$ for $\omega > 0$. Definition of the two paths is the same as in Fig. 4.3.

we are dealing with a hole excitation. In the limit where $\gamma_e \ll |\omega_e|$ is also much smaller than the scales of variation of $\widetilde{R}_{\rm eff}(\omega_+,\omega_-)$, the electron radar signal in the frequency domain given by Eq. (4.22) can be approximated as:

$$\widetilde{X}_+(\omega;\tau_2) \simeq \frac{\gamma_e}{\sqrt{\pi}}\mathrm{e}^{-\mathrm{i}\omega_e\tau_2}\widetilde{R}_{\rm eff}(\omega+\omega_e,\omega_e)\,. \tag{4.25}$$

Whenever ω_e and $\omega+\omega_e$ have the same sign, we are accessing the electron to electron or hole to hole effective scattering whereas whenever ω_e and $\omega+\omega_e$ do not have the same sign, we are accessing electron to hole or hole to electron effective scattering.

This immediately suggests a naive protocol to recover information on the Franck Condon factor in the frequency domain: injecting an energy resolved electronic excitation at ω_e and measuring the current at ω leads to

$$[X_+(\omega;\tau_2)]_{\rho_{\rm em}} = \frac{\gamma_e}{\sqrt{\pi}}\,\mathrm{e}^{-\mathrm{i}\omega_e\tau_2}\,\widetilde{\mathcal{Z}}(\omega_e)\,\widetilde{\mathcal{F}}_{\rho_{\rm em}}(\omega) \tag{4.26}$$

This is very seducing since $\widetilde{\mathcal{F}}_{\rho_{\rm em}}(\omega)$ can be obtained from a measure of relative contrast and phase in an interferometry experiment. The two measurements to compare being when the external radiation is switched on versus switched off. However the obvious limitation comes from the limited bandwidth of these measurements which, as mentioned in Sec. 3.4.1, does not exceed 20 GHz.

4.3.2 Time resolved wave packets

We now discuss how Eqs. (4.10) and (4.11) can be used to interpret experimental data obtained by recording interference fringes on the dc average current measured at the output of the MZI, when the probes have short wave-packets.

An (incorrect) time resolved heuristics

We consider a normalized Gaussian single electron wave packet:

$$\varphi_{\rm tr}(t) = \frac{1}{\sqrt{v_F\tau_e\sqrt{\pi}}} {\rm e}^{-(t-t_e)^2/2\tau_e^2} {\rm e}^{-{\rm i}\omega_e(t-t_e)} \tag{4.27}$$

with t_e the emission time, $\hbar\omega_e$ the emission energy and τ_e the duration of this single electron wave packet.

One could then be tempted to take the limit $\tau_e \to 0$ by considering that the limit of the Gaussien is, up to a refactor, a δ distribution. Following this idea, using Eq. (4.10) to compute the average time dependent current and brutally taking the limit $\tau_e \to 0$ leads to, at first order in τ_e:

$$X_+(t) \simeq \tau_e R(t_e+\tau_2, t_e)\, \delta(t-\tau_2-t_e) \tag{4.28}$$

The condition $t = t_e + \tau_2$ is not surprising: it comes from ballistic propagation along the reference arm of the MZI and, $X_+(t)$ is then proportional to the amplitude for the electron to enter branch 1 at t_e and exit it at time t. Itegrating over t would then lead to

$$X_+^{(\rm dc)} \simeq \tau_e R(t_e+\tau_2, t_e)\,. \tag{4.29}$$

This suggests the following heuristics: a short wave packet samples the Franck-Condon factor at the exit time $t_e + \tau_2$ of the electronic wave-packet. Consequently, sweeping the emission time t_e of the probe wave-packet would thus give access to $\mathcal{F}_{\rho_{\rm em}}(t_e+\tau_2)$ thereby providing us with a time resolved probe of the electromagnetic radiation via the Franck-Condon factor.

However, this naive computation does not take into account the constraint that the incoming single electron excitation must be restricted to positive energies due to the presence of the Fermi sea. Consequently, taking abruptly the $\tau_e \to 0$ limit does not lead to correct results.

Of course, introducing a positive finite energy shift via the factor ${\rm e}^{-{\rm i}\omega_e(t-t_e)}$ in front of the r.h.s of Eq. (4.27) with $\omega_e \gg 2\pi v_F/\tau_e$ leads

to a wave packet with negligible weight at negative energies. But it also introduces a fast oscillating term $\mathrm{e}^{-\mathrm{i}\omega_e(t-t'-\tau_2)}$ in front of $R(t,t') = \mathcal{Z}_1(t-t')\mathcal{F}_{\rho_{\rm em}}(t)$ in the radar equation (4.10). This means that we are probing electronic decoherence at energies close to $\hbar\omega_e$. But, as shown in Ref. [66], electronic decoherence is expected to be worse at high energies and may indeed kill the interference signal.

In order to mitigate this problem, the proper approach consists of introducing electronic wave packets that are close to the Fermi surface and whose duration can be shifted arbitrarily: these are the Levitons. Let us now consider these specific excitations to obtain explicit previsions.

Case of Leviton excitations

Let us now consider the case of a Leviton wave-packet of width τ_e. Its wave function is Lorentzian in the time domain and exponential in the frequency domain [91]. We are interested in the interference contribution to the outgoing electrical current for a Leviton of duration τ_e injected at time t_e.

Because of the simple expression for the Leviton wave packet in the frequency domain, the electron radar equation in the frequency domain (see Eq. (4.22)) gives us a convenient form for $X_+^{(\rm dc)}$ suitable for numerical evaluations:

$$X_+^{(\rm dc)} = \int_{\mathbb{R}} \widetilde{\mathcal{F}}_{\rho_{\rm em}}(\Omega)\, \mathrm{e}^{-\mathrm{i}\Omega(t_e+\tau_2)}\, f_{\tau_e,\tau_2}(\Omega) \frac{\mathrm{d}\Omega}{2\pi} \tag{4.30}$$

in which the filter

$$f_{\tau_e,\tau_2}(\Omega) = 4\pi\tau_e \int_{|\Omega|/2}^{+\infty} \widetilde{\mathcal{Z}}_1\left(\omega - \frac{\Omega}{2}\right) \mathrm{e}^{-2\omega\tau_e} \mathrm{e}^{-\mathrm{i}(\omega-\frac{\Omega}{2})\tau_2} \frac{\mathrm{d}\omega}{2\pi} \tag{4.31}$$

contains all the effects of electronic decoherence along branch 1 and ballistic propagation along branch 2 of the interferometer.

We now discuss the properties of this filter. The first point to notice is that, for $\Omega \geq 0$, a change of variables immediately leads to

$$\begin{aligned} f_{\tau_e,\tau_2}(\Omega \geq 0) &= 4\pi\tau_e \mathrm{e}^{-\Omega\tau_e} \int_0^{+\infty} \widetilde{\mathcal{Z}}_1\left(\omega\right) \mathrm{e}^{-2\omega\tau_e} \mathrm{e}^{-\mathrm{i}\omega\tau_2} \frac{\mathrm{d}\omega}{2\pi} \\ &= \mathrm{e}^{-\Omega\tau_e} f_{\tau_e,\tau_0}(0)\,. \end{aligned} \tag{4.32}$$

We can thus factorize the filter in two parts, the first one is a decreasing exponential factor which only depends on Ω. Its typical width is τ_e^{-1} and

so this exponential only reflect the duration of the Leviton and does not include any electronic decoherence effects. By contrast, the second part $f_{\tau_e,\tau_2}(0)$ includes the decoherence but does not depends on Ω. However, this is not true for $\Omega \leq 0$ since in this case, the same rewriting leads to

$$f_{\tau_e,\tau_2}(\Omega \leq 0) = 4\pi\tau_e \mathrm{e}^{-|\Omega|\tau_e} \mathrm{e}^{-i|\Omega|\tau_2} \int_0^{+\infty} \widetilde{\mathcal{Z}}_1\left(\omega + |\Omega|\right) \mathrm{e}^{-2\omega\tau_e} \mathrm{e}^{-\mathrm{i}\omega\tau_2} \frac{\mathrm{d}\omega}{2\pi} \tag{4.33}$$

There, we still have a prefactor $\mathrm{e}^{-|\Omega|\tau_e - \mathrm{i}|\Omega|\tau_2}$ which reflects the Leviton's structure but the second part is not $f_{\tau_e,\tau_2}(0)$ anymore. It depends on Ω via $\widetilde{Z}_{1,\mathrm{el}}(\omega + |\Omega|)$ in the integrand.

In the end, one has to resort to numerics to compute the precise expression for the filter. However, the integral in the r.h.s. of Eq. (4.33) is cut-off at frequencies $\omega \gtrsim \tau_e^{-1}$ by the exponential. The difference between this integral and the one appearing in $f_{\tau_e,\tau_2}(0)$ comes from the shift by $|\Omega|$ in $\widetilde{\mathcal{Z}}_1\left(\omega + |\Omega|\right)$. But if, for some reason, we are considering a regime where $\widetilde{\mathcal{Z}}_1\left(\omega + |\Omega|\right)$ does not decay too much for $\omega\tau_e \lesssim 1$, then maybe, one can neglect the difference between the two integrals that appear in the r.h.s. of Eq. (4.33) and $f_{\tau_e,\tau_2}(0)$. Under this "wild" approximation, then

$$f_{\tau_e,\tau_2}(\Omega \leq 0) \simeq \mathrm{e}^{-|\Omega|(\tau_e + \mathrm{i}\tau_2)} f_{\tau_e,\tau_2}(0)\,. \tag{4.34}$$

Almost exactly as Eq. (4.32), it shows that the Ω-dependant prefactor is determined by the timewidth of the Leviton wavepacket and τ_2, not on the electronic decoherence which only governs the second part $f_{\tau_e,\tau_2}(0)$. Of course, this is the result of an approximation and in practical cases, one should always provide an exact numerical estimation of the filter.

These considerations suggest that $f_{\tau_e,\tau_2}(\Omega)$ is expected to be a low pass filter. The limit $\tau_e \to 0^+$ may even lead to a vanishing signal since, in the case of the two counter-propagating edge channel model considered in Sec. 2.4, a very short Leviton may experience fractionalization as it propagates across the radiation coupler. For short wave packets, this would kill the electronic interference signal. Note that since the Leviton's duration τ_e appears in the expression of the filter, it indeed limits the time resolution on $\mathcal{F}_{\rho_{\mathrm{em}}}(t_e + \tau_2)$.

Finally, in the absence of external radiation, since $\mathcal{F}_{|0\rangle}(t) = 1$, we obtain

$$\left[X_+^{(\mathrm{dc})}\right]_{|0\rangle} = 4\pi\tau_e \int_0^{+\infty} \widetilde{\mathcal{Z}}_1(\omega)\, \mathrm{e}^{-2\omega\tau_e} \mathrm{e}^{-\mathrm{i}\omega\tau_2} \frac{\mathrm{d}\omega}{2\pi} = f_{\tau_e,\tau_2}(0)\,. \tag{4.35}$$

This quantity, which does not depend on t_e but still depends on τ_2 represents the base interference contribution for the dc outgoing current from the MZI. It is the base signal on which we are trying to see the t_e dependent change of contrast when the external radiation is present. Obviously, one expects that using shorter Levitons ($\tau_e \to 0$) leads to a smaller base signal $\left[X_+^{(\mathrm{dc})}\right]_{|0\rangle}$.

The take home message from this discussion is that the limiting time resolution for accessing the Franck-Condon factor is basically given by temporal width of the Leviton. This experimentally controlled parameter must then be chosen carefully to mitigate electronic decoherence so that the interference signal remains observable. The compromise discussed in Sec. 4.1 is that τ_e must be choosen small enough to have the time resolution needed to sample the Franck-Condon factor but not too small to avoid excessive electronic decoherence.

Numerical results for the base contrast for Leviton excitations

To conclude this section, let us now discuss numerical estimates for the base signal $\left[X_+^{(\mathrm{dc})}\right]_{|0\rangle}$, also called the vacuum baseline. When using short wave packets, one has to carefully tune τ_2 to maximize this signal in the absence of external radiation. The minimal precision on τ_2 must be comparable to the duration τ_e of the Leviton wavepacket to synchronize the times of flight along the target and along the reference branch of the MZI. If not synchronized, then the interference signal will not be visible on the dc average current.

We have calculated $\max_{\tau_2} \left|X_+^{(\mathrm{dc})}\right|_{\tau_e,\tau_2}$ when injecting Levitons of width τ_e with no external radiation ($\rho_{\mathrm{em}} = |0\rangle\langle 0|$). We chose a radiation coupler built from two counterpropagating edge channels in total electrostatic influence over a distance l with a geometric capacitance C_g. Fig. 4.6 depicts $\max_{\tau_2} \left|X_+^{(\mathrm{dc})}\right|$ as a function of $v_F\tau_e/l$. These graphs are plotted for different values of the dimensionless coupling constant

$$\alpha = \frac{e^2 l}{h v_F C_g} \tag{4.36}$$

encoding the importance of Coulomb interaction effects within this radiation coupler (see Sec. 2.4).

As expected, at fixed coupling, electronic decoherence is stronger for shorter Leviton pulses due to their high energy components. At a given

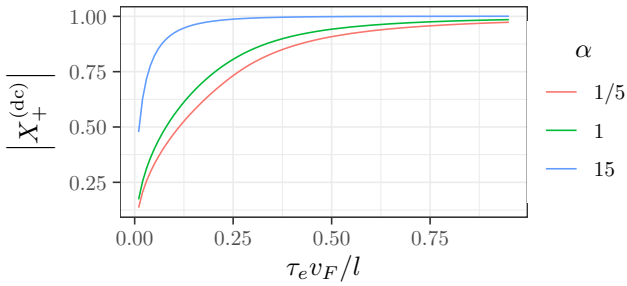

Figure 4.6: Contrast $|X_+^{(\mathrm{dc})}|$ of dc-current interference fringes for Leviton of duration τ_e as function of $\tau_e v_F/l$ in the absence of external radiation (vacuum baseline). The radiation coupler involves two counter-propagating edge channels in total mutual electrostatic influence over a distance l. Curves have been plotted for $\alpha = 1/5$ (red), 1 (green) and 15 (blue).

τ_e, the decoherence is also stronger for low α. A Coulomb dominated regime (large α) leads to better results, an effect already predicted [106] and observed [60] when an electron of energy $\hbar\omega_e$ propagates across a metallic island with Coulomb energy $E_C \gg \hbar\omega_e$. Finally, 50 % contrast can be achieved when considering Levitons of durations $\tau_e \gtrsim l/10\,v_F$ which, in the case of $l = 10\,\mu\mathrm{m}$ and $v_F = 10^5\,\mathrm{m\,s^{-1}}$, corresponds to pulses of duration down to 10 ps.

This analysis shows that, with a reasonable model of a realistic radiation coupler, it is possible to obtain a strong base signal even when using Levitons of width in the tens of ps and even below. We now discuss the possible signatures of experimentally relevant classical and quantum radiations.

4.4 Predictions for classical and quantum radiation

We now consider various types of radiations that are directly relevant for forthcoming experiments. As a first step, we will discuss the behavior of the Franck-Condon factor $\mathcal{F}_{\rho_{\mathrm{em}}}(t)$ that encodes the information on the incoming radiation. Then, motivated by the experiments, we will deepen the discussion by considering the interference contrast on the dc current $X_+^{(\mathrm{dc})}$ when injecting Leviton wavepacket of given duration τ_e

to see more quantitatively how the conclusions on $\mathcal{F}_{\rho_{\rm em}}(t)$ translate in terms of the experimental signal $X_+^{(\rm dc)}$.

In Sec. 4.4.1, we consider classical radiation under the form of a time dependent drive applied to the upper branch of the MZI via a capacitance. Then, we consider quantum states of radiation. In Sec. 4.4.2, we discuss the ability of the electron radar to detect squeezing. Then, we turn to Non Gaussian quantum radiation and analyze the ability to detect a single edge magnetoplasmon in Sec. 4.4.3.

4.4.1 Classical radiation

Let us assume that a classical drive $V_g(t)$ is applied to a top gate capacitively coupled to the edge channel in the region $|x| \leq l/2$ via a geometric capacitance C_g as depicted on Fig. 4.7. This is the model illustrated in Fig. 4.2-b but without dynamical degrees of freedom coupled to the top gate ($Z(\omega) = 0$). It corresponds to the limit of a an infinite number of electronic channels in the top gate's lead in Ref. [136]. For simplicity, we assume that l is the total length of branch 1 of the MZI.

Because there are no external dynamical degrees of freedom in this simplified model of a top gate, the scattering process can be described in terms of the input/output relations for the edge channel's EMP mode current $i_{\rm in}(\omega)$ and $i_{\rm out}(\omega)$ which takes the form:

$$i_{\rm out}(\omega) = t(\omega)\, i_{\rm in}(\omega) + Y(\omega)\, V_g(\omega) \tag{4.37}$$

where $t(\omega)$ denotes the EMP transmission amplitude across the region $|x| \leq l/2$ and the admittance $Y(\omega)$ describes the response of the outgoing current to the top gate potential $V_g(\omega)$. Under the hypotheses of total mutual influence between the top gate and the $|x| \leq l/2$ region of the edge channel, $Y(\omega)$ is the finite frequency admittance of the electrical dipole formed by the top gate and the edge channel. It is related to $t(\omega)$ by [167, 53, 35]:

$$Y(\omega) = \frac{e^2}{h}(1 - t(\omega))\,. \tag{4.38}$$

Although these quantities could, in principle, be inferred from finite frequency admittance measurements, predictions for these coefficients depend on the specific model. Sec. 2.3.2 gives the expressions obtained from a discrete element model *à la* Büttiker in which the top gate and the $|x| \leq l/2$ region are the two plates of a capacitor with geometric capacitance C_g.

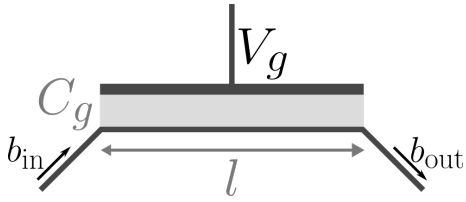

Figure 4.7: A top gate is capacitively coupled to the $|x| \leq l/2$ region of a chiral edge channel. It is driven by a time dependent gate voltage $V_g(t)$. C_g denotes the geometric capacitance between the two conductors.

The gate voltage translates the edge magnetoplasmon operator $b_{\text{in}}(\omega)$ by $-Y(\omega)V_g(\omega)/e\sqrt{\omega}$. So in terms of fermionic filed, it introduces a phase factor in front of the fermionic field coming out of the radiation coupler which is given by

$$\mathcal{F}_{V_g}(t) = \mathrm{e}^{\frac{\mathrm{i}e}{\hbar}\int_{\mathbb{R}}\Gamma(t-\tau)V_g(\tau)\,\mathrm{d}\tau} \tag{4.39}$$

in which $\Gamma(\tau)$ is the inverse Fourier transform of $-R_K Y(\omega)/\mathrm{i}\omega$. We already saw $\Gamma(\tau)$ as a filtering function when we linked the Franck-Condon factor to full counting statistics in Sec. 4.2.3. This form shows that the effective single particle scattering amplitude $R_{\text{eff}}(t,t')$ retains the form given by Eq. (4.11) with $\mathcal{Z}_1(\tau)$ determined by injecting the expression $t(\omega) = 1 - R_K Y(\omega)$ in Eq. (4.5) and $\mathcal{F}_{V_g}(t)$ playing the role of the Franck-Condon factor $\mathcal{F}_{\rho_{\text{em}}}(t)$ from the full quantum theory.

As explained in Sec. 2.4, the importance of Coulomb interactions within the $|x| \leq l/2$ region depends on the dimensionless coupling constant

$$\alpha = \frac{e^2 l}{h v_F C_g} \tag{4.40}$$

which is the ratio of the single electron charging energy e^2/C_g to the kinetic energy scale $\hbar v_F/l$ associated with the $|x| \leq l/2$ region or, equivalently, the ratio C_q/C_g of the quantum capacitance over the geometrical capacitance. In the voltage locked regime ($\alpha \ll 1$), the voltage drop at the capacitance vanishes and therefore the electrons directly see the gate voltage $V_g(t)$. In the Coulomb blocked regime ($\alpha \gtrsim 1$), Coulomb interactions are so strong that they tend to block charge accumutation below the top gate.

The voltage locked regime

At very small α, $t(\omega) \simeq \mathrm{e}^{\mathrm{i}\omega l/v_F}$ and $U(t) \simeq V_g(t)$. In this regime, the electrochemical capacitance $C_\mu = C_g C_q/(C_g + C_q) \simeq C_q$ is dominated by the quantum capacitance C_q and the electrons within the $|x| \leq l/2$ region experience the gate potential $V_g(t)$. For $\alpha \ll 1$, $t(\omega) \simeq \mathrm{e}^{\mathrm{i}\omega l/v_F}$. Consequently, the elastic scattering amplitude has close to unit modulus at low energy $\omega \to 0$ (see Sec. III.C of [35]): electronic decoherence can be neglected. In other terms, there is no back-action of the incoming electron on the edge channel mediated by the top-gate which could lead to significant electronic decoherence.

Since in this regime $\mathcal{Z}_1(\omega) \sim \mathrm{e}^{\mathrm{i}\omega l/v_F}$, the effective scattering amplitude can be approached by

$$R_{\mathrm{eff}}(t,t') \simeq \delta\left(\tau - \frac{l}{v_F}\right) \mathcal{F}_{V_g}(t)\,. \tag{4.41}$$

At very small α, $\Gamma(\tau) = \mathbf{1}_{[0,l/v_F]}(\tau)$ and therefore, we get:

$$R_{\mathrm{eff}}(t,t') \simeq \delta\left(\tau - \frac{l}{v_F}\right) \mathrm{e}^{\frac{\mathrm{i}e}{\hbar}\int_0^{\tau_1} U(\tau)\,\mathrm{d}\tau} \tag{4.42}$$

with $\tau_1 = l/v_F$ and $U(t) = V_g(t)$ as expected.

As α is increased, electronic decoherence starts to appear but, as long as we keep the energy of the electronic excitation low enough, it can be neglected. The first effect of increasing α is to modify the voltage seen by the electrons below the top gate. As shown in Sec. 2.3.2, the electrons see and effective voltage which is a filtering of $V_g(\omega)$ (see Eq. (2.51)).

To summarize, in the voltage locked regime, the MZI detects the accumulated electric phase associated with the time dependent potential $V_g(t)$ and the results may be interpreted within a single particle framework.

The Coulomb blocked regime

The limit of large α corresponds to the regime dominated by Coulomb interactions. They so strong that no charge accumulates on either plates of the capacitor (neither on the $|x| \leq l/2$ interaction region of the edge channel not on the top gate). But, as explained in Sec. 2.3.2, the outgoing edge magnetoplasmon mode $b_{\mathrm{out}}(\omega)$ has a very small response to the external time dependent voltage. This means that the electron radar is

weakly responding to the external voltage applied to the top gate. However, electronic decoherence is not a problem in this limit. This echoes the results obtained recently in Ref. [61] in which a similar phenomenon occurs in a MZI where the top gate in the strong coupling regime is replaced by a metallic island with strong enough Coulomb interaction.

4.4.2 Squeezed radiation

We now consider a Gaussian state of the quantum electromagnetic field, that is to say any state whose quadrature variables follow Gaussian distributions, and discuss the ability of the electron radar to detect squeezing. We show that for a generic Gaussian state of the incoming radiation, the electron radar probes squeezing in a specific mode defined by the radiation coupler and we provide a simple criterion to make differenciate between a squeezed state and a non-squeezed state in this mode. Then, the experimentally relevant case of a radiation coupler exhibiting a resonance around a given frequency with a high quality factor will be considered. The analysis is pushed forward, up to obtaining predictions for the contrast of interference fringes on with Levitons of fixed duration.

General squeezing criterion

Optimal electromagnetic mode for squeezing detection Given the complexities involved in the measurement of a squeezed state, it is of relative importance for this state to be contained within the electromagnetic mode for which the electronic quantum radar will be the most sensitive. This mode is determined by the geometry of the radiation coupler and represents the optimal coupling point between the electrical and radiation channels. As such, it is fully characterized by the non-diagonal coefficient of the EMP scattering matrix $S_{ba}(\omega)$. To identify this mode, let's have a look at the expression of the Franck-Condon factor:

$$\mathcal{F}_{\rho_{\rm em}}(t) = \left\langle : D_{a_{\rm in}}\left[S_{ba}^{*}\Lambda_t\right] : \right\rangle_{\rho_{\rm em}}, \tag{4.43}$$

where

$$D_{a_{\rm in}}\left[S_{ba}^{*}\Lambda_t\right] = \exp\left(\int_0^{\omega_c}\left(S_{ba}^{*}\Lambda_t a_{\rm in}^{\dagger}(\omega) - \text{c.c.}\right)\mathrm{d}\omega\right). \tag{4.44}$$

We have introduced ω_c which is an UV cut-off below which all the incoming radiation is emitted. Introducing now the normalized EMP mode:

$$\alpha_t = \frac{1}{\mathcal{N}^{1/2}} \int_0^{\omega_c} \frac{S_{ba}(\omega)}{\sqrt{\omega}} \, \mathrm{e}^{-\mathrm{i}\omega t} \, a(\omega) \mathrm{d}\omega \,, \tag{4.45}$$

we can then rewrite the expression of $\mathcal{F}_{\rho_{\rm em}}(t)$ in Eq. (4.46) in a simpler way:

$$\mathcal{F}_{\rho_{\rm em}}(t) = \left\langle : D_{\alpha_t} \left[\sqrt{\mathcal{N}} \right] : \right\rangle_{\rho_{\rm em}} . \tag{4.46}$$

With this expression we see that the Franck-Condon factor is the average of a normal ordered displacement operator for the mode α_t [2] with the amplitude $\sqrt{\mathcal{N}}$. Thus α_t is the only filtered mode at which the radiation coupler is sensitive, explaining why α_t is the most suited mode for probing squeezing. Note that α_t and $\alpha_t^\dagger$ satisfy the canonical commutation relation$[\alpha_t, \alpha_t^\dagger] = \mathbf{1}$. To determine the factor of normalization $\mathcal{N}$ we just have to compute the equation:

$$\mathcal{N} = \int_0^{\omega_c} |S_{ba}(\omega)|^2 \, \frac{\mathrm{d}\omega}{\omega} \,. \tag{4.47}$$

To get an insight of the physical interpretation of $\mathcal{N}$, we can rewrite Eq. (4.47) into:

$$\mathcal{N} = \int_0^{\omega_c} |S_{ba}(\omega) \lambda_t^*(\omega)|^2 \, \mathrm{d}\omega \,. \tag{4.48}$$

From this equation we deduce that $\mathcal{N}$ is the average photon number transmitted into the radiation channel by a time-localized single electron excitation propagating within the electronic channel of the radiation coupler. The integral in the r.h.s. of the equations above is convergent in the infrared (low frequency) since $S_{ba}(\omega)$ is linear at small ω and the convergence in the ultraviolet (high frequency) is ensured by the UV cutoff.

Gaussian approximation Computing the Franck-Condon factor $\mathcal{F}_{\rho_{\rm em}}(t)$ using a Gaussian approximation for the $(\alpha_t, \alpha_t^\dagger)$ mode leads to:

$$\mathcal{F}_{\rho_{\rm em}}(t) = \mathrm{e}^{i\phi(t)} \times \mathrm{e}^{-\mathcal{N}\left(\langle (\Delta Y_t)^2 \rangle_{\rho_{\rm em}} - \langle (\Delta Y_t)^2 \rangle_{|0\rangle}\right)} \,. \tag{4.49}$$

where the phase $\phi(t)$ is due to the average value $\langle \alpha_t \rangle$ and can be viewed as arising from the classical voltage felt by the electrons within the upper

[2] The result is now independent of the UV cutoff ω_c since all modes with $\omega \geq \omega_c$ are in the vacuum state and therefore do not contribute to $\mathcal{F}_{\rho_{\rm em}}(t)$.

branch of the MZI. The other contribution comes from the Gaussian fluctuations of the incoming radiation which can change the modulus of the Franck-Condon factor. Eq. (4.49) provides a sufficient criterion for squeezing: as soon as $|\mathcal{F}_{\rho_{\rm em}}(t)| > 1$ there is squeezing since this is a signature of the fact that, for these values of t, fluctuations of the quadrature

$$Y_t = \frac{\mathrm{i}}{\sqrt{2}}\left(\alpha_t^\dagger - \alpha_t\right) . \tag{4.50}$$

are smaller than in the vacuum state: $\langle(\Delta Y_t)^2\rangle_{\rho_{\rm em}} < \langle(\Delta Y_t)^2\rangle_{|0\rangle}$.

Squeezing around a given frequency

Because of its relevance for experiments, let us discuss the ability of the electron radar to detect squeezed radiation in an electromagnetic mode around $\omega \simeq \omega_0$ within a bandwidth γ_0 such that $Q_0 = \omega_0/\gamma_0$ is significantly larger than one. Then $S_{ba}(\omega)$ can be taken as constant for $|\omega - \omega_0| \leq \gamma_0/2$. We assuming that each mode within this bandwidth is prepared in a squeezed vacuum (see Appendix C) with squeezing paramereter z. Using in addition the narrow bandwidth approximation, the Franck-Condon factor $\mathcal{F}_{|\mathrm{Sq}_z\rangle}(t)$ of the squeezed state $|\mathrm{Sq}_z\rangle$ is given by

$$\mathcal{F}_{|\mathrm{Sq}_z\rangle}(t) \simeq \mathrm{e}^{\frac{|S_{ba}(\omega_0)|^2}{Q_0}\sinh(2|z|)[\cosh(2|z|)\cos(2\omega_0 t-\phi_0)-\sinh(2|z|)]} \tag{4.51}$$

where $\phi_0 = \mathrm{Arg}(S_{ba}(\omega_0)) + \mathrm{Arg}(z)$. As expected, there are values of t for which the factor $\cosh(2|z|)\cos(2\omega_0 t - \phi_0) - \sinh(2|z|)$ in the exponential can have positive values leading to $|\mathcal{F}_{|\mathrm{Sq}_z\rangle}(t)| > 1$. In particular its maximum value is then

$$\max_t\left(\mathcal{F}_{|\mathrm{Sq}_z\rangle}(t)\right) = \mathrm{e}^{\frac{|S_{ba}(\omega_0)|^2}{2Q_0}(1-\mathrm{e}^{-4|z|})} > 1 \tag{4.52}$$

whereas its minimum value is

$$\min_t\left(\mathcal{F}_{|\mathrm{Sq}_z\rangle}(t)\right) = \mathrm{e}^{-\frac{|S_{ba}(\omega_0)|^2}{2Q_0}(\mathrm{e}^{4|z|}-1)} < 1 . \tag{4.53}$$

Let us recall that the compression factor, which quantifies the reduction of uncertainty in one quadrature at the expense of increased uncertainty in the other quadrature, for the squeezed mode in $|\mathrm{Sq}_z\rangle$ is given by

$e^{-4|z|}$ (see Eq. C.7). The compression is often expressed in decibels via the formula

$$\mathrm{dB}(z) = -10\,\log_{10}(\mathrm{e}^{-4|z|}) = \frac{40}{\log(10)}\,z \simeq 17.372\,z \tag{4.54}$$

so that a 3 dB squeezing corresponds to a 50 % noise reduction with respect to the vacuum. As of today, a compression of 18 % (0.86 dB) with respect to vacuum fluctuations has been achieved in quantum Hall edge channels [9]. Assuming a quality factor $Q_0 = 5$ and no losses ($|S_{ba}(\omega_0)|^2 = 1$) for the radiation coupler leads to an increase of the Franck-Condon factor by 1.8 % with respect to unity whereas a 3 dB squeezing would lead to an increase by 5.1 %.

Interference fringe contrast for Levitons

As mentioned in Sec. 4.3.2, time resolved sampling will be performed by Levitons of duration τ_e. Therefore, the discussion of Sec. 4.3.2 is directly relevant: the observed interference contrast on the dc current is not the contrast in the absence of radiation multiplied by the Franck-Condon factor $\mathcal{F}(t_e + \tau_2)$. We have to take into account the effect of electronic decoherence as well as the limited time resolution of these single electron pulses. In order to understand what happens, our discussion will assume that the filtering (4.30) of the Franck Condon factor by the filter defined by Eq. (4.31) can be approximated by a filtering by:

$$f_{\tau_e,\tau_2}(\Omega) = f_{\tau_e,\tau_2}(0)\,\mathrm{e}^{-|\Omega|\tau_e}\,\mathrm{e}^{\mathrm{i}\tau_2\,\min(0,\Omega)}\,. \tag{4.55}$$

We now decompose the time periodic Franck-Condon factor given by Eq. (4.51) in Fourier series:

$$\mathcal{F}_{|\mathrm{Sq}_z\rangle}(t) \simeq \mathrm{e}^{-\Lambda\sinh^2(2|z|)} \sum_{n\in\mathbb{Z}} I_{|n|}\left(\Lambda\cosh(2|z|)\sinh(2|z|)\right)\,\mathrm{e}^{-2\mathrm{i}n\omega_0(t-\tilde{t}_e)} \tag{4.56}$$

where $\Lambda = |S_{ba}(\omega_0)|^2/Q_0$ is introduced for simplicity and I_n denotes the modified Bessel function of order n. The time $\tilde{t}_e$ arises from the phase of $S_{ba}(\omega_0)$ as well as of the squeezing parameter. We will forget it in the following since it can be absorbed in a redefinition of the Leviton's injection times and does not matter for the discussion of interference contrast.

Because $|S_{ba}(\omega_0)|^2 \leq 1$ and Q_0 is significantly larger than 1, Λ is quite smaller than unity. Remembering also that experimentally reachable

squeezing factors are not very high and therefore, $\Lambda \cosh(2|z|) \sinh(2|z|) \lesssim 1$. Moreover, $I_n(x) \simeq (x/2)^n/n!$ for $n \geq 1$. Consequently, we are in a regime where most of the contribution is expected to come from the first harmonics: $n = 0$ and $n = \pm 1$ in Eq. (4.56). Let us retain only these harmonics for simplicity:

$$\mathcal{F}_{|\mathrm{Sq}_z\rangle}(t) \simeq \mathcal{F}_0(z,\Lambda) + \mathrm{e}^{-2i\omega_0 t}\mathcal{F}_1(z,\Lambda) + \mathrm{e}^{2i\omega_0 t}\mathcal{F}_{-1}(z,\Lambda) \tag{4.57}$$

where

$$\begin{aligned}
\mathcal{F}_0(z,\Lambda) &= \mathrm{e}^{-\Lambda \sinh^2(2|z|)} I_0\left(\Lambda \cosh(2|z|)\sinh(2|z|)\right) \\
&\simeq 1 - \Lambda \sinh^2(2|z|) + \mathcal{O}(\Lambda^2) \qquad (4.58a) \\
\mathcal{F}_{\pm 1}(z,\Lambda) &= \mathrm{e}^{-\Lambda \sinh^2(2|z|)}\, I_1\left(\Lambda \cosh(2|z|)\sinh(2|z|)\right) \\
&\simeq \frac{\Lambda}{2}\cosh(2|z|)\sinh(2|z|) + \mathcal{O}(\Lambda^2)\,. \qquad (4.58b)
\end{aligned}$$

The $n = 0$ harmonic contains the contrast obtained when averaging over the emission time t_e:

$$\overline{\left[X_+^{(\mathrm{dc})}\right]}^{t_e}_{\mathrm{Sq}(z)} = \left[X_+^{(\mathrm{dc})}\right]_{|0\rangle} \mathcal{F}_0(z,\Lambda)\,. \tag{4.59}$$

Since $|\mathcal{F}_0(z,\Lambda)| < 1$, this t_e-independent measurement is lower than the one when only vacuum injected in the radiation channel. This is the effect of the average number of photons in a squeezed vacuum: although such a quantum state has sub-vacuum fluctuations, on average over time, it has more fluctuations than the vacuum. This is measured by its average number of photons which increases with $|z|$. Therefore, increasing $|z|$ leads to more electronic decoherence when considering the time average over t_e.

Using the approximation given by Eq. (4.55), we finally obtain the relative contrast with respect to vacuum baseline as:

$$\begin{aligned}
\frac{\left[X_+^{(\mathrm{dc})}\right]_{\mathrm{Sq}(z)}}{\left[X_+^{(\mathrm{dc})}\right]_{|0\rangle}} &= \mathcal{F}_0(z,\Lambda) + \mathrm{e}^{-2\omega_0\tau_e}\left[\mathcal{F}_1(z,\Lambda)\,\mathrm{e}^{-2\mathrm{i}\omega_0 t_e}\right. \\
&\qquad \left. + \mathrm{e}^{2\mathrm{i}\omega_0(\tau_2+t_e)}\mathcal{F}_{-1}(z,\Lambda)\right]\,. \qquad (4.60)
\end{aligned}$$

The question is to determine whether or not the maximum modulus of this ratio as a function of t_e is greater than unity or not. To solve this

problem, we note that the r.h.s. of Eq. (4.60) is of the form

$$a + \frac{b}{2}\left(\mathrm{e}^{-\mathrm{i}\varphi} + \mathrm{e}^{\mathrm{i}(\varphi+\vartheta)}\right)$$

with, at first order in Λ:

$$a = 1 - \Lambda \sinh^2(2|z|) \tag{4.61a}$$

$$b = \Lambda \cosh(2|z|) \sinh(2|z|)\, \mathrm{e}^{-2\omega_0 \tau_e} \tag{4.61b}$$

$$\varphi = 2\omega_0 t_e \tag{4.61c}$$

$$\vartheta = 2\omega_0 \tau_2 \tag{4.61d}$$

Finding the maximum value of the relative contrast in modulus as we vary φ is detailed in Appendix D. The final result is a simple expression of the form

$$\max_{t_e} \left| \frac{\left[X_+^{(\mathrm{dc})}\right]_{\mathrm{Sq}(z)}}{\left[X_+^{(\mathrm{dc})}\right]_{|0\rangle}} \right| \simeq 1 + \Lambda \left(\eta \cosh(2z) \sinh(2|z|) - \sinh^2(2z)\right) + \mathcal{O}\left(\Lambda^2\right) \tag{4.62}$$

where $\Lambda = |S_{ba}(\omega_0)|^2 / Q_0$ and

$$\eta = \mathrm{e}^{-2\omega_0 \tau_e} \left|\cos(2\omega_0 \tau_2)\right| \tag{4.63}$$

This maximum is greater than unity for $0 < z < \mathrm{arctanh}(\eta)/2$. Surprisingly, above this value of the squeezing parameter, the contrast increase associated with transcient sub-vacuum fluctuations is not compensated by the drop of the time-averaged contrast with respect to the vacuum baseline. As discussed in Appendix D, this comes from the damping of the harmonics associated with the finite width of the Leviton. It does not happen for $\eta = 1$.

This effect associated with the finite duration of the probing Leviton can therefore hinder the observation of squeezing based on the simple criterion that, for some injection time, the maximum interference contrast $\left[X+^{(\mathrm{dc})}\right]_{\mathrm{Sq}(z)}$ is larger than the vacuum baseline $\left[X+^{\mathrm{dc})}\right]_{|0\rangle}$. As explained in Appendix in the D, avoiding this undesirable effect requires not exceeding $|z| = \mathrm{arctanh}(\eta)/2$. The maximum relative contrast with respect to the vacuum baseline is indeed obtained for $|z|_{\mathrm{opt}} = \mathrm{arctanh}(\eta)/4$ and is given by

$$\max_{|z|} \max_{t_e} \left| \frac{\left[X_+^{(\mathrm{dc})}\right]_{\mathrm{Sq}(z)}}{\left[X_+^{(\mathrm{dc})}\right]_{|0\rangle}} \right| \simeq 1 + \frac{\Lambda}{2}\left(1 - \sqrt{1-\eta^2}\right) + \mathcal{O}\left(\Lambda^2\right). \tag{4.64}$$

This discussion immediatly shows that the choice of the Leviton's duration must result from a compromise. On one hand, short Levitons lead to η closer to one which is good for increasing the relative contrast with respect to the vacuum baseline. One should notice that the maximally optimized contrast given by Eq. (4.64) sharply decays when η is lowered from 1 towards zero[3]. But, on the other hand, short Levitons experience a stronger decoherence and this leads to a reduced vaccum baseline contrast $\left|\left[X_+^{(\mathrm{dc})}\right]_{|0\rangle}\right|$ as shown on Fig. 4.6. Consequently, the overshoot above the vacuum baseline may become harder to measure.

Numerical results and discussion In order to discuss the experimental observability of a greater than unity relative contrast with respect to the vacuum, we have to use numerical evaluations. The above discussion suggests to choose ω_0 near a maximum of $|S_{ba}(\omega_0)|^2$. In the case of the radiation coupler built from two counter-propagating capacitively coupled edge channels discussed in Sec. 2.4, this operation point can be determined easily from Fig. 4.6. Here we will consider that $v_F = 10^5\,\mathrm{m\,s^{-1}}$ and $l = 10\,\mu\mathrm{m}$ which corresponds to a time of flight $l/v_F = 100\,\mathrm{ps}$.

Moreover, as mentioned before, it may be better to limit electronic decoherence. Naively, this could lead us to choose a strong coupling situation $\alpha = 15$ and ω_0 at the first resonance frequency on Fig. 2.13.

The numerical results are presented on Figs. 4.8 to 4.11. Before commenting them in details, let us mention that on all these plots, the black oscillating curves correspond to the full numerical evaluation of the contrast, taking into account the exact numerical evaluation of the filter $f_{\tau_e,\tau_2}(\Omega)$ as well as all the harmonics in the Fourier series expansion of the Franck-Condon factor. The dashed black horizontal line always corresponds to the vacuum baseline $\left|\left[X_+^{(\mathrm{dc})}\right]_{|0\rangle}\right|$. The dotted red line corresponds to the maximally optimized maximum contrast given by Eq. (4.64) whereas the dotted black line corresponds to the evaluation of Eq. (4.62) for the actual value of the squeezing parameter considered in the example. We have plotted the results for three values of the squeezing parameter: $z \simeq 0.0496$ corresponding to 18 % (or 0.86 dB)

[3]Moreover, one should remember that τ_2 is chosen to maximize the vacuum baseline which drops quickly to zero when τ_2 is shifted away from its optimal value by more than τ_e. Consequently, $|\cos(2\omega_0\tau_2)|$ cannot be optimized by changing τ_2. It may generically be below unity.

noise reduction demonstrated in Ref. [9], $z \simeq 0.0719$ corresponding to 1.25 dB (or 25 %) noise reduction and $z \simeq 0.1733$ corresponding to 3 dB (or 50 %) noise reduction.

Let us first discuss results for Levitons of duration 15 ps and compare the voltage locked ($\alpha = 1/5$) and Coulomb blocked ($\alpha = 15$) regimes of the radiation coupler. As mentioned before, the choices of ω_0 are different depending on the regime and are optimized in the sense that they maximize $\Lambda = |S_{ba}(\omega_0)|^2/Q_0$.

Figures 4.8 and 4.9 present the contrast of the interference fringes for Levitons as a function of their injection time, computed from the analytical expresssions (4.30) and (4.31) combined with Eq. (4.56). We immediatly notice that, at some operating points, the contrast in the presence of the squeezed vacuum does exceed the vacuum baseline. The overshoot is small: of the order of 0.3 % on a baseline of 57.5 %. The best numbers are obtained in the voltage locked regime for 1.25 dB squeezing and $\omega_0 l/v_F = \pi$. This may seem difficult to observe but according to our collaborator, G. Fève, the degree of precision reached on average current measurements is such that this is not beyond reach. In other words, the sensitivity of d.c. current measurement is not an issue. In fact, G. Fève pointed out that the main experimental risk resides in the stability of the experiment between the measurement with the squeezed radiation "on" versus when the radiation is switched "off". A small drift in the experiment or within the sample could scramble the baseline and hinder the increase of the contrast above the vacuum baseline which we view as the smoking gun of squeezing detection by the MZI.

Note that the results depicted on Fig. 4.8 show a rather good agreement between the numerical evaluation and the simplified models discussed in the previous paragraph. The tendencies that were discussed there are clearly visible: the maximum contrast goes below the vacuum baseline if the squeezing parameter is too high, such as for 3 dB squeezing at $\omega_0 l/v_F = \pi$.

We immediatly see on Fig. 4.9 that, in the Coulomb blocked regime ($\alpha = 15$), the overshoot over the vacuum baseline is much harder to see. The drop of the maximum occurs already between the 0.868 dB and 1.15 dB noise reduction and the overshoot over the vacuum baseline is of the order of 0.1 %. This deterioration is mainly associated with the difference between ω_0 in the two situations: going from $\omega_0 l/v_F = \pi$ (voltage locked case) to 5.5 (Coulomb blocked case) changes $\mathrm{e}^{-2\omega_0\tau_e}$ from 0.390 to 0.192. This clearly degrades the situation as explained in

Appendix D: for example, without the effect of $|\cos(2\omega_0\tau_2)| < 1$, $|z|_{\rm opt}$ would go down from 0.103 (1.79 dB) to 0.049 (0.84 dB).

We have thus considered much shorter Levitons of duration 2.5 ps in order to increase the value of $e^{-2\omega_0\tau_e}$ and therefore of η. Figures 4.10 and 4.11 present the same results as Figures 4.8 and 4.9 but for $\tau_e = 2.5$ ps.

The first obvious observation is the decrease of the vacuum baseline as expected from Fig. 4.6. Note that the obtained values are not catastrophic: 0.20 to 0.23 in the voltage locked regimes and 0.67 in the Coulomb blocked regime thereby showing the protective effects of strong Coulomb interactions.

As expected, in the voltage locked regime, the best figures of merit are obtained for $\omega_0 l/v_F = \pi$ so that the radiation coupler provides the best coupling between the electronic interferometer and the external radiation. Compared to 15 ps Levitons, we see that increasing the squeezing leads to a stronger effect here whereas, on Fig. 4.10, a 3 dB squeezing is above the optimum discussed in Appendix D. Note that in absolute, the contrast increase for 1.25 dB is still of the order of 0.3 %, same as with 15 ps but it comes on top of a baseline of 0.23 instead of 0.575: this represents a factor two improvement in the relative contrast increase with respect to the vacuum baseline between 15 ps and 2.5 ps Levitons!

In the Coulomb blocked regime ($\alpha = 15$), results are presented on Fig. 4.11. Using 2.5 ps Levitons instead of 15 ps ones brings a notable improvement in the figures of merit: the contrast overshoot is of the order of 1 % on a baseline of 67.7 % instead of 0.1 % on a 96.5 % baseline!

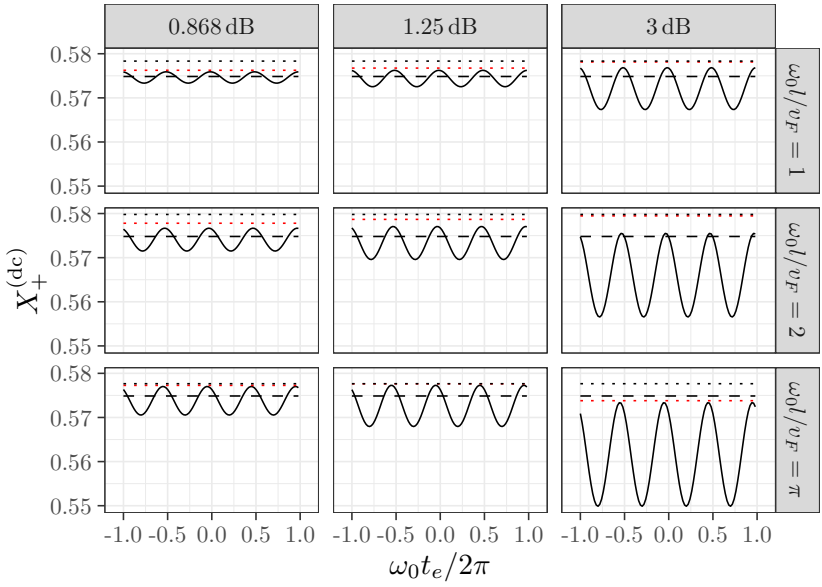

Figure 4.8: The various panels present the interference contrast $\left[X_+^{(\mathrm{dc})}\right]$ for Leviton excitations of width $\tau_e = 15\,\mathrm{ps}$ assuming a $10\,\mu\mathrm{m}$ long radiation coupler with $v_F = 10^5\,\mathrm{m\,s^{-1}}$ and coupling strength $\alpha = 1/5$. The plots show the absolute contrast as a function of the dimensionless injection time $\omega_0 t_e/2\pi$ for different values of the squeezing parameter z (expressed in dB) and different values of ω_0, ranging from $\omega_0 l/v_F = 1$ to $\omega_0 l/v_F = \pi$. The dashed black horizontal line corresponds to the vacuum baseline $\left[X_+^{(\mathrm{dc})}\right]_{|0\rangle}$. The dotted black line is independent of the squeezing parameter z and corresponds to the maximally optimized maximum contrast given by Eq. (4.64) whereas the dotted red line corresponds to the evaluation of Eq. (4.62) for the actual value of the squeezing parameter z considered in the example.

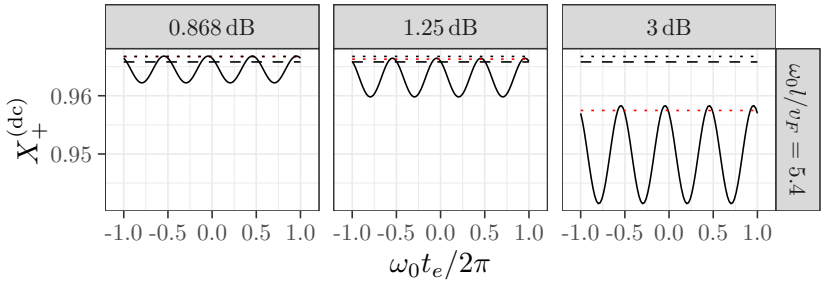

Figure 4.9: The various panels present the interference contrast $\left[X_+^{(\mathrm{dc})}\right]$ for Leviton excitations of width $\tau_e = 15\,\mathrm{ps}$ assuming a $10\,\mu\mathrm{m}$ long radiation coupler with $v_F = 10^5\,\mathrm{m\,s^{-1}}$ and coupling strength $\alpha = 15$. The plots show the absolute contrast as a function of the dimensionless injection time $\omega_0 t_e/2\pi$ for different values of the squeezing parameter z (expressed in dB) and $\omega_0 l/v_F = 5.5$ right on the first resonance observed on Fig. 2.13. Caption for the various line types is the same as for Fig. 4.8.

4.4.3 Fock states

We now consider the problem of detecting Fock states in a specific EMP mode denoted here by χ. This state being non-Gaussian, the Gaussian result given by Eq. (4.49) breaks down.

The Franck-Condon factor

We consider Fock states in the mode associated with the normalized single photon state χ. An explicit computation detailed in Appendix A.2 shows how to obtain the explicit expression for the Franck-Condon factor $\mathcal{F}_{|N,\chi\rangle}(t)$ by re-expressing the infinite displacement operator appearing in its definition in an orthonormal basis $(\chi_n)_n$ involving the normalized mode χ:

$$D_a\left[\alpha\right] = \bigotimes_{n\geq 0} D_{a_n}\left[\int_0^{+\infty} \alpha(\omega)\ \langle\chi_n|\omega\rangle\ \mathrm{d}\omega\right] \tag{4.65}$$

where $\alpha(\omega) = S^*_{ba}(\omega)\Lambda_t(\omega)$. An explicit evaluation of the matrix element of a displacement operator in a Fock state with N photons then leads to

$$\mathcal{F}_{|N;\chi\rangle}(t) = L_N\left(2\pi\,|\langle\chi|S^*_{ba}\Lambda_t\rangle|^2\right) \tag{4.66}$$

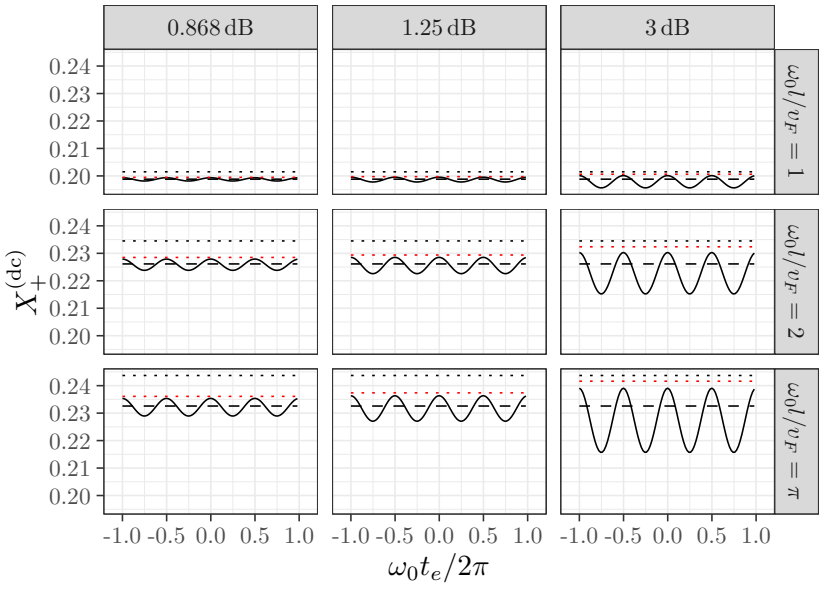

Figure 4.10: The various panels present the interference contrast $\left[X_+^{(\mathrm{dc})}\right]$ for Leviton excitations of width $\tau_e = 2.5\,\mathrm{ps}$ assuming a $10\,\mu\mathrm{m}$ long radiation coupler with $v_F = 10^5\,\mathrm{m\,s^{-1}}$ with coupling strength $\alpha = 1/5$. The plots show the absolute contrast as a function of the dimensionless injection time $\omega_0 t_e/2\pi$ for different values of the squeezing parameter z (expressed in dB) and different values of ω_0, ranging from $\omega_0 l/v_F = 1$ to $\omega_0 l/v_F = \pi$. Caption for the various line types is the same as for Fig. 4.8.

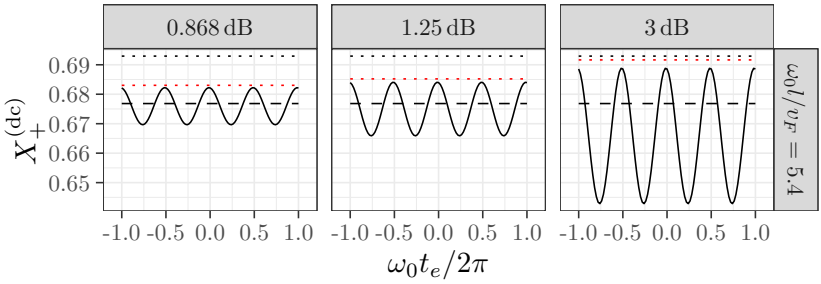

Figure 4.11: The various panels present the interference contrast $\left[X_+^{(\mathrm{dc})}\right]$ for Leviton excitations of width $\tau_e = 2.5\,\mathrm{ps}$ assuming a $10\,\mu\mathrm{m}$ long radiation coupler with $v_F = 10^5\,\mathrm{m\,s^{-1}}$ with coupling strength $\alpha = 15$. The plots show the absolute contrast as a function of the dimensionless injection time $\omega_0 t_e/2\pi$ for different values of the squeezing parameter z (expressed in dB) and $\omega_0 l/v_F = 5.5$ right on the first resonance observed on Fig. 2.13. Caption for the various line types is the same as for Fig. 4.8.

in which L_N is the N-th Laguerre polynomial and

$$\langle S_{ba}^* \Lambda_t | \chi \rangle = -\int_0^{+\infty} \frac{S_{ba}(\omega)}{\sqrt{\omega}} \mathrm{e}^{-\mathrm{i}\omega t} \chi(\omega)\, \frac{\mathrm{d}\omega}{2\pi}\,. \tag{4.67}$$

We now focus on the specific example of an EMP mode $\chi(\omega)$ centered at ω_0 with lorentzian lineshape of width γ_0, assuming ω_0/γ_0 significantly larger than unity, as expected from spontaneous emission by a quantum two level emitter.

Results and discussion

In order to determine whether or not single to few EMP detection is possible by the electron radar, we have numerically evaluated the quantity

$$x(t) = 2\pi\, |\langle \chi | S_{ba}^* \Lambda_t \rangle|^2 \tag{4.68}$$

in an experimentally realistic situation. More precisely, we assume that the radiation coupler consists of two counter propagating edge channels capacitively coupled over a distance $l = 10\,\mu\mathrm{m}$ (see Sec. 2.4) so that $v_F = 10^5\,\mathrm{m/s}$ leads to $v_F/l = 10\,\mathrm{GHz}$. Fig. 4.12 then depicts $|\Gamma_{ba}(\omega)|^2$ (dashed lines) as a function of $\omega l/v_F$ in the voltage locked ($\alpha = 1/10$)

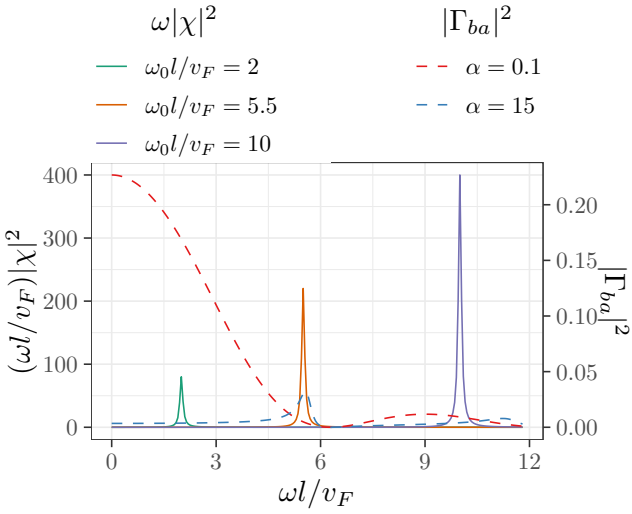

Figure 4.12: Current noise spectra for a single EMP of energy $\hbar\omega_0$ with Lorentzian linewidth γ_0 for $\omega l/v_F = 2$ (green curve), 5.5 (red curve) and 10 (purple curve) superimposed with $|\Gamma_{ba}(\omega)|^2$ defined by Eq. (4.17) for the model of two counter propagating edge channels (see Sec. 2.4) in the voltage locked regime ($\alpha = 1/10$, dashed red curve) and Coulomb blocked regime ($\alpha = 15$, dashed blue curve).

and Coulomb blocked ($\alpha = 15$) regimes. As explained in Appendix E, this describes how the radiation coupler filters the excess current noise associated with the EMPs propagating within the radiation channel. In the voltage locked regime, the radiation coupler acts as a low pass filter for the excess current noise whereas, in the Coulomb blocked regime, we see a resonance peak for $\omega_0 l/v_F = 5.5$. These curves are superimposed with the current noise power spectrum for a single EMP of duration $\gamma_0^{-1} = 1\,\mathrm{ns} = 10\, l/v_F$ and energy $\hbar\omega_0$ such that $\omega_0 l/v_F = 2$, 5.5 and 10 corresponding to respective frequencies 3.2 GHz, 8.75 GHz and 15.9 GHz.

Numerical estimates of $x(t)$ for the six sets of parameters (three EMP resonances and two values of α) considered on Fig. 4.12 are presented on Fig. 4.13. When the EMP resonance is chosen where $\Gamma_{ba}(\omega)$ has the highest values ($\omega_0 l/v_F = 2$ for the voltage locked regime and $\omega_0 l/v_F = 5.5$ for the Coulomb blocked regime), $x(t)$ values higher than 0.05 can be achieved.

At fixed $\omega_0 l/v_F$ the increase or decrease of the maximum value of $x(t)$

when going from the voltage locked to the Coulomb blocked regime is consistent with the evolution of the response $|\Gamma_{ba}(\omega_0)|^2$: it only increases when ω_0 is chosen at resonance where the $\Gamma_{ba}(\omega)$ response in enhanced when going from $\alpha = 1/10$ to $\alpha = 15$.

These numerical predictions can be fitted with an evaluation of $x(t)$ that exploits the narrow band structure of the EMP:

$$x(t) \simeq \frac{|S_{ba}(\omega_0)|^2}{\omega_0^2} \left| \int_0^{+\infty} \sqrt{\omega}\chi(\omega)\, \mathrm{e}^{-\mathrm{i}\omega t} \frac{\mathrm{d}\omega}{\sqrt{2\pi}} \right|^2 \tag{4.69}$$

As shown in Appendix E, the r.h.s. can then be rewritten as

$$x(t) = 2\pi \frac{\gamma_0}{\omega_0} \, |S_{ba}(\omega_0)|^2 \, \frac{\langle \mathcal{J}_Q(t) \rangle_{|1;\chi\rangle}}{\gamma_0 \hbar \omega_0} \, . \tag{4.70}$$

in which

$$\mathcal{J}_Q(t) = \frac{R_K}{2} \, : i(t)^2 : \, . \tag{4.71}$$

denotes the instantaneous heat current operator injected in the radiation channel expressed in terms of the electrical current $i(t)$. In the end, when γ_0/ω_0 is small enough and provided N is not very large, using the expansion $L_N(x) \simeq 1 - Nx + \mathcal{O}(x^2)$ for the Laguerre polynomial, we have:

$$\frac{[X_+(t)]_{|N;\chi\rangle}}{[X_+(t)]_{|0\rangle}} \simeq 1 - 2\pi N \frac{\omega_0}{\gamma_0} \, |S_{ba}(\omega_0)|^2 \, \frac{\langle \mathcal{J}_Q(t) \rangle_{|1;\chi\rangle}}{\gamma_0 \hbar \omega_0} \, . \tag{4.72}$$

The only hypothesis for deriving this expression is that the spectral width of the EMP is small compared to the scale of variation of the transparency $|S_{ba}(\omega)|^2$ of the radiation coupler, no matter the precise ω dependence of this quantity.

The precise comparison with numerical evaluations shows that the analytical result given by Eq. (4.70) is quite good except on very short time scales where the higher frequency details are expected to matter. It also departs from the numerical evaluation of $x(t)$ in the Coulomb blocked regime for $\omega_0 l/v_F = 5.5$. This is expected since this specific case is the one where the narrow band approximation used to derive the analytical expression is the least satisfied.

Finally, we have computed the dc-current contrast decrease, optimized over τ_2, for the examples considered here when injecting Leviton excitations of duration $\tau_e = l/10v_F = 10\,\mathrm{ps}$ compared to the same situation when the external radiation is switched off. Remember that, with

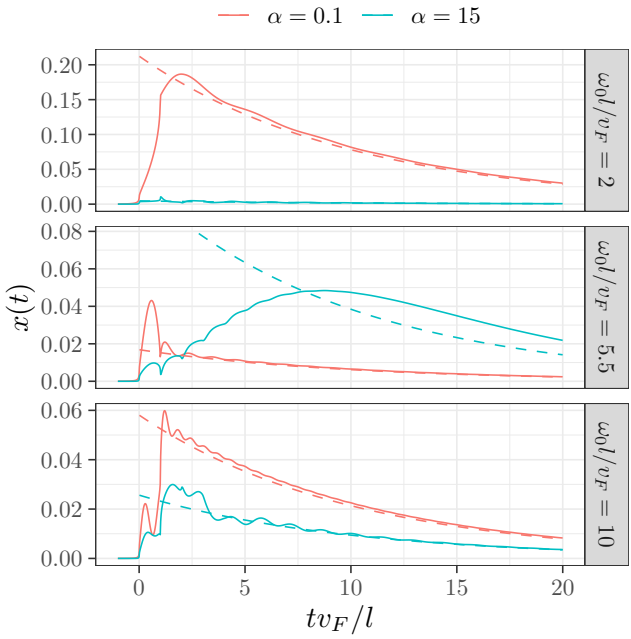

Figure 4.13: Plots of $x(t)$ as a function of tv_F/l when using a single energy EMP with energy $\hbar\omega_0$ and Lorentzian lineshape of width γ_0 using the model of two counter-propagating edge channels at $l/v_F = \gamma_0^{-1}/10$ in the voltage locked regime ($\alpha = 1/10$, red curves) and in the Coulomb blocked regime ($\alpha = 15$, blue curves). Three different values of $\omega_0 l/v_F$ have been considered: 2, 5.5 and 10. Dashed curves correspond to the analytic expression given by Eq. (4.70).

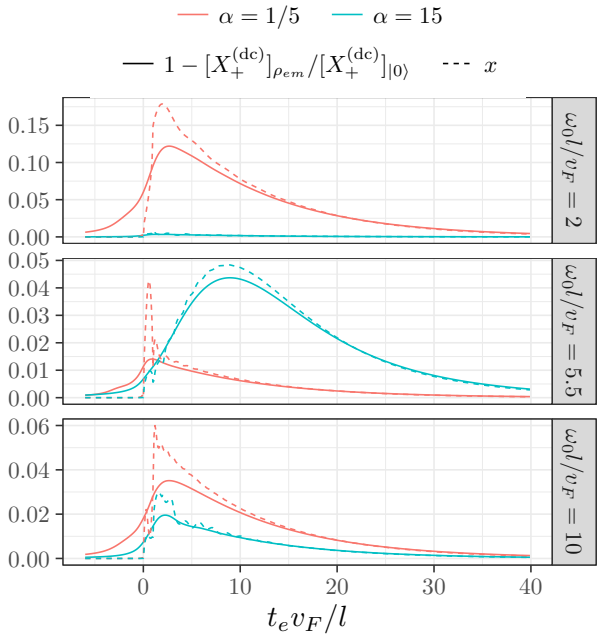

Figure 4.14: Plot of $X_+^{(\mathrm{dc})}$ as a function of the injection time t_e of a Leviton excitation of duraction $\tau_e = l/10v_F = \gamma_0 - 1/100$ with the same parameters as on Fig. 4.13. Dashed cuves correspond to $x(t_e)$.

the parameters considered here, the latter contrast is expected to be above 50 % (see Sec. 4.3.2). The results, presented on Fig. 4.14, confirm that an observable signal can be expected and that the relative contrast drop is not too far from the one obtained by using $|\mathcal{F}_{|1;\chi\rangle}(t_e)|$. The dominant effect in the amplitude of the effect comes from the transparenty of the radiation coupler in the bandwith of the incident radiation. The smoothing of the curves compared to $x(t)$ reflects the filtering of high frequencies associated with the finite duration of the Leviton as well as with electronic decoherence.

Chapter 5

Conclusion

5.1 Summary of the results

In this thesis, we have presented the theory of the single electron radar, an interferometric measurement system for classical or quantum electromagnetic fields operating in the microwave range. It leverages the electron's sensitivity to such fields in order to reconstruct pertinent information about them.

Our central result is the expression of this quantity as a convolution of an effective single particle scattering amplitude which encodes information on the external radiation by the fourth representation of the excess single electron coherence of the source. This fonction, which we call the electronic ambiguity function by analogy with the concept introduced by Woodward in classical radar theory [192], plays the role of the point spread function that describes the imaging through the MZI of the effective single particle scattering induced by the external radiation.

Explicit predictions for this effective single particle scattering are presented when the MZI is capacitively coupled to the external radiation. Various models of the component ensuring this capacitive coupling – the radiation coupler – have been considered.

In the introduction of this thesis, we had identified the performance objectives for this system:

1. Sensitivity to single-photon fields
2. Capability to probe quantum-state of the electromagnetic fields
3. Sensitivity to radiation modes down to GHz frequencies

4. Achievement of sub-nanosecond time resolution

5. Adjustable design characteristics

In order to discuss the first three items a realistic model for a capacitive coupler involving two capacitively coupled counter propagating edge channels has been considered.

Concerning the first item, we show that a single EMP propagating in the radiation edge channel could be detected since experimentally realistic parameters may lead a variation of the time resolved electronic interferences fringes of the order of 5 to 10 % over a baseline contrast above 50 % during the fly by of a single EMP. Concerning the seond item, by considering Gaussian states for the incident radiation, an operational criterion for squeezing detection for a mode in the GHz frequency range via short duration wavepackets is given. Realistic estimates suggest that a 1.25 to 3 dB squeezing within a nearby edge channel could, in principle lead to a potentially observable 0.5 % increase in the contrast of the Aharonov Bohm electronic interference fringes on the average dc current signal when using sufficiently short Leviton pulses. Although squeezed radiation has recently been generated within quantum Hall edge channels [9], these encouraging estimates call for further progresses in the generation and control of quantum states of EMPs. All computations are done for few to tens of ps Levitons which have sub-nanosecond time resolution, thereby ensuring the fourth point of the list.

Concerning the last item, we have discussed the potential of well known techniques from classical radar engineering such as randomization and chirping for improving our ability to probe very short dynamical time scales of the incident electromagnetic radiation. An interesting perspective would be to design a set of single electron excitations enabling a full reconstruction of the effective single-particle amplitude induced by the coupling to the external radiation. This question arises from the observation that, in the classical radar theory, infinite chirps [116] turn the signal of the radar into a Radon transform of the target's scattering amplitude for the electromagnetic radiation used to illuminate it. In this context, the inverse Radon transform, a technique commonly used in computated tomography scans [156], quantum optics [179, 128] and even for reconstructing the quantum state of solitary electrons [72], provides a tomographic reconstruction of the target's scattering amplitude. However, in the context considered in this work, due to the presence of the Fermi sea, perfect infinite chirps cannot be synthetized, thereby

leaving the problem of tomographic reconstruction of the effective single electron scattering amplitude open for further investigations.

5.2 Perspectives

5.2.1 Experimental implementation

Alongside our modeling efforts, the experimental team of Gwendal Fève – our collaborators – have implemented a single electron interferometric measurement of a time-dependent classical voltage. They achieved this by exploiting single-electron properties with a Fabry-Pérot Interferometer (FPI), depicted on the left panel of Fig. 5.1. The choice of the Fabry Perot geometry was mainly motivated by fabrication considerations: MZIs in the quantum Hall regime require the so-called "air bridge" to collect the electrical current from the internal part of the device [108]. By comparison, the Fabry-Pérot geometry is easier to manufacture.

In this setup, the Quantum Point Contacts QPC1 and QPC3 serve as adjustable electronic beam splitters, creating the Fabry-Pérot cavity. The intermediate QPC2 is always left open. Consequently as the propagation is chiral, electrons circulate unidirectionally within the cavity, entering before QPC3 and exiting after QPC1. QPC2 is polarized using two different lines. As such it serves a dual purpose: the top part is connected to an a.c. line and is used to apply tha classical time dependent branch to the upper part of the internal loop of the FP interferometer. The bottom part of QPC2 is connected to a d.c. line and is used to slightly change the area delimited by the internal loop via the application of a d.c. voltage.

The Fabry-Pérot cavity permits multiple reflections and therefore is much more complicated to analyze in the presence of electronic decoherence than the MZI. However, in the experiment performed in Paris, several experimental facts were observed when feeding the interferometer with a dc current bias an applying no time dependent voltage ($V(t) = 0$ on Fig. 5.1) [69, 113]:

- First of all the interference pattern was not observed in function of the Aharonov Bohm flux threading the interferometer but in function of the d.c. voltage bias applied to the lower top gate of QPC2 (V_{dc} on Fig. 5.1). This means that the FP interferometer is indeed dominated by Coulomb charging effects [98] which is not the regime considered in the present thesis.

- The dependence on the gate voltage only involved one harmonic: this means that contributions stemming from paths which wind more than once are heavily suppressed, probably by electronic decoherence. In other terms, in practice, the FP interferometer effectively behaves as a MZI.

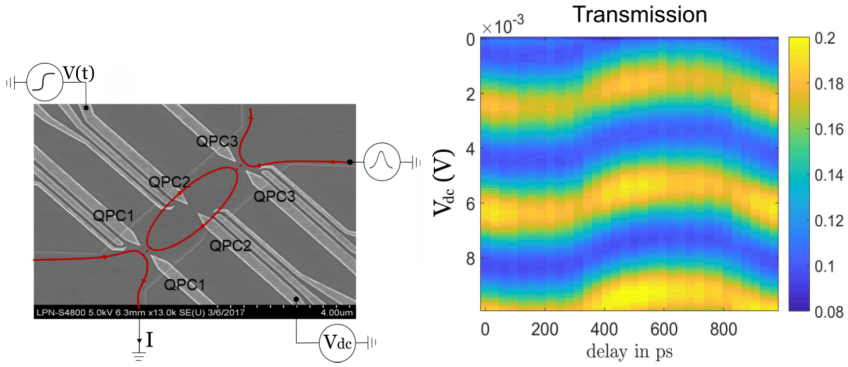

Figure 5.1: *Left panel*: Electronic microscope image of the electronic Fabry-Pérot interferometer. An alectronic cavity is delimited by QPC1 and QPC3 whereas QPC2 is used to deform the cavity with a dc voltage bias applied to the bottom lower branch top gate whereas a time dependent voltage (the classical radiation) is applied to the upper branch top gate. The average dc current is measured after QPC1. *Right panel*: Experimental data for the normalized average dc current as a function of the dc voltage bias ($V_{\rm dc}$ – vertical axis) and the injection time of the Levitons (horizontal axis).

Gwendal Fève's team the conducted this experiment using probing single electrons with a train of Leviton excitations of typical width 35 ps separated by 1 ns. A sinusoidally oscillating voltage $V(t)$ at a frequency of 1 GHz was then applied to the ac port of QPC2. The frequency of the Leviton train matches the one of the time periodic voltage we wish to probe in order to ensure that each Leviton of the train is injected at the same time modulo the period. Then, the average DC current exiting the interferometer is measured over a large number of periods to obtain a good signal to noise ratio. Finally, $V_{\rm dc}$ is varied to reveal the interference pattern of the FP interferometer and the time delay of the Leviton train is also varied so that the single electron excitations sample the voltage induced phase at different times.

The results are displayed on the right panel of Fig. 5.1. Here, the Transmission, a representation of the normalized current, is shown as a function of the Leviton injection time (horizontal axis) and of the dc potential potential $V_{\rm dc}$. At fixed injection time, the $V_{\rm dc}$ oscillation is the interference pattern of the FP interferometer. As the injection time of the Leviton is varied, it experiences the electrostatic phase associated with the polarization of the upper top gate of QPC2 at a different time. Because the duration of the Leviton as well as its time of flight beneath this top gate is very short, it samples the ac voltage $V(t)$ within a certain time window which is sliding as the injection time is varied.

This explains why the right panel of Fig. 5.1 displays a fringe pattern (in function of $V_{\rm dc}$) that follows the time dependence of $V(t)$ over a period of 1 ns, consistent with frequency 1 GHz of the ac drive $V(t)$.

This first experiment validates the concept of a single electron interferometer to probe electromagnetic field with sub-nanosecond time scales. Of course, this is only a first proof of concept for classical radiation but it is a first important step. Work is in progress to attempt a quantitative analysis of the experimental data beyond the simple single particle scattering approach presented in [113].

The path forward will involve using a Mach-Zehnder Interferometer (MZI) setup to demonstrate the electron radar and try to probe quantum radiation instead of classical one. The idea would be to use another quantum Hall edge channel as the radiation channel in order to minimize the risks associated with sample fabrication. Future endeavors will aim to corroborate our predictions through the probing of the squeezed vacuum and Fock states for the EMPs. However this is not a purely experimental challenge. The weak signals unraveled by the work presented in this PhD suggest that further theoretical explorations will help making suitable choices for the sample design.

First of all, a modelization effort of quantum radiation sources within quantum Hall edge channels should be pursued. For example, although squeezing has been observed within quantum Hall edge channel in a consistent way with theoretical predictions [9], this work only considered mode at a given frequency. Understanding the full structure of time dependent fluctuations of the current at the output of a driven QPC is work in progress by G. Rebora, I. Safi and P. Degiovanni. This will help identifying the best modes for sub-vacuum detection and thus put constraints on the radiation coupler design.

This motivates a detailed exploration and comparison of the various

radiation couplers introduced in Chapter 2 to put all chances of observing squeezing on our side. The shaping of the electronic wave packets may also be explored with the same perspective.

Finally, single EMP generation has also never been demonstrated and proposals for single EMP sources should be explored. A preliminary step in this direction consists of an in-depth study of EMP cavities, a line of research currently explored by Gerbold Ménard in G. Fève's group.

5.2.2 Towards quantum metrology

Carl W. Helstrom recognized the inherent complexities brought by wave-particle duality to measurement close to the quantum limit. This understanding acknowledged two major conjugated constraints: the diffraction limit and photon shot noise. In 1969, Helstrom tackled these fundamental issues head-on, publishing a groundbreaking paper on quantum measurement [101]. He innovatively applied the statistical theory of estimation to the quantum realm, giving birth to a new reformulation known as quantum estimation theory [102]. In this paper, Helstrom presented a key theoretical tool known as the Helstrom information, symbolized as $\mathrm{HI}(\theta)$. This quantity provides a means to identify the utmost resolution achievable when estimating a parameter θ (such as the squeezing parameter or any parameter parametrizing a family of quantum states to be discriminated by the electron radar) of a quantum system represented by a density matrix ρ. The unique aspect of this tool is its applicability regardless of the type of measurement apparatus employed for the estimation process. Formally, for any unbiased estimator $\hat{\theta}$ of a measurement series, the variance $\mathrm{var}\left(\hat{\theta}\right)$ always exceed the reciprocal of the Helstrom information at the corresponding θ value, represented as:

$$\mathrm{var}\left(\hat{\theta}\right) \geq \mathrm{HI}^{-1}(\theta)\,. \tag{5.1}$$

This inequality generalizes the Cramer Rao inequality in classical estimation theory, which essentially has the same form with the Fisher information replacing $\mathrm{IH}(\theta)$. These tools have been extensively used in quantum metrology with applications to atomic clocks and atom interferometers and discussions of quantum-enhancement of metrological performances via many-body entanglement [151].

We think that this framework could be used to characterize the metrological performances of the electron radar. The computation of $\mathrm{HI}(\theta)$ would signify the maximal resolution limit that the radar can ever

aspire to achieve in the estimation of θ. A more realistic determination of the radar's resolution can be achieved by evaluating the variance of the measured quantities in the electron radar by incorporating all noise sources of the experimental system. One could then infer from this an estimation of var $\left(\hat{\theta}\right)$ during a measurement process. This method allows for a quantifiable measure of how closely the radar's resolution approaches the theoretical limit given by the inverse of the Helstrom information.

5.2.3 Signal processing techniques

On a more practical level, parameter estimation in the experiment involves the marriage of carefully designed measurements protocols and sophisticated post-processing algorithms that efficiently extract estimated parameters from raw data. This require inverting the linear problem which consists of the radar equation in the presence of noise. This is a well known problem in signal processing for which well known techniques exist. The single electron tomography presented in [16] uses max-like estimation from a constrained Bayesian framework to determine the single electron coherence from the experimental noise data measured at the output of the HOM interferometer. Using such deconvolution algorithms will certainly be extremely useful for reconstructing the effective single electron scattering matrix defined by the amplitudes $\widetilde{R}(\omega, \tau)$.

Further research avenues may include the identification and cataloging of typical radiation signatures when subjected to radar probing. With this catalogue of signatures, an unknown radiation's most probable properties could be swiftly discerned when probed, by cross-referencing with the list of known signatures. This methodology presents an exciting prospect for future research in electronic radar technology.

Appendix A

Notations and normalizations

In this appendix, we first recall the basic conventions used for fermionic modes and electronic single particle states within the present work. We also present the conventions used for bosonic excitations.

A.1 Electronic modes and wave packets

The mode decomposition for fermionic fields is defined by

$$\psi(t) = \int_{\mathbb{R}} c(\omega)\, \mathrm{e}^{-\mathrm{i}\omega t} \frac{\mathrm{d}\omega}{\sqrt{2\pi v_F}} \tag{A.1}$$

so that these modes obey the canonical anticommutation relations

$$\{c(\omega), c^\dagger(\omega')\} = \delta(\omega - \omega')\,. \tag{A.2}$$

Equivalently, we have

$$c(\omega) = \sqrt{\frac{v_F}{2\pi}} \int_{\mathbb{R}} \psi(t)\, \mathrm{e}^{\mathrm{i}\omega t} \mathrm{d}t\,. \tag{A.3}$$

Given an electronic wave packet described by a normalized wave function $\varphi_{\mathrm{e}}(x)$ such that

$$\int_{\mathbb{R}} |\varphi_{\mathrm{e}}(x)|^2\, \mathrm{d}x = 1 \tag{A.4}$$

Throughout this paper, we will use the notation $\varphi_{\mathrm{e}}(t)$ for $\varphi_{\mathrm{e}}(-v_F t)$ so that

$$v_F \int_{\mathbb{R}} |\varphi_{\mathrm{e}}(t)|^2\, \mathrm{d}t = 1\,. \tag{A.5}$$

We define

$$\widetilde{\varphi}_{\mathrm{e}}(\omega) = v_F \int_{\mathbb{R}} \varphi_{\mathrm{e}}(t)\, \mathrm{e}^{\mathrm{i}\omega t}\, \mathrm{d}t \tag{A.6}$$

so that

$$\frac{1}{v_F} \int_{\mathbb{R}} |\widetilde{\varphi}_{\mathrm{e}}(\omega)|^2\, \frac{\mathrm{d}\omega}{2\pi} = 1\,. \tag{A.7}$$

The creation operator for the electronic wave packet φ_{e} is then defined as

$$\psi^\dagger[\varphi_{\mathrm{e}}] = v_F \int_{\mathbb{R}} \varphi_{\mathrm{e}}(t) \psi^\dagger(t)\, \mathrm{d}t \tag{A.8a}$$

$$= \int_{\mathbb{R}} \widetilde{\varphi}_{\mathrm{e}}(\omega) c^\dagger(\omega)\, \frac{\mathrm{d}\omega}{\sqrt{2\pi v_F}} \tag{A.8b}$$

A.2 Conventions for bosonic excitations

A normalized excitation is described by $\chi(\omega)$ for $\omega > 0$ such that

$$\int_0^{+\infty} |\chi(\omega|^2\, \frac{\mathrm{d}\omega}{2\pi} = 1 \tag{A.9}$$

so that the single particle state

$$|\chi\rangle = \int_0^{+\infty} \chi(\omega)\, b^\dagger(\omega)\, |\emptyset\rangle\, \frac{\mathrm{d}\omega}{\sqrt{2\pi}} \tag{A.10}$$

is normalized. If we define the corresponding creation operator

$$b^\dagger[\chi] = \int_0^{+\infty} \chi(\omega)\, b^\dagger(\omega)\, \frac{\mathrm{d}\omega}{\sqrt{2\pi}} \tag{A.11}$$

and its hermitian conjugate $b[\chi]$, these operators obey the commutation relations

$$\Big[b[\chi_1], b^\dagger[\chi_2]\Big] = \langle \chi_1 | \chi_2 \rangle\, \mathbf{1} \tag{A.12}$$

where $\langle \chi_1 | \chi_2 \rangle$ denotes the scalar product

$$\langle \chi_1 | \chi_2 \rangle = \int_0^{+\infty} \chi_1(\omega)^* \chi_2(\omega)\, \frac{\mathrm{d}\omega}{2\pi}\,. \tag{A.13}$$

on the space $\mathcal{L}_2(\mathbb{R}^+)$ of square summable functions on $\mathbb{R}^+$. Note that with these conventions $\chi(\omega) = \sqrt{2\pi}\, \langle \omega | \chi \rangle$ where $|\omega\rangle = b^\dagger(\omega)\, |\emptyset\rangle$ is the single photon state resolved in energy.

Finally, when given an orthonormal basis of normalized single particle states $|\chi_n\rangle$ indexed by n, the mode operators $b(\omega)$ can be expressed in terms of the $b_n = b[\chi_n]$ as

$$b(\omega) = \frac{1}{\sqrt{2\pi}} \sum_n \chi_n(\omega)\, b_n \,. \tag{A.14}$$

Starting from a normalized single particle state $|\chi\rangle$, we can express $b^\dagger(\omega)$ in terms of $b^\dagger[\chi]$ and of $b^\dagger[\chi_\perp]$ where $|\chi_\omega^\perp\rangle$ denotes the normalized projection of $|\omega\rangle$ on the space of single particle excitations orthogonal to $|\chi\rangle$:

$$b^\dagger(\omega) = \langle\chi|\omega\rangle\; b^\dagger[\omega] + \sqrt{1 - |\,\langle\chi|\omega\rangle\,|^2}\, b^\dagger[\chi_\omega^\perp] \,. \tag{A.15}$$

Appendix B

Derivation of the radar equation

In this Appendix, the single radar equation for the outgoing average electrical current is derived. We will first derive it within the framework of time dependent single particle scattering theory (linear electron quantum optics) using a technique which can then be adapted to the presence of Coulomb interaction effects which belong to the non-linear regime of electron quantum optics.

B.1 Time-dependent single particle scattering approach

We consider a MZI as depicted on Fig. 3.6 and discussed in Sec. 3.2.1. Let us recall that the single electron scattering matrices of the two QPC are assumed to be energy independent and given by:

$$S_\alpha = \begin{pmatrix} \sqrt{T_\alpha} & \mathrm{i}\sqrt{R_\alpha} \\ \mathrm{i}\sqrt{R_\alpha} & \sqrt{T_\alpha} \end{pmatrix} \tag{B.1}$$

in which T_α and R_α respectively denote the transmission and reflection probabilities at QPC $\alpha = A$ or B ($T_\alpha + R_\alpha = 1$).

The main idea is to express the outgoing electron field in branch 1 in terms of incoming fields by back-tracing it from the output to the input of the MZI interferometer. Assuming free propagation long the branch

2, with time of flight τ_2 leads to

$$\psi_{1\mathrm{out}}(t) = \sqrt{T_B}\,\psi_{1,B_-}(t) + \mathrm{i}\sqrt{R_B}\,\psi_{2,B_-}(t) \tag{B.2a}$$

$$= \mathrm{i}\sqrt{R_B}\,\mathrm{e}^{-i\phi_{\mathrm{AB}}/2}\left(\sqrt{T_A}\,\psi_{2\mathrm{in}}(t-\tau_2)\right.$$

$$\left. + \mathrm{i}\,\sqrt{R_A}\,\psi_{1\mathrm{in}}(t-\tau_2)\right) \tag{B.2b}$$

$$+ \sqrt{T_B}\,\mathrm{e}^{\mathrm{i}\phi_{\mathrm{AB}}/2}\psi_{1,B_-}(t) \tag{B.2c}$$

in which $\psi_{\alpha,B_-}(t)$ denotes the fermionic field right before the QPC B and $\psi_{\alpha_{\mathrm{in}}}(t)$ denotes the incoming fields right before QPC A. Equation (B.2c) involves the outgoing fermionic field from the radiation coupler. In the case where propagation within this region can be described by a time dependent linear scattering, we can relate it linearly to the incoming field ψ_{1,A_+} by

$$\psi_{1,B_-}(t) = \int_{\mathbb{R}} R(t,t')\psi_{1,A_+}(t')\,\mathrm{d}t' \tag{B.3}$$

which assumes that no electron can be injected from any other channel than the branch 1 of the MZI[1]. This enables us to write down the fully general expression for the outgoing electrical current $i_{1\mathrm{out}}(t) = -ev_F : (\psi^\dagger_{1\mathrm{out}}\psi_{1\mathrm{out}}) : (t)$ in terms of the incoming electronic fields. We obtain the outgoing current operator $i_{1\mathrm{out}}(t)$ as

$$i_{1\mathrm{out}}(t) = \widehat{I}_0(t) - e\left(\mathrm{e}^{\mathrm{i}\varphi_{\mathrm{AB}}}\widehat{I}_+(t) + \mathrm{e}^{-\mathrm{i}\varphi_{\mathrm{AB}}}\widehat{I}_-(t)\right) \tag{B.4}$$

in which, at the operator level

$$\widehat{I}_+(t) = -\mathrm{i}\sqrt{T_B R_B}\int_{\mathbb{R}} R(t,t')\left[\sqrt{T_A}\psi^\dagger_{2_{\mathrm{in}}} - \mathrm{i}\sqrt{R_A}\psi_{1_{\mathrm{in}}}\right](t-\tau_2)$$

$$\times\left[\sqrt{T_A}\psi_{1_{\mathrm{in}}} + \mathrm{i}\sqrt{R_A}\psi_{2_{\mathrm{in}}}\right](t')\,\mathrm{d}t'\,. \tag{B.5}$$

When computing the average current, only terms that contain the same numbers of $\psi^\dagger_{\alpha_{\mathrm{in}}}$ and $\psi_{\alpha_{\mathrm{in}}}$ are retained since the MZI is fed by two independent electron sources. Consequently the AB-flux dependent part of the average current is $\langle I_+(t)\rangle = -e\sqrt{R_A T_A R_B T_B}\,X_+(t)$ where

$$X_+(t) = \int_{\mathbb{R}} R(t,t')\left(\mathcal{G}^{(e)}_{1\mathrm{in}} - \mathcal{G}^{(e)}_{2\mathrm{in}}\right)(t'|t-\tau_2)\,\mathrm{d}t'\,. \tag{B.6}$$

[1]We will discuss other cases later but for the average current, any other contribution would be irrelevant.

This is the time domain electron radar equation given by Eq. (4.10). When the electron source is connected to $1_{\rm in}$, after introducing the ambiguity function $A_S(\Omega,\tau)$ of the source S defined by Eq. (3.37) and $\tilde{R}(\Omega,\tau)$ defined by Eq. (3.35), we finally obtain the electron radar equation under the form given by Eq. (3.34). Note that, within the single particle scattering formalism, this equation is valid for any electron source, not necessarily emitting a single electron excitation.

B.2 The interacting case

B.2.1 The plasmon scattering approach

Let us now consider the case where Coulomb interactions cannot be neglected within the radiation coupler. We shall model it using the EMP scattering formalism discussed in Sec. 2.2.1.

Note that the starting point of Eq. (B.2) is still valid. But, contrary to the previous paragraph, the main challenge is now to backtrack the fermionic field along the branch 1 of the MZI. Equivalently, we have to express $\psi_{1,B_-}(t)$ in terms of the incoming fields $\psi_{\alpha_{\rm in}}$ for $\alpha = 1,\, 2$. In order to do so, we consider the fermionic field $\psi_{1,B_-}(t)$, expressed it in terms of the outgoing edge-magnetoplasmon modes and use the edge-magnetoplasmon scattering matrix to express it in terms of the incoming modes into the radiation coupler.

To simplify the notation, the EMP modes along the branch 1 of the MZI will be denoted by $b_\alpha(\omega)$ with $\alpha = {\rm in}$ or $\alpha = {\rm out}$ depending whether they are incoming (position A_+) or outgoing (position B_-). In the same way, the electromagnetic modes within the radiation channel are denoted by $a_\alpha(\omega)$. The scattering matrix describing the coupling between the edge channel and the electromagnetic modes is

$$S(\omega) = \begin{pmatrix} S_{bb}(\omega) & S_{ba}(\omega) \\ S_{ab}(\omega) & S_{aa}(\omega) \end{pmatrix} \tag{B.7}$$

so that

$$\begin{pmatrix} b_{\rm out}(\omega) \\ a_{\rm out}(\omega) \end{pmatrix} = S(\omega) \begin{pmatrix} b_{\rm in}(\omega) \\ a_{\rm in}(\omega) \end{pmatrix} \tag{B.8}$$

Using the bosonization formula for the fermionic field,and back-propagating the bosonic mode operators across the radiation coupler, $\psi_{1{\rm out}}(t)$ can be expressed as

$$\psi_{1,B_-}(t) = {\rm e}^{{\rm i}\Theta}\psi_{1,A_+}(t)\, D_{b_1}[(S_{bb}^*-1)\Lambda(t)] \otimes D_a[S_{ba}^*\Lambda(t)] \tag{B.9}$$

where the phase Θ is independent from t. Therefore, we need to compute the correlator $\mathcal{G}^{(e)}_{\rho_i,B_-}(1,t|2,t)$ which is equal to

$$\langle \psi^\dagger_{2,A_+}(t-\tau_2)\psi_{1,A_+}(t)\, D_{b_1}[(S^*_{bb}-1)\Lambda(t)]\, D_a[S^*_{ba}\Lambda(t)]\rangle \tag{B.10}$$

in which the correlator is taken over the incoming many-body state $\rho_i = \rho_S \otimes \rho_{\rm em}$ which is the tensor product of the many body electronic state ρ_S injected by the source by the incoming radiation state $\rho_{\rm em}$ for the $a(\omega)$ modes.

B.2.2 The Franck-Condon factor

Let us now discuss how the correlator (B.10) can be evaluated. First of all, the part that depends on the incident radiation state $\rho_{\rm em}$ can be singled out thanks to the identity:

$$\begin{aligned}\langle D_a[S^*_{ba}\Lambda(t)]\rangle_{\rho_{\rm em}} &= \langle D_a[S^*_{ba}\Lambda(t)]\rangle_{|0\rangle} \\ &\quad\times \langle :\, D_a[S^*_{ba}\Lambda(t)]\, :\rangle_{\rho_{\rm em}}\end{aligned} \tag{B.11}$$

in which we have introduced the bosonic normal ordering $:\cdots:$. All the dependence in the incident radiation state $\rho_{\rm em}$ is thus contained in the average value of the normal ordered displacement operator $:D_a[S^*_{ba}\Lambda(t)]:$ for the $a(\omega)$ modes. The average value $\langle D_a[S^*_{ba}\Lambda(t)]\rangle_{|0\rangle}$ is taken over the vacuum state for the $a(\omega)$ modes which means that it can be reabsorbed into the correlator given by Eq. (B.10) except that this time the quantum average is taken over the state $\rho_{S,0} = \rho_S \otimes |0\rangle\langle 0|$. This can be summarized by

$$\mathcal{G}^{(e)}_{\rho_i,B_-}(1,t|2,t) = \mathcal{G}^{(e)}_{\rho_{S,0},B_-}(1,t|2,t) \tag{B.12a}$$

$$\times \langle :\, D_a[S^*_{ba}\Lambda(t)]\, :\rangle_{\rho_{\rm em}} \tag{B.12b}$$

since $\rho_{S,0} = \rho_S \otimes |0\rangle\langle 0|$ corresponds to a situation where no incident radiation is sent onto the MZI. Therefore, the correlator $\mathcal{G}^{(e)}_{\rho_{S,0},B_-}(1,t|2,t)$ is exactly the one appearing when computing the average current flowing out of the MZI in the absence of electromagnetic radiation sent onto it via the $a(\omega)$ modes. This problem corresponds to the problem of electronic decoherence within the MZI.

In the end, the effect of the radiation injected into the radiation coupler is described by the factor

$$\mathcal{F}_{\rho_{\rm em}}(t) = \langle :\, D_a[S^*_{ba}\Lambda(t)]\, :\rangle_{\rho_{\rm em}} \tag{B.13}$$

which is the exact analogous of the Franck-Condon factor that appears in the spectroscopy of complex molecules [49].

B.2.3 Electronic propagation contribution

The electronic coherence $\mathcal{G}^{(e)}_{\rho_{S,0},B_-}(1,t|2,t)$ is more difficult to evaluate because it corresponds to the outgoing single electron coherence after propagation across the MZI in the presence of Coulomb interactions within the branch 1 of the MZI. It turns out that simple and physically transparent expressions can be found in the case where S is an ideal single electron source. In this case, the state S is of the form

$$\rho_S = \psi^\dagger_{1\mathrm{in}}[\varphi_e]\,|F\rangle\,\langle F|\,\psi_{1\mathrm{in}}[\varphi_e] \tag{B.14}$$

where $|F\rangle$ corresponds to the Fermi sea with chemical potential $\mu = 0$ in the two incoming electronic channels of the MZI and $\psi^\dagger_{1\mathrm{in}}[\varphi_e]$ creates a single electron excitation with with wave function φ_e injected into the MZI (position A_-).

Expressing $\psi^\dagger_{1\mathrm{in}}[\varphi_e]$ in terms of $\psi^\dagger_{1,A_+}[\varphi_e]$ and $\psi^\dagger_{2,A_+}[\varphi_e]$ enables us to show that

$$\begin{aligned}\mathcal{G}^{(e)}_{\rho_{S,0},B_-}(1,t|2,t) = -\mathrm{i}\sqrt{R_A T_A} \times \langle F,0_a|\psi_{2,A_+}[\varphi_e]\psi^\dagger_{2,A_+}(t-\tau_2)\\ \psi_{1,B_-}(t)\psi^\dagger_{1,A_+}[\varphi_e]|F,0_a\rangle \qquad \text{(B.15a)}\\ = -\mathrm{i}\sqrt{R_A T_A}\ \times \langle F_2|\psi_{2,A_+}[\varphi_e]\psi^\dagger_{2,A_+}(t-\tau_2)|F_2\rangle\\ \times \langle F_1,0_a|\psi_{1,B_-}(t)\psi^\dagger_{1,A_+}[\varphi_e]|F_1,0_a\rangle \qquad \text{(B.15b)}\end{aligned}$$

in which $|F,0_a\rangle$ denotes the tensor product of the Fermi sea in both branches of the MZI and the ground state for the environmental modes. Since φ_e is an electronic excitation above the Fermi level, the contribution associated with propagation along the branch 2 of the MZI can be readily evaluated:

$$\langle\psi_{2,A_+}[\varphi_e]\psi_{2,A_+}(t-\tau_2)\rangle_{|F_2\rangle} = \varphi_e(t-\tau_2)^*\,. \tag{B.16}$$

We are thus left with evaluating:

$$\begin{aligned}\langle\psi_{1,B_-}(t)\psi^\dagger_{1,A_+}[\varphi_e]\rangle_{|F_1,0_a\rangle} =\\ \int_{\mathbb{R}} v_F\varphi_e(t')\langle\psi_{1,B_-}(t)\psi_{1,A_+}(t')\rangle_{|F_1,0_a\rangle}\,\mathrm{d}t'\,.\end{aligned} \tag{B.17}$$

The time domain amplitude

$$\mathcal{Z}_1(\tau) = v_F\langle\psi_{1,B_-}(\tau)\psi^\dagger_{1,A_+}(0)\rangle_{|F_1,0_a\rangle} \tag{B.18}$$

is the elastic single electron scattering amplitude across the branch 1 of the MZI. It is related to the elastic scattering amplitude $\mathcal{Z}_{\mathrm{el},1}(\omega)$ computed in Refs. [52, 65] by a Fourier transform:

$$\mathcal{Z}_1(\tau) = \int_0^{+\infty} \mathcal{Z}_{\mathrm{el},1}(\omega_e)\, \mathrm{e}^{-\mathrm{i}\omega_e \tau} \frac{\mathrm{d}\omega_e}{2\pi}\,. \tag{B.19}$$

A direct evaluation of the r.h.s. of Eq. (B.18) from bosonization leads to Eq. (4.6) whereas the evaluation of $\mathcal{Z}_{\mathrm{el},1}(\omega)$ can be done using the expressions given in Ref. [66, 35] which we recall here for completeness:

$$\mathcal{Z}_{\mathrm{el},1}(\omega) = 1 + \int_0^{\omega} B(\omega')\, \mathrm{d}\omega' \tag{B.20}$$

in which $B(\omega)$ is the solution of the integral equation

$$\omega B(\omega) = S_{bb}(\omega) - 1 + \int_0^{\omega} B(\omega')(S_{bb}(\omega') - 1)\mathrm{d}\omega' \tag{B.21}$$

with initial condition $B(0^+) = (\mathrm{d}S_{bb}/\mathrm{d}\omega)(\omega = 0^+)$. Finally, we obtain:

$$\langle \psi_{1,B_+}(t)\psi^\dagger_{1,A_+}[\varphi_e]\rangle_{|F_1,0_a\rangle} = \int_{\mathbb{R}} \varphi_e(t')\mathcal{Z}_1(t-t')\, \mathrm{d}t'\,. \tag{B.22}$$

The correlator $\langle \psi_{2,A_+}[\varphi_e]\psi^\dagger_{2,B_-}(t-\tau_2)\rangle_{|F_2\rangle}$ could also rewritten in a similar way

$$\langle \psi_{2,A_+}[\varphi_e]\psi^\dagger_{2,B_-}(t)\rangle_{|F_2\rangle} = \int_{\mathbb{R}} \varphi_e(t')^* \mathcal{Z}_2(t-t')^*\, \mathrm{d}t' \tag{B.23}$$

using the elastic scattering amplitude $\mathcal{Z}_2(\tau) = \delta(\tau - \tau_2)$ corresponding to ballistic propagation during time of flight τ_2.

Note that this form of the correlator $\langle \psi_{2,A_+}[\varphi_e]\psi_{2,B_-}(t)\rangle$ remains valid in the presence of electronic decoherence along branch 2 of the MZI provided it is not caused by direct or indirect interactions (bath mediated) between the two branches of the MZI. This means that there must be no crosstalk between the two branches: each of these branch do interact with their own environment which are prepared in their ground states. In this case, we should use the elastic scattering amplitude $\mathcal{Z}_{\mathrm{el},2}(\omega_e)$ for $\omega_e > 0$ to define $\mathcal{Z}_2(\tau)$. The elastic scattering amplitude $\mathcal{Z}_{\mathrm{el},2}(\omega_e)$ can be computed in terms of the finite frequency admittance of the branch 2.

B.2.4 General result

Let us finally collect the general result for the inter-branch coherence $\mathcal{G}_{\rho_{S,0},B_-}(1,t|2,t)$ right before the second QPC in the general situation where each of the branches involves Coulomb interactions, and possibly a coupling to its own radiation channel fed by the vacuum state. In the absence of external radiation, the expression

$$v_F \mathcal{G}^{(e)}_{\rho_{S,0},B_-}(1,t|2,t) = \int_{\mathbb{R}^2} v_F \varphi_e(t-\tau_1)\,\varphi_e(t-\tau_2)^*\,\mathcal{Z}_1(\tau_1)\,\mathcal{Z}_2(\tau_2)\,\mathrm{d}\tau_1\,\mathrm{d}\tau_2 \tag{B.24}$$

has a physically transparent interpretation: each wave packet gets propagated according to the elastic scattering amplitude $\mathcal{Z}_\alpha(\tau)$ along the corresponding branch.

In the presence of incoming radiation arriving on each radiation coupler of each branch α in independent respective quantum stated described by the density operators $\rho_{\mathrm{em},\alpha}$, Eq. (B.12) generalizes to

$$\begin{aligned}\mathcal{G}^{(e)}_{\rho_i,B_-}(1,t|2,t) = \mathcal{G}^{(e)}_{\rho_{S,0},B_-}(1,t|2,t)\times \\ \prod_{\alpha=1,2} \left\langle : D_{a_\alpha}\left[\left(S^{(\alpha)}_{ba}\right)^* \Lambda(t)\right] : \right\rangle_{\rho_{\mathrm{em},\alpha}}\end{aligned} \tag{B.25a}$$

In the end, the interference signal $X_+(t)$ is given by

$$\begin{aligned}X_+(t) = v_F \int_{\mathbb{R}^2} \varphi_e(t-\tau_1)\varphi_e(t-\tau_2)^*\times \\ R_{\mathrm{eff},1}(t,t-\tau_1)\,R_{\mathrm{eff},2}(t,t-\tau_2)\,\mathrm{d}\tau_1,\mathrm{d}\tau_2\end{aligned} \tag{B.26}$$

in which the effective single particle scattering amplitudes are given by the product of the elastic scattering amplitude by the Franck-Condon factor:

$$R_{\mathrm{eff},\alpha}(t,t') = \mathcal{Z}_\alpha(t-t')\,\mathcal{F}_{\rho_{\mathrm{em},\alpha}}(t) \tag{B.27}$$

thus leading to the single electron radar equation (4.10) which reduces to Eq. (4.11) in the case of ballistic propagation in time τ_2 along branch 2 and no coupling to external radiation on this branch.

Last but not least, in the presence of Coulomb interactions, the radar equation is valid only for an incoming single electron excitation injected into the electronic MZI!

Appendix C

Squeezing

C.1 Squeezed vacuum in a single mode

In this Appendix, we recall the basics needed to describe the squeezed vacuum for a single mode[1]:

$$|\mathrm{Sq}_z\rangle = \mathrm{e}^{z(a^\dagger)^2 - z^* a^2}\,|0\rangle \tag{C.1}$$

where a and $a^\dagger$ are the creation and destruction operators for a single mode and $z \in \mathbb{C}$. The squeezing operator $\mathbb{S}_z$ equal to $\mathrm{e}^{z(a^\dagger)^2 - z^* a^2}$, performs a Bogoliubov transformation on the original mode operators:

$$\mathbb{S}_z^\dagger a\, \mathbb{S}_z = \cosh(2|z|)\, a + \mathrm{e}^{\mathrm{i}\varphi} \sinh(2|z|)\, a^\dagger\,. \tag{C.2}$$

This enables us to compute the expectation value of any products of a and $a^\dagger$ in the state $|\mathrm{Sq}_z\rangle$ as the expectation value of the same expression in terms of the Bogoliubov transformed operators

$$a_z = \cosh(2|z|)\, a + \mathrm{e}^{\mathrm{i}\varphi} \sinh(2|z|)\, a^\dagger \tag{C.3a}$$

$$a_z^\dagger = \cosh(2|z|)\, a^\dagger + \mathrm{e}^{\mathrm{i}\varphi} \sinh(2|z|)\, a \tag{C.3b}$$

where $\varphi = \mathrm{Arg}(z)$. More precisely

$$\langle \mathcal{O}[a, a^\dagger] \rangle_{|\mathrm{Sq}_z\rangle} = \langle \mathcal{O}[a_z, a_z^\dagger] \rangle_{|0\rangle} \tag{C.4}$$

Applying this relation to the quadrature

$$X_\vartheta = \frac{1}{\sqrt{2}} \left(\mathrm{e}^{\mathrm{i}\vartheta} a + \mathrm{e}^{-\mathrm{i}\vartheta} a^\dagger \right) \tag{C.5}$$

[1] Note that $|\mathrm{Sq}_0\rangle = |0\rangle$.

leads to

$$\langle X_\vartheta \rangle_{|\mathrm{Sq}_z\rangle} = 0 \tag{C.6a}$$

$$\langle (\Delta X_\vartheta)^2 \rangle_{|\mathrm{Sq}_z\rangle} = \frac{1}{2} + \sinh^2(2|z|) \tag{C.6b}$$

$$+ \cosh(2|z|)\sinh(2|z|)\,\cos(2\vartheta + \varphi) \tag{C.6c}$$

which shows that the fluctuations are anisotropic in the Fresnel plane for this harmonic mode, that $\mathrm{Arg}(z)$ determines the principal axes of the ellipsoid of fluctuations. Its extrema are:

$$\max_\vartheta \langle (\Delta X_\vartheta)^2 \rangle_{|\mathrm{Sq}_z\rangle} = \frac{1}{2}\cosh(4|z|) + \frac{1}{2}\sinh(4|z|) = \frac{1}{2}\,\mathrm{e}^{4|z|} \tag{C.7a}$$

$$\min_\vartheta \langle (\Delta X_\vartheta)^2 \rangle_{|\mathrm{Sq}_z\rangle} = \frac{1}{2}\cosh(4|z|) - \frac{1}{2}\sinh(4|z|) = \frac{1}{2}\,\mathrm{e}^{-4|z|} \tag{C.7b}$$

The vacuum fluctuations being given by $1/2$, the state $|\mathrm{Sq}_z\rangle$ appears as squeezed with sub-vacuum fluctuations compressed at most by a factor $\mathrm{e}^{-4|z|} < 1$ as soon as $|z| \neq 0$. Note that with $\vartheta = \omega_0 t$, we recover the non stationary fluctuations of an harmonic mode of energy $\hbar\omega_0$ as a function of time. These fluctuations have pulsation $2\omega_0$.

Since the isotropic part of the fluctuations corresponds to $\frac{1}{2} + \langle a^\dagger a \rangle_{|\mathrm{Sq}_z\rangle}$, Eq. (C.6b) gives us the average photon number in the squeezed vacuum $|\mathrm{Sq}_z\rangle$:

$$\langle a^\dagger a \rangle_{|\mathrm{Sq}_z\rangle} = \sinh^2(2|z|) \tag{C.8}$$

Thinking of this harmonic mode as an optical mode, the above discussion shows that increasing the squeezing parameter z increases the average number of photons. A squeezed vacuum is thus on average more noisy than the true vacuum and moreover, although increasing its squeezing decreases its minimal fluctuations, it also increases its average noise.

Appendix D

Optimal operating point for squeezing detection

In this section, we discuss the optimization problem that appears in squeezing detection.

As discussed in Sec. 4.4.2, this involves finding the maximum value of the modulus of

$$\mathcal{R}(\vartheta,\varphi) = a + b\left(\mathrm{e}^{-\mathrm{i}\varphi} + \mathrm{e}^{\mathrm{i}(\vartheta+\varphi}\right) \tag{D.1}$$

with $(a,b) \in (\mathbb{R}^+)^2$ when varying φ, everything else being fixed. Since

$$|\mathcal{R}(\vartheta,\varphi)|^2 = a^2 + b^2\cos^2\left(\varphi+\frac{\vartheta}{2}\right) + 2ab\cos\left(\frac{\vartheta}{2}\right)\cos\left(\varphi+\frac{\vartheta}{2}\right) \tag{D.2}$$

the maximum value is reached whenever

$$\cos\left(\varphi+\frac{\vartheta}{2}\right) = \mathrm{sign}\left[\cos\left(\frac{\vartheta}{2}\right)\right]$$

and is given by

$$\max_{\varphi}\left[|\mathcal{R}(\vartheta,\varphi)|\right] = \sqrt{a^2+b^2+2ab\left|\cos\left(\frac{\vartheta}{2}\right)\right|}. \tag{D.3}$$

Using Eqs. 4.57 and (4.58) and keeping only the first order in Λ then leads to the following expression for the relative contrast with respect

to the situation where no external radiation is present:

$$\max_{t_e}\left(\frac{\left[X_+^{(\mathrm{dc})}\right]_{\mathrm{Sq}(z)}}{\left[X_+^{(\mathrm{dc})}\right]_{|0\rangle}}\right)=1+\Lambda\left(\eta\cosh(2|z|)\sinh(2|z|)-\sinh^2(2|z|)\right)+\mathcal{O}(\Lambda^2) \tag{D.4}$$

where

$$\eta=\mathrm{e}^{-2\omega_0\tau_e}\left|\cos(2\omega_0\tau_2)\right| \tag{D.5}$$

satisfies $0\leq\eta\leq 1$ and contains the effect of filtering associated with the Leviton's shape in the approximation scheme discussed in Sec. 4.4.2. The function

$$F_\eta(z)=\eta\cosh(2z)\sinh(2|z|)-\sinh^2(2z) \tag{D.6}$$

governs the maximum value of the contrast as first order in Λ as a function of the squeezing parameter z (here taken real positive for simplicity). For $\eta<1$, this function increases from 0 for $z=0$ to a maximum value

$$\max_{z>0}(F_\eta(z))=\frac{1}{2}\left(1-\sqrt{1-\eta^2}\right) \tag{D.7}$$

which is obtained for

$$z_{\mathrm{opt}}=\frac{1}{2}\operatorname{arctanh}(\eta)\,. \tag{D.8}$$

Then it decreases for $z>z_{\mathrm{opt}}$, reaching zero for $z=2z_{\mathrm{opt}}$ and then, it becomes negative. For larger squeezing parameters, it behaves as

$$F_\eta(z)\simeq\frac{1}{2}-\frac{1}{4}(1-\eta)\,\mathrm{e}^{4z}\,. \tag{D.9}$$

For $\eta=1$, $F_1(z)$ grows to its $z\to+\infty$ limit which is $1/2$. To illustrate this point, we have plotted $F_\eta(z)$ as a function of the squeezing parameter (expressed in dB) for various values of η on Fig. D.1.

Finally, this shows that there is an optimal value of squeezing which leads to an absolute minimum of the contrast of the interferences fringes. When one exceeds this optimal value, the lowering of the average base line discussed on page 152 does not compensate the gain associated with transient sub-vacuum fluctuations anymore. Consequently, the maximum achievable contrast is lower than the baseline measured in the absence of external radiation.

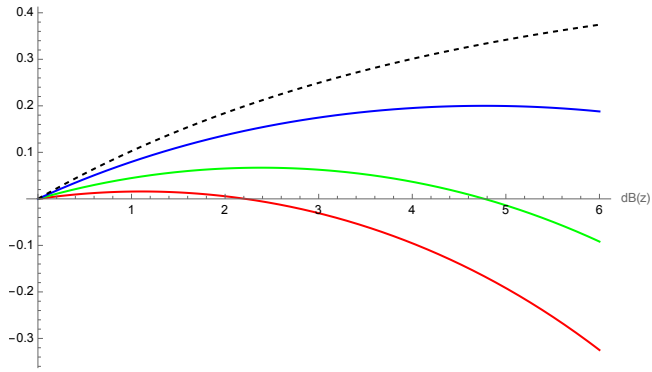

Figure D.1: Plots of $F_\eta(z)$ defined by Eq. (D.6) as a function of z (expressed in dB via Eq. (4.54)) for $\eta = 1/4$ (red curve), $\eta = 1/2$ (green curve) and $\eta = 4/5$ (blue curve) and $\eta = 1$ (dashed curve).

Appendix E

Single EMP detection

We now discuss the evaluation of the parameter $x(t) = 2\pi|\,\langle\chi|S^*_{ba}\Lambda_t\rangle\,|^2$ that appears in the evaluation of the Franck-Condon factor for Fock states (see Eq. (4.66)). The qualitative behavior of this quantity can be understood by using a time/frequency representation of the current noise. The case of a narrow band EMP then leads to analytical approximated expressions for $x(t)$.

E.1 Time frequency analysis of current noise

Using $\widehat{\imath}(\omega) = -e\sqrt{\omega}\,b(\omega)$ $(\omega > 0)$ for a single chiral integer quantum Hall edge channel, $x(t) = 2\pi|\,\langle\chi|S^*_{ba}\Lambda_t\rangle\,|^2$ can be expressed in terms of the excess current noise $\Delta S^{(i)}_{|1;\chi\rangle}(t,t')$ of a single quantum EMP in the mode χ:

$$x(t) = \frac{2\pi^2}{e^2}\int_{\mathbb{R}^2}\Gamma_{ba}(t-t_+)\,\Gamma_{ba}(t-t_-)^*\Delta S^{(i)}_{|1;\chi\rangle}(t_+,t_-)\mathrm{d}t_+\mathrm{d}t_-\,. \quad \text{(E.1)}$$

The physical meaning of this expression is better understood in terms of the Wigner function $\Delta W^{(i)}_\rho(t,\omega)$ of the excess current noise

$$\Delta W^{(i)}_\rho(t,\omega) = \int_{\mathbb{R}}\Big\langle :\widehat{\imath}\Big(t-\frac{\tau}{2}\Big)\widehat{\imath}\Big(t+\frac{\tau}{2}\Big): \Big\rangle_{\rho,c}\,\mathrm{e}^{\mathrm{i}\omega\tau}\mathrm{d}\tau \quad \text{(E.2)}$$

in which $\langle A\,B\rangle_c$ denotes the connected correlator $\langle A\,B\rangle - \langle A\rangle\langle B\rangle$. Introducing the Ville transform associated with $\Gamma_{ba}(t)$:

$$W_{\Gamma_{ba}}(t,\omega) = \int_{\mathbb{R}}\Gamma_{ba}\left(t+\frac{\tau}{2}\right)\,\Gamma_{ba}\left(t-\frac{\tau}{2}\right)\,\mathrm{e}^{\mathrm{i}\omega\tau}\mathrm{d}\tau\,. \quad \text{(E.3)}$$

leads to

$$x(t) = \frac{2\pi^2}{e^2} \int_{\mathbb{R}^2} W_{\Gamma_{ba}}(t-\tau,\omega)\, \Delta W^{(i)}_{|1;\chi\rangle}(\tau,\omega)\, \frac{\mathrm{d}\omega \mathrm{d}\tau}{2\pi}\,. \tag{E.4}$$

This shows that the radiation coupler's response function $\Gamma_{ba}(\tau)$ leads to time-frequency filtering of of the excess quantum current noise of the single EMP state $|1,\chi\rangle$. The time resolution for single EMP detection is thus limited by the duration of the excess current noise associated with the single EMP as well as by the response time of the radiation coupler, typically the time scale appearing in Γ_{ba} (see Sec. 4.2.3).

E.2 Current noise of a single EMP

For the single plasmon with wave-function χ, the average excess current $\langle i(t)\rangle_{|1;\chi\rangle}$ is zero and the Wigner function of the excess current noise defined in Eq. (E.2) is given by

$$\begin{aligned}\Delta W^{(i)}_{|1;\chi\rangle}(t,\omega) = \frac{e^2}{2\pi} \int_{|\Omega|\leq 2|\omega|} \mathrm{e}^{-\mathrm{i}\Omega t} \sqrt{\omega^2 - \frac{\Omega^2}{4}} \\ \times \chi\left(|\omega| + \frac{\Omega}{2}\right) \chi\left(|\omega| - \frac{\Omega}{2}\right)^* \frac{\mathrm{d}\Omega}{2\pi}\,.\end{aligned} \tag{E.5a}$$

In the case of a narrowband single plasmon centered at the energy $\hbar\omega_0$ with Lorentzian linewidth γ_0

$$\chi(\omega) = \frac{\sqrt{\gamma_0}\,\Theta(\omega)}{\omega - \omega_0 + \frac{\mathrm{i}\gamma_0}{2}}\,. \tag{E.6}$$

such that $\gamma_0 \ll \omega_0$, the Wigner function of the excess current noise can be approximated by the usual expression for such energy resolved excitations:

$$\Delta W^{(i)}_{|1;\chi\rangle}(t,\omega) \simeq \Theta(t)\, \frac{e^2\omega_0}{2\pi}\, 4\gamma_0 t\, \mathrm{sinc}\left(2(|\omega| - \omega_0)t\right)\, \mathrm{e}^{-\gamma_0 t}\,. \tag{E.7}$$

E.3 Filtering of current noise

If the EMP has a narrow band compared to the typical scale of variation of $\Gamma_{ba}(\omega)$, the variation of $S_{ba}(\omega)$ around ω_0 can be neglected and this leads to Eq. (4.69). One then recognizes

$$\frac{e^2}{2\pi} \left| \int_0^{+\infty} \sqrt{\omega}\chi(\omega)\, \mathrm{e}^{-\mathrm{i}\omega t} \frac{\mathrm{d}\omega}{\sqrt{2\pi}} \right|^2 = \int_{\mathbb{R}} \Delta W^{(i)}(t,\omega)\, \frac{\mathrm{d}\omega}{2\pi} \tag{E.8}$$

which in turns is related to the average instantaneous heat current carried by the single EMP in state χ. The expression of $\mathcal{J}_Q(t)$ in terms of the current $i(t)$ leads to

$$\langle \mathcal{J}_Q(t) \rangle_\rho = \frac{R_K}{2} \left(\langle i(t) \rangle_\rho^2 + \int_{\mathbb{R}} \Delta W_\rho^{(i)}(t,\omega) \, \frac{\mathrm{d}\omega}{2\pi} \right) \tag{E.9}$$

which then, because $\langle i(t) \rangle_{|1;\chi\rangle} = 0$, enables us to obtain Eq. (4.70) from Eq. (4.69). For a single energy resolved EMP with energy $\hbar\omega_0$ and Lorentzian lineshape of width γ_0, the instantaneous heat current is given by

$$\langle \mathcal{J}_Q(t) \rangle_{|1;\chi\rangle} = \hbar\omega_0 \Theta(t) \, \gamma_0 \, \mathrm{e}^{-\gamma_0 t} \tag{E.10}$$

and carries an average energy $\int_{\mathbb{R}} \langle \mathcal{J}_Q(t) \rangle_{|1;\chi\rangle} \mathrm{d}t = \hbar\omega_0$ as expected.

Bibliography

[1] I. Ahmed, J. A. Haigh, S. Schaal, S. Barraud, Y. Zhu, C.-m. Lee, M. Amado, J. W. A. Robinson, A. Rossi, J. J. L. Morton, and M. F. Gonzalez-Zalba. "Radio-Frequency Capacitive Gate-Based Sensing". In: *Phys. Rev. Applied* 10 (1 July 2018), p. 014018. DOI: 10.1103/PhysRevApplied.10.014018.

[2] C. Altimiras, H. Le Sueur, U. Gennser, A. Cavanna, D. Mailly, and F. Pierre. "Tuning energy relaxation along quantum Hall edge channels". In: *Phys. Rev. Lett.* 105 (2010), p. 226804. DOI: https://doi.org/10.1103/PhysRevLett.105.226804.

[3] C. Altimiras, H. le Sueur, U. Gennser, A. Cavanna, D. Mailly, and F. Pierre. "Non-equilibrium edge channel spectroscopy in the integer quantum Hall regime". In: *Nature Physics* 6 (2010), p. 34.

[4] M. Aluffi, T. Vasselon, S. Ouacel, H. Edlbauer, C. Geffroy, P. Roulleau, D. C. Glattli, G. Georgiou, and C. Bauerle. "Ultrashort electron wavepackets via frequency-comb synthesis". arXiv:2212.12311.

[5] T. Ando, A. Fowler, and F. Stern. "Electronic properties of two-dimensional systems". In: *Review of Modern Physics* 54 (1982), p. 437.

[6] N. Ashcroft and D. Mermin. *Solid state physics*. Saunders College Publishing, 1976.

[7] A. Aspect, J. Dalibard, and G. Roger. "Experimental test of Bell's inequalities using time varying analysers". In: *Phys. Rev. Lett.* 49 (1982), p. 1804.

[8] A. Baca, F. Ren, J. Zolper, R. Briggs, and S. Pearton. "A survey of Ohmic contacts to III-V compound semiconductors". In: *Thin Solid Films* 308-309 (1997), p. 599.

[9] H. Bartolomei, R. Bisognin, H. Kamata, J.-M. Berroir, E. Bocquillon, G. Ménard, B. Plaçais, A. Cavanna, U. Gennser, Y. Jin, P. Degiovanni, C. Mora, and G. Fève. "Observation of edge magnetoplasmon squeezing in a quantum Hall conductor". In preparation. 2022.

[10] H. Bartolomei, M. Kumar, R. Bisognin, A. Marguerite, J.-M. Berroir, E. Bocquillon, B. Plaçais, A. Cavanna, Q. Dong, U. Gennser, Y. Jin, and G. Fève. "Fractional statistics in anyon collisions". In: *Science* 368 (2020), pp. 173–177. DOI: 10.1126/science.aaz5601.

[11] C. Bauerle, D. Glattli, T. Meunier, F. Portier, P. Roche, P. Roulleau, S. Takada, and X. Waintal. "Coherent control of single electrons: a review of current progress". In: *Reports on Progress in Physics* 81 (2018), p. 056503. DOI: 10.1088/1361-6633/aaa98a.

[12] G. Bergmann. "Weak localization in thin films: a time-of-flight experiment with conduction electrons". In: *Physics Reports* 107 (1984), pp. 1–58. DOI: https://doi.org/10.1016/0370-1573(84)90103-0.

[13] A. Bertoni. "Perspectives on solid-state flying qubits". In: *J. Comput. Electron.* 6 (2007), p. 67.

[14] A. Bertoni, P. Bordone, R. Brunetti, C. Jacoboni, and S. Reggiani. "Quantum Logic Gates based on Coherent Electron Transport in Quantum Wires". In: *Phys. Rev. Lett.* 84 (2000), pp. 5912–5915. DOI: 10.1103/PhysRevLett.84.5912.

[15] A. Bertoni. "Charge-Based Solid-State Flying Qubits". In: *Encyclopedia of Complexity and Systems Science*. Ed. by R. A. Meyers. New York, NY: Springer, 2009, pp. 1011–1027. DOI: 10.1007/978-0-387-30440-3_67.

[16] R. Bisognin, H. Bartolomei, M. Kumar, I. Safi, J.-M. Berroir, E. Bocquillon, B. Plaçais, A. Cavanna, Y. Gennser, Y. Jin, and G. Fève. "Microwave photons emitted by fractionally charged quasiparticles". In: *Nature Communications* 10 (2019), p. 1708. DOI: 10.1038/s41467-019-09758-x.

[17] R. Bisognin, A. Marguerite, B. Roussel, M. Kumar, C. Cabart, C. Chapdelaine, A. Mohammad-Djafari, J. .-. Berroir, E. Bocquillon, B. Plaçais, A. Cavanna, U. Gennser, Y. Jin, P. Degiovanni, and G. Fève. "Quantum tomography of electrical currents". In: *Nature*

Communications 10 (2019), p. 3379. DOI: 10.1038/s41467-019-11369-5.

[18] Y. Blanter and M. Buttiker. "Shot noise in mesoscopic conductors". In: *Physics Reports* 336 (2000), p. 1.

[19] Y. Blanter, F. Hekking, and M. Büttiker. "Interaction constants and dynamic conductance of a gated wire". In: *Phys. Rev. Lett.* 81 (1998), p. 1925.

[20] E. Bocquillon, V. Freulon, J.-M. Berroir, P. Degiovanni, B. Plaçais, A. Cavanna, Y. Jin, and G. Fève. "Coherence and indistinguability of single electrons emitted by independent sources". In: *Science* 339 (2013), p. 1054. DOI: 10.1126/science.1232572.

[21] E. Bocquillon. "Electron quantum optics in quantum Hall edge channels". PhD thesis. Université Pierre et Marie Curie, 2012.

[22] E. Bocquillon, V. Freulon, J.-M. Berroir, P. Degiovanni, B. Plaçais, A. Cavanna, Y. Jin, and G. Fève. "Separation between neutral and charge modes in one dimensional chiral edge channels". In: *Nature Communications* 4 (2013), p. 1839. DOI: 10.1038/ncomms2788.

[23] E. Bocquillon, V. Freulon, F. Parmentier, J.-M. Berroir, B. Plaçais, C. Wahl, J. Rech, T. Jonckheere, T. Martin, C. Grenier, D. Ferraro, P. Degiovanni, and G. Fève. "Electron quantum optics in ballistic chiral conductors". In: *Ann. Phys. (Berlin)* 526 (2014), pp. 1–30. DOI: 10.1002/andp.201300181.

[24] E. Bocquillon, F. Parmentier, C. Grenier, J.-M. Berroir, P. Degiovanni, D. Glattli, B. Plaçais, A. Cavanna, Y. Jin, and G. Fève. "Electron quantum optics: partitioning electrons one by one". In: *Phys. Rev. Lett.* 108 (2012), p. 196803.

[25] C. J. Bordé, C. Salomon, S. Avrillier, A. van Lerberghe, C. Bréant, D. Bassi, and G. Scoles. "Optical Ramsey fringes with traveling waves". In: *Phys. Rev. A* 30 (1984), pp. 1836–1848. DOI: 10.1103/PhysRevA.30.1836.

[26] V. B. Braginsky, Y. Vorontsov, and K. Thorne. "Quantum nondemolition measurements". In: *Science* 209 (1980), p. 547.

[27] M. Brune, J. Bernu, C. Guerlin, S. Deléglise, C. Sayrin, S. Gleyzes, S. Kuhr, I. Dotsenko, J. M. Raimond, and S. Haroche. "Process Tomography of Field Damping and Measurement of Fock State Lifetimes by Quantum Nondemolition Photon Counting in a Cavity". In: *Phys. Rev. Lett.* 101 (2008), p. 240402. DOI: 10.1103/PhysRevLett.101.240402.

[28] M. Brune, S. Haroche, J. M. Raimond, L. Davidovich, and N. Zagury. "Manipulation of photons in a cavity by dispersive atom-field coupling: Quantum-nondemolition measurements and generation of "Schrödinger cat" states". In: *Phys. Rev. A* 45 (7 Apr. 1992), pp. 5193–5214. DOI: 10.1103/PhysRevA.45.5193.

[29] O. Brune. "Synthesis of a finite two-terminal network whose driving-point impedance is a prescribed function of frequency". In: *J. Math. and Phys.* 10 (1931), pp. 191–236.

[30] M. Büttiker. "Absence of backscattering in the quantum Hall effect in multiprobe conductors". In: *Phys. Rev* **B** 38 (1988), p. 9375.

[31] M. Büttiker. "Capacitance, admittance and rectification properties of small conductors". In: *J. Phys.: Condens. Matter* 5 (1993), p. 9361.

[32] M. Büttiker, A. Prêtre, and H. Thomas. "Dynamic conductance and the scattering matrix of small conductors". In: *Phys. Rev. Lett.* 70 (1993), p. 4114. DOI: 10.1103/PhysRevLett.70.4114.

[33] M. Büttiker, H. Thomas, and A. Prêtre. "Mesoscopic Capacitors". In: *Phys. Lett. A* 180 (1993), p. 364.

[34] C. Cabart. "Measurement and control of electronic coherences". PhD thesis. Ecole Normale Supérieure de Lyon, 2018.

[35] C. Cabart, B. Roussel, G. Fève, and P. Degiovanni. "Taming electronic decoherence in 1D chiral ballistic quantum conductors". In: *Phys. Rev. B* 98 (2018), p. 155302. DOI: 10.1103/PhysRevB.98.155302.

[36] K. E. Cahill and R. J. Glauber. "Density operators for fermions". In: *Phys. Rev. A* 59 (1999), pp. 1538–1555. DOI: 10.1103/PhysRevA.59.1538.

[37] V. Calero, M. .-. Suarez, R. Salut, F. Baida, A. Caspar, F. Behague, N. Courjal, L. Galtier, L. Gillette, L. Duvillaret, G. Gaborit, and M. .-. Bernal. "An ultra wideband-high spatial resolution-compact electric field sensor based on Lab-on-Fiber technology". In: *Scientific Reports* 9.1 (2019), p. 8058. DOI: 10.1038/s41598-019-44644-y.

[38] J. Cano, A. C. Doherty, C. Nayak, and D. J. Reilly. "Microwave absorption by a mesoscopic quantum Hall droplet". In: *Phys. Rev. B* 88 (16 Oct. 2013), p. 165305. DOI: 10.1103/PhysRevB.88.165305.

[39] O. Carnal and J. Mlynek. "Young's double-slit experiment with atoms: A simple atom interferometer". In: *Phys. Rev. Lett.* 66 (1991), pp. 2689–2692. DOI: 10.1103/PhysRevLett.66.2689.

[40] A. H. Castro Neto, F. Guinea, N. M. R. Peres, K. S. Novoselov, and A. K. Geim. "The electronic properties of graphene". In: *Rev. Mod. Phys.* 81 (2009), pp. 109–162. DOI: 10.1103/RevModPhys.81.109.

[41] W. Cauer. "Die Verwirklichung der Wechselstromwiderst ände vorgeschriebener Frequenzabh ängigkeit". In: *Archiv für Elektrotechnik* 17 (1926), pp. 355–388.

[42] J. Chalker, Y. Gefen, and M. Veillette. "Decoherence and interactions in an electronic Mach-Zehnder interferometer". In: *Phys. Rev. B* 76 (2007), p. 085320.

[43] D. Chen, H. Zhang, J. Sun, M. Pandit, G. Sobreviela, Y. Wang, Q. Zhang, X. Chen, A. Seshia, and J. Xie. "Ultrasensitive Resonant Electrometry Utilizing Micromechanical Oscillators". In: *Phys. Rev. Applied* 14 (1 July 2020), p. 014001. DOI: 10.1103/PhysRevApplied.14.014001.

[44] A. Cho and J. Arthur. "Molecular beam epitaxy". In: *Progress in Solid State Chemistry* 10 (1975), pp. 157–191.

[45] T. Christen and M. Büttiker. "Low frequency admittance of a quantum point contact". In: *Phys. Rev. Lett.* 77 (1996), p. 143.

[46] T. Christen and M. Büttiker. "Low frequency admittance of quantized Hall conductors". In: *Phys. Rev. B* 53 (1996), p. 2064.

[47] A. N. Cleland and M. L. Roukes. "A nanometre-scale mechanical electrometer". In: *Nature* 392.6672 (1998), pp. 160–162. DOI: 10.1038/32373.

[48] L. Cohen. “Generalized Phase-Space Distribution Functions”. In: *Journal of Mathematical Physics* 7 (2005), pp. 781–786. DOI: 10.1063/1.1931206.

[49] E. Condon. “A Theory of Intensity Distribution in Band Systems”. In: *Phys. Rev.* 28 (6 Dec. 1926), pp. 1182–1201. DOI: 10.1103/PhysRev.28.1182.

[50] A. D. Cronin, J. Schmiedmayer, and D. E. Pritchard. “Optics and interferometry with atoms and molecules”. In: *Rev. Mod. Phys.* 81 (3 July 2009), pp. 1051–1129. DOI: 10.1103/RevModPhys.81.1051.

[51] D. Dasenbrook and C. Flindt. “Dynamical Scheme for Interferometric Measurements of Full-Counting Statistics”. In: *Phys. Rev. Lett.* 117 (14 Sept. 2016), p. 146801. DOI: 10.1103/PhysRevLett.117.146801.

[52] P. Degiovanni, C. Grenier, and G. Fève. “Decoherence and relaxation of single electron excitations in quantum Hall edge channels”. In: *Phys. Rev. B* 80 (2009), 241307(R).

[53] P. Degiovanni, C. Grenier, G. Fève, C. Altimiras, H. le Sueur, and F. Pierre. “Plasmon scattering approach to energy exchange and high-frequency noise in $\nu = 2$ quantum Hall edge channels”. In: *Phys. Rev. B* 81 (2010), 121302(R). DOI: 10.1103/PhysRevB.81.121302.

[54] S. Deléglise, I. Dotsenko, C. Sayrin, J. Bernu, M. Brune, J.-M. Raimond, and S. Haroche. “Reconstruction of non-classical cavity field states with snapshot of their decoherence”. In: *Nature* 455 (2008), p. 510.

[55] A. Delgard, B. Chenaud, U. Gennser, A. Cavanna, D. Mailly, P. Degiovanni, and C. Chaubet. “Coulomb interactions and effective quantum inertia of charge carriers in a macroscopic conductor”. In: *Phys. Rev. B* 104 (2021), p. L121301. DOI: 10.1103/PhysRevB.104.L121301.

[56] A. Delgard, B. Chenaud, U. Gennser, A. Cavanna, D. Mailly, P. Degiovanni, and C. Chaubet. “Supplementary material (Detailed computations and complementary experimental results)”. 2021.

[57] F. Dolde, M. W. Doherty, J. Michl, I. Jakobi, B. Naydenov, S. Pezzagna, J. Meijer, P. Neumann, F. Jelezko, N. B. Manson, and J. Wrachtrup. "Nanoscale Detection of a Single Fundamental Charge in Ambient Conditions Using the NV^- Center in Diamond". In: *Phys. Rev. Lett.* 112 (9 Mar. 2014), p. 097603. DOI: 10.1103/PhysRevLett.112.097603.

[58] J. Dubois, T. Jullien, C. Grenier, P. Degiovanni, P. Roulleau, and D. C. Glattli. "Integer and fractional charge Lorentzian voltage pulses analyzed in the framework of photon-assisted shot noise". In: *Phys. Rev. B* 88 (2013), p. 085301. DOI: 10.1103/PhysRevB.88.085301.

[59] J. Dubois, T. Jullien, F. Portier, P. Roche, A. Cavanna, Y. Jin, W. Wegscheider, P. Roulleau, and D. C. Glattli. "Minimal excitation states for electron quantum optics using Levitons". In: *Nature* 502 (2013), p. 659. DOI: 10.1038/nature12713.

[60] H. Duprez, E. Sivre, A. Anthore, A. Aassime, A. Cavanna, U. Gennser, and F. Pierre. "Transmitting the quantum state of electrons across a metallic island with Coulomb interaction". In: *Science* 366 (2019), pp. 1243–1247. DOI: 10.1126/science.aaw7856.

[61] H. Duprez, E. Sivre, A. Anthore, A. Aassime, A. Cavanna, A. Ouerghi, U. Gennser, and F. Pierre. "Macroscopic Electron Quantum Coherence in a Solid-State Circuit". In: *Phys. Rev. X* 9 (2019), p. 021030. DOI: 10.1103/PhysRevX.9.021030.

[62] A. C. Elitzur and L. Vaidman. "Quantum mechanical interaction-free measurements". In: *Foundations of Physics* 23.7 (1993), pp. 987–997.

[63] A. Facon, E.-K. Dietsche, D. Grosso, S. Haroche, J.-M. Raimond, M. Brune, and S. Gleyzes. "A sensitive electrometer based on a Rydberg atom in a Schrödinger-cat state". In: *Nature* 535.7611 (2016), pp. 262–265. DOI: 10.1038/nature18327.

[64] D. Ferraro, A. Feller, A. Ghibaudo, E. Thibierge, E. Bocquillon, G. Fève, C. Grenier, and P. Degiovanni. "Wigner function approach to single electron coherence in quantum Hall edge channels". In: *Phys. Rev. B* 88 (2013), p. 205303. DOI: 10.1103/PhysRevB.88.205303.

[65] D. Ferraro, B. Roussel, C. Cabart, E. Thibierge, G. Fève, C. Grenier, and P. Degiovanni. "Real-Time Decoherence of Landau and Levitov Quasiparticles in Quantum Hall Edge Channels". In: *Phys. Rev. Lett.* 113 (2014), p. 166403. DOI: 10.1103/PhysRevLett.113.166403.

[66] D. Ferraro, C. Wahl, J. Rech, T. Jonckheere, and T. Martin. "Electronic Hong-Ou-Mandel interferometry in two-dimensional topological insulators". In: *Phys. Rev. B* 89 (7 Feb. 2014), p. 075407. DOI: 10.1103/PhysRevB.89.075407.

[67] D. Ferry and S. Goodnick. *Transport in nanostructures*. Cambridge University Press, 1997.

[68] G. Fève. "Quantification du courant alternatif: la boite quantique comme source d'électrons uniques sub-nanoseconde". PhD thesis. Université Pierre et Marie Curie (Paris 6), 2006.

[69] G. Fève. "Single-electron interferences in Fabry-Perot cavities". Presentation at the final Sequoia Meeting. Oct. 2021.

[70] G. Fève, A. Mahé, J. Berroir, T. Kontos, B. Plaçais, D. C. Glattli, A. Cavanna, B. Etienne, and Y. Jin. "An on-demand single electron source". In: *Science* 316 (2007), p. 1169. DOI: 10.1126/science.1141243.

[71] P. Flandrin. *Explorations in Time-Frequency Analysis*. Cambridge University Press (Cambridge), 2018.

[72] J. D. Fletcher, N. Johnson, E. Locane, P. See, J. P. Griffiths, I. Farrer, D. A. Ritchie, P. W. Brouwer, V. Kashcheyevs, and M. Kataoka. "Continuous-variable tomography of solitary electrons". In: *Nature Communications* 10.1 (2019), p. 5298. DOI: 10.1038/s41467-019-13222-1.

[73] V. Freulon. "Etude de la décohérence de paquets d'onde monoélectroniques dans les canaux de bord de l'effet Hall quantique entier". PhD thesis. Ecole Normale Supérieure, 2014.

[74] V. Freulon, A. Marguerite, J.-M. Berroir, B. Plaçais, A. Cavanna, Y. Jin, and G. Fève. "Hong-Ou-Mandel experiment for temporal investigation of single-electron fractionalization". In: *Nature Communications* 6 (2015), p. 6854. DOI: 10.1038/ncomms7854.

[75] N. Friis. "Reasonable fermionic quantum information theories require relativity". In: *New Journal of Physics* 18.3 (2016), p. 033014.

[76] N. Friis. "Unlocking fermionic mode entanglement". In: *New Journal of Physics* 18.6 (2016), p. 061001.

[77] J. Gabelli, G. Fève, J. Berroir, B. Plaçais, A. Cavanna, B. Etienne, Y. Jin, and D. Glattli. "Violation of Kirchhoff's laws for a coherent RC circuit". In: *Science* 313 (2006), p. 499. DOI: 10.1126/science.1126940.

[78] J. Gabelli, G. Fève, T. Kontos, J.-M. Berroir, B. Plaçais, D. C. Glattli, B. Etienne, Y. Jin, and M. Büttiker. "Relaxation time of a chiral quantum R-L circuit". In: *Phys. Rev. Lett.* 98 (2007), p. 166806.

[79] G. Gasse, C. Lupien, and B. Reulet. "Observation of squeezing in the electron quantum shot noise of a tunnel junction". In: *Phys. Rev. Lett.* 111 (2013), p. 136601. DOI: 10.1103/PhysRevLett.111.136601.

[80] A. K. Geim and K. S. Novoselov. "The rise of graphene". In: *Nature Materials* 6 (2007), pp. 183–191. DOI: 10.1038/nmat1849.

[81] G. Georgiou, C. Geffroy, C. Bäuerle, and J.-F. Roux. "Efficient Three-Dimensional Photonic–Plasmonic Photoconductive Switches for Picosecond THz Pulses". In: *ACS Photonics* 7 (2020), pp. 1444–1451. DOI: 10.1021/acsphotonics.0c00044.

[82] T. Giamarchi. *Quantum physics in one dimension*. Oxford university Press, 2003.

[83] D. Glattli. "Quantum shot noise of conductors and general noise measurement methods". In: *Eur. Phys. J. Special Topics* 172 (2009), p. 163. DOI: doi.org/10.1140/epjst/e2009-01049-y.

[84] D. Glattli, P. Jacques, A. Kumar, P. Pari, and L. Saminadayar. "A noise detection scheme with 10 mK noise temperature resolution for semiconductor single electron devices". In: *J. Appl. Phys.* 81 (1997), pp. 7350–7356.

[85] D. Glattli, A. Kumar, L. Saminadayar, Y. Jin, and B. Etienne. "Experimental test of the quantum shot noise reduction theory". In: *Physica* **B** 227 (1994), p. 161.

[86] R. Glauber. "Photon correlations". In: *Phys. Rev. Lett.* 10 (1962), p. 84.

[87] R. Glauber. "The quantum theory of optical coherence". In: *Phys. Rev.* 130 (1963), p. 2529. DOI: 10.1103/PhysRev.130.2529.

[88] S. Gleyzes, S. Kuhr, C. Guerlin, J. Bernu, S. Deléglise, U. Busk Hoff, M. Brune, J.-M. Raimond, and S. Haroche. "Quantum jumps of light recording the birth and death of a photon in a cavity". In: *Nature* 446 (2007), p. 297.

[89] P. L. Gould, G. A. Ruff, and D. E. Pritchard. "Diffraction of atoms by light: The near-resonant Kapitza-Dirac effect". In: *Phys. Rev. Lett.* 56 (1986), pp. 827–830. DOI: 10.1103/PhysRevLett.56.827.

[90] C. Grenier. "Electron quantum optics". PhD thesis. Ecole Normale Supérieure de Lyon, 2011.

[91] C. Grenier, J. Dubois, T. Jullien, P. Roulleau, D. C. Glattli, and P. Degiovanni. "Fractionalization of minimal excitations in integer quantum Hall edge channels". In: *Phys. Rev. B* 88 (2013), p. 085302. DOI: 10.1103/PhysRevB.88.085302.

[92] C. Grenier, R. Hervé, E. Bocquillon, F. Parmentier, B. Plaçais, J.-M. Berroir, G. Fève, and P. Degiovanni. "Single electron quantum tomography in quantum Hall edge channels". In: *New Journal of Physics* 13 (electron quantum optics, 2011), p. 093007. DOI: 10.1088/1367-2630/13/9/093007.

[93] C. Grenier, R. Hervé, G. Fève, and P. Degiovanni. "Electron quantum optics in quantum Hall edge channels". In: *Mod. Phys. Lett. B* 25 (2011). Proceedings of the Statphys 24 satellite meeting "International Conference on Frustrated Spin Systems, Cold Atoms and Nanomaterials" (Hanoi, 14-16 July 2010), pp. 1053–1073.

[94] C. Guerlin, J. Bernu, S. Deléglise, C. Sayrin, S. Gleyzes, S. Kuhr, M. Brune, J.-M. Raimond, and S. Haroche. "Progressive field-state collapse and quantum non-demolition photon counting". In: *Nature* 448 (2007), p. 889.

[95] G. Haack, M. Moskalets, and M. Büttiker. "Glauber coherence of single electron sources". In: *Phys. Rev. B* 87 (2013), 201302(R). DOI: 10.1103/PhysRevB.87.201302.

[96] G. Haack, M. Moskalets, J. Splettstoesser, and M. Büttiker. "Coherence of single-electron sources from Mach-Zehnder interferometry". In: *Phys. Rev. B* 84 (2011), 081303(R). DOI: 10.1103/PhysRevB.84.081303.

[97] J. L. Hall. "Nobel Lecture: Defining and measuring optical frequencies". In: *Rev. Mod. Phys.* 78 (2006), pp. 1279–1295. DOI: 10.1103/RevModPhys.78.1279.

[98] B. I. Halperin, A. Stern, I. Neder, and B. Rosenow. "Theory of the Fabry-Pérot quantum Hall interferometer". In: *Phys. Rev. B* 83 (2011), p. 155440. DOI: 10.1103/PhysRevB.83.155440.

[99] S. Haroche, M. Brune, and J. M. Raimond. "From cavity to circuit quantum electrodynamics". In: *Nature Physics* 16.3 (2020), pp. 243–246. DOI: 10.1038/s41567-020-0812-1.

[100] S. Haroche and J.-M. Raimond. *Exploring the quantum.* Oxford University Press, 2006.

[101] C. Helstrom. "Quantum detection and estimation theory". In: *Journal of Staitstical Physics* 1 (1969), p. 231.

[102] C. Helstrom. *Quantum detection and estimation theory.* Academic Press (New York), 1976.

[103] C. Hong, Z. Ou, and L. Mandel. "Measurement of subpicosecond time intervals between two photons by interference". In: *Phys. Rev. Lett.* 59 (1987), p. 2044.

[104] P.-A. Huynh, F. Portier, H. le Sueur, G. Faini, U. Gennser, D. Mailly, F. Pierre, W. Wegschider, and P. Roche. "Quantum coherence engineering in the integer quantum Hall regime". In: *Phys. Rev. Lett.* 108 (2012), p. 256802. DOI: 10.1103/PhysRevLett.108.256802.

[105] J. Hwang, M. M. Fejer, and W. E. Moerner. "Scanning interferometric microscopy for the detection of ultrasmall phase shifts in condensed matter". In: *Phys. Rev. A* 73 (2 Feb. 2006), p. 021802. DOI: 10.1103/PhysRevA.73.021802.

[106] E. G. Idrisov, I. P. Levkivskyi, and E. V. Sukhorukov. "Dephasing in a Mach-Zehnder Interferometer by an Ohmic Contact". In: *Phys. Rev. Lett.* 121 (2 July 2018), p. 026802. DOI: 10.1103/PhysRevLett.121.026802.

[107] R. Ionicioiu, G. Amaratunga, and F. Udrea. "Quantum computation with ballistic electrons". In: *Int. J. Mod. Phys. B* 15 (2001), p. 125.

[108] Y. Ji, Y. Chung, D. Sprinzak, M. Heiblum, D. Mahalu, and H. Shtrikman. "An electronic Mach-Zenhder interferometer". In: *Nature* 422 (2003), p. 415. DOI: doi:10.1038/nature01503.

[109] M. Johansson. "Comment on 'Reasonable fermionic quantum information theories require relativity'". ArXiv:1610.00539. 2016.

[110] T. Jullien, P. Roulleau, P. Roche, A. Cavanna, Y. Jin, and D. C. Glattli. "Quantum tomography of an electron". In: *Nature* 514 (Oct. 2014), pp. 603–607. DOI: 10.1038/nature13821.

[111] H. Kamata, N. Kumada, M. Hashisaka, K. Muraki, and T. Fujisawa. "Fractionalized wave packets from an artificial Tomonaga-Luttinger liquid". In: *Nature Nanotechnology* 9 (2014), p. 177.

[112] P. L. Kapitza and P. A. M. Dirac. "The reflection of electrons from standing light waves". In: *Mathematical Proceedings of the Cambridge Philosophical Society* 29.2 (1933), pp. 297–300. DOI: 10.1017/S0305004100011105.

[113] V. Kashcheyevs, P. Degiovanni, B. Roussel, M. Kataoka, J. D. Fletcher, L. Freise, N. Ubbelhode, G. Fève, H. Bartolomei, F. Couëdo, A. Kadykov, W. Poirier, P. Roulleau, F. D. Parmentier, and F. Hohls. "Single-electron wave packets for quantum metrology: concepts, implementations and applications". Sequoia project (17FUN04) technical report. 2021. DOI: 10.7795/EMPIR.FUN04.RE.20220228.

[114] J. Keeling, A. Shytov, and L. Levitov. "Coherent particle transfer in an on-demand single-electron source". In: *Phys. Rev. Lett.* 101 (2008), p. 196404. DOI: 10.1103/PhysRevLett.101.196404.

[115] D. W. Keith, C. R. Ekstrom, Q. A. Turchette, and D. E. Pritchard. "An interferometer for atoms". In: *Phys. Rev. Lett.* 66 (1991), pp. 2693–2696. DOI: 10.1103/PhysRevLett.66.2693.

[116] J. R. Klauder, A. C. Price, S. Darlington, and W. J. Albersheim. "The theory and design of chirp radars". In: *The Bell system Technical Journal* 34 (1960), pp. 745–808.

[117] I. Klich. "Full counting statistics". In: *Quantum Noise*. Ed. by Y. V. Nazarov. Kluwer, 2003.

[118] K. v. Klitzing, G. Dorda, and M. Pepper. "New Method for High-Accuracy Determination of the Fine-Structure Constant Based on Quantized Hall Resistance". In: *Phys. Rev. Lett.* 45.6 (Aug. 1980), pp. 494–497. DOI: 10.1103/PhysRevLett.45.494.

[119] N. Kumada, H. Kamata, and T. Fujisawa. "Edge magnetoplasmon transport in gated and ungated quantum Hall systems". In: *Phys. Rev. B* 84 (2011), p. 045314. DOI: 10.1103/PhysRevB.84.045314.

[120] N. Kumada, P. Roulleau, B. Roche, M. Hashisaka, H. Hibino, I. Petkovi ć, and D. C. Glattli. "Resonant Edge Magnetoplasmons and Their Decay in Graphene". In: *Phys. Rev. Lett.* 113 (26 Dec. 2014), p. 266601. DOI: 10.1103/PhysRevLett.113.266601.

[121] Y. Kuznetsova, A. Neumann, and S. R. J. Brueck. "Imaging interferometric microscopy–approaching the linear systems limits of optical resolution". In: *Opt. Express* 15 (2007), pp. 6651–6663. DOI: 10.1364/OE.15.006651.

[122] R. Landauer. "The noise is the signal". In: *Nature* 392 (1998), p. 658.

[123] R. Laughlin. "Anomalous quantum Hall effect: an incompressible quantum fluid with fractionally charged excitations". In: *Phys. Rev. Lett.* 50 (1983), pp. 1395–1398.

[124] L. Levitov, H. Lee, and G. Lesovik. "Electron counting statistics and coherent states of electric current". In: *J. Math. Phys.* 37 (1996), p. 4845.

[125] I. Levkivskyi and E. Sukhorukov. "Energy relaxation at the quantum Hall edge". In: *Phys. Rev. B* 85 (2012), p. 075309.

[126] I. Levkivskyi and E. Sukhorukov. "Dephasing in the electronic Mach-Zehnder interferometer at filling factor $\nu = 2$". In: *Phys. Rev. B* 78 (2008), p. 045322.

[127] I. P. Levkivskyi and E. V. Sukhorukov. "Noise-Induced Phase Transition in the Electronic Mach-Zehnder Interferometer". In: *Phys. Rev. Lett.* 103 (2009), p. 036801. DOI: 10.1103/PhysRevLett.103.036801.

[128] A. I. Lvovsky and M. G. Raymer. "Continuous-variable optical quantum-state tomography". In: *Rev. Mod. Phys.* 81 (2009), pp. 299–332. DOI: 10.1103/RevModPhys.81.299.

[129] A. Mahé, F. Parmentier, E. Bocquillon, J. Berroir, D. Glattli, T. Kontos, B. Plaçais, G. Fève, A. Cavanna, and Y. Jin. "Current correlations of an on-demand single electron source as an evidence of single particle emission". In: *Phys. Rev. B* 82 (2010), p. 201309.

[130] A. Mahé, F. Parmentier, G. Fève, J. Berroir, T. Kontos, A. Cavanna, B. Etienne, Y. Jin, D. Glattli, and B. Plaçais. "Subnanosecond single electron source in the time domain". In: *Journal of Low Temperature Physics* 153 (2008), p. 339.

[131] P. Mailoli, T. Meunier, S. Gleyzes, A. Auffèves, G. Nogués, M. Brune, J.-M. Raimond, and S. Haroche. "Nondestructive Rydberg atoms counting with mesoscopic fields in a cavity". In: *Phys. Rev. Lett.* 94 (2005), p. 113601.

[132] A. Marguerite. "Two-particle interferometry for quantum signal processing". PhD thesis. Université Pierre et Marie Curie (Paris 6), 2017.

[133] A. Marguerite, E. Bocquillon, J.-M. Berroir, B. Plaçais, P. Degiovanni, and G. Fève. "Two-particle interferometry in quatum Hall edge channels". In: *Physica Status Solidi B* 254 (2017), p. 1600618. DOI: 10.1002/pssb.201600618.

[134] A. Marguerite, C. Cabart, C. Wahl, B. Roussel, V. Freulon, D. Ferraro, C. Grenier, J. .-. Berroir, B. Placais, T. Jonckheere, J. Rech, T. Martin, P. Degiovanni, A. Cavanna, Y. Jin, and G. Fève. "Decoherence and relaxation of a single electron in a one-dimensional conductor". In: *Phys. Rev. B* 94 (2016), p. 115311. DOI: 10.1103/PhysRevB.94.115311.

[135] N. Marzari, A. A. Mostofi, J. R. Yates, I. Souza, and D. Vanderbilt. "Maximally localized Wannier functions: Theory and applications". In: *Rev. Mod. Phys.* 84 (2012), pp. 1419–1475. DOI: 10.1103/RevModPhys.84.1419.

[136] M. Misiorny, G. Fève, and J. Splettstoesser. "Shaping charge excitations in chiral edge states with a time-dependent gate voltage". In: *Phys. Rev. B* 97 (7 2018), p. 075426. DOI: 10.1103/PhysRevB.97.075426.

[137] G. Montambaux and E. Akkermans. *Physique mésoscopique des électrons et des photons*. Savoirs Actuels. EDP Sciences, 2004.

[138] M. Moskalets. "Noise of a single-electron emitter". In: *Phys. Rev. B* 88 (2013), p. 035433. DOI: 10.1103/PhysRevB.88.035433.

[139] M. Moskalets. "Single-electron second-order correlation function $G^{(2)}$ at nonzero temperatures". In: *Phys. Rev. B* 98 (2018), p. 115421. DOI: 10.1103/PhysRevB.98.115421.

[140] M. Moskalets. "Two-electron state from the Floquet scattering matrix perspective". In: *Phys. Rev. B* 89 (2014), p. 045402. DOI: 10.1103/PhysRevB.89.045402.

[141] M. Moskalets, G. Haack, and M. Büttiker. "Single-electron source: Adiabatic versus nonadiabatic emission". In: *Phys. Rev. B* 87 (2013), p. 125429.

[142] J. Nakamura, S. Liang, G. C. Gardner, and M. J. Manfra. "Direct observation of anyonic braiding statistics". In: *Nature Physics* 16 (2020), pp. 931–936. DOI: 10.1038/s41567-020-1019-1.

[143] Y. V. Nazarov and M. Kindermann. "Full counting statistics of a general quantum mechanical variable". In: *The European Physical Journal B - Condensed Matter and Complex Systems* 35 (2003), pp. 413–420. DOI: 10.1140/epjb/e2003-00293-1.

[144] C. Neuenhahn and F. Marquardt. "Dephasing by electron-electron interactions in a ballistic interferometer". In: *New Journal of Physics* 10 (2008), p. 115018.

[145] C. Neuenhahn and F. Marquardt. "Universal dephasing in a chiral 1D interacting fermion system". In: *Phys. Rev. Lett.* 102 (2009), p. 046806.

[146] S. Nigg, R. Lòpez, and M. Büttiker. "Mesoscopic charge relaxation". In: *Phys. Rev. Lett.* 97 (2006), p. 206804.

[147] K. S. Novoselov, A. K. Geim, S. V. Morozov, D. Jiang, M. I. Katsnelson, I. V. Grigorieva, S. V. Dubonos, and A. A. Firsov. "Two-dimensional gas of massless Dirac fermions in graphene". In: *Nature* 438 (2005), pp. 197–200. DOI: 10.1038/nature04233.

[148] F. D. Parmentier, E. Bocquillon, J.-M. Berroir, D. Glattli, B. Plaçais, G. Fève, M. Albert, C. Flindt, and M. Büttiker. "Current noise spectrum of a single-particle emitter: Theory and experiment". In: *Phys. Rev. B* 85 (2012), p. 165438. DOI: 10.1103/PhysRevB.85.165438.

[149] F. Parmentier, A. Mahé, A. Denis, J.-M. Berroir, D. Glattli, B. Plaçais, and G. Fève. "A high sensitivity ultra-low temperature RF conductance and noise measurement setup". In: *Rev. Sci. Instrum.* 82 (2011), p. 013904.

[150] B. Peaudecerf, T. Rybarczyk, S. Gerlich, S. Gleyzes, J. M. Raimond, S. Haroche, I. Dotsenko, and M. Brune. "Adaptive Quantum Nondemolition Measurement of a Photon Number". In: *Phys. Rev. Lett.* 112 (2014), p. 080401. DOI: 10.1103/PhysRevLett.112.080401.

[151] L. Pezzè, A. Smerzi, M. K. Oberthaler, R. Schmied, and P. Treutlein. "Quantum metrology with nonclassical states of atomic ensembles". In: *Rev. Mod. Phys.* 90 (2018), p. 035005. DOI: 10.1103/RevModPhys.90.035005.

[152] R. de Picotto, M. Reznikov, M. Heiblum, V. Umansky, G. Bunin, and D. Mahalu. "Direct observation of a fractional charge". In: *Nature* 389 (1997), p. 162.

[153] D. Pines and P. Nozières. *The theory of quantum liquids*. Perseus Book, 1966.

[154] A. Prêtre, H. Thomas, and M. Büttiker. "Dynamics admittance of mesoscopic conductors: discrete potential model". In: *Phys. Rev. B* 54 (1996), p. 8130.

[155] J. G. Proakis and M. Salehi. *Communication Systems Engineering*. 2nd edition. Prentice Hall, Inc., 2001.

[156] J. Radon. "On the determination of functions from their integral values along certain manifolds". In: *IEEE Transactions on Medical Imaging* 5 (1986), pp. 170–176. DOI: 10.1109/TMI.1986.4307775.

[157] G. Rebora, D. Ferraro, R. H. Rodriguez, F. D. Parmentier, P. Roche, and M. Sassetti. "Electronic Wave-Packets in Integer Quantum Hall Edge Channels: Relaxation and Dissipative Effects". In: *Entropy* 23.2 (2021). DOI: 10.3390/e23020138.

[158] M. Richards. *Fundamentals of radar signal processing*. 2nd edition. McGraw Hill Higher Education, 2014.

[159] R. Rodriguez, F. Parmentier, D. Ferraro, P. Roulleau, U. Gensser, A. Cavanna, M. Sassetti, F. Portier, D. Mailly, and P. Roche. "Relaxation and revival of quasiparticles injected in an interacting quantum Hall liquid". In: *Nature Communications* 11 (2020), p. 2426. DOI: 10.1038/s41467-020-16331-4.

[160] P. Roulleau, F. Portier, P. Roche, A. Cavanna, G. Faini, U. Gennser, and D. Mailly. "Tuning Decoherence with a Voltage Probe". In: *Phys. Rev. Lett.* 102.23 (June 2009), p. 236802. DOI: 10.1103/PhysRevLett.102.236802.

[161] P. Roulleau, F. Portier, P. Roche, A. Cavanna, G. Faini, U. Gennser, and D. Mailly. "Direct Measurement of the Coherence Length of Edge States in the Integer Quantum Hall Regime". In: *Phys. Rev. Lett.* 100 (2008), p. 126802. DOI: 10.1103/PhysRevLett.100.126802.

[162] B. Roussel. "Autopsie d'un courant électrique quantique". PhD thesis. Université de Lyon, 2017.

[163] B. Roussel, C. Cabart, G. Fève, and P. Degiovanni. "Processing quantum signals carried by electrical currents". In: *Physical Review X Quantum* 2 (2021), p. 020314.

[164] B. Roussel, C. Cabart, G. Fève, E. Thibierge, and P. Degiovanni. "Electron quantum optics as quantum signal processing". In: *Physica Status Solidi B* 254 (2017), p. 16000621. DOI: 10.1002/pssb.201600621.

[165] B. Roussel, P. Degiovanni, and I. Safi. "Perturbative fluctuation dissipation relation for nonequilibrium finite-frequency noise in quantum circuits". In: *Phys. Rev. B* 93 (4 Jan. 2016), p. 045102. DOI: 10.1103/PhysRevB.93.045102.

[166] G. Roussely, E. Arrighi, G. Georgiou, S. Takada, M. Schalk, M. Urdampilleta, A. Ludwig, A. D. Wieck, P. Armagnat, T. Kloss, X. Waintal, T. Meunier, and C. Bäuerle. "Unveiling the bosonic nature of an ultrashort few-electron pulse". In: *Nature Communications* 9.1 (2018), p. 2811. DOI: 10.1038/s41467-018-05203-7.

[167] I. Safi. "A dynamic scattering approach for a gated interacting wire". In: *Eur. Phys. J.* **D** 12 (1999), p. 451. DOI: 10.1007/s100510051026.

[168] I. Safi and H. J. Schulz. "Transport in an inhomogeneous interacting one-dimensional system". In: *Phys. Rev. B* 52 (24 Dec. 1995), R17040–R17043. DOI: 10.1103/PhysRevB.52.R17040.

[169] I. Safi and H. Schulz. "Transport through a single band wire connected to measuring leads". In: *Quantum Transport in Semiconductor Submicron Structures*. Ed. by B. Kramer. Kluwer Academic Press, Dordrecht, 1995, p. 159.

[170] I. Safi. "Fluctuation-dissipation relations for strongly correlated out-of-equilibrium circuits". In: *Phys. Rev. B* 102 (4 2020), p. 041113. DOI: 10.1103/PhysRevB.102.041113.

[171] L. Saminadayar, D. Glattli, Y. Jin, and B. Etienne. "Observation of the $e/3$ fractionally charged Laughlin quasi-particle". In: *Phys. Rev. Lett.* 79 (1997), pp. 2526–2529.

[172] L. Saminadayar, P. Mohanty, R. Webb, P. Degiovanni, and C. Bauerle. "Electron coherence at low temperatures: the role of magnetic impurities". In: *Physica E* 40 (2007), p. 12.

[173] T. Shen, G. Gao, and H. Morkoç. "Recent developments in Ohmic contacts for III-V compound semiconductors". In: *Journal of Vacuum Science and Technology B* 10 (1992), p. 2113.

[174] J. Singleton. *Band theory and electronic properties of solids*. Oxford: Oxford University Press, 2001.

[175] K. S. Singwi and A. Sjölander. "Resonance Absorption of Nuclear Gamma Rays and the Dynamics of Atomic Motions". In: *Phys. Rev.* 120 (1960), pp. 1093–1102. DOI: 10.1103/PhysRev.120.1093.

[176] A. O. Slobodeniuk, E. G. Idrisov, and E. V. Sukhorukov. "Relaxation of an electron wave packet at the quantum Hall edge at filling factor $\nu = 2$". In: *Phys. Rev. B* 93 (2016), p. 035421. DOI: 10.1103/PhysRevB.93.035421.

[177] A. O. Slobodeniuk, I. P. Levkivskyi, and E. V. Sukhorukov. "Equilibration of quantum Hall edge states by an Ohmic contact". In: *Phys. Rev. B* 88 (16 Oct. 2013), p. 165307. DOI: 10.1103/PhysRevB.88.165307.

[178] S. Slussarenko and G. Pryde. "Photonic quantum information processing: a concise review". In: *Applied Physics Review* 6 (2019), p. 041303.

[179] D. T. Smithey, M. Beck, M. G. Raymer, and A. Faridani. "Measurement of the Wigner distribution and the density matrix of a light mode using optical homodyne tomography: Application to squeezed states and the vacuum". In: *Phys. Rev. Lett.* 70 (1993), p. 1244. DOI: 10.1103/PhysRevLett.70.1244.

[180] D. Strickland and G. Mourou. "Compression of amplified chirped optical pulses". In: *Optics Communications* 55 (1985), pp. 447–449. DOI: https://doi.org/10.1016/0030-4018(85)90151-8.

[181] E. Sukhorukov, A. Jordan, S. Gustavsson, R. Leturq, T. Ihn, and K. Ensslin. "Conditional statistics of electron transport in interacting nanoscale conductors". In: *Nature Physics* 3 (2007), p. 243.

[182] S. Sze. *Semiconductor devices: physics and technology*. 2nd edition. John Wiley and Sons, Inc., 2002.

[183] S. Tewari, P. Roulleau, C. Grenier, F. Portier, A. Cavanna, U. Gennser, D. Mailly, and P. Roche. "Robust quantum coherence above the Fermi sea". In: *Phys. Rev. B* 93 (2016), p. 035420. DOI: 10.1103/PhysRevB.93.035420.

[184] E. Thibierge. "Cohérence à un et deux électrons en optique quantique électronique". PhD thesis. Ecole Normale Supérieure de Lyon, 2015.

[185] E. Thibierge, D. Ferraro, B. Roussel, C. Cabart, A. Marguerite, G. Fève, and P. Degiovanni. "Two-electron coherence and its measurement in electron quantum optics". In: *Phys. Rev. B* 93 (2016), 081302(R). DOI: 10.1103/PhysRevB.93.081302.

[186] D. C. Tsui, H. L. Stormer, and A. C. Gossard. "Two-dimensional magnetotransport in the extreme quantum limit". In: *Phys. Rev. Lett.* 48 (1982), p. 1559.

[187] R. Tung. "The physics and chemistry of the Schottky barrier height". In: *Applied Physics Review* 1 (2014), p. 011304.

[188] C. Tzara. "Diffusion des photons sur les atomes et les noyaux dans les cristaux". In: *J. Phys. Radium* 22 (1961), pp. 303–307.

[189] C. Wahl, J. Rech, T. Jonckheere, and T. Martin. "Interactions and charge fractionalization in an electronic Hong-Ou-Mandel interferometer". In: *Phys. Rev. Lett.* 112 (2014), p. 046802.

[190] G. Wannier. "The structure of electronic excitation levels in insulating crystal". In: *Physical Review* 52 (1937), p. 191.

[191] G. C. Wick, A. S. Wightman, and E. P. Wigner. "The Intrinsic Parity of Elementary Particles". In: *Phys. Rev.* 88 (1 Oct. 1952), pp. 101–105. DOI: 10.1103/PhysRev.88.101.

[192] P. Woodward. *Probability and information theory, with applications to radar*. McGraw-Hill, New York, 1953.

[193] E. Zakka-Bajjani, J. Ségala, F. Portier, P. Roche, D. Glattli, A. Cavanna, and Y. Jin. "Experimental test of the high frequency quantum shot noise theory in a quantum point contact". In: *Phys. Rev. Lett.* 99 (2007), p. 236803.

[194] T. Zibold, P. Vogl, and A. Bertoni. "Theory of semiconductor quantum-wire-based single- and two-qubit gates." In: *Phys. Rev. B* 76 (2007), p. 195301.

[195] J. Ziman. *Principles of the theory of solids*. Cambridge University Press, 1972.

Summary

Recent advances in quantum nano-electronics have lead to the manufacturing of electrical circuits in which quantum electrical currents involving one to a few electrons can be generated controlled and characterized. This breakthrough has spurred the development of sophisticated quantum sensing technologies, such as the electron quantum radar (EQR) introduced in this work.

The EQR is an interferometric sensor leveraging both the sensitivity to electromagnetic fields and the long coherence time of single electrons to probe the quantum state of microwave radiations with sub nanosecond time resolution. It is designed as a Mach-Zehnder interferometer (MZI) with one branch coupled to the radiation to be probed. As a single-electron propagates along both branches of the MZI, its wave function is altered by the radiation. This shift is imprinted in the interferences contribution to the average electrical current exiting the interferometer which then provides information about the radiation.

Part of this work focuses on the shaping of single electron wave-packets and on the design of the radiation coupler which coupled the incoming single electron to the electromagnetic radiation to be probed. These two elements determine the EQR's resolving power for each probed radiation. Finally, the EQR's sensing capabilities are evaluated through specific examples, such as probing squeezed states or single photon detection, demonstrating its potential to measure properties of quantum radiation in both time and frequency domains in realistic forthcoming experiments.

Keywords: electron quantum optics, quantum coherence, electronic interferences, Coulomb interaction, quantum sensing quantum optics,

Résumé

Les progrès récents en nanoélectronique quantique ont permis la fabrication de circuits permettant de générer, contrôler et caractériser des courants constitués de un à quelques électrons. Cette percée a engendré de nouvelles technologies quantiques de détection, telles que le radar quantique à électrons (RQE) présenté dans cette thèse.

Le RQE est un capteur exploitant la sensibilité aux champs électromagnétiques et la cohérence d'électrons uniques pour sonder l'état quantique d'un rayonnement micro-ondes avec une résolution temporelle sub-nanoseconde. Il est conçu comme un interféromètre de Mach-Zehnder (IMZ) dont l'une des branches est couplée au champ à sonder. En traversant l'interféromètre, la fonction d'onde d'un électron est modifiée par le rayonnement. Ce changement est encodé dans les interférences contenues dans le courant électrique moyen sortant de l'IMZ qui permettent de remonter à des informations sur le rayonnement.

Deux chapitres sont consacrés au design du coupleur, couplant les électrons au champ électromagnétiques à sonder, ainsi qu'à la modulation des états monoélectroniques injectés. Ces deux éléments déterminent en grande partie le pouvoir de résolution du RQE pour un rayonnement donné. Enfin nous discutons la capacité du RQE à sonder des champs électromagnétiques aux temps courts sur des exemples spécifiques, tel que la mesure du bruit non stationnaire d'un vide quantique comprimé ou la détection de photons uniques. On montre ainsi son potentiel pour résoudre en temps et en fréquence les propriétés d'un rayonnement quantique.

Mots-clés: optique quantique électronique, cohérence quantique, interférences électroniques, interaction Coulombienne, détecteurs quantiques, optique quantique,